Study of the Galactic Center and dark matter search with H.E.S.S.

Lucia Rinchiuso

▶ **To cite this version:**

Lucia Rinchiuso. Study of the Galactic Center and dark matter search with H.E.S.S.. High Energy Astrophysical Phenomena [astro-ph.HE]. Université Paris Saclay (COmUE), 2019. English. NNT : 2019SACLS180 . tel-02298659

HAL Id: tel-02298659

https://theses.hal.science/tel-02298659

Submitted on 27 Sep 2019

HAL is a multi-disciplinary open access archive for the deposit and dissemination of scientific research documents, whether they are published or not. The documents may come from teaching and research institutions in France or abroad, or from public or private research centers.

L'archive ouverte pluridisciplinaire **HAL**, est destinée au dépôt et à la diffusion de documents scientifiques de niveau recherche, publiés ou non, émanant des établissements d'enseignement et de recherche français ou étrangers, des laboratoires publics ou privés.

université PARIS-SACLAY

UNIVERSITÉ PARIS SUD
Comprendre le monde, construire l'avenir

Irfu - CEA Saclay
Institut de recherche sur les lois fondamentales de l'Univers

NNT : 2019SACLS180

Thèse de doctorat

Study of the Galactic Center and dark matter search with H.E.S.S.

Thèse de doctorat de l'Université Paris-Saclay
préparée à Université Paris-Sud

Ecole doctorale n°576 Particules, Hadrones, Énergie et Noyau: Instrumentation, Imagerie, Cosmos et Simulation (PHENIICS)
Spécialité de doctorat: Astroparticules et Cosmologie

Thèse présentée et soutenue à Saclay, le 3 juillet, par

LUCIA RINCHIUSO

Composition du Jury :

Réza ANSARI Professeur, Université Paris-Sud (LAL)	Président
Gautier HAMEL DE MONCHENAULT Directeur de recherche, CEA (IRFU/SPP)	Examinateur
Frédéric MAYET Professeur, Université Grenoble Alpes (LPSC)	Rapporteur
Aldo MORSELLI Directeur de recherche, INFN - Università di Roma "Tor Vergata"	Examinateur
Emmanuel MOULIN Chercheur, CEA (IRFU/DPhP)	Directeur de thèse
Reshmi MUKHERJEE Professeur, Barnard College - Columbia University	Rapporteur

Astronomy compels the soul to look upward,
and leads us from this world to another.
Plato

Acknowledgment

First I want to thank Emmanuel for supervising me during these 3 years of PhD. For sharing his passion for science and his enthusiasm. For dealing with my "Italian drama" moments. Thanks to the referees for improving my thesis with their suggestions and for the appreciation of my work (it means a lot to me!). And thanks to all the members of the jury for reading my manuscript and for the interesting discussions raised by their questions.
I want to thank the H.E.S.S. group at CEA for teaching me a lot and for all the meals that we shared. For the mentoring in science and for helping me to improve my French.
Thanks to Bertrand for being my mentor at CEA.

A huge thank to the other students of the H.E.S.S. group at CEA, Monica, Halim, Anke, Matthias and Yann, for sharing the joy and pain of this PhD and for the fun moments spent together also outside the lab. A special thank to Monica for sharing the office, as well as the hype and the desperate moments of this last tough year.
Thanks to the current and former PhD students at CEA for the Friday lunch and the hilarious emails.

I want to thank the H.E.S.S. colleagues who always treated me as equal even if I was the last arrived. A special thank to Mathieu and Jean-Philippe for the exchanges about the software, and to the Editorial Boards and A&R reviewers of my papers. I want to thank Louise for bringing together the *Glory Duck* group, and Aion for being the postdoc that was missing here in my lab. Thanks also to Denys, Vincent and Celine for being the heart of the astroparticle working group.

Thanks to the PhD students and postdocs from H.E.S.S. for sharing science, but also some fun moments and a beer. A special thank to Daniel for his parties, Michelle and Anton for the great moments at the summer school, Marion for the adventure on the road in Namibia (so much fun and empowering) and Gabriel for the support in and out the hospital on shift.
A big thank also to the "invisible" part of H.E.S.S. that makes all our work possible. Thanks to the on-site crew and personnel for teaching me so much and for sharing life stories. It

was an enriching experience.

Thanks to Claire, Kumiko and Joe for the work together on our project about the Galactic Center excess.
A great thank to Nick and Tracy for the fruitful collaboration and the time spent discussing on our projects. It was a great opportunity for a deep exchange between theory and experiment. Thanks also to Oscar for joining our second project.

Thanks to the old and new friends from the summer school, in particular Carlo, Enrico, Federica, Ottavio, Nandita, Giada and Matteo with whom I shared hilarious moments and that fought the angry seagulls with me.
Thanks to all the people that I met during my travels that taught me that there are many ways to be yourself, enjoy life and build your own future.
Thanks to the former NPAC and Erasmus students with some of which we are still in touch. Those 6 months will always be one of the most incredible periods of my life.
Thanks to the friends from all over the world that have joined this part of my life.
I want to thank also the friends from Elegua for bringing some *calor latino* in this gray city.

Thanks to my friends in Italy, in particular Romina, Benedetta, Zo and Erry because despite the distance every time that I'm back it feels as if I had never left.
A huge thank to the Italian Corner for being my foster family in Paris. For being the brothers and sisters (and sometimes kids :p) that I've never had.
Thanks to Pedro for being a wonderful surprise in my life that made my everyday better, being able to appreciate the mess that I am and understand my weirdness.

Last but not least, thanks to my family (my parents and my grandma) for supporting me even when it means setting me free and for the unconditional love that goes beyond time and distance.

Table of contents

Acknowledgment i

List of figures xi

List of tables xvii

Synthèse xix

Introduction xxxvi

I High energy astrophysics with H.E.S.S. 1

1 Very-high-energy gamma rays 3

1.1 Preamble . . . 4

1.2 Mechanisms of acceleration of cosmic rays . . . 4

1.2.1 Cosmic rays and their spectrum . . . 4

1.2.2 Second order Fermi acceleration . . . 6

1.2.3 First order Fermi acceleration: diffusive shock acceleration . . . 6

1.3 Mechanisms of production of gamma rays . . . 7

1.3.1 Leptonic processes . . . 7

1.3.2 Hadronic processes . . . 8

1.3.3 Dark matter annihilation and decay . . . 9

1.4 Cosmic accelerators . . . 9

1.5 Observations and instruments . . . 11

1.5.1 Satellite experiments . . . 11

1.5.2 Ground-based water tanks . . . 12

1.5.3 Ground-based atmopsheric Cherenkov telescopes . . . 13

1.6 Fundamental physics with very high energy gamma rays . . . 13

2 The H.E.S.S. experiment 15

2.1 Development of air showers and Cherenkov light . . . 16

2.1.1 Development of atmospheric showers . . . 16
2.1.2 Cherenkov light emission . . . 18
2.2 The H.E.S.S. instrument . . . 19
2.2.1 Phase I . . . 20
2.2.2 Phase II . . . 21
2.3 Event identification and selection . . . 22
2.3.1 Trigger definition and quality cuts . . . 22
2.3.2 Calibration . . . 23
2.3.3 Reconstruction and analysis chain . . . 23
2.4 Observation techniques and background measurements . . . 26
2.4.1 Observation modes . . . 26
2.4.2 Background measurement techniques . . . 27
2.5 Instrument response functions (IRFs) and sensitivity . . . 29
2.5.1 Effective area . . . 29
2.5.2 Energy threshold . . . 30
2.5.3 Energy resolution . . . 30
2.5.4 Angular resolution . . . 30
2.6 H.E.S.S. I versus H.E.S.S. II event reconstruction . . . 32
2.6.1 Reconstruction modes . . . 32
2.6.2 Acceptance and sensitivity . . . 32

II The Galactic Center region 35

3 The inner region of the Milky Way 37
3.1 Multi-wavelenght observations of the Galactic Centre region . . . 38
3.2 TeV emitters in the Galactic Center region . . . 41
3.2.1 The inner 50 parsecs . . . 41
3.2.2 G09+01 and HESS J1745-303 . . . 43
3.2.3 H.E.S.S. Galactic plane survey . . . 44
3.3 Diffuse emissions in the GeV-TeV energy ranges . . . 45
3.3.1 The Central Molecular Zone . . . 45
3.3.2 The ‘Galactic Center ridge’ emission . . . 45
3.3.3 Fermi Galactic Diffuse Emission . . . 47
3.3.4 The Galactic Center excess detected by Fermi-LAT . . . 48
3.4 Galactic Center outflows . . . 49
3.4.1 The *Pevatron* . . . 49
3.4.2 Fermi bubbles . . . 51
3.4.3 Radio and X-ray outflows . . . 52

4 Millisecond pulsars and TeV Galactic Center diffuse emission **53**
4.1 Millisecond pulsars population and the Galactic Center excess 54
4.1.1 Explaining the GeV Galactic Center excess seen by Fermi-LAT . . . 54
4.1.2 Connecting the GeV Galactic Center excess and the TeV diffuse emission ? 56
4.2 Millisecond pulsars as PeV proton accelerators 57
4.3 Injection and propagation of accelerated protons 58
4.3.1 Proton injection spectrum of the source 58
4.3.2 Diffusive transport equation 59
4.4 H.E.S.S. diffuse emission and the Fermi-induced MSP population 60
4.4.1 Expected cosmic-ray density distribution 60
4.4.2 Millisecond pulsars population in the Galactic Center region 61
4.4.3 Cosmic-ray density distribution from a bulge and disk population of millisecond pulsars 62
4.4.4 Millisecond pulsars diffuse gamma-ray spectrum and luminosity . . . 63
4.5 Discussion and perspectives 65

5 The Galactic Center region observations with H.E.S.S. II **67**
5.1 The Inner Galaxy Survey 68
5.1.1 Main goals of the survey 68
5.1.2 Observational pointing strategy 69
5.2 The H.E.S.S.-II dataset 71
5.2.1 Observation status before the IGS 71
5.2.2 The IGS campaigns 73
5.3 Observation parameters and data taking 2014-2018 75
5.3.1 Zenith angle and offset distributions 75
5.3.2 Sky time exposure maps 77
5.4 Excess and significance sky maps. 77
5.4.1 Comparison with observations at other wavelengths 79
5.5 Energy spectrum of HESS J1745-290 80
5.6 Outlook 82

III Dark matter quest **85**

6 The invisible Universe: Dark Matter **87**
6.1 From observations to the dark matter paradigm 88
6.1.1 Astrophysical evidences of dark matter 88
6.1.2 The standard cosmological model 90
6.1.3 Cosmological measurements 91

6.1.4 Cosmological parameters and thermal relic density of cold DM particles 95
6.2 Dark matter candidates . . . 96
6.2.1 MACHOs . . . 96
6.2.2 Non-WIMP particles . . . 97
6.2.3 WIMPs . . . 98
6.3 Issues with ΛCDM and alternative theories . . . 99
6.4 Dark matter detection strategies . . . 99
6.4.1 Direct searches . . . 99
6.4.2 Searches at colliders . . . 101
6.4.3 Indirect searches . . . 102
6.4.4 Complementarity of the detection techniques . . . 104
6.5 Dark matter density distributions at Galactic scale . . . 107
6.6 Astrophysical targets for dark matter search with gamma rays . . . 109
6.7 Gamma-ray flux from dark matter annihilation . . . 111
6.8 Dark matter annihilation spectra in gamma rays . . . 112
6.8.1 Continuum signal . . . 112
6.8.2 Mono-energetic γ line . . . 113
6.8.3 Astrophysical and particle physics signal enhancement . . . 114

7 Likelihood analysis technique for the search for dark matter signatures 117
7.1 The likelihood method . . . 118
7.1.1 Definition of the likelihood function . . . 118
7.1.2 The log-likelihood ratio test statistic . . . 119
7.2 Application to dark matter search . . . 119
7.2.1 The likelihood function for a counting experiment . . . 119
7.2.2 Monte Carlo setup . . . 120
7.2.3 Significance of an excess . . . 120
7.2.4 Definition of observed and expected limits . . . 121
7.2.5 Size of the background region . . . 123
7.2.6 Performarces of 1D and 2D-binned versus integrated likelihood . . . 124
7.3 Impact of uncertainties on the limits . . . 125
7.3.1 Statistical uncertainty on the J-factor . . . 125
7.3.2 Systematic uncertainties . . . 126
7.3.3 Impact of the energy resolution . . . 127
7.3.4 Uncertainty on the background residual background determination . 129
7.4 Exclusion versus modeling of background components . . . 129
7.5 The profiling likelihood technique . . . 131
7.6 Summary . . . 133

IV Searches for dark matter with H.E.S.S. data 135

8 Dark matter gamma-line search in the Galactic Center region with H.E.S.S. I 137

8.1 Observations and data set . . . 138
8.1.1 H.E.S.S. observation strategy of the GC . . . 138
8.1.2 Gamma-ray excess and significance sky maps . . . 138
8.2 Construction of the gamma-ray-like event PDFs . . . 139
8.2.1 Choice of the regions of interest . . . 139
8.2.2 Definition of the exclusion regions . . . 142
8.2.3 Energy-dependent event distributions . . . 142
8.3 Residual background measurement in the Galactic Center region . . . 143
8.3.1 The *Reflected Background* method . . . 143
8.3.2 Construction of the energy-dependent background PDFs . . . 145
8.3.3 Expected residual background PDF from blank-field observations . . . 146
8.4 Search for a gamma-ray signal excess . . . 146
8.4.1 Excess significance in each ROI . . . 146
8.4.2 Expected dark matter *gamma line* signal . . . 149
8.5 Constraining the annihilation cross section . . . 150
8.5.1 Expected and observed limits . . . 150
8.5.2 Comparison with other experiments . . . 151
8.5.3 Impact of cuspy dark matter profiles . . . 153
8.6 Study of the sources of systematics uncertainties . . . 154
8.6.1 Energy scale and energy resolution . . . 154
8.6.2 Test of azimuthal symmetry . . . 154
8.6.3 Impact of the Night Sky Background morphology . . . 156
8.7 Discussion and perspectives . . . 157

9 Dark matter signal search with the Inner Galaxy Survey 159

9.1 2014-2018 observational datasets . . . 160
9.1.1 Definition of the regions of interest . . . 160
9.1.2 Exclusion regions for dark matter search with H.E.S.S. II . . . 161
9.2 *Mono* analysis of the IGS data . . . 162
9.2.1 *Mono* effective area . . . 162
9.2.2 Construction of the *ON* and *OFF* event *PDFs* . . . 164
9.2.3 Data unblinding and expected signal . . . 167
9.2.4 Observed and expected constraints on the annihilation cross section 169
9.2.5 Comparison with previous H.E.S.S.-I limits and other experiments . 171
9.3 Towards an *hybrid* analysis of IGS data . . . 172
9.3.1 *Combined* reconstruction . . . 172
9.3.2 Definition of the PDFs in *combined* reconstruction . . . 174

9.4 Outlook and perspectives 176

10 Dark matter searches towards newly detected ultra-faint DES dwarf galaxies 177

10.1 Ultra-faint dwarf galaxies recently detected by DES 178
10.2 H.E.S.S. observations and datasets 179
10.2.1 Selection of targets among DES dSph 179
10.2.2 Gamma-ray excess and significance sky maps 180
10.3 Dark matter density profiles 180
10.3.1 Measured J-factors 180
10.3.2 J-factor statistical and systematic uncertainties 182
10.3.3 Predicting J-factors 183
10.4 ON and OFF PDF measurements 184
10.4.1 Definition of the regions of interest and background measurement . . 184
10.4.2 ON and OFF energy-dependent event PDFs 185
10.5 Constraints on the annihilation cross section 187
10.5.1 Expected and observed limits in different channels 187
10.5.2 Individual versus combined limits 195
10.5.3 Effect of the statistical uncertainty on the J-factor 195
10.5.4 Comparison with other experiments 197
10.6 Outlook and perspectives 198

V Prospects for dark matter searches with Cherenkov telescope arrays 201

11 Search for Wino dark matter towards the Galactic Center with H.E.S.S. 203

11.1 The Wino model : a prototype dark matter candidate 204
11.2 Expected annihilation signal 205
11.2.1 Definition of the regions of interest 205
11.2.2 Total spectrum: line, *endpoint* and *continuum* contributions 206
11.2.3 Cored dark matter profiles 207
11.3 Analysis of mock H.E.S.S.-I-like observations 208
11.3.1 Cosmic-ray background 208
11.3.2 Expected residual background rate in the regions of interest 209
11.4 Forecast limits on Wino annihilation in H.E.S.S.-I-like observations 210
11.4.1 Limits on the annihilation cross section 210
11.4.2 DM distribution at the Galactic Center for pure Wino DM 212
11.5 Prospects for DM search with IGS-like observation strategy. 214
11.5.1 IGS-like region of interest 214

11.5.2 Expected limits for different cored DM profiles 214
11.6 Discussion and perspectives 216

12 Prospects for the study of specific DM models with CTA towards the GC 217
12.1 The Cherenkov Telescope Array 218
12.1.1 A two-site observatory 218
12.1.2 Instrument response functions and flux sensitivity 220
12.2 CTA sensitivity to continuum and line dark matter signals 221
12.2.1 Definition of the region of interest and the expected signal and background 221
12.2.2 Forecast limits on dark matter properties with CTA towards the Galactic Center 222
12.3 Scanning the pMSSM parameter space 223
12.4 CTA sensitivity to heavy weakly-interacting DM 227
12.4.1 Sensitivity to Wino dark matter 227
12.4.2 Higgsino dark matter model 229
12.4.3 Constraints on Higgsino dark matter 230
12.5 Astrophysical backgrounds for CTA 232
12.5.1 Galactic Diffuse Emission 232
12.5.2 Low-latitude Fermi Bubbles templates 235
12.5.3 Point-like Fermi-LAT sources in the field of view 235
12.5.4 Effect of these components on the limits 237
12.6 Discussion and perspectives 238

Conclusions 243

Bibliography 245

List of figures

1.1 Cosmic-ray spectrum. 5
1.2 Sketches of the leptonic mechanisms of production of VHE gamma rays. . . 8
1.3 Sketch of pion decay. 9
1.4 Fermi-LAT instrument. 11
1.5 HAWC observatory site. 12

2.1 Electromagnetic and hadronic showers. 17
2.2 Cherenkov light emitted by an electromagnetic shower in the atmosphere. . 19
2.3 Image of atmospheric showers in the camera. 19
2.4 H.E.S.S. telescopes. 20
2.5 Stereoscopic reconstruction of an air shower. 22
2.6 Mean Scale Shower Goodness 26
2.7 *Standard* background measurement. 28
2.8 *Wobble* background measurement. 28
2.9 H.E.S.S. effective areas as function of the energy. 29
2.10 H.E.S.S. energy resolution and energy bias. 31
2.11 H.E.S.S. angular resolution for the *Model++* and *Hillas* reconstruction chains. 31
2.12 H.E.S.S.-II reconstruction configurations. 32
2.13 H.E.S.S.-II acceptance and sensitivity per reconstruction type. 33

3.1 Sky images of the GC region at different wavelenghts. 39
3.2 H.E.S.S. excess map of the inner 200 pc of the GC region. 42
3.3 Sgr A* composite spectrum. 43
3.4 TeV emission HESS J1745-303 observed by H.E.S.S. in the vicinity of the GC. 44
3.5 Significance excess map of the inner part of the H.E.S.S. Galactic Plane Survey. 46
3.6 Fermi-LAT spectra measured in the GC region and its components. 48
3.7 Differential fluxes for the GeV gamma-ray excess in the $15^\circ \times 15^\circ$ region around the GC. 49
3.8 Gamma-ray excess map of the inner 200 pc of the GC region and zoom on the *Pevatron* emission. 50

3.9 VHE gamma-ray spectrum of the GC diffuse emission and the central source HESS J1745-290, and CRs distribution in the inner 50 pc of the GC region. 50
3.10 Templates of the high-latitude and low-latitude harder Fermi Bubble components. 52

4.1 Schematic of the bulge, the disk and the CMZ, together with their basic characteristics. 55
4.2 Cosmic-ray density $w_{\rm CR}$ in this work for one MSP with and without spallation, compared to the one assumed by H.E.S.S.. 61
4.3 Normalized distribution of MSPs in the Galactic bulge and in the Galactic disk as function of the distance of the sources from the GC. 62
4.4 Total CR density profile in the bulge and in the disk. 63
4.5 Diffuse gamma-ray energy spectrum. 64
4.6 Integrated gamma-ray luminosity above 1 TeV versus distance from the GC. 65

5.1 H.E.S.S.-II NSB map of the GC region. 69
5.2 Schematic of the 14 pointing positions of the Inner Galaxy Survey. 70
5.3 Distribution of the *offset* between the GC position and the pointing position for the GC observations taken in 2014 and 2015. 72
5.4 Zenith angle distributions for the GC observations taken in 2014 and 2015. 72
5.5 Gamma-ray sky acceptance maps in Galactic longitude and latitude for the GC observations taken in 2014 and 2015. 73
5.6 Gamma-ray sky acceptance maps for the IGS obervations in 2016, 2017 and 2018, and overall H.E.S.S.-II acceptance in the full period 2014-2018. 74
5.7 Distribution of the *offset* between the GC position and the pointing position for the IGS observations taken in 2016, 2017 and 2018, and the overall 2014-2018 campaign. 75
5.8 Zenith angle distributions for the IGS observations taken in 2016, 2017 and 2018, and the overall 2014-2018 campaign. 76
5.9 Time exposure maps for H.E.S.S.-I, H.E.S.S.-II and overall observations of the GC region. 78
5.10 Projection of the time exposure maps for H.E.S.S.-I and H.E.S.S.-II observations during the next three years of the IGS. 78
5.11 Gamma-ray excess and significance sky maps for H.E.S.S.-II *CT5 Mono* reconstruction with *Ring Background* analysis. 79
5.12 Gamma-ray significance H.E.S.S.-II map with overlaid H.E.S.S. and CS line emission map significance contours. 80
5.13 H.E.S.S. significance map with overlaid the 5 GHz radio contours by the Green Bank Telescope. 81

5.14 Map of low-latitude Fermi Bubble emission detected by Fermi-LAT with overlapped H.E.S.S. significance contours. 81
5.15 Spectrum of Sgr A* with H.E.S.S.-II *Mono* analysis. 83

6.1 Rotation curve of NGC 3198. 89
6.2 The Abel 1689 galaxy cluster and the Bullet Cluster. 90
6.3 Planck 2018 CMB angular power spectrum as function of the multipole moment. 92
6.4 Maps of part of the 2dF Galaxy Redshift Survey and Sloan Digital Sky Survey and maps obtained with the Millennium simulations for the corresponding portions of the sky. 94
6.5 Summary of direct detection constraints on the spin-independent WIMP-nucleon elastic cross section. 101
6.6 Summary of collider DM searches with ATLAS and CMS in specific models. 103
6.7 Summary of indirect detection constraints on WIMP self-annihilation cross section. 104
6.8 Comparison of DM techniques through simplified models. 106
6.9 Lower limits on the EFT scale as function of the DM mass, compared for indirect, direct and collider searches. 106
6.10 DM density profiles of the Milky Way as function of the distance from the GC. 108
6.11 Tridimensional model of the Galactic halo assuming an Einasto profile. . . . 109
6.12 Gamma-ray spectra from annihilation of DM with mass 1 TeV. 113
6.13 The Sommerfeld effect intensity as function of the DM mass. 115

7.1 Event distributions of mock observations of the inner 1° of the GC for 250 h. 120
7.2 Example expected, observed, mean expected limits and containment bands. 122
7.3 Distribution of the log-values of $\langle\sigma v\rangle$ obtained through 100 realizations of background and signal measurements. 122
7.4 TS versus $\langle\sigma v\rangle$ for different α values. 123
7.5 TS value versus $\langle\sigma v\rangle$ for 2D-, 1D-binned and integrated likelihood 125
7.6 TS versus $\langle\sigma v\rangle$ with and without uncertainty on the J-factor. 126
7.7 Test of the systematic uncertainties on the measurements. 128
7.8 Impact of the energy resolution on a *gamma line*. 128
7.9 TS versus $\langle\sigma v\rangle$ for an uncertainty of 4% on the residual background. 129
7.10 Schematic of the exclusion or subtraction techniques that can be applied to DM search in a gamma-ray crowded region. 130
7.11 Exclusion versus modeling of the background. 131

8.1 Distribution of the observational zenith angle and time exposure map of H.E.S.S.-I GC dataset. 139

8.2 Excess and significance sky maps obtained from a *Ring Background* analysis of 10 years of H.E.S.S. I observations towards the GC. . . . 140
8.3 Integrated J-factor over θ as a function of θ for the Einasto profile and a 1 kpc core. . . . 140
8.4 Schematic of the seven H.E.S.S. ROIs with overlaid the exclusion regions. . 141
8.5 *ON PDFs* in 2D . . . 143
8.6 Schematic representation of an *ON* and a *OFF region* for a pointing position with the *Reflected Background* method. . . . 144
8.7 J-factor maps in Galactic coordinates of some *ON* and *OFF regions*. . . . 145
8.8 *ON* and *OFF* PDFs. . . . 147
8.9 *Measured OFF* and *expected OFF PDFs*. . . . 148
8.10 Expected DM line events distribution overlaid to the *ON* (blue) and *OFF PDFs*. . . . 150
8.11 95% C.L. U.L. on photons flux and DM annihilation cross section from 10 years of observation of the GC region with H.E.S.S. I. . . . 152
8.12 Comparison of H.E.S.S. limits on $\langle\sigma v\rangle$ for the Einasto profile to H.E.S.S., Fermi-LAT, MAGIC and VERITAS previous results and to H.E.S.S. limits obtained for other DM density profiles. . . . 153
8.13 Test of azimuthal symmetry. . . . 155
8.14 Night Sky Background test . . . 156

9.1 Schematic of the ROIs up to 3° with H.E.S.S.-I exclusion regions. . . . 161
9.2 H.E.S.S.-II *Mono* significance map with overlaid exclusion regions for DM search. . . . 162
9.3 H.E.S.S.-II *Mono* effective area for different ranges of *offset*. . . . 164
9.4 *ON* and *OFF PDFs* for ROIs 1 to 15. . . . 165
9.5 *ON* and *OFF PDFs* for ROIs 16 to 25. . . . 166
9.6 H.E.S.S.-II maps of the GC region in Galactic coordinates of some *ON* and *OFF regions*, expressed in terms of J-factor. . . . 168
9.7 95% C.L. H.E.S.S.-II *Mono* upper limits on the DM annihilation cross section in *continuum* channels as function of the DM mass. . . . 170
9.8 H.E.S.S.-II 95% C.L. observed upper limits on $\langle\sigma v\rangle$ vs $m_{\rm DM}$ compared to other previous results. . . . 172
9.9 Number of events reconstructed as gamma rays versus identification number of the telescope for different multiplicities. . . . 173
9.10 *Mono*, *Stereo*, *CT1-4* and overall *Combined PDFs* for DM search in a region of 3° around the GC. . . . 175

10.1 Gamma-ray excess maps for the five DES satellites of the Milky Way. . . . 181

10.2 Integrated measured J-factor in a region of dimension θ for Ret II and Tuc II as function of θ. 182
10.3 *Multiple OFF* regions of Ret II and Tuc IV. 185
10.4 *ON* (red) and *OFF PDFs* (black) for each ROI for each target. No significant gamma-ray excess is observed on any target between the *ON* and *OFF* regions. 186
10.5 95% C.L. upper limits on $\langle\sigma v\rangle$ as function of the DM mass in the W^+W^- annihilation channel on the five DES targets. 188
10.6 95% C.L. upper limits on $\langle\sigma v\rangle$ as function of the DM mass in the $\gamma\gamma$ annihilation channel on the five DES targets. 189
10.7 95% C.L. upper limits on $\langle\sigma v\rangle$ as function of the DM mass in the ZZ, e^+e^-, $\mu^+\mu^-$, $\tau^+\tau^-$, $b\bar{b}$ and $t\bar{t}$ annihilation channels on Ret II. 190
10.8 95% C.L. upper limits on $\langle\sigma v\rangle$ as function of the DM mass in the ZZ, e^+e^-, $\mu^+\mu^-$, $\tau^+\tau^-$, $b\bar{b}$ and $t\bar{t}$ annihilation channels on Tuc II. 191
10.9 95% C.L. upper limits on $\langle\sigma v\rangle$ as function of the DM mass in the ZZ, e^+e^-, $\mu^+\mu^-$, $\tau^+\tau^-$, $b\bar{b}$ and $t\bar{t}$ annihilation channels on Tuc III. 192
10.10 95% C.L. upper limits on $\langle\sigma v\rangle$ as function of the DM mass in the ZZ, e^+e^-, $\mu^+\mu^-$, $\tau^+\tau^-$, $b\bar{b}$ and $t\bar{t}$ annihilation channels on Tuc IV. 193
10.11 95% C.L. upper limits on $\langle\sigma v\rangle$ as function of the DM mass in the ZZ, e^+e^-, $\mu^+\mu^-$, $\tau^+\tau^-$, $b\bar{b}$ and $t\bar{t}$ annihilation channels on Gru II. 194
10.12 Combined 95% C.L. upper limits on $\langle\sigma v\rangle$ as function of the DM mass. . . . 196
10.13 Combined 95% C.L. upper limits on $\langle\sigma v\rangle$ as function of the DM mass mass including the uncertainty on the J-factor. 197
10.14 95% C.L. combined upper limits from this work on W^+W^+ compared to previous results and other experiments. 198

11.1 Diagram of the annihilation $\chi\chi \to \gamma X$. 205
11.2 Theoretical Wino annihilation spectrum into gamma rays. 206
11.3 Dark matter core profiles for forecast H.E.S.S.-I-like limits on the Wino annihilation cross section. 208
11.4 Differential flux and rate of the expected Wino signal and modeled H.E.S.S.-I-like residual background. 209
11.5 H.E.S.S.-I sensitivity to Wino DM for Einasto profile. 210
11.6 Impact of the spectral contributions to the Wino *gamma line*. 211
11.7 95% C.L. upper limits on the J-factor as function of the Wino DM mass. . 212
11.8 Upper limits on Wino DM annihilation cross section for a selection cored DM density profiles and lower limits on the size of the DM core. 213
11.9 Forecast 95% C. L. limits on the Wino annihilation cross section for IGS-like observation strategy. 215

12.1 Artist view of CTA telescopes. 219

12.2 Schematic of the two CTA sites. 219
12.3 CTA instrument response functions for the Southern site. 220
12.4 CTA expected flux sensitivity at 5σ for 50 hours of observations. 221
12.5 95% C.L. forecast upper limits for CTA in the inner 5° of the Galactic halo, assuming an Einasto profile. 223
12.6 CTA constraints on $\langle\sigma v\rangle$ compared to those by H.E.S.S. and Fermi-LAT and for different DM profiles. 224
12.7 Distribution of p9MSSM points with $\Delta\chi^2 \leq 5.99$. 226
12.8 CTA forecast upper limits on Wino annihilation cross section as function of its mass. 227
12.9 95% C.L. CTA forecast limits on Wino annihilation cross section assuming different DM profiles. 228
12.10 Higgsino annihilation spectrum. 230
12.11 CTA forecast upper limits on Higgsino annihilation cross section as function of its mass. 231
12.12 Spatial map of the *GDE scenario 1* in Galactic coordinates. 233
12.13 Background and and DM differential flux and count rate with CTA. 234
12.14 Spatial map of the *GDE scenario 2* in Galactic coordinates. 235
12.15 Spatial map of the low-latitude Fermi Bubbles in Galactic coordinates. . . . 236
12.16 CTA forecast limits on heavy DM annihilation cross section assuming different background contributions. 238

List of tables

1.1 Main characteristics of the currently operating IACTs: H.E.S.S., MAGIC and VERITAS. . . . 13

5.1 Galactic longitude and latitude of the 14 pointing positions of the Inner Galaxy Survey. . . . 70
5.2 Observation live time, mean zenith angle and mean offset of H.E.S.S.-II data taking in the GC region after quality cuts. . . . 71
5.3 Parameters of the simple power-law and power-law with exponential cutoff fits to the H.E.S.S.-II *Mono* spectrum of Sgr A*. . . . 82

6.1 Latest values of the cosmological parameters measured by Planck. . . . 96

8.1 Dimensions of each ROI and their integrated J-factor. . . . 142
8.2 Number of counts in the *measured OFF* and *expected OFF PDFs* and relative difference between the counts for each ROI. . . . 146
8.3 Counts of measured events in the *ON* and *OFF regions* and significance of the excess in the *ON region*, ROI-by-ROI. . . . 149
8.4 Parameter values for different DM profiles used in this work. . . . 154

9.1 List of excluded regions in the DM analysis. . . . 163
9.2 Number of counts in the *ON* and *OFF PDFs* and significance of the photons excess in the signal region for each ROI. . . . 167
9.3 Number of events for reconstruction type at different steps of the reconstruction chain. . . . 174

10.1 DES satellite of the Milky Way observations with H.E.S.S.. . . . 180
10.2 J-factors for DES dwarf spheroidal galaxies satellites of the Milky Way. . . . 183
10.3 Counts measurement in DES satellites Observed by H.E.S.S.. . . . 187

11.1 Definition of the ROIs and their J-factor. . . . 207
11.2 Parametrization of the CR spectra of protons, helium and electrons. . . . 208

12.1 Parameters of the spectral model of the two GDE scenarii. . . . 232

12.2 Parameters of the exponential cutoff power-law spectrum of the Fermi Bubbles. 236

Synthèse

Introduction L'astronomie gamma à très haute énergie (THE, E$\gtrsim$ 100 GeV) a ouvert la voie à l'étude des processus non thermiques les plus violents à l'oeuvre dans l'Univers. Les rayons gamma aux THE sont produits lors de l'interaction des rayons cosmiques (RC) accélérés dans les objets galactiques comme les restes de supernova et les trous noirs, et dans les objets extragalactiques comme noyaux actifs de galaxies. L'origine et les mécanismes d'accélération des RC sont encore largement débattus. L'une des cibles les plus intéressantes pour ce type d'études est la région du Centre Galactique (CG) où une émission de rayons gamma diffus au TeV a été détectée à proximité du trou noir supermassif central Sagittarius A*, ce qui suggère la présence d'un accélérateur de protons jusqu'aux énergies du PeV, *i.e.* un Pevatron. Un scénario alternatif suggère que la même région pourrait abriter une population de pulsars millisecondes non résolue qui pourrait accélérer des protons jusqu'au PeV.

Les rayons gamma THE sont une sonde puissante pour rechercher la physique fondamentale au-delà du modèle standard de la physique des particules. La matière noire (MN) contribue à environ 85% au contenu en matière de l'Univers, toutefois la nature de cette MN est à ce jour encore inconnue. Une classe importante de candidats MN consiste en des particules élémentaires massives non baryoniques qui interagissent, autre que gravitationellement, seulement par interaction faible avec la matière standard, appelées WIMPs. Dans la mesure où ils sont suffisamment massifs, les WIMPs peuvent s'auto-annihiler dans des régions denses de l'Univers et produire des rayons gamma dans la gamme d'énergie du TeV. La cible la plus prometteuse pour détecter la MN est sans doute le centre de notre galaxie. Les galaxies naines satellites de la Voie Lactée étant les systèmes les plus dominés par la MN dans l'Univers, sont des cibles de confirmation idéales en cas de détection d'un signal MN au Centre Galactique. Les télescopes imageurs à effet Tcherenkov atmosphérique (IACT) sont conçus pour détecter les rayons gamma de THE, des programmes d'observations conséquents sont dédiés à la recherche de physique fondamentale et en particulier à la recherche de signaux de MN.

Le système stéréoscopique à haute énergie (H.E.S.S.) est un ensemble de 5 IACTs détectant des rayons gamma dans la gamme d'énergie entre environ 50 GeV et plusieurs dizaines de TeV. Grâce à son emplacement unique dans l'hémisphère sud, H.E.S.S. est

un instrument idéal pour observer la région du CG et une sélection de galaxies naines satellites de la Voie Lactée. Ces objets sont les cibles les plus prometteuses pour effectuer les recherches indirectes de MN sondant une plage en masses de MN qui ne sont pas à la portée des recherches effectuées auprès des collisionneurs. Les observations vers la région du CG et une sélection de galaxies naines ont permis d'établir des contraintes fortes sur les propriétés de la MN dans la plage en masse du TeV. La prochaine génération de réseaux IACT est le Cherenkov Telescope Array (CTA). L'excellente sensibilité du CTA pourrait apporter une contribution décisive à la recherche de la MN sous forme de WIMPs.

Cette thèse de doctorat se concentre sur les recherches indirectes de MN avec les observations de la région du CG et des galaxies naines proches avec H.E.S.S.. Elle est divisée en quatre parties. Dans la première partie, le concept et les instruments de l'astronomie gamma sont présentés. Le chapitre 1 décrit brièvement les mécanismes d'accélération des rayons cosmiques et de production des rayons gamma ainsi que leurs sources. Le chapitre 2 présente succinctement la technique de détection des rayons gamma avec les IACTs et une description de l'expérience H.E.S.S., ses techniques d'observation et de mesure du bruit de fond ainsi que ses performances.

La deuxième partie se concentre sur l'étude de la région du CG à THE. Le chapitre 3 fournit un aperçu des observations multi-longueurs d'onde de la région et les sources de rayons gamma de THE détectées. Le chapitre 4 présente un modèle de processus radiatif hadronique développé afin d'expliquer l'émission diffuse au TeV détectée par H.E.S.S. à proximité du CG, comme étant produite par des protons accélérés par une population non encore résolue de pulsars millisecondes dans le bulbe galactique. Le chapitre 5 présente les observations du programme Inner Galaxy Survey mené par H.E.S.S. et les résultats des premières analyses des observations de H.E.S.S.-II dans la région du CG.

La troisième partie est centrée sur la question ouverte de la nature de la MN et des moyens mis en oeuvre pour l'étudier. Dans le chapitre 6, le paradigme de la MN, les principaux candidats MN et la distribution de MN sont rappelés ainsi que les techniques de détection, le signal attendu pour la détection indirecte de MN s'auto-annihilant ainsi que les objets ciblés les plus pertinents en rayons gamma de THE. Le chapitre 7 présente la technique d'analyse de données par maximum de vraisemblance utilisée pour la recherche indirecte par modélisation mathématique ainsi que les tests de performances effectués pour caractériser le potentiel de la méthode et l'impact des incertitudes sur les paramètres pertinents pour la détection indirecte en rayons gamma de THE.

La quatrième partie présente les résultats de mes recherches de MN avec les données H.E.S.S.. Dans le chapitre 8, les résultats de la recherche des signaux de lignes mono-énergétiques de MN sont présentés avec les 10 ans de prises de données par H.E.S.S. I vers la région du GC. Dans le chapitre 9 sont présentés les résultats de l'analyse des données de la première recherche de MN effectuée avec le H.E.S.S.-II sur les données de l'Inner Galaxy Survey. Le chapitre 10 décrit l'analyse de données et les résultats obtenus pour la recherche

de MN vers une sélection de satellites de la Voie Lactée récemment détectés par la mission Dark Energy Survey.

La cinquième partie est consacrée à l'étude de modèles spécifiques de MN lourdes avec des observations simulées de H.E.S.S. et de CTA. Le chapitre 11 présente la sensibilité attendue avec H.E.S.S. pour le candidat de MN Wino dans la région du CG en utilisant les calculs les plus récents sur le spectre d'annihilation du Wino en rayons gamma. Dans le chapitre 12, la sensibilité du futur observatoire CTA aux candidats MN canoniques que sont le Wino et le Higgsino dans le centre du halo Galactique est calculée et une étude détaillée de l'impact du fond astrophysique standard sur la sensibilité de CTA est réalisée. L'impact des contraintes H.E.S.S. et de la sensibilité de CTA est présentée dans le cadre de modèles supersymétriques minimaux avec une étude de complémentarité avec la recherche directe.

Chapitre 1 Ce chapitre donne un aperçu de l'astrophysique des rayons gamma à THE et des processus sous-jacents. Les RC chargés sont accélérés par divers objets de l'Univers. Grâce aux processus d'interaction leptoniques et hadroniques, ils peuvent produire des rayons gamma à THE qui sont utilisés pour étudier l'Univers non thermique. Des expériences au sol et par satellite utilisant différentes techniques de détection ont été réalisées dans ce contexte. Dans les sections 1.1, 1.2 et 1.3 sont introduits l'idée de l'Univers non-thermique, les mécanismes d'accélération des rayons cosmiques et de production de rayons gamma. La section 1.4 présente les principaux accélérateurs de rayons cosmiques au TeV et au-delà. Dans la section 1.5 les principaux instruments qui sondent l'Univers non-thermique en détectant directement ou indirectement les rayons gamma sont présentés. La section 1.6 mentionne des sujets de physique fondamentale de premier plan qui peuvent être étudiés par la détection des rayons gamma aux très hautes énergies.

Chapitre 2 Dans ce chapitre, l'expérience H.E.S.S. est présentée. La production de photons Tcherenkov à partir de rayons gamma interagissant avec l'atmosphère est expliquée ainsi que les techniques de détection des rayons gamma de THE et le rejet du fond. Les principales performances du réseau H.E.S.S. sont présentées à la fin. Le processus qui produit un signal gamma détectable avec les télescopes Tcherenkov est décrit dans la section 2.1. Les deux phases de l'expérience H.E.S.S. sont présentées dans la section 2.2. La technique de sélection et de reconstruction des événements est expliquée dans la section 2.3.3. Dans la section 2.4 les modes d'observation et les techniques pour déterminer le fond sont présentés. Les fonctions de réponse de l'instrument (IRFs) de H.E.S.S. et les performances sont données dans la section 2.5. Les différentes méthodes de reconstruction d'événements utilisées pendant les phases 1 et 2 de H.E.S.S. sont décrites dans la section 2.6.

Chapitre 3 La région du CG, située à environ 8,5 kpc du Soleil, est une région très peuplée et active qui a été largement observée à différentes longueurs d'onde. Chaque longueur d'onde utilisée permet de fournir des informations sur différents objets et processus

et il est crucial d'avoir une vue d'ensemble multi-longueurs d'onde de la physique du CG. Aux énergies les plus élevées, dans les rayons gamma à THE, plusieurs sources ponctuelles et étendues ont été observées dans la région du CG, ainsi que des émissions diffuses. Dans la section 3.1 nous introduisons l'idée d'observations à multi-longueurs d'onde et donnons un aperçu des résultats des observations dans la région du CG avec différents instruments. Dans les sections 3.2 et 3.3 nous présentons les émissions des vestiges de supernova, des nébuleuses à vent de pulsar et du trou noir supermassif central à proximité du CG, ainsi que les émissions diffuses détectées par H.E.S.S. et Fermi-LAT dans les quelques degrés centraux de la Galaxie. La présence d'écoulements galactiques qui pourraient être des indices d'activité du trou noir central est discutée dans la section 3.4.

Chapitre 4 Dans ce chapitre, nous étudions la possibilité d'expliquer l'émission diffuse au TeV du CG détectée par H.E.S.S. présentée dans la section 3.3 avec une population non résolue de pulsars millisecondes dans le bulbe galactique. Cette population de pulsars millisecondes a été invoquée par Fermi-LAT pour expliquer l'émission diffuse au GeV détectée vers le CG, connu comme l'excès du CG, par des processus d'émission leptonique. Ce scénario peut être étendu aux processus d'émission hadroniques qui produisent des rayons gamma dans la gamme d'énergie au TeV comme explication la plus probable de l'émission diffuse vue par H.E.S.S.. Une estimation du nombre de pulsars nécessaires pour reproduire l'émission diffuse de H.E.S.S. par l'accélération des protons des rayons cosmiques et leur interaction avec les nuages moléculaires est donnée. Cette dernière est cohérente avec l'estimation donnée par l'interprétation de l'excès au CG par Fermi-LAT.

Dans la section 4.1, les excès de rayons gamma au GeV et au TeV détectés par Fermi-LAT et H.E.S.S., respectivement, (voir les section 3.3 et section 3.4) pourraient être liés à la présence d'une population de pulsars millisecondes non résolus dans le bulbe Galactique. Cette population pourrait accélérer les électrons et reproduire l'excès au GeV par des processus leptoniques. Une fraction des particules accélérées peut également être constituée de protons. La même idée est appliquée à l'excès au TeV en ionvoquant des processus d'accélération hadroniques. Dans la section 4.2 nous expliquons comment les pulsars millisecondes peuvent accélérer les protons jusqu'à des énergies du PeV et dans la section 4.3 nous détaillons le processus d'injection et de propagation de ces protons dans la région centrale de la Voie Lactée. Dans la section 4.4 nous définissons la distribution de la densité des RC et la distribution des pulsars millisecondes dans notre modèle et étudions dans quelles conditions le spectre en énergie et la luminosité des rayons gamma diffus produits par notre modèle peuvent être compatibles avec les mesures de H.E.S.S.. Ce travail a été publié dans JCAP en 2018.

Une population de pulsars millisecondes déduite des mesures de Fermi-LAT dans le bulbe galactique pourrait expliquer l'excès au TeV détecté par H.E.S.S. dans la région du CG. Ce n'est pas la seule explication possible, mais c'est un scénario novateur. En

effet, une telle population de pulsars millisecondes est capable de reproduire l'excès de Fermi-LAT jusqu'à 100 GeV en invoquant les processus d'accélération leptoniques (effet Compton inverse) et les mesures au TeV par H.E.S.S. par processus hadronique (collision *pp*). Il est intéressant de noter qu'une quantité incertaine dans le modèle est le *baryon loading*, qui définit la proportion de protons accélérés par rapport aux électrons accélérés. Cette quantité n'est pas mesurée avec précision, les contraintes actuelles montrent qu'elle peut être de l'ordre de $10^{-2} - 10^{-3}$. Notre étude suppose un coefficient de diffusion standard, celui du disque Galactique. Cependant, dans une étude récente des observations de Geminga et PSR B0656+14, un coefficient de diffusion plus faible a été déduit dans le voisinage des pulsars. Si cette condition est valable non seulement à proximité des objets étudiés, mais dans tout le milieu interstellaire, notre modèle peut devenir incompatible avec les mesures H.E.S.S. car le temps de diffusion deviendrait trop long pour permettre aux protons de diffuser sur la région de l'émission gamma mesurée.

Un scénario alternatif aux pulsars millisecondes est le trou noir supermassif Sagittarius A* agissant comme un Pevatron. De nouvelles observations de H.E.S.S. permettraient d'augmenter la statistique au THE et contraindraient les propriétés de la population de pulsars millisecondes et de Sagitarrius A*. Une augmentation de la statistiques des rayons gamma aux plus hautes énergies pourraient éventuellement montrer une coupure nette attribuable à une source unique et fournir des informations pour faire la distinction entre les deux scénarios. Dans notre modèle, une coupure à haute énergie impliquerait une faible efficacité d'accélération ou une limite supérieure basse sur le champ magnétique. Par ailleurs, une étude actualisée de l'extension et de la morphologie de l'excès diffus au TeV de H.E.S.S. avec de nouvelles données sera cruciale pour tenter de faire la distinction entre les deux scénarios. Par exemple, la distribution spatiale du flux de l'émission diffuse dans le cas d'une source unique au centre de la Galaxie serait plus piquée vers le centre comparé à celle obtenue dans le cas d'une population étendue de sources de type pulsars millisecondes. Des scénarios qui incluent des annihilations de particules de matière noire ou une injection d'une population de supernova peuvent également être trouvés dans la littérature pour expliquer l'excès au CG par Fermi-LAT. Cependant, le scénario de la matière noire est en contradiction avec l'absence de signal dans les galaxies naines observée par Fermi-LAT avec une sensibilité jusqu'à l'échelle naturelle de section efficace d'annihilation de la matière noire jusqu'à une centaine de GeV en masse. Dans le scénario des supernovae, il faudrait au moins une douzaine de supernovae pour produire l'émission diffuse observée, mais il n'y a aucune preuve de l'existence d'une telle population dans le voisinage du CG.

Les observations multi-longueurs d'onde, par exemple dans la radio avec le futur réseau kilométrique carré (SKA), pourraient également fournir des informations cruciales pour confirmer ou rejeter l'hypothèse des pulsars millisecondes. Ces radiotélescopes de nouvelle génération devraient avoir la sensibilité nécessaire pour détecter et résoudre les pulsars millisecondes dans la région du CG.

Chapitre 5 Dans ce chapitre, la stratégie déployée pour les observations de la région du CG avec H.E.S.S. II est présentée ainsi que les principaux objectifs de ce programme d'observation. L'ensemble des données de la campagne à long terme est discuté. Les premières cartes du ciel à rayons gamma H.E.S.S. II dans cette région sont montrées et comparées aux observations à d'autres longueurs d'onde. Une mise à jour du spectre de la source centrale de rayons gamma à THE HESS J1745-290 est faite.

La section 5.1 présente la stratégie et les objectifs du programme d'observation de la région central de la Galaxie, et la section5.2 donne un état des des lieux des observations conduites jusqu'à fin 2018. Les résultats des observations 2014-2018 de la région du CG sont discutés dans les sections 5.3 et 5.4. Le spectre en énergie de la source centrale HESS J1745-290 est calculé dans la section 5.5. Les résultats de ces premières analyses ont été utilisés au cours des trois dernières années pour des propositions d'observations internes à H.E.S.S. qui ont accordé chaque année environ 100 heures d'observations vers la région du Centre Galactique.

Les observations de la région centre de notre galaxie est un programme de science-clé à long terme. On s'attend à ce qu'il donne des résultats importants sur la recherche de MN sous forme de WIMPs et des emissions diffuses galactiques comme les bulles de Fermi et le lobe du CG observé en radio. L'amélioration de la compréhension des différentes émissions diffuses dans la région du CG est attendue grâce à l'augmentation des statistiques sur les photons, mais aussi grâce à la stratégie de pointage axée sur les latitudes à quelques degrès du CG où les bulles de Fermi sont observées jusqu'à 1 TeV et où le halo de MN s'étend. Une première étude pour la recherche de la matière noire dans plusieurs canaux d'annihilation est présentée au chapitre 9. Des recherches sur les éjecta sont en cours dans le cadre de la collaboration H.E.S.S.. Les premières cartes du ciel H.E.S.S. II montrent une émission diffuse plus étendue que celle détectée précédemment avec H.E.S.S. I. Cette émission n'est que partiellement corrélée aux nuages de gaz massifs de la Zone Moléculaire Centrale. Elle pourrait être liée à la présence du Pevatron au CG détecté précédemment par H.E.S.S., capable d'accélérer des protons au PeV qui diffusent ensuite dans la région du CG. Un scénario alternatif est la présence d'une population encore hypothétique de pulsars millisecondes dans le bulbe galactique. Des études spectrales et morphologiques pourrait révéler des corrélations avec des mesures à d'autres longueurs d'onde et permettre de mettre en évidence des émissions faibles comme un ejecta au TeV corrélé avec le lobe radio détecté au centre Galactique ou encore l'émission basse latitude des bulles de Fermi. Une étude plus approfondie de l'émission diffuse pourrait aider à distinguer entre un seul accélérateur de protons PeV ou une population d'émetteurs non résolus et sur l'activité du trou noir central Sgr A* qui pourrait avoir causé l'éjection de particules aux THE. Une modélisation spectrale et morphologique affinée des émissions diffuses standard dans les régions du CG devrait également augmenter la sensibilité de H.E.S.S. à la MN dans la région du CG. Le futur réseau CTA prévoit de modéliser le fond astrophysique standard dans cette région.

Chapitre 6 Ce chapitre présente brièvement le paradigme de la matière noire. À partir des mesures cosmologiques, la MN constitue environ 24% du contenu matière-énergie de l'Univers, et 85% de la matière totale contenue dans l'Univers. A l'échelle des galaxies, la présence de matière noire est requise pour expliquer les mesures astrophysiques telles que les courbes de rotation des galaxies et la dynamique des amas de galaxies. Il est intéressant de noter qu'un nouveau type de matière invisible permet de reproduire la densité relique de la MN mesurée en cosmologie ainsi que la dynamique des amas et des galaxies.Elle peut consister en de nouvelles particules élémentaires prédites dans de nombreuses extensions du modèle standard comme une pièce manquante dans le modèle standard de la physique des particules en tant que particules massives n'interagissant que faiblement (WIMPs) outre l'interaction gravitationnelle. Plusieurs techniques ont été mises au point pour la recherche de cette nouvelle particule et pour la gamme en masse au TeV la technique la plus adaptée est la recherche indirecte. L'intensité d'un éventuel signal de MN dépend du mécanisme sous-jacent du processus d'auto-annihilation qui donne naissance aux spectres gamma et de la distribution de MN dans les cibles les plus prometteuses.

La section 6.1 introduit les mesures astrophysiques et cosmologiques qui conduisent à la nécessité de la MN au-delà du modèle standard et discute les implications pour le modèle standard de cosmologie, le modèle ΛCDM. Dans la section 6.2 les principaux candidats de MN sont présentés. Les limites du modèle ΛCDM et des modèles alternatifs qui n'incluent pas la MN sont discutées dans la section 6.3. Dans la section 6.4 les différentes techniques de recherche de MN sous forme de WIMPs sont détaillées. La distribution de densité de MN attendue et les principales cibles pour la recherche indirecte sont discutées dans les sections 6.5 et 6.6. Les spectres d'annihilation de la MN et le flux de rayons gamma attendu dû à son auto-annihilation sont présentés dans les section 6.8 et section 6.7.

Chapitre 7 Le traitement des processus aléatoires nécessite une description statistique des événements observés en termes de fonctions de densité de probabilité. L'une des approches statistiques les plus utilisées en physique des hautes énergies pour rechercher un signal faible dans un ensemble de données observées sur un fond mesuré ou modélisé est la technique de vraisemblance. Dans ce chapitre, nous rappelons la fonction de vraisemblance et le test statistique du rapport logarithmique de vraisemblance, et définissons leur application aux recherches indirectes de MN qui aboutissent à des contraintes ou des mesures des propriétés de candidats MN. Nous étudions ensuite l'effet sur les limites du binning de la fonction de vraisemblance, le profilage, l'incertitude systématique sur les mesures, la résolution énergétique du détecteur et l'incertitude statistique sur le facteur J qui est relié à la densité de MN dans l'objet considéré. Des exemples sont donnés sur les limites calculées à l'aide de données simulées d'observations H.E.S.S. I. Ces observations sont supposées fournir 250 heures d'exposition homogène dans 1° autour du CG et le signal recherché est dû à l'annihilation de MN en $b\bar{b}$, sauf indication contraire. Le profil Einasto est choisi pour

calculer le facteur J. Le but de ce chapitre est d'étudier le comportement de différents tests statistiques du rapport de vraisemblance et l'impact de l'incertitude sur les paramètres pertinents pour les recherches de MN, et non d'en déduire des contraintes pertinentes par rapport aux observations.

La fonction de vraisemblance et le test statistique du rapport logarithmique de vraisemblance sont présentées dans la section 7.1. Leur application à la recherche de la MN est décrite dans la section 7.2. Dans la section 7.3 l'impact sur les limites de MN des incertitudes sur les paramètres de vraisemblance est quantifié et discuté. Les traitements alternatifs du fond astrophysique standard sont discutés dans la section 7.4 et la technique de profilage de probabilité est discutée dans la section 7.5.

Les tests statistiques du rapport logarithmique de vraisemblance sont une méthode optimale pour rechercher les signaux faibles dus à de nouveaux phénomènes dans la physique des astroparticules à haute énergie. Il peut être appliqué facilement aux recherches de MN et dans ce cas, une approche bidimensionnelle fournit la sensibilité la plus élevée. Il est utilisé dans la partie IV et la partie V de ce travail pour fixer les limites supérieures sur la section efficace d'annihilation de la MN, en l'absence d'un excès significatif de rayons gamma dans les régions où le signal MN est recherché. Les limites attendues et observées ont été définies et la technique permettant d'obtenir les limites attendues moyennes et leurs bandes d'incertitude est expliquée. Cette section montre l'amélioration ou la dégradation des contraintes de MN par rapport aux paramètres clés intervenant dans le test statistique. Comme nous l'avons expliqué, les paramètres de nuisance peuvent être inclus dans la probabilité pour tenir compte des incertitudes statistiques et systématiques. En l'absence de certitude sur la nature de la distribution du paramètre de nuisance, celui est modélisée comme un paramètre de nuisance gaussien.

Chapitre 8 Le CG est sans doute l'une des principales cibles pour la recherche indirecte de MN en rayons gamma. Dans ce chapitre, nous analysons un ensemble de données H.E.S.S. I provenant de 10 années d'observations vers cette région prometteuse. La technique de mesure du fond résiduel et de comparaison avec les événements dans la région du signal est expliquée. Ensuite, l'hypothèse de présence d'une ligne gamma monoénergétique provenant de l'annihilation de la MN est testée par rapport à l'hypothèse de l'absence de signal sur les données. En l'absence d'excès significatif de photons, des contraintes sont calculées sur le flux et la section efficace d'annihilation de la MN. Les sources d'incertitudes systématiques sont étudiées et sont quantifiées. L'ensemble des données et la construction des distributions d'événements sont présentés dans les section 8.1 et section 8.2, respectivement. Dans les sections 8.3 et 8.4 la mesure du fond résiduel et la définition du signal attendu sont détaillées. Les contraintes obtenues sur la section efficace d'annihilation de la MN sont présentées dans la section 8.5 et une étude des incertitudes systématiques est présentée dans la section 8.6. Ce travail a été publié dans Phys. Rev. Lett. en 2018.

L'analyse de l'ensemble des données H.E.S.S. I vers le CG pour la recherche de lignes gamma monoénergétiques à partir de l'annihilation de la MN montre la puissance des techniques d'analyse les plus efficaces, *Model++*, appliquées pour la sélection et la reconstruction des rayons gamma utilisés en recherche indirecte de MN avec les télescopes Tcherenkov. Les résultats précédents de la recherche de MN avec H.E.S.S. dans le même canal d'annihilation avaient été publiés en 2013. L'ensemble complet des données H.E.S.S. I utilisé dans le cadre de ce travail double les statistiques disponibles sur les photons. De plus, la reconstruction et la sélection des photons du *Model ++* améliorent la sensibilité du H.E.S.S. à basse énergie par rapport à l'analyse des données brutes utilisant la chaine d'analyse de type *HAP* utilisée précédemment. Une approche avec un test de vraisemblance bi-dimensionnel est maintenant standard dans la région du CG depuis les résultats de H.E.S.S. de la recherche du signal de MN dans les canaux de *continuum* en 2016. L'inclusion de l'information spatiale et spectrale bin par bin spécifique aux signaux de MN attendus par rapport aux bruits de fond améliore également la sensibilité. Une analyse événement par événement n'est pas optimale pour un ensemble de données aussi important que $\sim$ 1.5 million d'événements reconstruits comme rayons gamma. La technique d'extraction du fond dite du *fond réfléchi* est développée spécifiquement pour la recherche de MN dans cette région complexe où des émissions brillantes de rayons gamma astrophysiques standard sont présentes. L'attention est portée sur la présence d'un signal de MN également dans les régions de mesure du fond et sur sa considération dans la fonction de vraisemblance.

Toutes les améliorations mentionnées ci-dessus nous ont permis de fixer avec ce travail les limites les plus fortes jusqu'à présent sur la section efficace d'annihilation dans la gamme de masse au TeV pour l'annihilation de la MN en deux photons. La meilleure limite de 4×10^{-28} cm^3 s^{-1} est obtenue à 1 TeV. La section efficace de la relique thermique n'est pas encore sondée, si aucun autre facteur d'augmentation du flux attendu comme l'effet Sommerfeld (voir section 6.8.3) très efficace dans le cas de modèles de WIMPs spécifiques, i.e. Wino and Higgsino, n'est considéré sur le signal de ligne. Avec le réseau complet de télescopes H.E.S.S.-II et la nouvelle stratégie d'étude de la région du CG, notre sensibilité à la MN devrait augmenter. Les premiers résultats incluant le télescope CT5 sont présentés dans le chapitre 9.

Chapitre 9 L'ensemble de données H.E.S.S. II accumulé en 2014-2018 au CG a été utilisé pour les recherches de MN dans les canaux d'annihilation du *continuum*, incluant les observations effectuées avec le Inner Galaxy Survey. Les régions d'intérêt ont été mises à jour et étendues grâce à la stratégie de pointé du Inner Galaxy Survey et à des statistiques significatives à des latitudes galactiques $|b| > 1°$. Des corrections d'acceptance dans le calcul des comptages mesurés et du signal attendu sont introduites afin de prendre en compte les grands décalages par rapport au CG. De plus, les régions d'exclusion mises à jour par rapport à l'analyse H.E.S.S.-I sont définies. Les premières contraintes sur la section efficace

d'annihilation de la matière noire avec CT5 sont calculées. La stratégie pour une analyse de recherche de matière noire CT1-5 est discutée à la fin du chapitre.

L'ensemble de données, la définition de la région d'intérêt et les régions d'exclusion pour H.E.S.S. II sont décrits dans la section 9.1. L'analyse des données de H.E.S.S.-II, dont l'étude de l'Inner Galaxy Survey constitue la partie la plus significative, est présentée dans la section 9.2. La construction des distributions d'événements (PDFs) dans la région du signal, *ON*, et du bruit de fond, *OFF*, est détaillée. Les premières contraintes H.E.S.S.-II sur la section efficace de l'annihilation de MN sont calculées en utilisant seulement le télescope CT5 (reconstruction *Mono*), et comparées aux autres études. Le cadre d'une analyse combinée (CT1-5) à venir est ensuite discuté dans la section 9.3. Ces travaux feront l'objet d'un papier dans l'année à venir.

La première étude sur la MN réalisée avec H.E.S.S.-II, y compris les observations de l'Inner Galaxy Survey, a été réalisée. Elle montre que la sensibilité de l'expérience a augmenté. La reconstruction des événements *Mono* et la présence d'un excès d'émission diffuse non significatif ($\sim 2\sigma$) dans la région d'intérêt limitent la possibilité de sonder la section efficace de l'annihilation thermique dans la plupart des canaux. L'excès sur la région d'intérêt de 3° est compatible avec zéro, mais l'effet d'intégration sur les régions où la plupart du signal attendu et l'émission diffuse observée semblent dégrader légèrement les limites observées par rapport aux limites attendues. L'échelle naturelle est atteinte par les limites observées par H.E.S.S.-II *Mono* sur la section d'annihilation uniquement dans le canal $\tau^+\tau^-$. Malgré la sensibilité meilleure que 3×10^{-26} cm^3 s^{-1} dans le canal W^+W^-, les limites observées ne sondent pas la section de la relique thermique dans ce canal. Un faible excès de rayons gamma diffus est observé, qui peut provenir d'une émission diffuse due au Pevatron plus étendue que celle observée par H.E.S.S. I, des bulles de Fermi ou d'autres émissions plus faibles reliées à Sagittarius A*. Si des émissions diffuses plus étendues ou plus intenses sont détectées dans la région d'intérêt pour la recherche de MN avec les observations futures, il sera crucial d'avoir une meilleure compréhension du spectre et de la morphologie de cette émission dans le CG afin de la modéliser et d'exploiter pleinement la sensibilité de H.E.S.S.-II.

Cette étude montre à la fois qu'il existe des perspectives prometteuses pour la recherche sur la MN et qu'il y a des limitations. L'analyse H.E.S.S.-II *Combinée* en cours de développement devrait permettre d'augmenter les statistiques grâce à la contribution des cinq télescopes, puis d'améliorer la sensibilité à la MN, probablement au point où d'autres canaux d'annihilation pourraient explorés la section efficace thermique. D'autre part, les nouvelles observations contiennent davantage de fond astrophysique gamma standard qui ne peut pas être complètement rejeté lors de l'analyse parce qu'il couvre une partie non négligeable de la région qui contient le plus fort signal de MN attendu. La dégradation des limites observées due à ce faible bruit de fond par rapport à la sensibilité prometteuse souligne la nécessité de faire des études précises et dédiées de ces émissions pour les modéliser afin de les prendre

correctement en compte lors de la recherche d'un signal de MN faible dans la région très chargée en rayons gamma de THE du CG.

Chapitre 10 H.E.S.S. a observé une sélection de satellites de la Voie Lactée récemment découverts par le télescope optique DES, en utilisant le réseau complet de cinq télescopes. H.E.S.S. a été le premier parmi les IACTs à lancer une campagne d'observation de ces objets. Des recherches de MN dans plusieurs canaux d'annihilation ont été effectuées vers ces satellites. Les cibles, leurs observations et la mesure ou l'estimation de leur facteur J sont discutés au début du chapitre. En l'absence de d'excès significatif, les limites sur la section d'annihilation en fonction de la masse sont alors calculées pour les signaux de lignes mono-énergétique gamma et le *continuum*. Les résultats sont discutés et comparés à d'autres limites d'autres expériences.

Les cibles et les ensembles de données sont présentés dans les section 10.1 et section 10.2. Les facteurs J dans cette analyse sont extraits de la détermination la plus récente disponible dans la littérature, et certaines mesures du facteur J et techniques de rpdiction ainsi que leurs incertitudes sont discutées dans la section 10.3. Les observations de ces objets sont le résultat des propositions d'observation internes que j'ai menées pendant deux ans, incluant les calculs de sensibilité sur le potentiel de H.E.S.S. dans le cadre des recherches de MN. Dans la section 10.4 les régions *ON* et *OFF* sont discutées et dans la section 10.5 les contraintes sur la section efficace d'annihilation de MN sont calculées dans plusieurs canaux d'annihilation pour chaque cible ainsi que pour une combinaison des observations sur les cinq objets. Les résultats sont comparés à ceux d'autres études. Ce travail a été présenté à l'ICRC19 et sera soumis pour publication dans Phys. Rev. D en septembre 2019.

H.E.S.S. est compétitif dans la recherche de MN vers les galaxies sphéroïdales naines avec le réseau complet H.E.S.S.-II. Plus précisément, cette dernière analyse des satellites nains de la Voie Lactée produit les limites les plus fortes sur la section efficace d'annihilation de MN dans plusieurs canaux au-dessus de plusieurs TeV. H.E.S.S. a été le premier télescope Tcherenkov à observer une sélection de candidats DES, exploitant sa position privilégiée dans l'hémisphère sud d'où la plupart de ces objets peuvent être observés. Les contraintes obtenues par des télescopes Tcherenkov au sol sont particulièrement intéressantes pour la recherche de signaux de lignes gamma, qui dans la gamme multi-TeV pourraient être augmentés, par exemple par l'effet Sommerfeld, et ne sont pas accessibles par Fermi-LAT à des masses aussi élevées.

Puisque les expériences actuelles ciblent des objets dans différentes parties du ciel et utilisent différentes techniques pour détecter les rayons gamma, une méthode prometteuse pour améliorer les recherches de MN est de combiner les efforts dans le futur. Un projet est en cours afin de combiner les données des différents détecteurs de rayons gamma à haute énergie pour améliorer la sensibilité à l'annihilation de la MN vers les galaxies naines. Le projet comprend les IACTs H.E.S.S., MAGIC et VERITAS, Fermi-LAT et HAWC.

Chaque expérience fournit la valeur du test statistique versus la section efficaces à plusieurs masses pour les cibles déjà utilisées pour les publications par les collaborations calculées avec les facteurs J convenus. Les résultats seront ensuite combinés ensemble au niveau du test statistique sans partager l'ensemble des données brutes. Les limites combinées couvriront une plage de masse DM de 1 GeV à 100 TeV, avec des valeurs de section efficace d'annihilation comprises entre environ 10^{-21} cm^3 s^{-1} et 10^{-27} cm^3 s^{-1}.

Comparées au CG, les galaxies naines sont des régions avec un bruit de fond de faible niveau: la détection d'un signal de MN vers l'une d'elles serait sans ambiguïté. Par ailleurs, si le profil de MN du halo galactique est avec un cœur et de grande taille, les limites calculées vers les galaxies naines deviennent compétitives avec celles du CG en considérant des rayons de cœur de l'ordre du kpc.

Chapitre 11 Dans ce chapitre, les limites attendues sur la section efficace d'annihilation de la MN sont calculées pour une analyse de type H.E.S.S. I des observations simulées vers le CG et un modèle spécifique de MN lourde et faiblement en interaction. Le candidat MN Wino et le cadre de calcul de son spectre d'annihilation en gamma sont décrits. La modélisation du bruit de fond et du signal attendus dans les observations de type H.E.S.S.-I. est présentée. Les contraintes attendues sur les propriétés de la MN sont présentées et discutées. Plusieurs profils de densité de MN au CG sont testés. Une stratégie d'observation du type H.E.S.S.-II est aussi testée.

La section 11.1 présente le candidat de MN Wino et son spectre. Le cadre d'analyse ainsi que le signal et le fond attendus dans la région du CG sont expliqués dans les sections 11.2 et 11.3. Les contraintes attendues sur la section efficace d'annihilation du Wino sont calculées pour une analyse H.E.S.S. I dans la section 11.4 et pour une analyse qui utilise la stratégie de l'Inner Galaxie Survey dans la section 11.5. Cette étude a été publié dans Phys. Rev. D en 2019.

Cette étude montre que les observations H.E.S.S. du CG sont très puissantes pour sonder la MN sous forme de Wino. H.E.S.S. I est capable d'exclure le Wino dans une large gamme de masses en supposant un profil de MN piqué au CG. Les limites sont moins strictes pour les profils à cœur. Les derniers calculs du spectre d'annihilation du Wino, y compris les contributions autres qu'au niveau l'ordre dominant dans la région du *endpoint*, oú l'énergie des photons est proche de la masse de matière noire, améliorent considérablement la sensibilité de H.E.S.S.. L'incertitude théorique est négligeable par rapport aux incertitudes systématiques dans les recherches de lignes gamma dans la région du GC.

Une approche qui nous permet d'étendre notre région d'intérêt pour la recherche de la MN, comme celle qui est appliquée avec H.E.S.S. II pendant l'étude de l'Inner Galaxy Survey (voir Chap. 5), est plus efficace que simplement augmenter les statistiques photon dans une région limitée autour du CG. Les perspectives de recherche de MN avec CTA dans une région de plusieurs degrés autour du CG sont discutées dans le chapitre suivant.

Chapitre 12 La nouvelle génération de IACTs CTA devrait apporter une contribution décisive à la recherche indirecte de MN sous forme de WIMPs, grâce à sa sensibilité accrue par rapport aux instruments actuels. La sensibilité attendue sur la section efficace d'annihilation de la MN sont calculées dans ce chapitre. La sensibilité obtenue peut être confrontée à des prédictions obtenues dans le cadre de modèles supersymétriques phénoménologiques minimaux (pMSSM). De plus, la sensibilité à certains modèles spécifiques de MN lourde pure (Wino, Higgsino) est calculée. Dans la section 12.1, l'observatoire CTA est brièvement présenté, ainsi que les fonctions de réponse simulées de l'instrument et sa sensibilité en flux. Les contraintes sur l'annihilation de la MN dans le continuum et les lignes gamma vers le CG sont calculées dans la section 12.2 et utilisées pour placer des contraintes dans l'espace des paramètres du pMSSM dans la section 12.3 en se concentrant sur les modèles de MN au TeV. Cette étude est acceptée pour publication dans JHEP 2019. Les contraintes pour les candidats purs Wino et Higgsino sont calculées dans la section 12.4 et l'effet sur les limites de plusieurs composantes de bruit de fond astrophysiques standards dans la région du CG est quantifié dans la section 12.5. Ce travail sera soumis pour publication dans Phys. Rev. D. à l'automne 2019.

Les observations de CTA sont très prometteuses pour la détection de la MN dans la région du CG. La sensibilité de CTA pourra atteindre la section efficace de la relique thermique dans la plupart des canaux d'annihilation. D'après le balayage du pMSSM, on observe que le candidat Wino est largement sondé et que le Higgsino est également à portée de main. Ils peuvent être sondés dans des régions de l'espace de paramètres qui ne peuvent être atteintes que par CTA. Des recherches spécifiques pour l'annihilation de Winos purs et Higgsino purs montrent la sensibilité de CTA à la MN au TeV. Le Wino pourrait en effet être complètement exclu par CTA. De plus, le Higgsino avec sa masse thermique est à accessible (avec une faible marge). La contribution non attendue au *endpoint* (incluse dans le spectre Wino) est non négligeable et permettrait d'améliorer sensiblement le potentiel de CTA. La stratégie de recherche de MN avec CTA sera de modéliser le plus précisément possible les fonds astrophysiques standards qui sont détectés dans la région du CG au-dessus du fond résiduel. Cette approche pourrait améliorer la sensibilité jusqu'à environ 50%. En pratique, l'émission diffuse Galactique peut dégrader la sensibilité jusqu'à un facteur de 20% et les bulles de Fermi à basse latitude jusqu'à 30% supplémentaires. La différence entre les modèles d'émission diffuse extrapolés selon différentes hypothèses n'affecte les limites qu'au niveau de quelques pour cent. Les limites ne sont pas fortement sensibles aux différents comportements spatiaux des différents modèles de bruits de fond astrophysiques. On s'attend à ce que CTA ait la sensibilité nécessaire pour sonder la section efficace de la relique thermique dans de nombreux canaux d'annihilation pour des profils de densité de MN piqué au CG et il pourrait également être capable de sonder le Higgsino à sa masse thermique et exclure le Wino dans toute la plage de masse raisonnable. CTA pourrait donc

être en mesure d'apporter une contribution cruciale pour apporter une réponse à la question de la nature de la MN dans les modèles de WIMPs lourds les plus naturels.

Conclusion Dans ce travail, les études de la région du CG dans les rayons gamma à THE et des recherches indirectes de MN dans la gamme de masse au GeV-TeV ont été présentées.

La région du CG est un environnement très riche pour étudier l'astrophysique des rayons gamma de THE. Elle est très peuplée de nombreuses sources de rayons gamma à THE. En plus des sources ponctuelles et modérément étendues, une émission diffuse au TeV a été détectée dans les 50 pc internes autour du CG et dans les 300 pc le long du plan Galactique. La nature de cette émission fait encore l'objet d'un débat. Alors que l'interprétation la plus plausible est basée sur une source unique qui accélère les protons jusqu'aux énergies du PeV, le *Pevatron*, dont le trou noir supermassif Sagittius A* est la contrepartie la plus probable, un scénario alternatif a été discuté. Bien qu'elle n'ait pas encore été résolue, une population de pulsars millisecondes dans le bulbe Galactique, à la lumière de la détection d'un excès au CG par Fermi-LAT, pourrait reproduire une telle émission diffuse au TeV. Un modèle de l'accélération et de la propagation des protons dans le milieu interstellaire fixe une contrainte sur le nombre de pulsars à $N_{\rm b}(L_{\rm CR}(t_{\rm sd}) > 10^{33}\,{\rm erg\,s^{-1}}) \sim 7 \times 10^4$, afin de reproduire le spectre en énergie du diffus et sa luminosité en rayons gamma mesurés par H.E.S.S.. Récemment, l'étude de l'Inner Galaxy Survey réalisée avec H.E.S.S. II dans les plusieurs degrés intérieurs du CG a montré que l'émission diffuse dans cette région est de plus en plus étendue spatialement avec la nouvelle stratégie d'observation. Des analyses spécifiques dans H.E.S.S. sont en cours afin d'étudier si l'origine de cette émission pourrait être liée au *Pevatron* détecté récemment, aux éjecta sortants du lobe radio ou aux bulles de Fermi à basse latitude Galactique. De nouvelles observations pourraient également aider à faire la distinction entre les scénarios de population de pulsars millisecondes et le trou noir Sagittarius A* au CG.

Étant donné sa proximité, la région du CG, qui devrait contenir une grande quantité de MN, est la cible la plus prometteuse pour les recherches indirectes par rayons gamma de THE. Dix années d'observations de la région du CG avec H.E.S.S. I ont été analysées pour fixer les limites les plus contraignantes jusqu'à présent sur la section efficace d'annihilation de MN dans le canal $\chi\chi\chi \to \gamma\gamma$ dans la plage en énergie du TeV. À 1 TeV, elles atteignent 4×10^{-28} cm^3 s^{-1}, améliorant les résultats précédents d'un facteur d'environ six. Cinq années de données de H.E.S.S. II prises pendant l'Inner Galaxy Survey ont également été analysées pour la recherche indirecte de MN. en utilisant une analyse $CT5 - Mono$. Plusieurs canaux pour le signal *continuum* ont été testés. La sensibilité attendue se situe en dessous de la section efficace de la relique thermique dans le canal $\chi\chi\chi\chi \to W^+W^-$, l'échelle naturelle pour l'annihilation de la MN est cependant sondée uniquement dans le canal $\chi\chi\chi \to \tau^+\tau^-$ en raison d'un léger excès non significatif dans la région du signal. La haute sensibilité de CT5 dans la gamme d'énergie de la centaine de GeV a amélioré les

limites H.E.S.S. précédentes à 300 GeV d'un facteur de 5 à 7, selon le canal d'annihilation. L'analyse combinée en cours exploitant la stéréoscopie et le réseau hybride devrait permettre d'améliorer encore les contraintes dans la plage de masse au TeV.

D'autres cibles pour la recherche de MN sont considérées complémentaires au CG, ce dernier abritant un fond astrophysique standard important et dont le profil central de densité de MN est assez incertain. Un environnement plus propre est offert par les galaxies naines qui sont les objets les plus dominé par la MN dans l'Univers. Celles du Groupe Local, relativement proches de la Terre, sont privilégiées. Dans ces galaxies aucune émission standard en rayons gamma de THE n'est détectée à ce jour. Pour les galaxies naines satellites de la Voie Lactée, et particulièrement pour les galaxies naines de faible luminosité optique, le signal de MN attendu les place comme des cibles de premiers plans.. H.E.S.S. a observé une sélection de satellites de la Voie Lactée découvertes par DES avec un fort signal MN attendu pour rechercher la MN dans les canaux du *continuum* et de la ligne gamma. En l'absence de signal significatif, les premières contraintes des IACTs sur ces cibles ont été calculées sur la section efficace d'annihilation de la MN, les plus contraignante pour les masses de MN supérieures à plusieurs TeV. Afin d'exploiter la complémentarité entre les instruments à rayons gamma actuels et leurs lots de données, un projet est en cours afin d'effectuer une recherche combinée sur une sélection de galaxies naines observées par Fermi-LAT, HAWC, H.E.S.S., MAGIC et VERITAS.

Au-delà des recherches de MN indépendantes du modèle de MN sous-jacent mentionnées ci-dessus, des modèles spécifiques de MN peuvent être testés avec H.E.S.S.. Les limites prédites sur la section efficace d'annihilation pour la Wino ont été calculées à partir d'observations fictives de type H.E.S.S.-I de la région du GC. Cette étude a montré que H.E.S.S. peut exclure le candidat de MN Wino jusqu'à une masse de 10 TeV pour des profils piqués au CG. Un candidat de matière noire Wino de masse 2.9 TeV, tel qu'attendu par production thermique dans l'Univers primordial, peut être exclu pour les profils de densité de MN avec un core jusqu'à 5 kpc. La recherche de MN dans le halo galactique intérieur est un sujet scientifique de premier plan pour le prochain réseau de IACTs CTA. Des observations simulées de la région du CG avec l'observatoire CTA-Sud, ont été utilisées pour calculer la sensibilité à l'annihilation de la MN dans canaux du *continuum* et de la ligne gamma. CTA aura la sensibilité nécessaire pour sonder la section efficace de la relique thermique dans la plupart des canaux d'annihilation du *continuum* pour les profils de MN piqués. Il sondera une région importante du modèle pMSSM, y compris les régions qui sont très difficiles ou même hors de portée pour la détection directe, soit sous le *plancher* des neutrinos, et les recherches de collisionneurs pour WIMP au-dessus de 1 TeV. Deux candidats spécifiques à la MN lourde, le Wino et le Higgsino, respectivement, ont été considérés. CTA sera en mesure de sonder le modèle Wino jusqu'à 40 TeV et le modèle Higgsino jusqu'à plusieurs TeV, en fonction des hypothèses sur le spectre d'annihilationV. L'impact du fond astrophysique standard tel que l'émission diffuse Galactique et éventuellement l'émission de bulles de

Fermi à basse latitude Galactique sur la sensibilité CTA attendue a été calculé et a montré une dégradation des limites allant jusqu'à 50%. Pourvu que le fond astrophysique puisse être soigneusement modélisé et que les incertitudes systématiques soient contrôlées à un niveau nettement inférieur à celui des IACTs actuels, les observations avec CTA de la région du CG fourniront un apport crucial à la recherche de MN sous forme de WIMP.

Introduction

Very-high-energy (VHE, E$\gtrsim$ 100 GeV) gamma-ray astronomy opened the path for the study of the most violent non-thermal processes that take place in the Universe. VHE gamma rays are produced by cosmic rays (CRs) accelerated both in Galactic objects like supernova remnants and in extragalactic ones like supermassive black holes hosted at the center of galaxies. The origin and the mechanisms of acceleration of CRs are still debated. One of the most interesting targets for this kind of studies is the Galactic Center (GC) region where a TeV diffuse gamma-ray emission has been observed in the vicinity of the central supermassive black hole Sagittarius A*, which suggests the presence of an extreme accelerator of protons up to PeV energies (Pevatron). An alternative scenario assumes that the same region could host a yet unresolved population of pulsars, which could to accelerate protons up to PeV.

VHE gamma rays are a powerful probe to search for fundamental physics beyond the Standard Model of particle physics. About 85% of the matter that constitutes the Universe is believed to be dark matter (DM). A prominent class of DM candidate is a category of massive non-baryonic elementary particles that interact, besides gravitationally, only weakly with standard matter, called WIMPs. Provided they are massive enough, self-annihilating WIMPs are expected to produce VHE gamma rays in the GeV-TeV energy range. The most promising target to detect DM is arguably the center of our Galaxy, with the nearby dwarf galaxies being the most DM dominated systems in the Universe, as confirmation targets in case of signal detection at the Galactic Center. These objects can be observed by means of ground-based imaging atmospheric Cherenkov telescopes (IACTs), designed to detect VHE gamma rays.

The High Energy Spectroscopic System (H.E.S.S.) is an array of IACTs sensitive to gamma rays in the energy range between about 100 GeV up to several ten TeV. Thanks to its unique location in the Southern hemisphere H.E.S.S. is a well-suited instrument to observe the GC region and a selection of dwarf galaxies satellites of the Milky Way. Their observations were used to set the most stringent constraints obtained so far on DM properties. The next-generation IACT array will be the Cherenkov Telescope Array (CTA). Its expected sensitivity could bring decisive input to the nature of DM.

The PhD thesis focuses on indirect DM searches with the observations of the GC region and nearby dwarf galaxies with H.E.S.S.. It is divided in four parts.
In the **first part** the concept and instruments of gamma-ray astronomy are introduced. In Chap. 1 the mechanisms of acceleration of cosmic rays and production of gamma rays and their sources are briefly described. Chap. 2 presents the gamma-ray detection technique with IACTs and a description of the H.E.S.S. experiment, its observation and background measurement techniques and its performances is given.

The **second part** is focused on the GC region at VHE. In Chap. 3 the multi-wavelengths observations of the region and the detected VHE gamma-ray sources are introduced. Chap. 4 presents a hadronic radiative process model developed in order to explain the diffuse TeV emission detected by H.E.S.S. in the vicinity of the GC as produced by protons accelerated by an unresolved population of millisecond pulsars in the Galactic bulge. In Chap. 5 the Inner Galaxy Survey performed by H.E.S.S. is presented and the results of the first analysis of H.E.S.S.-II observations of the GC region are shown.

The **third part** is focused on the open question about DM nature and ways to study it. In Chap. 6 the DM paradigm, candidates and distribution are presented together with the detection techniques, the expected signal for indirect detection of self-annihilating DM, and the most relevant targeted objects in VHE gamma rays. Chap. 7 presents the likelihood technique used for indirect DM search and tests are performed to characterize the performance of the method and the impact of the uncertainty on its parameters.

The **fourth part** shows my searches for DM using H.E.S.S. data. In Chap. 8 the results of the legacy search for DM mono-energetic line signals is performed on 10 years of data taken by H.E.S.S. I towards the GC region are shown. In Chap. 9 the results of the data analysis of the first DM search carried out with the H.E.S.S.-II Inner Galaxy Survey are presented. Chap. 10 shows the analysis results of DM search towards a selection of ultra-faint satellites of the Milky Way recently detected by the Dark Energy Survey.

The **fifth part** is dedicated to studies of specific heavy DM models with mock observations of H.E.S.S. and CTA. Chap. 11 shows forecast limits on Wino dark matter with H.E.S.S. in the GC region using the latest computations of the Wino annihilation spectrum in gamma rays. In Chap. 12 the sensitivity of the future observatory CTA to Wino and Higgsino DM candidates in the inner Galactic halo is computed and a detailed study of the impact of standard astrophysical background on the CTA sensititivy is performed.

Part I

High energy astrophysics with H.E.S.S.

Chapter 1

Very-high-energy gamma rays

Contents

1.1 Preamble **4**
1.2 Mechanisms of acceleration of cosmic rays **4**
1.2.1 Cosmic rays and their spectrum 4
1.2.2 Second order Fermi acceleration 6
1.2.3 First order Fermi acceleration: diffusive shock acceleration 6
1.3 Mechanisms of production of gamma rays **7**
1.3.1 Leptonic processes 7
1.3.2 Hadronic processes 8
1.3.3 Dark matter annihilation and decay 9
1.4 Cosmic accelerators **9**
1.5 Observations and instruments **11**
1.5.1 Satellite experiments 11
1.5.2 Ground-based water tanks 12
1.5.3 Ground-based atmopsheric Cherenkov telescopes 13
1.6 Fundamental physics with very high energy gamma rays **13**

This chapter introduces succinctly the astrophysics of very-high-energy gamma-rays and the underlying processes [1]. Charged cosmic rays are accelerated by various objects in the Universe. Through leptonic and hadronic particle physics processes they can produce very-high-energy gamma rays that are used to study the non-thermal Universe. Satellite and ground-based experiments that use different detection techniques have been built in this context.
In Sec. 1.1 we introduce the idea of the non-thermal Universe. In Sec. 1.2 and Sec. 1.3 the mechanisms of acceleration of cosmic rays and of production of gamma rays are described. In Sec. 1.4 some cosmic-ray accelerators are presented. In Sec. 1.5 the main instruments that observe the non-thermal Universe by detecting directly or indirectly the gamma rays are shown. Sec. 1.6 presents some topics of fundamental physics that can be investigated through very-high-energy gamma-ray detection.

1.1 Preamble

The light emitted by the Sun, the stars and the light bulbs is thermal radiation. It is created by electrons that jump from one state to another inside an atom. Thermal radiation has a continuum spectrum, commonly known as blackbody spectrum. This radiation follows Stefan-Boltzman law ($E \propto T^4$) and its wavelength and frequency ν depend on the temperature T of the body that emitted it ($\nu \propto T$). The hotter the object the larger the frequency. Light at the highest energy, gamma rays, cannot be produced thermally because no object is hot enough. Gamma rays are produced in processes referred to as non-thermal processes, that imply particle interaction. Very-high-energy (VHE, E $>$ 100 GeV) gamma-ray astronomy is used to study the non-thermal Universe, related to extreme particle acceleration processes, like black holes and explosion or merging of massive stars. The characteristics of non-thermal radiation do not depend on the temperature of the source.

1.2 Mechanisms of acceleration of cosmic rays

1.2.1 Cosmic rays and their spectrum

After the discovery of radioactivity by Becquerel and Pierre and Marie Curie and the observation that electroscopes discharge spontaneously in the air due to a penetrating radiation, Victor Hess and Domenico Pancini excluded the terrestrial origin of this radiation. Pancini [2] found out that the radiation decreases in deep waters and Hess [3] found out that it increases with altitude. The term “cosmic rays” was introduced in the ’20s by Millikan to denote this extraterrestrial radiation [4]. The primary cosmic rays (CR) are charged particles and atomic nuclei, mainly protons, that can be produced by a wide variety of astrophysical sources in our galaxy and further away, and that eventually reach Earth. Since then CRs have been detected in a broad energy range. They are classified as low-energy (LE) CRs for

$E < 50$ MeV, high-energy (HE) for ~ 50 MeV-100 GeV, VHE for ~ 100 GeV-100 TeV, ultra-high-energy (UHE) for ~ 100 TeV-100 PeV and extremely-high-energy (EHE) above 100 PeV. Fig. 1.1 shows the power-law like CR spectrum [5]. A few distinctive features are visible: a modulation of the LE spectrum due to Solar wind activity, a change in index at $10^{15} - 10^{16}$ eV called "knee", and a change in spectrum at $10^{18} - 10^{19}$ eV called "ankle".

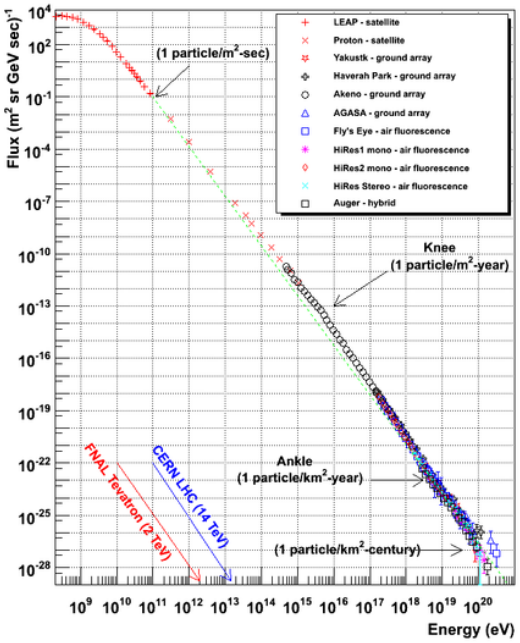

Figure 1.1: Cosmic-ray spectrum versus energy from 10^8 eV to 10^{21} eV. The "knee" and "ankle" features are visible. The rate of CR at different energies is given. A power-law with index -2.7 is shown in green. Figure extracted from Ref. [5].

The rate of detected CRs drastically decreases with increasing energy. CRs below the knee have a spectral index of ~ 2.7, those between the knee and the ankle of ~ 3.3 and those above the ankle of ~ 2.6. LE and HE CRs are assumed to be of Galactic origins while those above the ankle likely come from extragalactic sources. In the intermediate energy range a transition is expected between the Galactic and extragalactic CRs. VHE CRs reach Earth with a rate of 1 particle m^{-2} yr^{-1}. Detection of CRs with energy above 10^{20} eV was not expected because EHE CRs can efficiently interact with the Cosmic Microwave Background (CMB) radiation through processes $\gamma_{\mathrm{CMB}} + p \to p + \pi_0$ or $\gamma_{\mathrm{CMB}} + p \to n + \pi^+$ and loose energy, leading the a cutoff, known as Greisen–Zatsepin–Kuzmin (GZK) cutoff [6]. The detection of such EHE CRs by Auger puts a limit on the distance of their source of about 50 Mpc called GZK horizon, such that their probability to survive during the travel to Earth is larger.

1.2.2 Second order Fermi acceleration

Charged particles are accelerated when interacting with irregularities of a magnetic field. Enrico Fermi first introduced the concept of the CR acceleration process in the '50s and developed the second order Fermi acceleration mechanism [7]. Interstellar clouds perfectly ionized are perfect conductors. If initially magnetized they show irregularities in the magnetic field distribution. An incoming relativistic particle with a velocity $\approx c$ enters the cloud that is moving with velocity u. The particle moves randomly inside the cloud and interacts elastically with the cloud. Due to elastic diffusion on magnetic structures it is reflected off with increased energy as if the cloud was a magnetic mirror: head-on particles are accelerated and head-back particles are decelerated. The average energy gain due to random motion is $\langle \Delta E/E \rangle = 8/3(u/c)^2 = 8/3\beta^2$. This mechanism is called of "second order" because the gain per reflection depends on β^2. However, this theory is not sufficient to explain the detected CR spectrum. In fact this mechanism fails to effectively accelerate particles at energies beyond about the GeV. Since $u/c \ll 1$ a mechanism that produces a linear gain with u/c would be more efficient.

1.2.3 First order Fermi acceleration: diffusive shock acceleration

The Fermi mechanism was revisited and improved in the '70s developing the first order Fermi acceleration mechanism, also known as diffusive shock acceleration [8, 9]. The acceleration process takes place through the interaction of a relativistic particle with a strong shock wave at supersonic velocity. The shock propagates in the interstellar medium and particles are present both in the front and in the back of the shock. By crossing the shock from both directions the particles are scattered isotropically (in the gas rest frame). In the rest frame of the gas, upstream the shock a shock wave approaches with speed u_1 and the velocity of the gas beyond the shock is $u = u_1 - u_2 > 0$, where u_2 is the velocity of the gas in the shock wave rest frame. A relativistic particle that crosses the shock from upstream with speed v and angle θ with respect to the direction of the shock wave undergoes a small increase of energy $\Delta E = E(u/v)\cos\theta$ and is scattered behind the shock. The average gain per passage through the shock front is $\langle \Delta E/E \rangle \approx u/c$. In the rest frame of the gas downstream the shock the gas in front of the shock is approaching with speed u. So a particle that crosses the shock front downstream undergoes the same small increase of energy. This means that if a particle crosses several times the shock it will increase its energy at each passage. The collisions are always head-on and the particle never looses energy by crossing. The average gain for a full upstream-downstream-upstream passage is $\langle \Delta E/E \rangle = 4/3(u/c) = 4/3\beta$, linear with β.

The probability that a particle does not escape the acceleration region after n cycles is $P^n = (1 - \langle \Delta E/E \rangle)^n$. Given an initial number of particles N_0, after n cycles their number will be $N_n = N_0 P^n$. The energy of the particles after n cycles is $E_n = E_0(1 + \langle \Delta E/E \rangle)^n = E_0 \epsilon^n$,

and therefore $(N/N_0) = (E/E_0)^{\ln P/\ln \epsilon}$. The particles spectrum can then be approximated to $\mathrm{d}N/\mathrm{d}E \propto E^{-1+(\ln P/\ln \epsilon)}$, with $\ln P/\ln \epsilon \approx -1$ which gives a spectral index ~ 2 at the source. The diffusion of CRs in the medium softens the spectrum, producing an index $2.3 - 2.7$ far from the accelerators.

1.3 Mechanisms of production of gamma rays

VHE gamma-rays can be produced by accelerating electrons/positrons through what we refer to as leptonic processes, or protons through what we refer to as hadronic processes [10]. The relevance of a given acceleration process depends on the considered energy range. Synchrotron radiation dominates up to the tens keV, while bremsstrahlung is predominant in the GeV energy range and ICS becomes the dominating process in the GeV-TeV energy range together with pion decay. Each mechanism is briefly described below. Reviews with the computation details can be found in Refs. [11, 1].

1.3.1 Leptonic processes

Synchrotron radiation is produced when a charged particle interacts with an electromagnetic field. The particle is accelerated radially and moves in a spiral trajectory around the lines of the magnetic field. As shown in the panel of Fig. 1.2, a fast electron that is bent in a magnetic field produces synchrotron emission. This radiation is polarized and covers a wide range of the electromagnetic spectrum, from radio to hard X rays.

The characteristic energy of synchrotron emission for a particle of energy E and mass m that traverses a magnetic field of intensity B is

$$E_{\mathrm{syn}} = 3\mu_{\mathrm{B}} \left(\frac{E}{mc^2} \right)^2 B \sin\theta, \tag{1.1}$$

where θ is the angle of incidence and μ_{B} is Bohr magneton, a natural unit of the magnetic moment of an electron. A population of electrons with spectrum $\mathrm{d}N_{\mathrm{e}}/\mathrm{d}E_{\mathrm{e}} \propto E_{\mathrm{e}}^{-\alpha}$ produces gamma rays with spectrum $\mathrm{d}N_\gamma/\mathrm{d}E_\gamma \propto E_\gamma^{-(1+\alpha)/2}$.

Bremsstrahlung , also known as braking radiation, is the radiation produced by the deceleration of a particle (mainly electrons/positrons) when deflected by the Coulomb field of an atomic nucleus. The energy lost by the incoming electron is converted into a continuum spectrum of photons. Bremsstrahlung is the dominating radiating process for electrons/positrons above a few ten MeV and a few hundreds GeV for muons. Electrons with energy E, by interacting with atoms and molecules, can produce gamma rays with frequency up to $\nu = E/h$. The average gamma-ray energy is about 1/3 of the energy of the accelerated particle. TeV gamma rays can then be produced by electron accelerated to about a ten TeV. This radiation process is more efficient in dense environments.

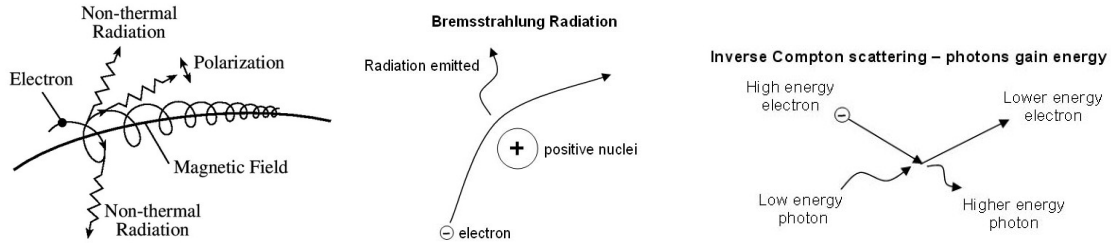

Figure 1.2: Sketches of the leptonic mechanisms of production of VHE gamma rays. *Left panel:* Diagram of the mechanism of synchrotron radiation production through the interaction of a charged particle with a magnetic field. Figure extracted from Ref. [12]. *Central panel:* Diagram of the bremsstrahlung process that produces gamma rays through breaking of an electron in the electric field of a positively charged nucleus. Figure extracted from Ref. [13]. *Right panel:* Diagram of the Inverse Compton scattering that produces VHE gamma rays through scattering of a very energetic electron against a low energy photon and their exchange of energy. Figure extracted from Ref. [13].

Inverse Compton Scattering (ICS) consists of the interaction between an accelerated electron and a low energy photon. It is a process of cooling of a relativistic electron whose energy is converted into photons. The right panel of Fig. 1.2 shows in a sketch how in the interaction the electron loses energy and the photon gains it.

The maximum frequency in the observer frame is $\nu/\nu_0 \approx 4\gamma^2$. The average frequency is $\langle\nu\rangle/\nu_0 \approx 4/3\gamma^2$, so that the spectrum is peaked towards the average frequency. Given a charged particle with energy E and mass m interacting with a target photon of energy ϵ, in the non-relativistic regime ($E\epsilon \ll m^2$) the ICS interaction cross section is close to the Thompson cross section $\sigma_{\rm ICS} = \sigma_{\rm T}(1-2\kappa_0)$, with $\kappa_0 = E\epsilon/m^2$. The Thompson cross section expresses as $\sigma_{\rm T} \approx 6.65 \times 10^{-25}$ cm^2. In this regime the average energy of the scattered photon is $E_\gamma \approx E^2\epsilon/m^2$. In the ultra-relativistic Klein-Nishina regime ($E\epsilon \gg m^2$), the ICS interaction cross section becomes $\sigma_{\rm ICS} = (3/8)\sigma_{\rm T}\kappa_0^{-1}\ln(4\kappa_0)$ and photons with the same energy of the initial electron can be produced. A population of electrons with spectrum $dN_{\rm e}/dE_{\rm e} \propto E_{\rm e}^{-\alpha}$ produces gamma rays with spectrum $\mathrm{d}N_\gamma/\mathrm{d}E_\gamma \propto E_\gamma^{-(1+\alpha)/2}$ in Thompson regime and a steeper spectrum $\mathrm{d}N_\gamma/\mathrm{d}E_\gamma \propto E_\gamma^{-(\alpha+1)}\ln(\kappa_0 + \mathrm{const})$ in Klein-Nishina regime.

1.3.2 Hadronic processes

Pion decay Neutral pions are produced in the interaction of accelerated protons with the interstellar gas. The neutral pions subsequently decay into photons [14]. A sketch in Fig. 1.3 shows accelerated protons that interact with a proton of the interstellar medium and produce either charged pions and neutral pions[1]. The charged pions produce muons together with the subsequent neutrinos, while the neutral pions mainly decay into pairs of gamma rays, $\pi_0 \to \gamma + \gamma$, with a 98.8% branching ratio and a lifetime $t_{\pi_0} = 8.4 \times 10^{-17}$ s.

[1]Neutral pions, π_0, are 1/3 and charged pions, π^+ and π^-, are 2/3 of the total [15].

This process most efficiently produces TeV gamma-rays. The gamma-ray emission traces the distribution of the gas with which the incident protons interact. The energy threshold of this interaction is at $2m_{\pi_0} \approx 270$ MeV and the gamma ray spectrum has a distinct feature: it has a maximum at $E_\gamma = m_{\pi_0}/2 \approx 67$ MeV. Protons with initial spectrum $\mathrm{d}N_\mathrm{p}/\mathrm{d}E_\mathrm{p} \propto E^{-\alpha}$ produce gamma rays with spectrum $\mathrm{d}N_\gamma/\mathrm{d}E_\gamma \underset{\sim}{\propto} E^{-\alpha+0.1}$ due to the slight energy dependency of the inelastic pp interaction. Interestingly, the joint detection of neutrinos (from charged pion decay) and gamma rays (from neutral pion decay) would be a clear signature of proton acceleration by an astrophysical object.

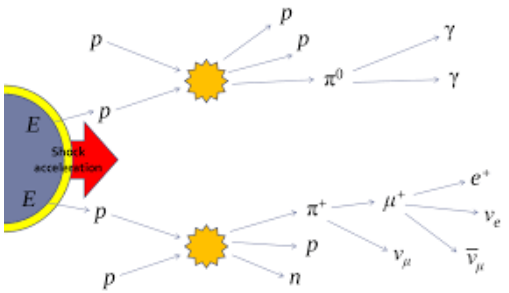

Figure 1.3: Sketch of pion decay. Accelerated protons interact with the protons of the interstellar medium producing pions. The charged pions decay into muons and the corresponding neutrinos, while the neutral pions produce couples of gamma rays.

1.3.3 Dark matter annihilation and decay

Gamma rays can also be produced by the self-annihilation of dark matter (DM) particles or by their decay. They can be primary or secondary products of these processes. More details on the production of gamma rays through DM annihilation and the obtained gamma-ray spectrum are given in Sec. 6.7 and Sec. 6.8.

1.4 Cosmic accelerators

Supernova Remnants The supernova remnant (SNR) results from the explosion of a star of mass larger than 8 times the solar mass into a supernova. The supernova is the end of the life of a very massive star that implodes into a neutron star (if the star has a mass between 10 and 29 solar masses) or a black hole (if the star has a mass at least three times the solar mass) or a white dwarf (if the star has mass below 10 solar masses) that accrete mass from a companion until collapse. The remnant is a structure made out of the expanding material ejected during the explosion that creates a shock front. Cosmic rays can be accelerated in the shock of SNR [16] and then produce gamma rays. About 10% of the energy of the explosion is expected to be released for CR acceleration. The first SNR detected in VHE gamma rays by H.E.S.S. is SNR RXJ1713.7-3946 [17].

Gamma-Ray Bursts Gamma-ray Bursts (GRBs) are short and intense jets of gamma rays of extragalactic origin. They are transient phenomena and among the brightest in the Universe. GRBs can be produced by the explosion of a very massive star into a black hole or by the merging of two neutron stars (or a neutron star and a black hole). Fermi-LAT has detected gamma rays emitted by prompt GRBs up to about 50 GeV. They have a luminosity of the order of 10^{52-54} erg s^{-1}. Hundreds of GRBs have been detected in the keV-MeV energy range [18]. For the first time the prompt emission of a GRB has been detected above 300 GeV by MAGIC [19]. After the first gamma-ray jet a longer-lived emission called afterglow is emitted, produced by the interaction of the ejecta and the interstellar medium. Recently, for the first time VHE gamma rays above 100 GeV produced by a GRB afterglow have been detected with H.E.S.S. [20].

Active Galactic Nuclei The Active Galactic Nuclei (AGN) are supermassive black holes harbored at the center of host galaxies, with mass a million to a billion times the mass of the Sun. They have an accretion disk of rotating gas that is visible in optical and X rays. AGNs also shine in gamma rays produced in a highly collimated relativistic jets [21]. When the jet is pointed towards Earth (at an angle smaller than $\sim 20^{\circ}$) the object is referred to as a blazar. Hundreds are detected at GeV energies and tens at TeV energies. Gamma rays are expected to be produced mainly through ICS on synchrotron electrons. A standard interpretation for AGN spectra is the synchrotron self-Compton [22]. The role of hadronic processes in the emission is not yet settled. The jets may be able to accelerate protons to EeV energies. Flares of PKS 2155-304 are among the brightest emissions from blazars [23].

Pulsars and Pulsar Wind Nebulae Pulsars (PSR) are the product of a supernova explosion at the end of life of a star with mass between 10 and 29 solar masses. After the outer layers are ejected the remaining core can be a neutron star with high rotation rate. The strong magnetic field at the surface accelerates charged particles, trap them in beams and ejects them from the poles. This kind of object is called pulsar because the emitted jets are periodically observed by Earth giving a pulsation effect. The typical periodicity is of the order of the second. One of the most energetic gamma-ray emitting PSR is the Vela Pulsar [24]. TeV events from the Vela pulsar have been recently detected by H.E.S.S. [25]. The particles that follow the lines of magnetic field around the PSR are not ejected in the beams and rotate with the neutron star itself. They can escape the PSR at the distance of the light cylinder after which they would need to travel faster than light to keep rotating with the core. They are injected in the interstellar medium and form the so called pulsar wind nebula (PWN). In the PWN shock waves are created and accelerate particles, *i.e.* gamma rays via ICS in the ambient radiation field can be effectively produced [26]. The best observed PWN in VHE gamma rays is the Crab Nebula [27].

1.5 Observations and instruments

1.5.1 Satellite experiments

Experiments built on satellites detect gamma rays directly, being outside the atmosphere. Due to their modest size (acceptance ~ 1 m^2) they can detect gamma rays in the few MeV to hundred GeV energy range. Gamma-ray telescopes on satellite have almost 100% duty cycle since they are not affected by the alternation of day and night, they have modest angular resolution $0.15° - 3.5°$, very good energy resolution $\sim 10\%E$ and wide field of view (FoV) > 2 sr. The example of currently operating gamma-ray telescopes on satellites are Fermi-LAT and AGILE. AGILE (Astro-Rivelatore Gamma a Immagini Leggero) is a satellite launched in 2007 [28]. It is equipped with a Gamma-Ray Imaging Detector (GRID) in the energy range 30 MeV-50 GeV, a silicon X-ray detector, SuperAGILE, in the range 18-60 keV, a non-imaging gamma-ray scintillator detector, Mini-Calorimeter (MCAL), that covers the energy range 350 keV-100 MeV and an anticoincidence detector that acts as a veto. Fermi-LAT is located on the space observatory Fermi Gamma-ray Space Telescope, formerly Gamma-ray Large Area Space Telescope (GLAST) [29]. Fig. 1.4 shows the Large Area Telescope (LAT) instrument. It consists of an anticoincidence detector, a tracker and a calorimeter. The anticoincidence detector acts as a veto in order to discriminate the background. In fact, in this part of the detector charged CRs cause a flash of light. The gamma rays then travel through the tracker where they encounter tungsten foils that convert them into electron/positron pairs. The cesium iodide calorimeter finally stops them and can measure the total energy of the initial gamma ray.

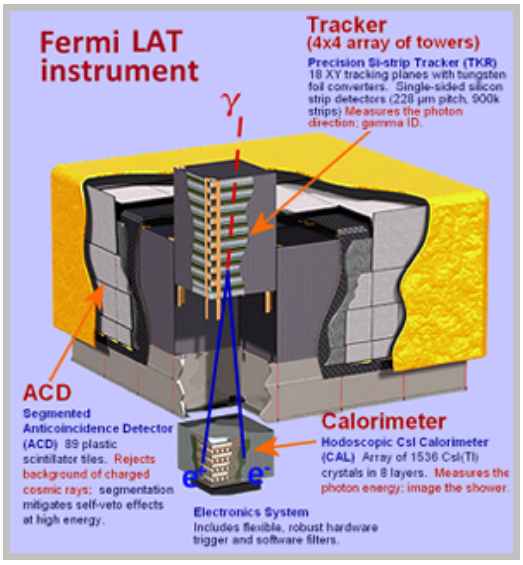

Figure 1.4: Representation of the LAT instrument with its subdetectors: anticoindicence detector (ACD), tracker and calorimeter. Figure extracted from Ref. [29].

1.5.2 Ground-based water tanks

Water tanks detect directly the secondary particles produced by the primary gamma rays that enter the atmosphere. They are located at high altitude to probe the core of the particle shower. The charged particles of the shower travel inside the water tanks producing Cherenkov light, which can be detected with photomultipliers (PMTs). The energy and direction of the primary gamma ray can be reconstructed. Gamma rays and CRs are discriminated thanks to the spatial distribution of their hits in the tanks array. Ground-based tanks observatories have a large surface and can detect photons at VHE energy, with best sensitivity beyond the TeV. They have modest energy resolution $\sim 50\%E$ and good angular resolution $0.2 - 0.8°$, pretty large FoV ~ 1 sr and long duty cycle $\sim 90\%$. The main current water tank gamma-ray observatory is HAWC (High Altitude Water Cherenkov observatory) [30] that comprises 300 tanks and is located in the Parque Nacional Pico de Orizaba in Mexico, at a high altitude of 4100 m above the sea level. Fig. 1.5 shows the HAWC array, the air shower produced in the atmosphere[2], the Cherenkov light produced in the tanks that hits the PMTs and the signature of a gamma-ray- or CR-induced shower in the array.

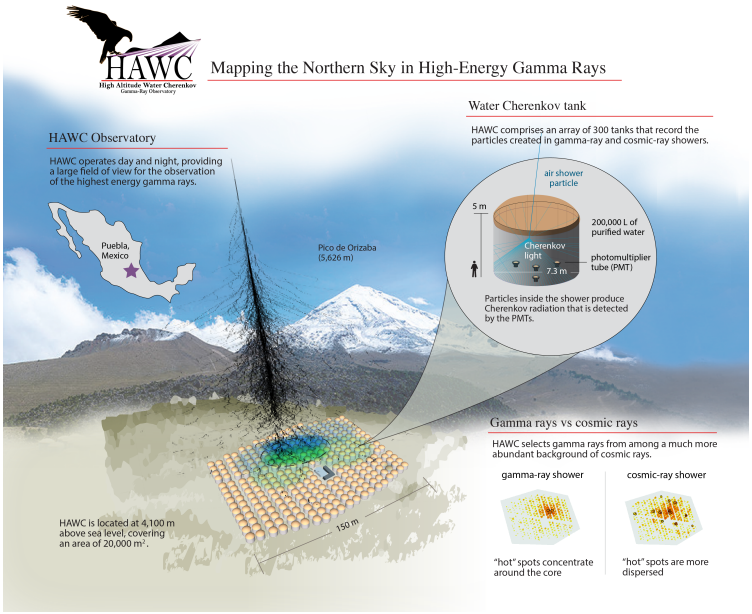

Figure 1.5: HAWC observatory site [30]. The development of a shower in the atmosphere and its projection onto HAWC tanks array is shown. The structure of a water tank and the detection technique of Cherenkov light is summarized.

[2]More information about the creation of an air shower and the production of Cherenkov light in given in Sec. 2.1 in the context of the atmospheric Cherenkov telescopes.

1.5.3 Ground-based atmopsheric Cherenkov telescopes

Ground-based imaging atmospheric Cherenkov telescopes (IACTs) detect VHE gamma rays indirectly. They detect the Cherenkov light produced by the charged particles electromagnetic showers initiated by gamma rays in the atmosphere. They cover a gamma-ray energy range between the ten GeV and hundred TeV. They have excellent energy resolution $\sim 10\%E$ and angular resolution $< 0.1^\circ$ per gamma ray, and short duty cycle $10 - 15\%$ because the data taking is stopped during day time and reduced in presence of the Moon. The FoV is also modest $\sim 5^\circ$ and pointed observations are needed. More details on the detection technique with IACTs are given in Chap. 2. The main current IACTs are H.E.S.S. (High Energy Spectroscopic System) [31], MAGIC (Major Atmospheric Gamma-ray Imaging Cherenkov telescope) [32] and VERITAS (Very Energetic Radiation Imaging Telescope Array System) [33]. The main characteristics of these gamma-ray telescopes are summarized in Tab. 1.1. In addition, the telescope FACT (First G-APD Cherenkov Telescope) [34] was

Name	Hemisphere	Altitude [m]	Number of telescopes	Mirror area [m^2]	Number of pixels	FoV [deg]	E_{thr} [TeV]
H.E.S.S.	South	1800	4+1	108/600	960/2048	5/3.2	0.1/0.03
MAGIC	North	2225	2	234	574	3.5	0.06
VERITAS	North	1275	4	106	299	3.5	0.1

Table 1.1: Main characteristics of the currently operating IACTs: H.E.S.S., MAGIC and VERITAS.

mounted in 2011 in La Palma on the MAGIC site in order to test a new technology in view of the next telescope array CTA (Cherenkov Telescope Array). Instead of the usual photomultiplier tubes, FACT camera uses Geiger-mode avalanche photodiods (G-APDs), which are more robust, can work at lower voltage and have better photon detection efficiency. The G-APDs pixels have also been tested in presence of strong moonlight in order to provide longer duty cycle, crucial especially for detection of transient emissions.

1.6 Fundamental physics with very high energy gamma rays

VHE gamma rays are crucial messengers for studying some fundamental physics subjects:

- quest for **dark matter**. This topic is widely discussed in Parts IV and V of this work.
- **photons absorption** through interaction with background radiation. The Universe becomes opaque to gamma rays when they interact with background photons and create electron-positron pairs. In the GeV-TeV energy range gamma rays can be absorbed by the Extragalactic Background Light (EBL), while ultra-high-energy photons (> 100 TeV) could interact also with the Cosmic Microwave Background

(CMB). The gamma-ray spectrum is attenuated by a factor $\exp(-\tau(E,z))$, where $\tau(E,z)$ is the optical depth that depends on the energy of the gamma rays and the distance of the source. Using standard EBL models, like the Franceschini model [35], the optic depth of gamma rays with energy 10 TeV is about 0.5 for sources at redshift $z = 0.01$ (corresponding to a distance of about 45 Mpc) and it increases up to 100 for sources at $z = 1$ (about 3 Gpc).

- **Lorentz Invariance Violation** (LIV). In some quantum gravity models modifications of the photon dispersion relation allow the speed of light to vary with energy. LIV is studied in VHE gamma-ray astrophysics through observation of transient sort-lived phenomena like GRBs, flares of AGNs or PSRs. Signatures of LIV could be a time lag between two energy ranges or a deviation from a standard spectrum, besides the corrections due to interaction of the photons with the EBL. LIV studies have been performed with H.E.S.S. on PKS 2155-304 [36] and Mrk 501 [37] flares.

- search for **primordial black holes** (PBH). They are hypothetic black holes formed in the very early Universe just after the Big Bang from gravitational collapse of dense regions, and not from collapse of massive stars as it is the case for astrophysical black holes. PBH could have mass in a very large range, from the Planck mass to thousands of solar masses. Signatures of PBH evaporation could be gamma-ray flares with duration from several microseconds to several seconds. Constraints of the PBH evaporation have been set with H.E.S.S. [38].

- **origin of cosmic rays**. Gamma-rays are produced through radiative processes by VHE CRs. So studying the sources of CR accelerated at TeV-PeV energies can shed light on the processes of acceleration of particles, and the objects that accelerate CR up to the knee. The search for Galactic pevatrons with H.E.S.S. [39] is crucial in this context.

Chapter 2

The H.E.S.S. experiment

Contents

2.1 Development of air showers and Cherenkov light 16
2.1.1 Development of atmospheric showers 16
2.1.2 Cherenkov light emission 18
2.2 The H.E.S.S. instrument 19
2.2.1 Phase I 20
2.2.2 Phase II 21
2.3 Event identification and selection 22
2.3.1 Trigger definition and quality cuts 22
2.3.2 Calibration 23
2.3.3 Reconstruction and analysis chain 23
2.4 Observation techniques and background measurements 26
2.4.1 Observation modes 26
2.4.2 Background measurement techniques 27
2.5 Instrument response functions (IRFs) and sensitivity 29
2.5.1 Effective area 29
2.5.2 Energy threshold 30
2.5.3 Energy resolution 30
2.5.4 Angular resolution 30
2.6 H.E.S.S. I versus H.E.S.S. II event reconstruction 32
2.6.1 Reconstruction modes 32
2.6.2 Acceptance and sensitivity 32

In this chapter the H.E.S.S. experiment is presented. The production of Cherenkov photons from gamma rays interacting with the atmosphere is explained together with the VHE gamma-ray detection techniques and the background rejection. The main performances of the H.E.S.S. array are presented at the end.
The process that produces gamma-ray signal detectable with Cherenkov telescopes is described in Sec. 2.1. The two phases of the H.E.S.S. experiment are introduced in Sec. 2.2. The event selection and reconstruction technique are explained in Sec. 2.3.3. In Sec. 2.4 the observation modes and the techniques to determine the background are presented. The instrument response functions (IRFs) of H.E.S.S. and the performances of the array are given in Sec. 2.5. The different event reconstruction methods used during phase 1 and 2 of H.E.S.S. are described in Sec. 2.6.

2.1 Development of air showers and Cherenkov light

2.1.1 Development of atmospheric showers

Particles that enter the Earth's atmosphere interact with the environment and create showers of secondary particles. The characteristics of the shower depend on the nature and properties of the initial particle [40], *i.e.* on the interaction that takes place.

Electromagnetic shower

The electromagnetic shower is a cascade of photons, electrons and positrons. It can be initiated by a gamma ray or CR electron[1]. Gamma rays, when interacting with matter, will produce an electron-positron pair. In turn, each electron and positron will undergo bremmshtralung in the vicinity of a nucleus and produce gamma rays. These processes will repeat creating a shower of electrons, positrons and photons. The initial particle must have enough energy to undergo pair production (in case of gamma rays) or bremsstrahlung (in case of CR electrons.). And the shower stops to grow when pair production is not possible anymore and other energy loss mechanisms other than bremsstrahlung (*e.g. ionization*) take place. This happens at an energy threshold $E_{\mathrm{thr}} = 800\,\mathrm{MeV}/(Z+1)$.

The shower length (or depth) X is defined by the radiation length X_0, which is characteristic of each material. This quantity is defined as the path during which a photon loses $7/9$ of $E_{\gamma,0}$ or an electron loses all but $1/e$ of its initial energy. So the photons interact slightly deeper in the atmosphere.
The shower depth is approximately defined as

$$X = X_0 \frac{\ln(E_{\gamma,0}/E_{\mathrm{thr}})}{\ln 2}. \tag{2.1}$$

[1]When taking about CR electrons we refer both to electrons and positrons

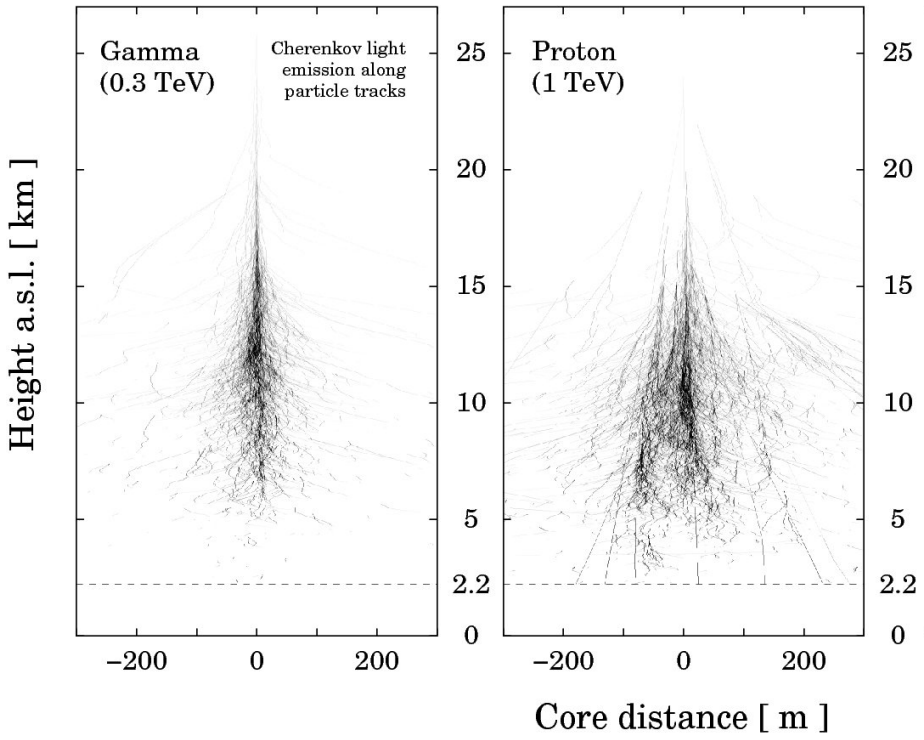

Figure 2.1: Electromagnetic and hadronic showers. *Left panel:* development of an electromagnetic shower initiated by a gamma ray of 300 GeV in the atmosphere. *Right panel:* development of an hadronic shower initiated by a CR proton of 1 TeV in the atmosphere. The proton interacts deeper in the atmosphere and develop a larger shower with sub-showers that move far from the core of the shower. Figure extracted from Ref. [40].

The width of the shower depends on the electron multiple scattering. Most of the shower is contained in about $2R_{\mathrm{M}}$, where R_{M} is the Molière radius, characteristic of the material. The development of an electromagnetic shower in the atmosphere is shown in the left panel of Fig. 2.1.

Hadronic shower

The development of showers by hadrons that enter the atmosphere is more complicated and based on nuclear interactions and decays. Sub-showers are visible:

1. hadronic component: nuclear fragments.

2. muonic component: kaons and charged pions produced during the nuclear interaction of the CR hadron with the atmosphere can decay into muons and the corresponding neutrinos.

3. electromagnetic component: muons decay in electrons or neutral pions that can decay into photons and may initiate an electromagnetic sub-shower.

Due to the various interactions that take place the hadronic showers are more spread than the electromagnetic ones and show sub-showers that can be significantly displaced from the shower axis due to the high momentum particles created in inelastic collisions.
The depth of the shower is defined by the nuclear interaction length λ. It is defined as the mean path traveled by an hadron in a material before undergoing inelastic nuclear interaction. In the air $\lambda > X_0$, so the hadronic showers initiate deeper in the atmosphere.
The development of a hadronic shower in the atmosphere is shown in the right panel of Fig. 2.1.

2.1.2 Cherenkov light emission

Relativistic charged particles that travel through a medium can produce Cherenkov light. This mechanism takes place when the speed of the particle v in a medium with refractive index n is larger than the light speed in the same material $u = c/n$, *i.e.* $v > c/n$.
A cone of light is emitted with characteristic angle α such that

$$\cos\alpha = \frac{u}{v} \qquad \text{and} \qquad \cos\alpha_{\max} = \frac{1}{n}. \tag{2.2}$$

The electrons and positrons of a very energetic shower can be relativistic enough to produce Cherenkov light [41]. The energy threshold for electrons is given by $E_{\rm th} = \gamma_{\rm th} m_{\rm e} c^2$, with $\gamma_{\rm th} = [1 - 1/n^2]^{-1/2}$, and in the atmosphere it is equal to about 20 MeV at 10 km altitude[2].
VHE gamma rays that cannot be directly observed (they do not reflect on mirrors) are detected through the Cherenkov light that they produce. The Cherenkov light has a wavelength $300 - 700$ nm and peaks at about 400 nm, the peak of sensitivity of PMTs. This is also the wavelength of the optical light produced by stars, which is an important background for the detection of Cherenkov light.
For a primary interaction depth of 10 km, a VHE gamma ray produces in the atmosphere a Cherenkov light cone that has overall (including the scattering of the electrons) a diameter of about 250 m at the ground, called the *light pool*. The ground-based Cherenkov telescopes that fall inside the cone are designed to detect the Cherenkov photons, as shown in the left panel of Fig. 2.2. Most of the Cherenkov photons produced by the shower arrive at the ground in about a few ns, so it is crucial to use in the cameras PMTs with GHz acquisition electronics. The Cherenkov light cone produced by the shower and its *light pool* are shown in the left and central panels of Fig. 2.2. The right panel shows the electromagnetic shower that crosses the atmosphere and its image on the focal plane of the camera after reflection on the mirror of a telescope.
The cameras of the IACTs can reconstruct the shower parameters through the Cherenkov light detected by each PMT. Monte Carlo images of showers initiated by a muon, a hadron and a photon are compared in Fig. 2.3. The analysis of the spatial (and temporal) image in

[2]The attenuation of the radiation when traversing the atmosphere is not accounted for in $E_{\rm th}$.

the camera provides the information about the energy, the direction and the nature of the initial particle.

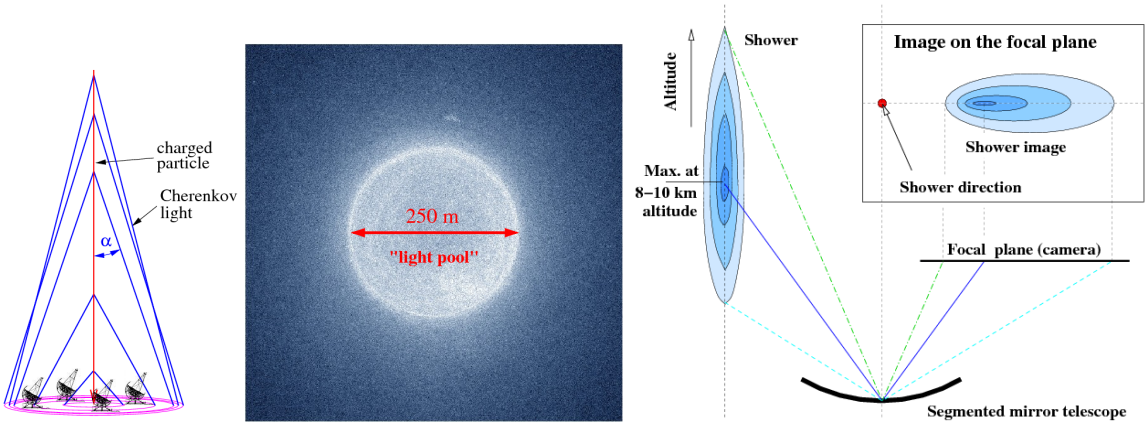

Figure 2.2: Cherenkov light emitted by an electromagnetic shower in the atmosphere. *Left:* Schematic of the Cherenkov light cone (blue) emitted with angle α by an electromagnetic shower that moves towards the ground (red flesh). The projection of the cone on the ground is also shown (magenta). *Center: light pool* of a Cherenkov light cone on the ground. *Right:* image of an atmospheric shower on the focal plane of the camera of a IACT after reflection on the mirror. Figure extracted from Ref. [41].

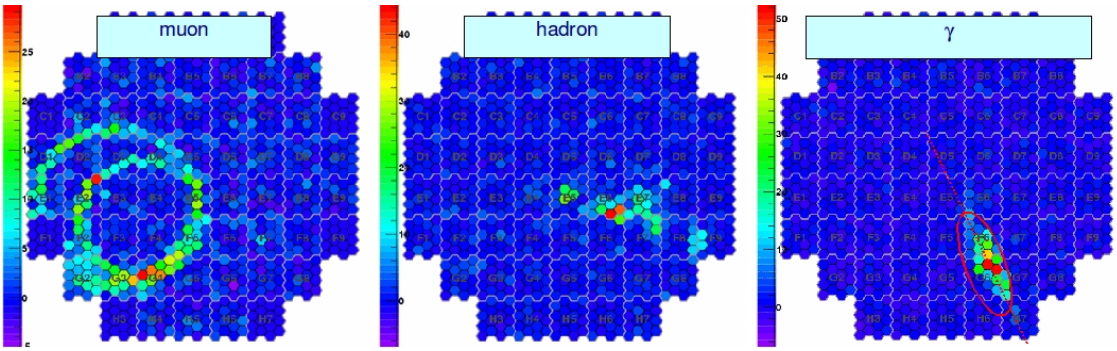

Figure 2.3: Image of atmospheric showers in the camera. From left to right, showers induced by a muon, a hadron and an photon, respectively.

2.2 The H.E.S.S. instrument

The High Energy Spectroscopic System (H.E.S.S.) is an array of IACTs. It is situated in Namibia at geographic coordinates 23°16′17″S and 16°30′00″E on a plateau at about 1800 m above sea level, in the region of Khomas Highland. The location has been chosen due to the dry climate, mild temperature and the reduced luminous pollution. Its unique position in the Southern hemisphere among the ground-based Cherenkov telescopes makes

it the best currently operating IACT to observe the Galactic plane and in particular the Galactic Center in VHE gamma rays.
The H.E.S.S. Collaboration consists of about 230 scientists from 13 countries and 42 institutes.

Figure 2.4: H.E.S.S. telescope array. The phase two large telescope CT5 is at the center of the array. The four first phase smaller telescopes CT1-4 are at the corners of the array. Figure extracted from Ref. [31].

2.2.1 Phase I

The experiment started at the end of 2003. At that time the array was composed of four IACTs [42]. The four telescopes are called CT1-4 and they are visible in Fig. 2.4. They are set on the corners of a square of 200 m and they stand at each cardinal point. Each one consists in a metallic rotating structure that moves in the azimuth and zenith directions (Alt-Az mount) and supports a camera and a Davies-Cotton mirror of diameter 12 m.

Mirrors

Each mirror [43, 44] is segmented into 382 smaller mirrors of circular shape. The total mirror area is 108 m^2. The mirror design is of Davies-Cotton design [45] with all the facets at the same focal length f, *i.e.* with a discontinuous surface. The focal length is 15 m and the focal ratio f/d is 1.2. Each individual mirror tile is aligned in order to focus at the position of the camera. The reflectivity is better than 80% in the Cherenkov light wavelength range.
The mount of the mirror has a fast drive system that allows to move the telescopes in altitude and azimuth to change the pointing position. It is controlled by servo-controlled AC motors and backup battery-driven DC motors. The drive system can reach a speed of 100° per minute. The mirror supports are built in order to be stable within 0.15 mrad rms over the full altitude range.

Camera

On each telescope a camera is mounted at the position of the focal point. The camera counts 960 photomultipliers (PMTs) with a field of view (FoV) of 0.16° (3 mrad) each, for a total FoV of 5° (in diameter). In front of every PMT a Winston cone is added in order to decrease the gaps, *i.e.* dead zones, increase the light collection surface and focus the light onto the active area of the PMT. Each PMT constitutes a pixel. The pixels are grouped by 16 into 60 drawers. The electronics for triggering and readout is integrated into the camera body. The single telescope trigger average rate is $200 - 300$ Hz. The effective pixel coincidence window is ~ 1.5 ns.

2.2.2 Phase II

In 2012 an additional larger telescope has been added in the middle of the array. The observational data taking has begun in 2014, starting the H.E.S.S.-II phase.

CT5

The large telescope, called CT5 [46], has a diameter of 28 m, for a total area of 614 m^2 of mirrors. The shape of the mirror is parabolic and the 875 mirror facets are hexagonal. The focal length is 36 m. CT5 is shown at the center of Fig. 2.4. The azimuth drive has a peak positioning speed of 200° per minute and the elevation drive a speed of 100° per minute. The displacement accuracy is about 1 mm.
The camera has 128 hexagonal pixels (drawers) for a total of 2048 PMTs and is equipped with Winston cones. The diameter of the camera is 2 m for a FoV of 3.2° on the sky. The effective signal integration time is of 16 ns. The typical mono trigger rate is 1.5 kHz.

Upgrade of CT1-4 cameras

In 2015-2016 the electronics of the cameras of the small telescopes has been upgraded to improve the overall performances of the array [47]. The upgrade reduced the stereo dead time, reduced the failure rate due to aging of the system and overall improved the performances of the telescopes. The new electronics is based on NECTAR readout chips [48]. The readout time is reduced from 450 μs to 15 μs in order to work in stereoscopic mode in coincidence with CT5 at higher trigger rate. Cabling scheme, ventilation, power supply and pneumatics have also been renovated.

2.3 Event identification and selection

2.3.1 Trigger definition and quality cuts

The low-level event selection and background rejection starts with three thresholds:

- S_1 on the number of photoelectrons in a single pixel. This defines a pixel that triggered and rejects the electronic noise and pedestal.

- S_2 on the number of nearby pixels that triggered (pixels in the same sector of the camera). This defines a telescope that triggered.

- S_3 on the number of telescopes that triggered (stereoscopy).

The thresholds of H.E.S.S. I were $S_1 = 4$ photoelectrons per pixel, $S_2 = 3$ pixels per sector and $S_3 = 2$ telescopes. The primary particle identification is based on the shape of the shower. Muons are recognized by their ring signature. They rarely trigger more than one telescope [49] since they are produced by high momentum particles in hadronic showers, *i.e.* they are isolated and can be efficiently discriminated thanks to the stereoscopy. In addition, the array of telescopes can take advantage of the stereoscopy, as shown in Fig. 2.5, to improve the reconstruction of the shape and direction of the shower. The intersection point between the major axis of the shower image reconstructed in each telescope provides a reconstruction of the direction (see Fig. 2.5).

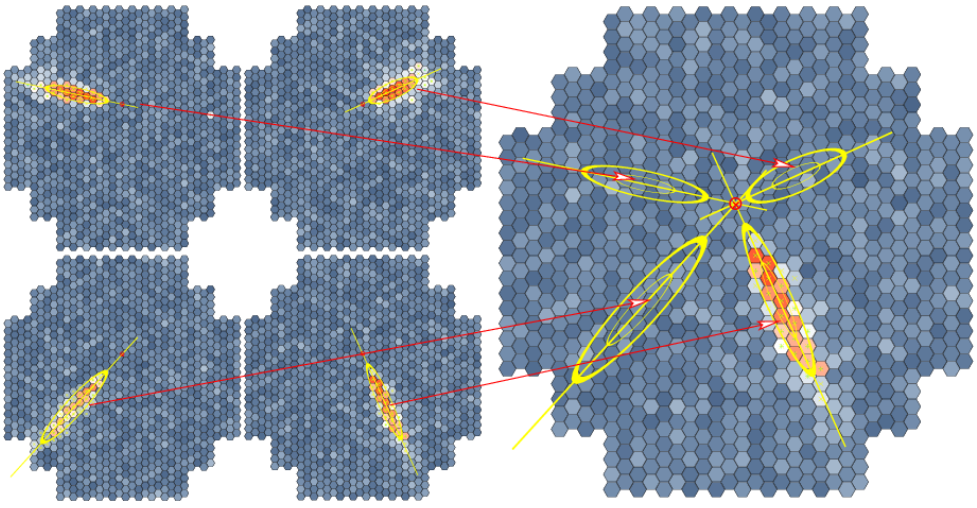

Figure 2.5: Stereoscopic reconstruction of an air shower. *Left panel:* reconstructed shower in each of the four cameras. *Right panel:* the four images are combined and from the direction of their main axes the direction of the gamma ray is reconstructed. Figure extracted from Ref. [41].

After triggering there are additional quality cuts. The unused pixels[3] in each camera cannot exceed 10%, the global trigger rate must be above 70% of the average of list of observations (*run* list) and the variation of the trigger rate between the telescopes cannot exceed 10%. In addition the weather conditions are monitored by a weather station and an infrared LIDAR scans the sky in order to detect clouds. The atmospheric conditions like humidity, temperature or presence of clouds can strongly affect the trigger rate or create inhomogeneities in the FoV [50].

2.3.2 Calibration

The analysis chain goes through several steps that include the calibration, the image parametrization and reconstruction of an event and the determination of the properties of the primary particle.
The parameters needed to reconstruct the signal amplitude are:

- the ratio between the high and low gain channels of amplification of the PMT signal,
- the pedestal in the two channels,
- the gain in every single pixels for the two channels,
- the coefficient of flat-field in each pixel necessary to obtain a uniform output allover the camera.

The calibration is made through dedicated *runs* that allow us to measure these parameters. This step is necessary to be able to properly convert the photoelectron signal recorded in the PMTs into ADC counts. In order to properly perform the calibration the broken pixels are first detected and excluded. For more details on the calibration of CT1-4 upgraded cameras see Ref. [51]. For the calibration of CT5 see Ref. [52].

The calibration procedure allows to measure the night sky background (NSB), that includes bright light spots or diffuse optical light, like the star light, the light from planets and zodiacal light. In absence of Cherenkov light the NSB measured in the PMTs dominates above the electronic noise. It represents a single-photoelectron rate of about $40 - 100$ MHz at large Galactic latitudes, while it reaches rates up to about ~ 300 MHz in the vicinity of the Galactic plane. The NSB has a strong impact on the width of the pedestal, *i.e.* on the energy threshold [53].

2.3.3 Reconstruction and analysis chain

The next step is to reconstruct the image of the showers on the cameras and classify gamma-like and hadron-like events based on the characteristics of their shower characteristics using the *runs* that pass the quality cuts.

[3] Broken pixels and pixels turned off in correspondence with a bright star.

Geometrical reconstruction based on the Hillas parameters

Two separate analysis chains are developed in H.E.S.S. and are used to cross-check the analysis results. The chain that was developed first is called *HAP* and it is based on the moments of the image of the shower on the camera, given its approximately elliptical shape. The geometrical parameters of the shower shape are called the Hillas parameters [54, 55] and are:

- width (signal RMS perpendicular to the main axis),
- length (signal RMS along main axis),
- center of gravity,
- orientation,
- compactness
- angular distance from the observer.

Semi-analytical shower modeling

A more sophisticated template based analysis has been developed [53]. It is called *Model++* and it is used in all the results presented in this work. The Cherenkov light distribution on the cameras is simulated and it is compared through a χ^2 test to the Cherenkov light distribution actually recorded by each pixel of the camera.

The shower model is build from the parametrization of the longitudinal, lateral and angular distribution of the charged particles in the electromagnetic shower simulated with KASKADE [56]. It accounts also for the depth of interaction, the collection efficiency and other factors like the atmospheric conditions that have effects on the atmospheric absorption. In addition, the model accounts for the NSB on a pixel-by-pixel basis and the broken or inactive pixels.
The Cherenkov photons distribution in the camera can be estimated by knowing:

- the characteristics of the longitudinal development of the shower,
- the distribution of charged particles in the shower,
- the energy of the electrons/positrons that produce Cherenkov light,
- their position with respect to their direction and the telescope,
- the Cherenkov photons production rate,
- the spatial distribution of the Cherenkov photons with respect to the electron,
- the opacity of the atmosphere.

In order to account for instrumental effects, the detector is also simulated through the code SMASH [57], including

- the collection efficiency and reflectivity of the mirrors,
- the Winston cones,
- the geometry of the telescopes,
- the conversion of the photoelectrons into ADC counts (response function, the integration window, etc.),
- the local and central trigger systems.

Monte Carlo simulations are performed for gamma, electrons, protons and nuclei, at different zenith angles, impact distance and energy bins, respectively. The information about the Cherenkov images in the camera obtained by careful simulation of the instrument and the shower development are stored in lookup tables.

The measured shower is compared pixel-by-pixel to the simulated shower templates through a maximum likelihood test. The log-likelihood function[4] writes $\ln \mathcal{L}(x|\mu) = P(x|\mu, \sigma_{\rm el}, \sigma_{\rm NSB}))$ and it represents the probability to observe a signal x in a pixel where a signal with intensity μ is expected, assuming that the width of the electronic background and NSB are $\sigma_{\rm el}$ and $\sigma_{\rm NSB}$, respectively. The total likelihood is the sum over the $N_{\rm pixel}$ pixels.

The separation between showers that are likely produced by gamma rays (gamma-like events) and by hadrons (hadron-like events) is made through the comparison to the measured shower image and simulated shower image templates. It is based on a quality parameter called *(mean scale) shower goodness* (MSSG) that quantify the agreement between the gamma-ray shower templates and the measurement in the pixel, knowing the electronic background and the NSB. The MSSG is defined as the difference between $\ln \mathcal{L}(x_{\rm i}|\mu_{\rm i})$ in the pixel i and the likelihood $\langle \ln \mathcal{L} \rangle|_{\mu_{\rm i}}$ predicted by the Monte Carlo simulations. It writes as:

$$\mathrm{MSSG} = -2 \frac{\sum_{\rm i} [\ln \mathcal{L}(x_{\rm i}|\mu_{\rm i}) - \langle \ln \mathcal{L} \rangle|_{\mu_{\rm i}}]}{\sqrt{2\mathrm{d.o.f}}}, \tag{2.3}$$

where the number of degrees of freedom d.o.f. is $N_{pixels} - 6$. Fig. 2.6 shows the reconstructed event distribution as function of the shower goodness parameter for excess of photons measured towards blazar PKS 2155-304 (blue)[5], compared to the simulated signal (red) and the background distribution around the source (gray). A standard cut at MSSG< 0.6 would retain 70% of photons and reject more than 95% of the background events. The background events that are misidentified as gamma-like events are called the residual background,

[4] More details on the method of the likelihood test are given in Chap. 7.

[5] The flare of PKS 2155-304 recorded in 2007 is an almost pure gamma-ray beam, *i.e.* the hadron contamination is negligible.

that can be measured with different techniques described in the following section. The energy, impact parameter and direction of the shower can be then reconstructed through the comparison with the simulated showers.

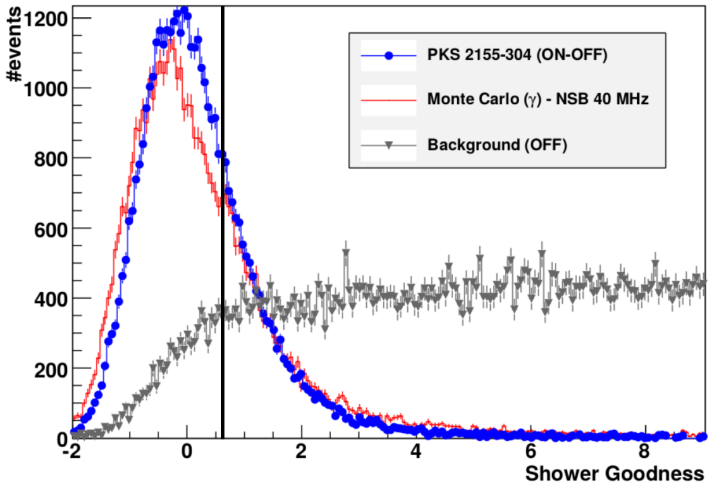

Figure 2.6: Events distribution as function of the shower goodness for a signal towards PKS 2155-304 (blue), background (gray) and signal simulation (red). A cut is set at MSSG<0.6 (black line). Figure extracted from Ref. [53].

2.4 Observation techniques and background measurements

2.4.1 Observation modes

The overall number of observation hours in one year is about 1000 hours ($\sim$ 12% duty cycle) since observations do not take place in presence of the Moon or Sun, that must be at least 18° below the horizon. The available dark time is distributed among all the targets of interest based on a yearly selection of targets after evaluation of observation proposals. Observations are performed preferentially at low zenith angle, only in few cases above 60°. A single observation is called *run* and has a length of 28 minutes.
Different observation strategies are possible. The first distinction is between:

- pointed observations: when a specific object is targeted and the observations are scheduled in advance based on the visibility above the horizon, better if close to zenith.

- survey: when a large region is targeted and scanned during several observations. Also these observations are scheduled in advance.

- transient observations: transient objects like GRBs, gravitational waves (GW) or blazar flares are targeted if an alert is received by another experiment. The observations are

not pre-scheduled. The observations are then mainly pointed, except for the case of GW for which a specific technique is adopted [58].

Then, for the pointed observations once the target has been chosen the position towards which the telescopes are pointed, referred to as pointing position, can be defined in different ways. The available background measurement techniques depend on the pointing mode (see Sec. 2.4.2). The old standard observation mode consists in defining the pointing position at the barycenter of the targeted object. The new standard observation mode is the *wobble* mode. In this case more than one pointing position is defined around the target position at a certain distance called observational *offset*. A usual choice is four perpendicular pointing positions at an *offset* 0.7° around the target for point-like sources.

2.4.2 Background measurement techniques

Depending also on the observation mode the residual background can be measured with different techniques.
The simplest technique is the *ON-OFF* mode and it is used for standard pointed observations. It consist in measuring the signal and the residual background in the same circular region centered at the target position, but during two different observations, close in time. Two contra of this technique are that the observation time is doubled with respect to using the same observation both for measuring signal and background, and the observation conditions cannot be exactly the same in the two subsequent observations.

For observations with pointing position at the position of the target the *Standard Ring Background* and *Standard Multiple OFF* techniques can be used. The first technique consists in measuring the residual background in an annular region around the signal region, such that the distance from the target is large enough to have null or almost null expected signal. If another object is present in the field of view it is excluded from the ring. The second technique is a variation and consists in measuring the background in disks of the same dimension of the signal region, such that they lie around the target all at the same distance from it, *i.e.* they lie on the ring of the *Standard Ring Background*. With these techniques the signal and background are measured during the same observation, in the same field of view, *i.e.* under the same observational conditions. A schematic is given in Fig. 2.7, where the signal region, *ON*, is represented in red and the background region, *OFF*, is in blue. In addition the exclusion regions are marked in orange.

For *wobble* observations the *Wobble Ring Background* and *Wobble Multiple OFF* modes are used. From now on they are referred to just as *Ring Background* and *Multiple OFF*. The background regions are build exactly in the same way as the previous techniques around the pointing position, but the signal region is not anymore coincident with the pointing position. The signal region is now at the same distance from the pointing position as the background region(s). In additional to the benefits of the *Standard* version of this mode, the acceptance of the camera, that degrades radially from the center of the camera (pointing

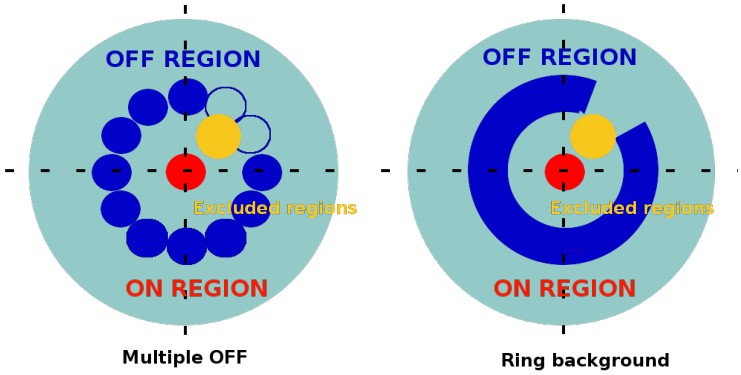

Figure 2.7: *Standard Multiple OFF* (left) and *Standard Ring Background* (right) techniques. The signal region (red) coincide with the target position and the pointing position. The background regions are shown (blue) and the excluded regions as well (orange).

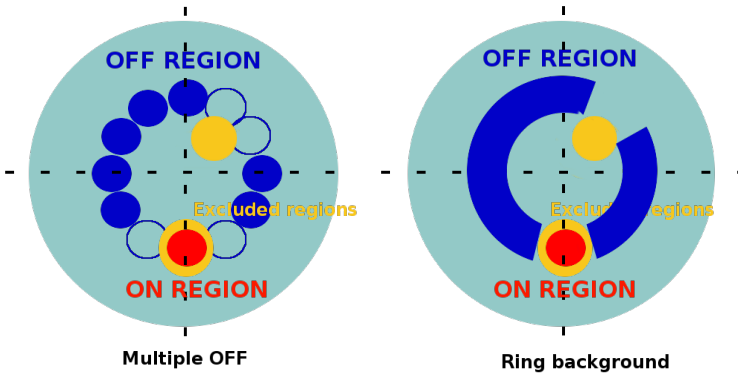

Figure 2.8: *(Wobble) Multiple OFF* (left) and *(Wobble) Ring Background* (right) techniques. The signal region (red) coincide with the target position but not with the pointing position that lay at the center of the axes. The background regions are shown (blue) and the excluded regions as well (orange). These are currently the standard methods to measure the residual background.

position) is now the same for the signal and the background regions, under assumption of azimuthal symmetry. An additional region is excluded around the target position to avoid signal contamination in the region where the residual background is measured. A schematic of these techniques is given in Fig. 2.8, with the same color legend as in the previous paragraph.

2.5 Instrument response functions (IRFs) and sensitivity

2.5.1 Effective area

The effective area[6] behavior as function of the gamma-ray energy depends strongly on the observational *offset* and zenith angle [53]. It also depends on the muon efficiency that quantifies the optical efficiency [59]. The degradation with the zenith angle is given in Ref. [60].

Fig. 2.9 compares the effective area of *Model++* (red) with standard (circles), faint (triangles) and loose (bottom-up triangles) analysis cuts to the *Hillas* (blue) analysis for a threshold of 60 photoelectrons (p.e.) (circles) or 200 p.e. (triangles, the most used in papers). *Model++* has a smaller effective area at high energy (>10 TeV), but it is comparable to *Hillas* 60 p.e. at lower energy and better than *Hillas* 60 p.e. in the hundreds-TeV energy range.

The effective area also degrades as function of the radial distance from the center of the camera [61]. The relative rate is still 70% at 1.5° and in the inner 1° the degradation is negligible.

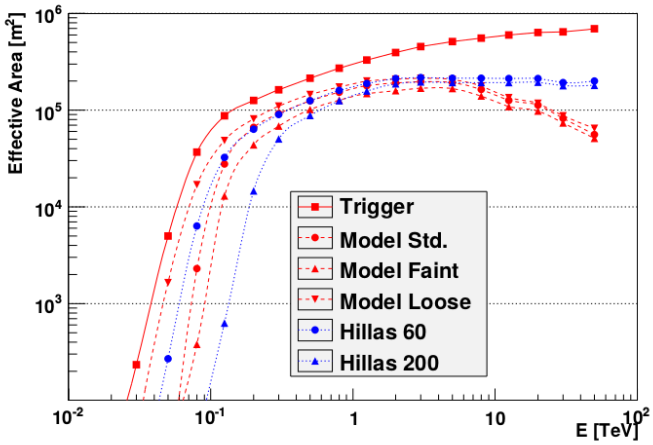

Figure 2.9: H.E.S.S. effective areas as function of the energy, compared for *Model++* (red dots) and *Hillas* (blue dots) event reconstruction algorithms. Figure extracted from Ref. [53].

[6]The effective area is often referred to as acceptance.

2.5.2 Energy threshold

The range of energy covered by the experiment depends on the fact that

- the initial gamma ray is energetic enough to initiate a shower that can produce Cherenkov light,
- the shower is energetic enough to produce enough Cherenkov light to be detected by the cameras,
- the shower is small enough (not too energetic) to be almost fully contained in the field of view of the telescope(s),
- the observation conditions may alter the development of the shower, *e.g.* the zenith angle affects the energy threshold. Indeed, for observations at large zenith angle (low altitude) the showers must cross a thicker layer of atmosphere and only the more energetic ones reach the telescopes.

The effective energy threshold is usually set as the value corresponding to 10% of the maximum effective area. The energy threshold after application of cuts on the parameters of the reconstructed showers with CT1-4 is 160 GeV for observations at zenith, 220 GeV at zenith 30°, 400 TeV at zenith 45° and 1.2 TeV at zenith 60°. For this reason small zenith observations are preferred, unless necessary.

2.5.3 Energy resolution

The energy resolution is defined as the rms of the $\Delta E/E = |E_{\rm reco} - E_{\rm true}|/E_{\rm true}$ distribution [53]. It is the probability to reconstruct mean energy E for an event with true energy $E_{\rm true}$. In most of the H.E.S.S. sensitivity range the energy resolution is about $10\%E$ and it always stays below $15\%E$ and above 5%, as shown in Fig. 2.10. It improves with the telescope multiplicity and it is pretty stable with the *offset* and the zenith angle. The bias on the reconstructed energy is about $5\%E$ in the whole sensitivity range and grows up to 20% only near the energy threshold due to trigger effects. A good energy resolution is crucial for good estimate of spectra and to distinguish peculiar narrow features in spectra. For CT5-only observations the energy resolution degrades up to about 30% in the hundred GeV energy range.

2.5.4 Angular resolution

The angular resolution is the 68% containment radius of the point spread function (PSF) [53] and for events reconstructed with *Model++* it is below 0.1° in the full energy range, with small dependency on the zenith angle. In the TeV energy range it is stable at 0.06° per gamma ray.
The angular resolution improves with the telescopes multiplicity. A good angular resolution

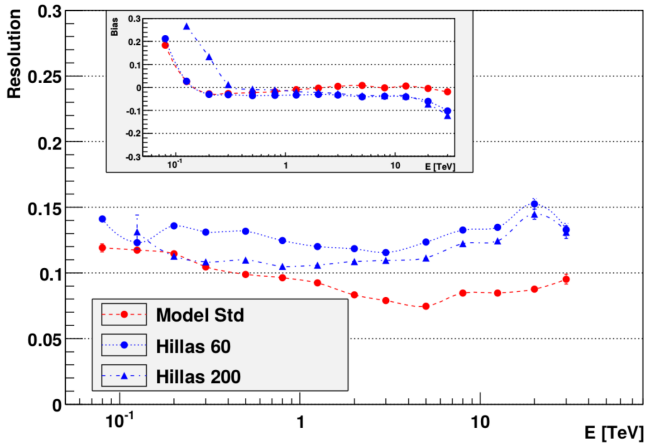

Figure 2.10: H.E.S.S. energy resolution and energy bias versus the energy, compared for *Model++* (red dots) and *Hillas* (blue dots) event reconstruction algorithms. The energy bias is at a few percents level and *Model++* energy resolution is pretty stable at about 10%E in the whole energy. Figure extracted from Ref. [53].

is crucial to distinguish nearby sources and to perform morphological studies of extended sources and diffuse emission.

As shown in Fig. 2.11 *Model++* (red dots) has a better angular resolution than *Hillas* (blue dots). The *Hillas* angular resolution degrades significantly at large zenith angles due to the reconstruction technique.

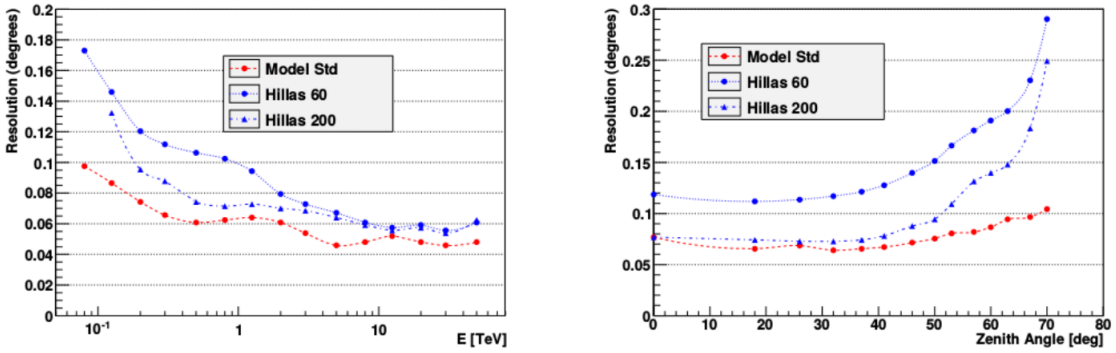

Figure 2.11: H.E.S.S. average angular resolution for the *Model++* (red dots) and *Hillas* (blue dots) reconstruction chains. *Left panel:* angular resolution as function of the energy. *Right panel:* angular resolution as function of the zenith angle. Figure extracted from Ref. [53].

2.6 H.E.S.S. I versus H.E.S.S. II event reconstruction

2.6.1 Reconstruction modes

With the hybrid H.E.S.S.-II array the data can be reconstructed in three main configurations [62]:

- *CT5-Mono*, also referred to simply as *Mono* since CT5 is the only telescope allowed to reconstruct in single-telescope mode a gamma-like event.
- *Stereo - CT1-5*, also referred to as *Stereo*, when CT5 is involved in the reconstruction together with at least one among the small telescopes.
- *Stereo CT1-4*, usually called *CT1-4* or *H.E.S.S.-I-like*, that take place when CT5 is not involved in the reconstruction or the data taking.

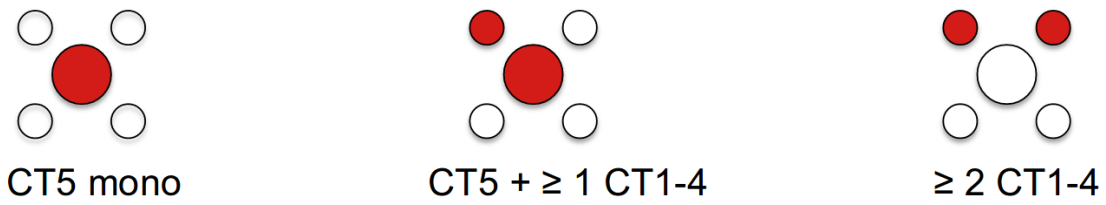

Figure 2.12: H.E.S.S.-II reconstruction configurations. *Left panel: CT5-Mono*, CT5 single-telescope reconstruction. *Central panel: Stereo* reconstruction that involves CT5 and at least one of the other telescopes. *Right panel: CT1-4* reconstruction in absence of CT5. Figure extracted from Ref. [62].

These configurations are summarized in Fig. 2.12.
An additional reconstruction class is the *Combined* configuration which is described in Sec. 9.3 and selects on an event-by-event basis the best among the three previously mentioned reconstruction methods.

2.6.2 Acceptance and sensitivity

With the full H.E.S.S.-II array the performances vary with the chosen reconstruction configuration [63]. The effective areas as function of the energy are compared for *CT1-4* (black dashed line), *Stereo - CT1-5* (green solid line), *Combined* (blue solid line) and *CT5 - Mono* (red solid line) analysis in the left panel of Fig. 2.13. The analyses that include CT5 have larger acceptance below few hundred GeV, *i.e.* lower energy threshold, thanks to the large size of the big telescope that makes it more sensible to the low energies. Events below 100 GeV can be detected in *CT5 - Mono* and *Combined* configurations. The *H.E.S.S.-I-like* reconstruction has the largest energy threshold. The *Combined* configuration has the overall best acceptance.

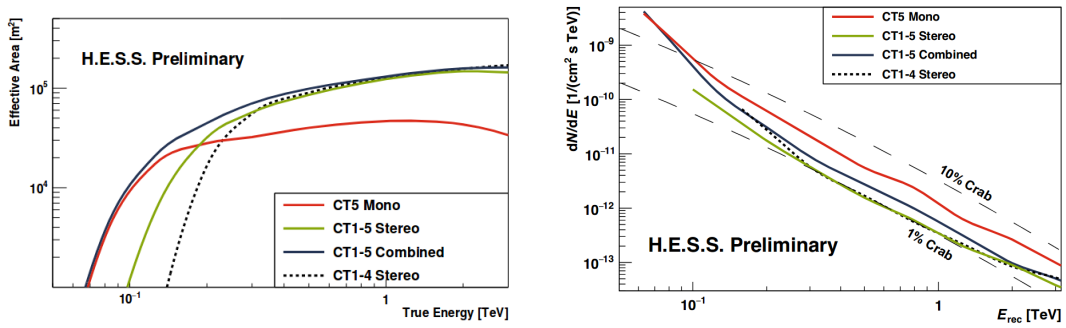

Figure 2.13: H.E.S.S.-II acceptance and sensitivity per reconstruction type. The *CT1-4* (black dashed line), *Stereo - CT1-5* (green solid line), *CT5 - Mono* (red solid line) and *Combined* (blue solid line) configurations are compared. *Left panel:* effective area as function of the energy after selection cuts. *Right panel:* differential flux as function of the energy. The curves (black long-dashed lines) corresponding to 1% and 10% of the Crab Nebula flux are shown. Figure extracted from Ref. [63].

A clear estimate of the performance of a IACT is given by its flux sensitivity. H.E.S.S. has a sensitivity of about 1% of the Crab nebula flux in 25 hours for zenith angle observations of a point-like source. A slightly larger or smaller sensitivity is obtained depending on the reconstruction configuration. The energy differential flux sensitivity of the H.E.S.S. array in *CT1-4* (black dashed line), *Stereo - CT1-5* (green solid line), *CT5 - Mono* (red solid line) and *Combined* (blue solid line) modes is shown in the right panel of Fig. 2.12. Accordingly to what observed on the effective areas, the reconstructions that include CT5 provide the best sensitivity below about 300 GeV, and the *CT5 - Mono* and *Combined* analysis are sensitive even below 100 GeV. The overall best sensitivity is obtained in the *Stereo - CT1-5* configuration, while the *Combined* one is the best compromise to have a good sensitivity that covers the largest energy range possible. The sensitivity above 3 TeV is not shown in the plot, but it is expected to degrade more quickly for the *CT5 - Mono* reconstruction.

Part II

The Galactic Center region

Chapter 3

The inner region of the Milky Way

Contents

3.1 Multi-wavelenght observations of the Galactic Centre region 38
3.2 TeV emitters in the Galactic Center region 41
3.2.1 The inner 50 parsecs 41
3.2.2 G09+01 and HESS J1745-303 43
3.2.3 H.E.S.S. Galactic plane survey 44
3.3 Diffuse emissions in the GeV-TeV energy ranges 45
3.3.1 The Central Molecular Zone 45
3.3.2 The 'Galactic Center ridge' emission 45
3.3.3 Fermi Galactic Diffuse Emission 47
3.3.4 The Galactic Center excess detected by Fermi-LAT 48
3.4 Galactic Center outflows 49
3.4.1 The *Pevatron* 49
3.4.2 Fermi bubbles 51
3.4.3 Radio and X-ray outflows 52

The Galactic Center region, situated at about 8.5 kpc from the Sun is a very crowded and active region that has been largely observed at different wavelengths. Each observation provided information on different objects and processes and it is crucial for having a complete overview of the Galactic Center physics. At the highest energies, in very-high-energy gamma rays, several point-like and extended sources have been observed in the Galactic Center region, as well as diffuse emissions.
In Sec. 3.1 we introduce the idea of wultiwavelength observations and give an overview of the outcome of Galactic Center region observations with different telescopes. In Sec. 3.2 and Sec. 3.3 we present the emissions from SNR, PWN and the central supermassive black hole in the vicinity of the Galactic Center, as well as the diffuse emissions detected by H.E.S.S. and Fermi-LAT in the inner few degrees of the Galaxy. The presence of Galactic outflows that could be hints of activity of the central black hole is discussed in Sec. 3.4.

3.1 Multi-wavelenght observations of the Galactic Centre region

Observing an astrophysical object at different wavelengths gives a comprehensive knowledge about it. Indeed, emissions at different frequencies give information on the underlying emission processes that take place at the source and the nearby radiation field and target material. When the same astrophysical object is detected at different frequencies the deduced spectral, spatial and chemical properties are confronted in order to determine if the emissions are counterparts from the same object. The angular resolution is crucial in order to match the emissions with the objects and to disentangle two separate nearby sources. This is particularly true in crowded environments like the Galactic Center (GC) region or to resolve the spatial morphology of the emission.

Radio waves

Radio waves have a frequency between 250 MHz and 300 GHz and wavelength 10 km to 10 cm and penetrate the Earth atmosphere. Observations in radio trace hot gas and atomic hydrogen. They allow us to probe the magnetic field distribution and intensity because the synchrotron emission is emitted also in radio, *i.e.* they are useful probes for discovery of SNRs and study of their structure. The first detection of an emission from the GC was in 1932 in radio. The top panel of Fig. 3.1 shows the 90 cm sky image of the GC region observed by MeerKAT in the frequency range $900 - 1670$ MHz [64]. SNRs (*e.g.* Sgr A East) and nebulae (*e.g.* Sgr A West) are visible, as well as molecular clouds (*e.g.* Sgr B, Sgr C and Sgr D). Non-thermal synchrotron radiation emitted from SNRs (*e.g.* G0.9+0.1 et G359.1-0.5) and as form of filaments ($B \sim \mu$G) along the Galactic magnetic field is visible.

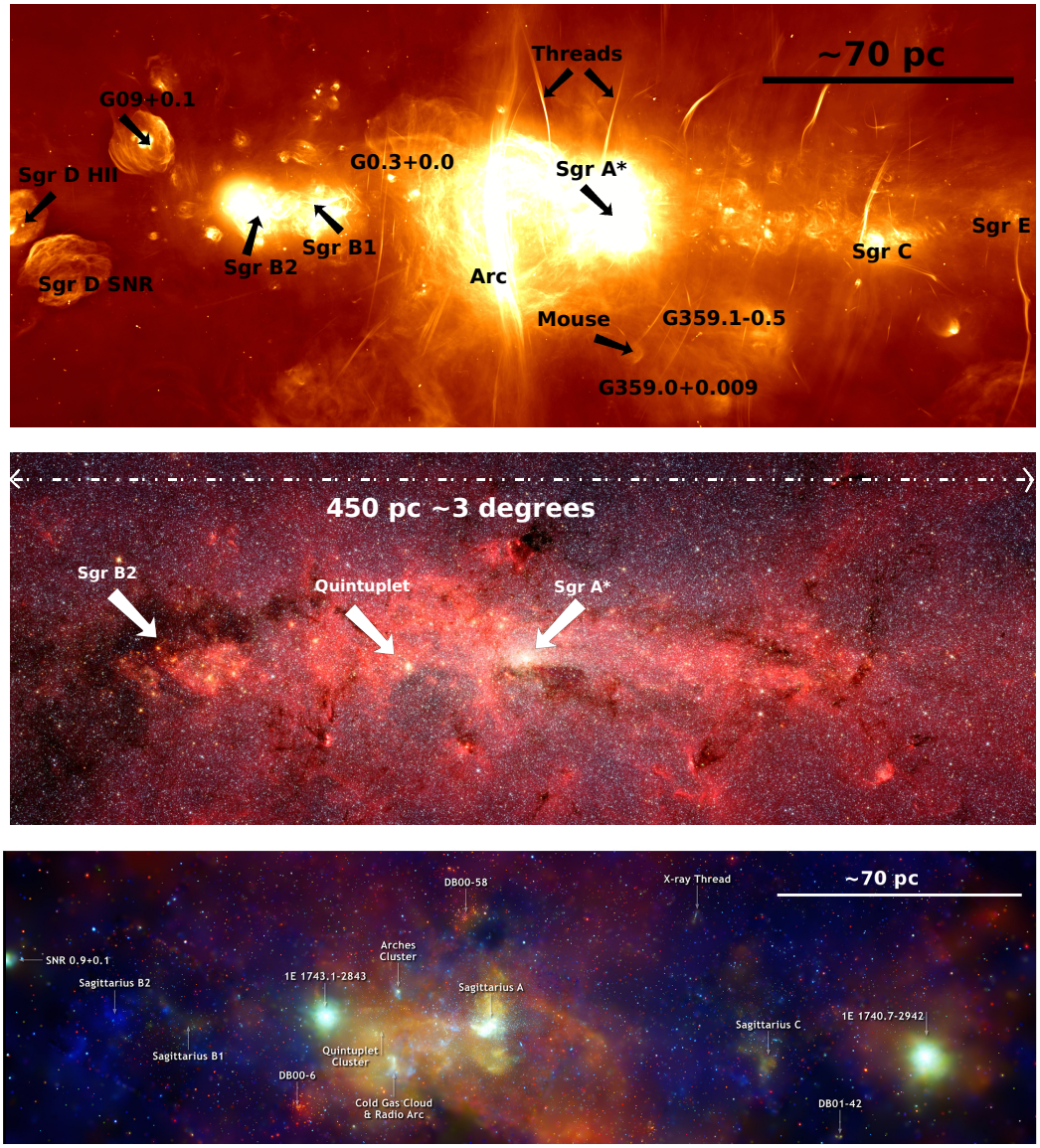

Figure 3.1: Sky images of the GC region at different wavelenghts. *Top panel:* MeerKAT $900 - 1670$ MHz radio observations [64]. *Central panel:* Spitzer [65] 3.6, 4.5, 5.8 and 8 μm IR observations. *Bottom panel:* composite Chandra [66] X-ray observations at $2 - 4$ keV (red), $4 - 6$ keV (green) and $6 - 9$ keV (blue).

Microwaves

Microwaves are at the highest radio frequencies between 250 MHz and 300 GHz corresponding to wavelength of 10 cm to 1 mm. They can partially enter the atmosphere. Microwave observations show the distribution of cold gas and dust. They are used to measure the distribution of carbon monoxide (CO) and carbon monosulfide (CS) that are tracers of the molecular hydrogen, hint of presence of a star forming region. In the GC region microwaves trace the Central Molecular Zone.

Infrared radiation

Infrared (IR) radiation covers frequencies between 300 GHz and 428 THz, *i.e* frequency from 1 mm to 700 nm. The near IR radiation (below 3 μm) penetrates the atmosphere. Mid and far IR (above 50 μm) see cold dust like dust-covered stars, faint stars and dense arcs of dust. Near IR radiation cuts through the dust showing cold objects and IR telescopes have angular resolution good[1] enough (*e.g.* ~ 2" for Spitzer) to resolve tiny clusters of stars around the Milky Way central black hole. The central panel of Fig. 3.1 shows a map of the GC Spitzer [65] IR ($2 - 9$ keV) observations that trace the intense activity of the region. The central star forming region is visible, as well as massive star clusters, like the Quintuplet.

Optical light and ultraviolet radiation

Optical light is at wavelength 700 to 400 nm and penetrates the atmosphere. It is used to observe stars, but it cannot cut through dust so dust-rich regions like the GC and the Galactic plane are obscured.
Ultraviolet (UV) light is emitted in the range of wavelengths between 400 and 10 nm and the low-frequency UV light penetrates the atmosphere. UV radiation is mainly produced by young, massive, early-type (O, A, and B spectral class) stars. They are the brightest stars in the GC region and the UV radiation is produced by ionization of the surrounding gas.

X rays

X rays have wavelength from 10 nm to 1 pm corresponding to $10^2 - 10^5$ eV energies. X rays cannot enter the atmosphere so they must be detected by instruments on satellites. They reveal hot gas and non-thermal processes (above about 10 keV) and are used to observe a wide variety of astrophysical objects. The bottom panel of Fig. 3.1 shows Chandra observations in X rays [66]. The background of the image is permeated by diffuse haze of X rays. This radiation is produced by the gas heated to millions of degrees by winds from massive young stars. X rays trace explosions of dying stars and outflows powered by Sgr A*. The filaments seen around Sgr A* could be flares due to accretion onto the black hole, but

[1]The angular resolution scales as the ratio between the wavelength and the lense radius.

also large scale magnetic structures that interact with streams of very energetic electrons produced by fast spinning neutron stars.

Gamma rays

Gamma rays cover the shortest wavelengths, below 1 pm and the highest energies, above the hundreds MeV. They interact with the atmosphere at about 10 km altitude so they are detected directly with satellite detectors and indirectly with ground-based Cherenkov telescopes. Gamma rays reveal non-thermal processes and are used to observe the objects that in Sec. 1.4 are listed as cosmic accelerators. In addition gamma rays can be produced in exotic processes like dark matter annihilation. A map of the GC region seen by H.E.S.S. in VHE gamma rays is shown in Fig. 3.2 and more information about the TeV emitters observed in this region is given in Sec. 3.2.

3.2 TeV emitters in the Galactic Center region

3.2.1 The inner 50 parsecs

Sagittarius A*

A strong TeV emission has been observed by H.E.S.S. at the position $(359.94°, -0.04°)$: HESS J1745-290. It is coincident with the supermassive black hole Sagittarius A* (Sgr A*) [67] at the center of the Milky Way. The emission detected by H.E.S.S. is visible in Fig.3.2 at the position marked with a black star in the top plot. Sgr A* has a mass 4.31×10^6 times larger than the mass of the Sun and it is located at the gravitational center of our galaxy. Variability of the emission from Sgr A* has been observed in X rays and IR [69], but not in gamma rays yet. In the composite multi-wavelength spectrum in Fig. 3.3 the difference of intensity between the quiescent and flaring state is striking, especially in X rays. The VHE gamma ray emission measured by H.E.S.S. is on the far right of the spectrum. H.E.S.S. spectrum [70] is well reproduced by a power-law function with exponential cutoff at 1.7 TeV with spectral index 2.10 and normalization 2.55×10^{-12} TeV^{-1} cm^{-2} s^{-1}. A good fit is obtained also for a smoothed broken power with photon indexes 2.02 and 2.63, break energy 2.57 TeV and normalization 2.57×10^{-12} TeV^{-1} cm^{-2} s^{-1}. The stochastic acceleration of electrons in the turbulent magnetic field in proximity of Sgr A* that was suggested as an explanation of the submillimiter emission would also describe the IR and X-ray flaring states. In addition charged particles are accreted onto the black hole. So protons could escape, accelerate, interact with the interstellar medium in the central star cluster and produce gamma rays [71]. A cutoff energy at $E_{\rm cut}$ would imply a cutoff on the initial proton spectrum at $E_{\rm p,\,cut} \approx E_{\rm cut}/30$, which would correspond to protons accelerated up to a few hundreds TeV. Energy-dependent diffusion models that predict competition between injection and escape of protons would explain a broken power-law spectrum. Part

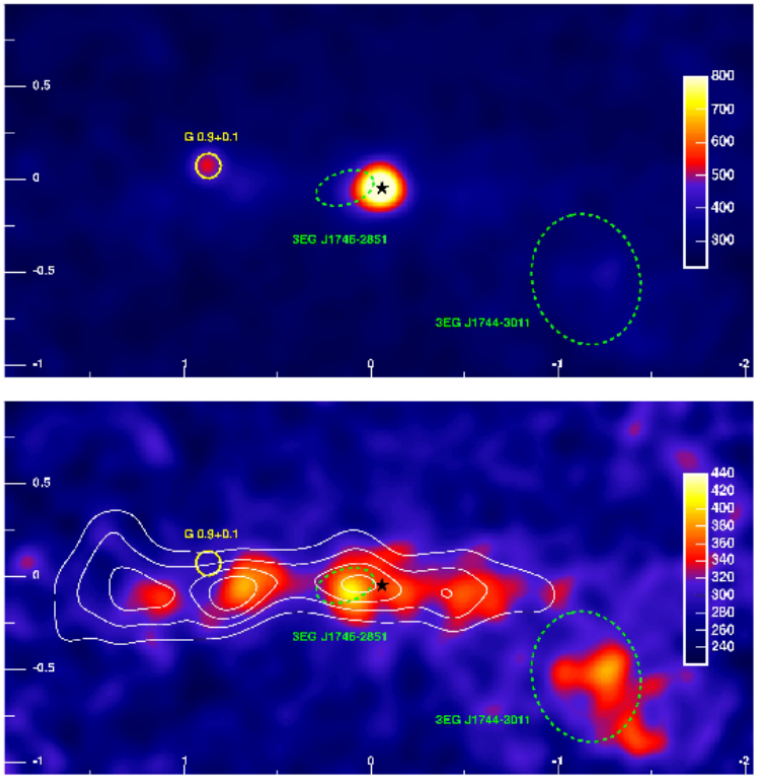

Figure 3.2: H.E.S.S. excess map [68] of the inner 200 pc of the GC region. *Top panel:* the brightest sources are visible: the central emitter HESS J1745-303 and the PWN/SNR HESS J1747-281. *Bottom panel:* map of the Galactic ridge emission after subtraction of the bright sources. The white contours from measurement of CS emission lines show the position of the gas dense central molecular clouds. The sources observed in the top panel are subtracted here.

of the TeV emission could also be attributed to Inverse Compton of electrons accelerated up to about 100 TeV in the nearby PWN G359.95-0.04.

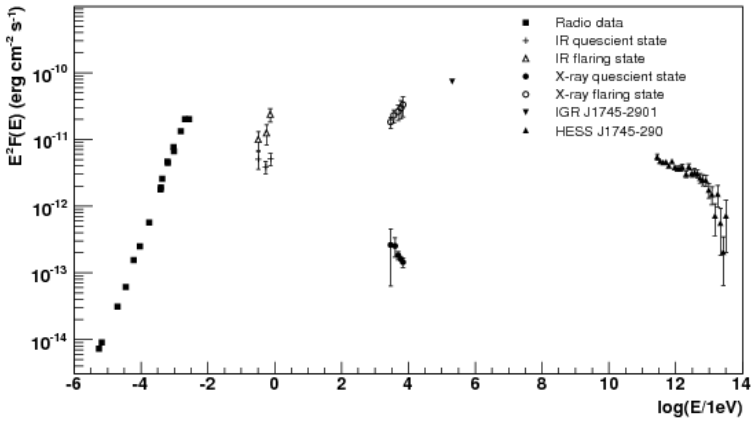

Figure 3.3: Sgr A* composite spectrum [70]. Spectra reconstructed in radio, IR, X rays and gamma rays are stacked. In IR and X rays variable flaring states have been observed.

HESS J1746-285

The point-like source that is the spatially closest to the GC is the TeV source HESS J1746-285 [72]. It has been detected above the GC ridge (see next section) at a location $(0.14°, -0.11°)$. It lies on the edge of a radio arc bubble observed in IR, connected to the young massive Quintuplet cluster. HESS J1746-285 position is coincident with G0.13-0.11 [73]. This object is a non-thermal filamentary structure. Its morphological, spectral, and luminosity properties strongly point towards a PWN hypothesis. Other possible counterparts of HESS J1746-285 exist, but the PWN is the most likely.

3.2.2 G09+01 and HESS J1745-303

HESS J1747-281

In the few-degrees region around the GC other bright sources are observed in TeV gamma rays. Among them, the TeV source HESS J1747-281 [74] has been detected at the position of the composite SNR/PWN G09+01. It is a point-like source located at $(0.87°, 0.08°)$ in Galactic longitude and latitude. In radio [75] it exhibits the typical SNR features of a bright compact core surrounded by a shell. The center was identified as a PWN thanks to observations in X rays [76]. It could host the young radio pulsar CXOU J174722.8-280915, but no pulsed emission has been detected in gamma rays. The position of G09+01 is shown as a yellow circle in Fig. 3.2, where H.E.S.S. emission from HESS J1747-281 is visible.

HESS J1745-303

The extended source HESS J1745-303 [77] has been first detected in TeV at a position $(358.71°, -0.64°)$ in Galactic coordinates and it is associated to the composite SNR G359.1-0.5. Its morphology is complex and in X rays the SNR shows substructures that cannot be explained by any canonical SNR plasma model [78]. They may be due to radiative transitions

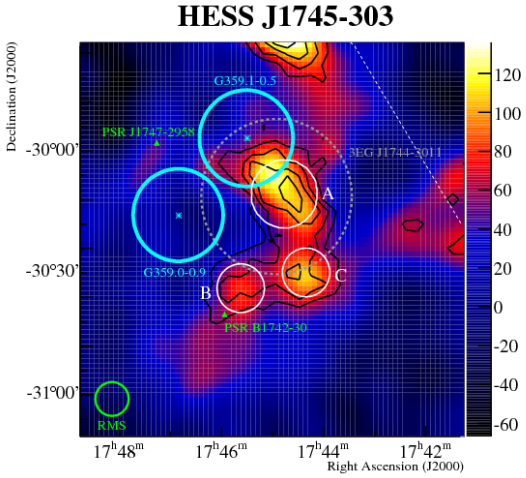

Figure 3.4: TeV emission HESS J1745-303 observed by H.E.S.S. [77] in the vicinity of the GC. The transition between the blue and the red happens at 3σ excess significance. The 4σ to 7σ statistical significance contours are shownin black. The position of the possible counterparts G359.1-0.5 and G359.0-0.9 are marked as cyan circles.

of free electrons in He-like, Si and S ions, suggesting an over-ionization of the plasma. The density of the SNR is not enough to explain emission through hadronic models, but the signal could be enhanced by the SNR shock when it interacts with a molecular cloud present in the same region detected in other wavelengths [79]. The emission detected by H.E.S.S. is shown in Fig. 3.4, together with the position of the associated SNR G359.1-0.5. Other possible counterpart candidates are overlaid for reference. The black contours represent the 4σ and 7σ H.E.S.S. excess significance levels. HESS J1745-303 may also be associated to the source 3EG J1744-3011 [80], but the error on its location shown as a gray dashed line is larger than the significant source observed by H.E.S.S.. The position of 3EG J1744-3011 is shown in Fig. 3.2 as green dashed circle. The gamma-ray emission from HESS J1745-303 is visible in the bottom panel.

3.2.3 H.E.S.S. Galactic plane survey

The Galactic Plane Survey (GPS) [81] is a reanalysis of the observations performed by H.E.S.S. I during 10 years. It is a comprehensive survey of the Galactic plane region. A total of about 2700 h were collected in a region from 250° to 65° in longitude and ±3°

in latitude. It confirmed 48 detected VHE gamma-ray sources and revealed 16 new ones. Thanks to the very good instrument angular resolution, sources close to another can be resolved. Among the detected sources 31 are identified as PWNs, SNRs and binary systems, while the remaining are still unidentified, even if most of them are likely associated to objects observed at other wavelengths like PWNs. Note that complex regions as shell-like sources and the GC region have not been reanalyzed. Sky maps of the inner part of the survey between 342° and 26° in Galactic latitude are shown in Fig. 3.5. The name of the sources and their counterparts from other catalogs are given. The maps show the significance of the detection. The full source catalog can be found in Ref. [81] together with the position, the size, the detection significance and the integrated flux above 1 TeV for each detected source. The GPS is used in Sec. 9.1 to chose the exclusion regions for dark matter search at the GC.

3.3 Diffuse emissions in the GeV-TeV energy ranges

3.3.1 The Central Molecular Zone

The Central Molecular Zone (CMZ) is a very dense star formation region at the center of our galaxy made of hot gas [82]. The clouds, that extend for about 300 pc along the Galactic plane, are revealed by the CS[2] line emissions in radio. The region includes several structures: Sgr A radio arc complex, Sgr B, Sgr C, and Sgr D. The mass of this regions is 3 to 8 times the solar mass and its average density is 100 times larger than outside the CMZ. The observations of the inner degrees of the GC region at different wavelengths that revealed expanding molecular rings, arc structures and the GC lobe are crucial to understand the processes that take plate at the GC. Indeed, all these structures could be due to explosive events in the GC region, but the mechanism of production is still unknown. Improved knowledge about the morphology, density and velocity of the underlying gas distribution could give information useful to find an answer.

3.3.2 The 'Galactic Center ridge' emission

The Galactic Center ridge emission is a large VHE gamma-ray emission that extends in the central 200 pc of the Milky Way. It has been detected by H.E.S.S. [68] that thanks to its very good angular resolution was able to reveal the morphology of the emission. The observations showed that the GC ridge emission is spatially-correlated with a complex of giant molecular clouds. The CS contours of the gas clouds is overlaid to H.E.S.S. map of the GC region in the bottom panel of Fig. 3.2. This map is obtained after subtraction of the bright point-like sources HESS J1745-290 and G0.9+0.1 in the top panel. The emission visible in the bottom right of the figure is HESS J1745-303, while the one that extends

[2]Many observations of the CMZ have been performed by detecting CO lines, but they strongly suffer from contamination from the foreground and the background.

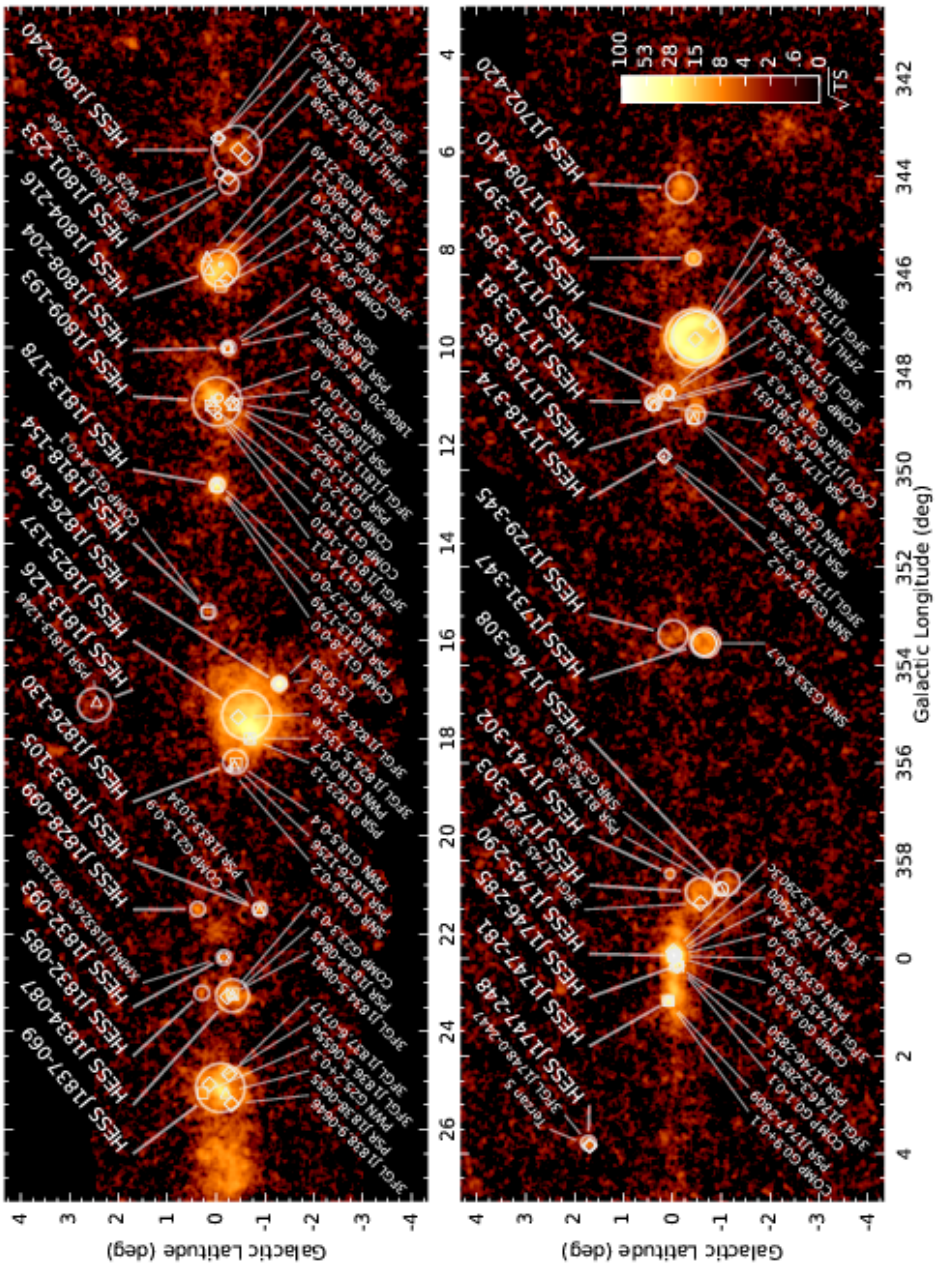

Figure 3.5: Significance excess map of the inner part of the H.E.S.S. Galactic Plane Survey [81]. The position and size of each detected source is marked with a white circle. The names of the H.E.S.S. detected objects and of their counterparts are given.

along the Galactic plane for about 200 pc in longitude and 30 pc in latitude is the ridge emission. Its spectrum has been extracted in the region $|\ell| < 0.8°$ in longitude and $|b| < 0.3°$ in latitude and it is well described by a power-law with spectral index 2.29. Due to the correlation with the CS map, the GC ridge emission is likely produced by CRs nuclei that interact with the CMZ. The spectrum of the initial CRs can be traced back and is expected to have an index of about 2.3. The hard spectrum, with respect to the neighborhood flux with spectral index 2.75, could be related to the short distance from the central accelerator, that does not allow strong energy losses. The number density of CRs with multi-TeV energies exceeds the local density by a factor from 3 to 9. This measurement points towards the presence of an additional injection of CRs above the CR local flux.

3.3.3 Fermi Galactic Diffuse Emission

The Galactic Diffuse Emission (GDE) is a diffuse background measured by Fermi-LAT in the MeV-GeV energy range and produced by standard astrophysical processes in the GC and Galactic plane region. It is due to electrons/positrons ICS, bremsstrahlung and pion decay. A diffuse emission in the GC region has been observed in the '70s and widely studied since then [83]. But the most accurate studies have been possible with Fermi-LAT [84], thanks to its large FoV, the unprecedented sensitivity and wider energy range (tens MeV to hundreds GeV) with respect to its predecessors. The GDE model depends strongly on the injected CRs spectrum and the modeling of the energy losses and gains (diffusion, re-acceleration, ...), *i.e.* it is strongly affected by assumptions on CR sources distribution and the gas distribution. It is also highly dependent on the interstellar radiation field (ISRF), the result of emission by stars, and subsequent scattering, absorption, and re-emission of the absorbed starlight by the dust in the interstellar medium (ISM) [85]. Models of the GDE can be computed feeding the ISM and ISRF parameters to the GALPROP code [86], which is constantly under update. The GDE is produced both by leptonic and hadronic processes, that are treatment following Refs. [87, 88]. The ICS takes place in the vicinity of CR accelerators and traces the distribution of VHE gamma-ray sources. Bremsstrahlung (that dominates the low energies) and pion decay (that dominates the high energies) take place in gas dense regions and molecular clouds, like the above mentioned CMZ. The gas-correlated emission does not trace the position of the sources that initially accelerate the CRs because they have the time to diffuse before interacting with ambient nuclei. However, they trace the distribution of gas. Most of the sources and gas clouds are in the few hundred kiloparsecs around the GC and along the Galactic plane. Since it is produced by CRs that interact with the ISM it can be used to study the propagation of CRs and the properties of the ISM. A recent Fermi-LAT spectral modeling of the GDE from Ref. [89] is shown in Fig. 3.6, obtained with GALPROP v54.1, and it is used in Sec. 12.5 to estimate the astrophysical

background in the GC region. The gas-correlated component (green squares) dominates the ICS (orange dots)[3].

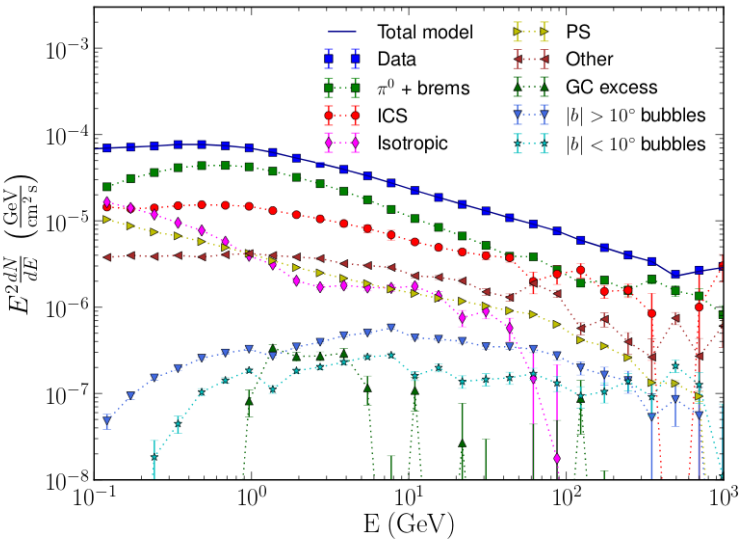

Figure 3.6: Fermi-LAT spectra measured in the GC region (blue squares) and its components [90]. The contributions to the GC region emission from gas-correlated GDE emission (green squares), ICS radiation (orange dots), isotropic background (magenta diamonds), point-like sources (yellow triangles), the GC GeV excess (green triangles) and high-latitude ($|b| > 10°$, indigo triangles) and low-latitude ($|b| < 10°$, teal stars) Fermi Bubbles are shown.

3.3.4 The Galactic Center excess detected by Fermi-LAT

A GeV GC gamma-ray excess (GCE) is detected by Fermi-LAT with respect to predictions based on a variety of interstellar emission model (IEM) in the inner 1° around the GC. The emission has first been interpreted as a possible signal of DM annihilation with mass $30 - 50$ GeV and relic cross section of the order of 10^{-26} cm^3 s^{-1} as predicted for thermal production, following an NFW [91] density profile (see for instance Refs. [92–94]). However, this hypothesis is not supported by the lack of DM signal detection in background-free targets like dwarf galaxies, where Fermi-LAT has set strong constraints below the relic cross section up to a few hundreds GeV [95]. The spectrum appears strongly dependent on the chosen IEM in the updated analyses [96, 90] with 6.5 years of Fermi-LAT observations including an additional population of electrons used in the modeling of the CMZ and three different point source catalogs. Spectra obtained in different analyses are compared in Fig. 3.7. Fits for power-law spectra and NFW profiles are shown with their uncertainty. In Ref. [89] the spectrum of the GC excess has been remodeled considering the interplay with

[3]The spectral parameters of the two components are given in Sec. 12.5.

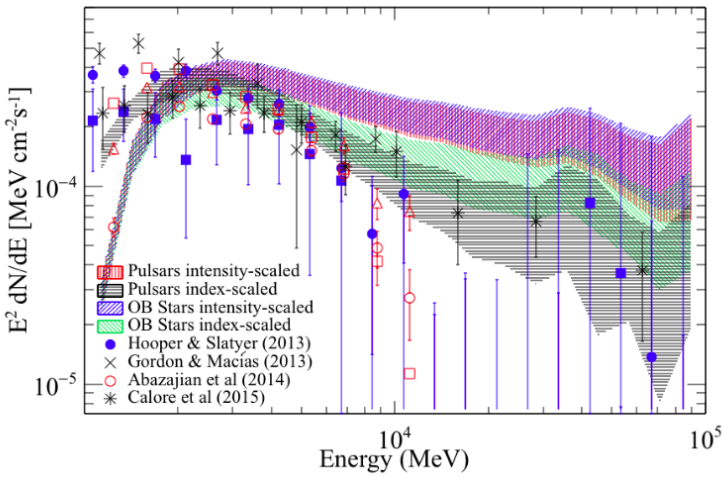

Figure 3.7: Differential fluxes for the GeV gamma-ray excess in the $15^\circ \times 15^\circ$ region around the GC [96]. The spectra obtained in different analyses of Fermi-LAT data are shown together with the power-law fits for NFW profiles.

the addition of low-latitude emission from the Fermi Bubbles (see Sec. 3.4). The spectrum is shown in Fig. 3.6 (green triangles). The nature of the GCE is still under study and one of the recently proposed promising hypothesis is that it could be produced by a population of millisecond pulsars in the Galactic bulge [97]. In addition, an excess of protons have been observed at higher energies by H.E.S.S. (see Sec. 3.4) and it could be due to the same underlying process.

3.4 Galactic Center outflows

3.4.1 The *Pevatron*

An excess of photons has been detected in the GC also by H.E.S.S. up to tens of TeV [39]. The measured spectrum and best fit of the TeV diffuse emission (scaled by a factor 10) and of HESS J1745-290 are shown in the left panel of Fig. 3.9. The characteristics of this emission have been derived in a open-ring-shaped region of interest. It is a ring of size 1.4×10^{-4} sr with inner radius 0.15° and outer radius 0.45°, cut at opening angles between -10° and 56°. The H.E.S.S. excess map in the inner 200 pc of the GC region is given in Fig. 3.8 and on the right it zooms on the GC TeV diffuse emission and shows the region of interest. The spectrum extracted in this region is well described by a power-law function without cutoff, with a photon index 2.32 and normalization 1.920×10^{-12} TeV^{-1} cm^{-2} s^{-1}. The normalization of the spectrum depends on the assumption of a standard diffusion coefficient $D = 6 \times 10^{29} (E/10\,\mathrm{TeV})^{1/3}$ cm^2 s^{-1} and constant injection rate $\dot{Q}_\mathrm{p}(\geq 10\,\mathrm{TeV}) \approx 4 \times 10^{37} (D/10^{30}\,\mathrm{cm}^2\,\mathrm{s}^{-1})$ erg s^{-1} above 10 TeV. Under the same assumptions also the radial

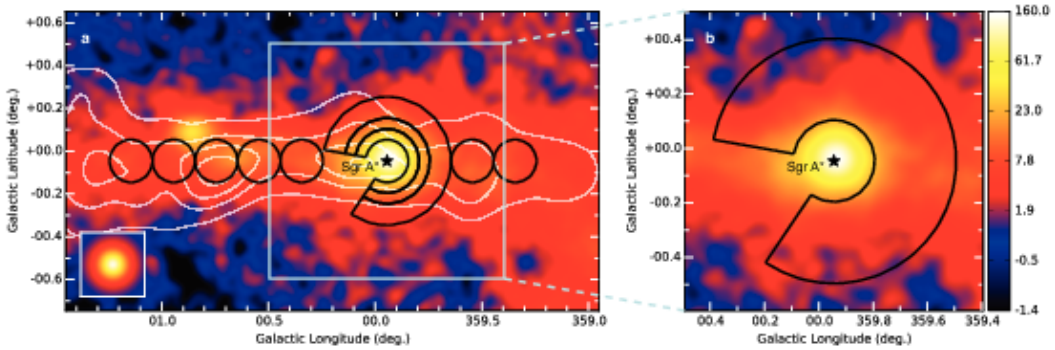

Figure 3.8: Gamma-ray excess map [39] of the inner 200 pc of the GC region. A zoom shows the *Pevatron* emission in the 70 pc around the GC. The open-annulus-shaped region of interest is drawn. The white contour lines indicate the density distribution of the CMS, as traced by its CS line emission.

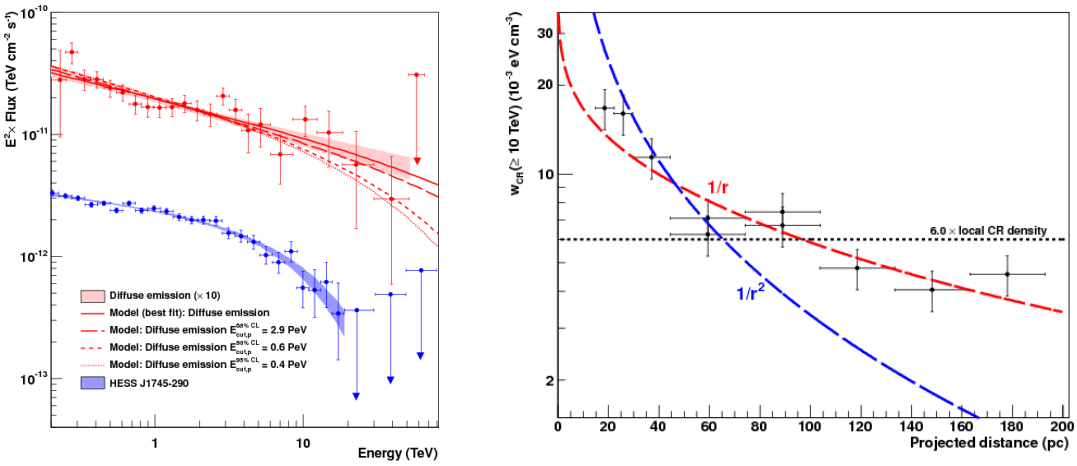

Figure 3.9: *Left panel:* VHE gamma-ray spectrum of the GC diffuse emission (red) and the central source HESS J1745-290 (blue). The power-law fit for the diffuse emission and power-law with exponential cutoff for central source are shown. *Right panel:* radial CRs distribution in the inner 50 pc of the GC region. A fit to the data of a $1/r$ (red dashed line),$1/r^2$ (blue dashed line) and an homogeneous (black dotted line) radial profiles integrated along the line of sight are shown. The $1/r$ profile is preferred.

distribution $w_{\rm CR}(E, r, t)$ of the CRs in the CMZ is measured. The dependences $w_{\rm CR} \propto 1/r$, $w_{\rm CR} \propto 1/r^2$ and $w \propto constant$ where tested, with the former better reproducing the data as shown in the right panel of Fig. 3.9. The disfavored scenarios would be expected if CRs are advected in a wind or for a single injection from a burst, respectively. The $1/r$ behavior indicates a quasi-continuum injection into the CMZ. The integrated luminosity above 1 TeV is 5.7×10^{34} erg s^{-1}. This emission has been interpreted in terms of gamma rays produced by extremely energetic protons, accelerated and ejected by the central emitter. Knowing that Sgr A* went through active phases the interpretation of the excess as a Galactic outflow is plausible. In order to obtain gamma rays at such high energies the protons must be accelerated up to PeV energies, and an object capable of producing them takes the name of *Pevatron*. Most standard accelerators have a cutoff at a few TeV instead. Alternative explanations for such an emission, besides the presence of a single *Pevatron* at the GC, have been suggested. A SNR scenario is plausible, but a single SNR would not produce such a large luminosity over a long timescale (> 100 yr) [98]. An interesting alternative is the presence of a population of unresolved millisecond PSRs in the vicinity of the GC. This scenario is studied in details in Chap. 4.

3.4.2 Fermi bubbles

Bubble-like structures have been observe in Fermi-LAT dataset [99]. They are two lobes that extend in the Northern and Southern hemispheres out of the GC, probably outflows linked to previous activity of the central emitter. They have been detected above the Galactic IEM computed with GALPROP and extend up to 55° in latitude and have a width of 40° in longitude. From the observations at latitudes $|b| > 10°$ a spectrum with slope 1.9 and energy cutoff 110 GeV was extracted [90]. More recent analyses [89] revealed the presence of a softer Fermi Bubble component at large latitude and a low-latitude ($|b| < 10°$) harder component. Templates of the regions of the high-latitude and low-latitude Fermi Bubbles are given in Fig. 3.10 and are used in Sec. 12.5 to model the astrophysical background in the GC region. The spectrum of the low-latitude Fermi Bubble emission has a photon index of 1.9 as well, which discriminates them from the GDE with a spectral index close to 2.4. While the high-latitude Fermi Bubbles spectrum softens significantly above 100 GeV, the spectrum of the low-latitude Fermi Bubbles does not show any significant hint for a cutoff. The low-latitude component could eventually be detected also in TeV gamma rays by H.E.S.S.. Fig. 3.6 shows the spectrum of the Fermi Bubbles in $|b| < 10°$ (teal stars) and $|b| > 10°$ (indigo triangles), together with the GeV excess (green triangles), the point-like sources (yellow triangles) and the GDE components (green squares and orange dots). The Fermi Bubbles have not been resolved yet at other wavelengths and the mechanism of production is not clear yet. However, synchrotron haze has been detected, that could be a radio counterpart in leptonic scenarios. Both leptonic and hadronic process of gamma-ray

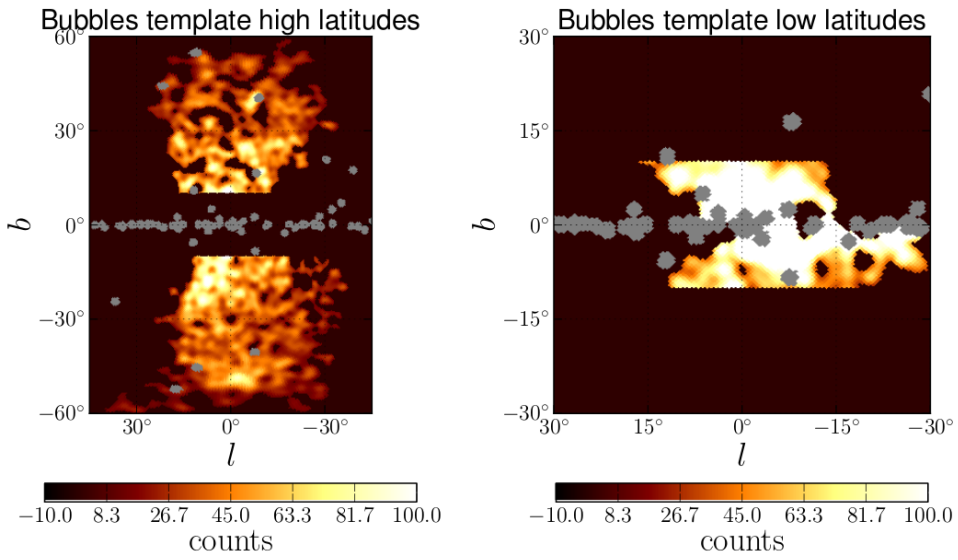

Figure 3.10: Templates of the high-latitude (left panel) and low-latitude (right panel) harder Fermi Bubble components [89]. The gray masks are excluded regions corresponding to other previously detected gamma-ray emissions.

production can reproduce the emission. Searches for faint Fermi Bubble emission at higher energies are ongoing in H.E.S.S. and may shed light on the underlying acceleration process.

3.4.3 Radio and X-ray outflows

Broadly collimated outflows ejected at the GC position directed perpendicular to the Galactic plane has been observed in radio and X rays.
An extended radio lobe jet-like emission [100] has been detected in the Nobeyama Radio Observatory dataset of a GC region radio survey at 10 GHz. Structures at scale of 1° have been detected above the Galactic plane near the GC. Observations at 5 GHz taken from the Bonn survey show the same features. Hints of presence of radio outflows in the GC region are obtained also by the Green Bank Telescope survey of the inner $4° \times 1°$ region of the Milky Way [101]. The observations have been taken at wavelengths 3.5, 6, 20 and 90 cm and show lobes of diffuse emission that extends above the Galactic plane, coming out of the vicinity of the GC.
Bursts and emission structures from the GC region have also been observed by the ROSAT all-sky survey and by Chandra in X rays [102]. Recently these structures have been resolved by XMM-Newton both in the Northern and Southern hemisphere. They share comparable X-ray brightness and color in the two hemispheres and are referred to as GC Chimneys [103].

Chapter 4

Millisecond pulsars and TeV Galactic Center diffuse emission

Contents

4.1 Millisecond pulsars population and the Galactic Center excess 54
4.1.1 Explaining the GeV Galactic Center excess seen by Fermi-LAT 54
4.1.2 Connecting the GeV Galactic Center excess and the TeV diffuse emission ? 56
4.2 Millisecond pulsars as PeV proton accelerators 57
4.3 Injection and propagation of accelerated protons 58
4.3.1 Proton injection spectrum of the source 58
4.3.2 Diffusive transport equation 59
4.4 H.E.S.S. diffuse emission and the Fermi-induced MSP population . . 60
4.4.1 Expected cosmic-ray density distribution 60
4.4.2 Millisecond pulsars population in the Galactic Center region 61
4.4.3 Cosmic-ray density distribution from a bulge and disk population of millisecond pulsars 62
4.4.4 Millisecond pulsars diffuse gamma-ray spectrum and luminosity 63
4.5 Discussion and perspectives 65

In this chapter we investigate the possibility to explain the TeV Galactic Center diffuse emission detected by H.E.S.S. presented in Sec. 3.3 with an unresolved population of millisecond pulsars in the Galactic bulge. This millisecond pulsar population scenario has been derived by Fermi-LAT to explain through leptonic emission processes the GeV diffuse emission detected towards the Galactic Center, known as the Galactic Center excess. This scenario can be extended to hadronic emission processes that produce gamma rays in the TeV energy range as the most likely explanation of the H.E.S.S. diffuse emission. An estimate of the number of pulsars required to reproduce the H.E.S.S. diffuse emission through cosmic-ray protons acceleration and their interaction with the molecular clouds is given.
In Sec. 4.1 the GeV and TeV gamma-ray excesses detected by Fermi-LAT and H.E.S.S., respectively, (see Sec. 3.3 and Sec. 3.4) could be related to the presence of a population of unresolved millisecond pulsars in the Galactic bulge. This population could accelerate electrons and reproduce the GeV excess through leptonic processes. A fraction of the accelerated particles may also consist in protons. In Sec. 4.2 we explain how millisecond pulsars can accelerate protons up to PeV energy and in Sec. 4.3 we explain the process of injection and propagation of these protons in the central region of the Milky Way. In Sec. 4.4 we define the cosmic-ray density distribution and millisecond pulsars distribution in our model and study under which conditions the modeled diffuse gamma-ray spectrum and luminosity can be compatible with H.E.S.S. measurements. This work has been published in Ref. [104].

4.1 Millisecond pulsars population and the Galactic Center excess

4.1.1 Explaining the GeV Galactic Center excess seen by Fermi-LAT

The Fermi-LAT collaboration has recently argued that the GeV excess (GCE, see Sec. 3.3) observed in their GC data set above the interstellar medium emission model (IEM) [105] can be explained by a yet unresolved population of millisecond pulsars (MSP) [97]. Pulsars (PSRs) are known to be able to accelerate electrons and positrons up to VHE [106]. The MeV to GeV gamma rays of the GCE detected by Fermi-LAT are then mainly interpreted as the product of the leptonic mechanisms described in Sec. 1.3. In order to reproduce the morphology of the GCE a bulge population of MSP is needed in addition to the well known Galactic disk population [97].
The Galactic disk is modeled as a cylinder of height about 1 kpc and its population of PSRs follows a Galactocentric Lorimer [107] spatial distribution $\propto r^n \mathrm{e}^{-r/\sigma}$. The Galactic bulge is a spherically symmetric structure that extends up to about 3 kpc from the GC. Both the regions have mean gas density $n_{\mathrm{gas}} \sim 1$ cm^{-1}. The luminosity function for gamma rays is

assumed to be the same for the disk and the bulge and it is modeled as a power-law in a range of luminosity $L_\gamma = [10^{33}, 10^{36}]$ erg s^{-1}. However, in the inner 200 pc of the galaxy a significantly denser region is present, known as the CMZ (see Sec. 3.3.1), with on average $n_{\rm gas} \sim 100$ cm^{-3}. A schematic of the bulge (yellow), the disk (blue) and the CMZ (red) is given in Fig. 4.1.

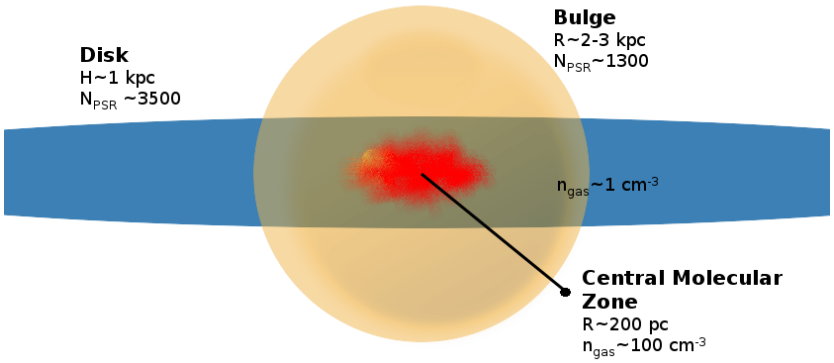

Figure 4.1: Schematic of the bulge (orange shaded disk), the disk (blue are) and the CMZ (red cloud), together with their basic characteristics.

MSPs are good candidates for some unassociated Fermi objects in the GC region. In fact, the sensitivity of current radio telescopes is found to be too low for good prospects of detectability of hypothetical MSP in the bulge [108]. From the catalog of Fermi-LAT sources, PSRs are distinguished from blazars due to the study of the shape of their emission spectrum. The derived selection criteria for PSRs based on the photon index and the energy cutoff are applied in the GC region in order to find PSRs candidates and constraint the parameters of a population of MSP. Their luminosity function is well fitted by a power-law $dN/dL \propto L^{-\beta}$ with index $\beta = 1.7$, assumed to be the same for the disk and bulge populations. The disk population expected to amount to 4000-16000 MSP in the luminosity range defined above. The lower limit comes from the identified gamma-ray PSRs and the upper limit from unassociated sources with characteristics compatible with the criteria of PSR selection. The bulge spatial distribution is considered spherically symmetric around the GC, $dN/dr \propto r^{-\alpha_{\rm b}}$, consistently with the morphology of the GC excess. The normalization of the bulge population, is then fitted to the data in order to reproduce the GC excess. A population of 800-3600 MSP is expected in the bulge. More information about the spatial distribution and CR density in the disk and bulge is given in Sec. 4.4.

4.1.2 Connecting the GeV Galactic Center excess and the TeV diffuse emission ?

In this work, we want to apply the idea of a Galactic bulge MSP population to explain the TeV excess detected by H.E.S.S. in the GC region [39] (see Sec. 3.4). Cosmic-ray electrons are not suitable to explain such an emission. First, electrons and positrons are difficult to accelerate up to VHE. Some extreme accelerators here the acceleration proceeds at the maximum possible rate allowed by classical electrodynamics can do it, but the accelerated electrons and positions undergo strong energy losses in the GC region due to ICS and synchrotron radiation. The mean free path of electron is a few pc. It would be difficult for them to propagate over the scale of the CMZ without losing a large fraction of their energy and produce gamma rays at energies in the ten TeV range, unless assuming unrealistically weak magnetic field. The time for diffusion of particles over a distance $r_{\rm diff} \sim 200$ pc, assuming a diffusion coefficient $D(E/10^{14}\,{\rm eV}) \sim 10^{30}$ cm^2 s^{-1} in standard interstellar conditions is

$$t_{\rm diff} = r_{\rm diff}^2/6D \sim 10^{11}\,{\rm s}\,(r_{\rm diff}/200\,{\rm pc})^2(D/10^{30}\,{\rm cm}^2\ {\rm s}^{-1}). \tag{4.1}$$

In comparison, the time scale of synchrotron losses is given by

$$t_{\rm syn} = 10^8\,{\rm s}\,(B/100\,\mu G)^{-2}(E_{\rm e}/10^{14})^{-1}, \tag{4.2}$$

assuming a typical magnetic field of $100\,\mu$G[1] and electrons at 100 TeV. Since $t_{\rm diff}$ is significantly larger than $t_{\rm syn}$ the diffuse emission cannot be reproduced under these conditions because the electrons primarily lose energy by synchrotron losses.
On the other hand, the proton-proton interaction time scale for TeV protons is

$$t_{\rm pp} = cn_{\rm H}\sigma_{\rm pp} \sim 10^{13}\,{\rm s}\,(n_{\rm H}/100{\rm cm}^3)^{-1}, \tag{4.3}$$

that depend on the hydrogen density $n_{\rm H}$ and the proton-proton inelastic cross section $\sigma_{\rm pp} \sim 50$ mb for protons of energy $\sim 10^{14}$ eV. Since $t_{\rm pp}$ is significantly larger than $t_{\rm diff}$ under these conditions, the protons are able to diffuse on a large spatial scale with negligible energy losses.
For this reason to explain the TeV emission an hadronic scenario is more plausible. Thus, in our study the main contribution to the GC TeV diffuse emission is due to the acceleration of protons up to PeV energies in the magnetosphere of a MSP population. This population is modeled with the same spatial distribution and luminosity function that reproduce the GCE detected by Fermi-LAT for acceleration of electrons. The contribution of leptonic radiative processes is not considered in this work,. They provide an additional component of the emission dominant below 100 GeV and sub-dominant in the TeV range. However,

[1]For comparison, the Galactic halo magnetic field measures 4 μG.

other studies [109] interpreted the H.E.S.S. TeV excess as coming from ICS of VHE electrons/positrons generated by Geminga-like PSRs in the GC region, *i.e.* assuming a leptonic scenario and a different PSR spatial distribution.

4.2 Millisecond pulsars as PeV proton accelerators

Electrons and protons are accelerated at the surface of PSRs, due to the strong magnetic fields in the region and the rotational energy of the star. A typical MSP has dipole magnetic field $B > 10^9$ G, initial spin period $P_{\rm i} \sim 1$ ms and radius $R_* = 6$ km. The electromagnetic luminosity given by the rotation and the magnetic field of the PSR can be converted into kinetic luminosity during the process of acceleration. In what follows we extract the main formulas from Ref. [110]. The CR and gamma-ray luminosities of MSPs can be derived.
The protons at the surface of the PSR can be accelerated up to

$$E_0 \sim 1.4{\times}10^{15}{\rm eV}\eta_{\rm acc}\left(\frac{\kappa}{10^3}\right)^{-1}\left[1{+}\left(\frac{m_{\rm p}}{2m_{\rm e}}\right)\left(\frac{\kappa}{10^3}\right)\right]^{-1}\left(\frac{B}{10^9\,{\rm G}}\right)\left(\frac{R*}{6\,{\rm km}}\right)^3\left(\frac{P_{\rm i}}{10^{-3}\,{\rm s}}\right)^{-2}, \quad (4.4)$$

where $\eta_{\rm acc}$ is the efficiency of the acceleration mechanism, $\kappa \sim 10^3$ is the pair multiplicity of ions-protons pairs produced in the PSR magnetosphere, and $m_{\rm p}$ and $m_{\rm e}$ are the proton and electron masses, respectively.
In order to have an efficient acceleration up to the PeV scale required to explain VHE diffuse emission the spin-down time scale $t_{\rm sd}$ must be accounted. It corresponds to a decrease of the PSR rotational energy due to electromagnetic emission, *i.e.* decrease of acceleration power, and it writes as

$$\begin{aligned} t_{\rm sd} &= 9Ic^3P^2/8\pi^2B^2R_*^6 \\ &\sim 9.8\times10^7{\rm yr}\left(\frac{I}{10^{45}\,{\rm g\ cm^2}}\right)\left(\frac{B}{10^9\,{\rm G}}\right)^{-2}\left(\frac{R*}{6\,{\rm km}}\right)^{-6}\left(\frac{P_{\rm i}}{10^{-3}\,{\rm s}}\right)^2, \end{aligned} \quad (4.5)$$

where I is the moment of inertia.
The CR energy at the moment of injection is then given by

$$E_{\rm CR}(t) = E_0(1 + t/t_{\rm sd})^{-1}. \quad (4.6)$$

and the CR protons luminosity by

$$\begin{aligned} L_{\rm CR}(t) &= \frac{9c^2I}{4ZeBR_*^3}E_{\rm CR}(t)(t+t_{\rm sd})^{-1} \\ &\sim 3.1\times10^{36}{\rm ergs^{-1}}\eta_{\rm acc}\left(\frac{\kappa}{10^3}\right)^{-1}\left[1+\left(\frac{m_{\rm p}}{2m_{\rm e}}\right)\left(\frac{\kappa}{10^3}\right)\right]^{-1}\left(\frac{B}{10^9\,{\rm G}}\right)^2\left(\frac{R*}{6\,{\rm km}}\right)^6\left(\frac{P_{\rm i}}{10^{-3}\,{\rm s}}\right)^4\left(1+\frac{t}{t_{\rm sd}}\right)^{-2}. \end{aligned} \quad (4.7)$$

The luminosity of the total population of $N_{\rm MSP}$ MSP is $L_{\rm MSP,tot} = N_{\rm MSP} L_{\rm MSP}$. The proton luminosity is defined as $L_{\rm p} = \eta_{\rm p} L_{\rm MSP}$, where $\eta_{\rm p}$ is the fraction of the PSR luminosity converted to protons acceleration. This fraction could be $\eta_{\rm p} \sim$0.1%, compared to $\eta_{\rm e} \sim 10\%$ for electrons. The gamma-ray luminosity from proton-proton interaction depends on the ratio $\tau_{\rm pp} = t_{\rm diff}/t_{\rm pp} \approx 10^{-2}$ between the diffusion and the interaction scale. So the gamma-ray luminosity for a population of MSP is proportional to

$$L_\gamma = \tau_{\rm pp} \eta_{\rm p} L_{\rm MSP,tot}. \tag{4.8}$$

Knowing that a single MSP has a spin-down luminosity of the order $L_{\rm MSP} \sim 10^{36}$ erg s^{-1}, the luminosity budget of MSP in the Galactic bulge is large enough to reproduce the gamma-ray luminosity measured by H.E.S.S. $L_{\gamma>1\,\rm TeV} \sim 5 \times 10^{34}$ erg s^{-1}, even in case of small efficiency in proton acceleration.

4.3 Injection and propagation of accelerated protons

4.3.1 Proton injection spectrum of the source

If gamma rays of energy ϵ are considered to be produced entirely by proton-proton interaction with a target of mass Mc and subsequent pion decay, their spectrum writes

$$\frac{{\rm d}^3 N_\gamma}{{\rm d}\epsilon {\rm d}t {\rm d}r}(\epsilon, r, t) = \eta_{\rm N} \int {\rm d}E \frac{{\rm d}^3 N_{\rm p}}{{\rm d}E {\rm d}t {\rm d}r}(E, r, t) \frac{{\rm d}\sigma_{\rm pp,\gamma}}{{\rm d}\epsilon}(\epsilon, E) = \frac{\eta_{\rm N} Mc}{m_{\rm p}} \int {\rm d}E w_{\rm CR}(E, r, t) \frac{{\rm d}\sigma_{\rm pp,\gamma}}{{\rm d}\epsilon}(\epsilon, E) \tag{4.9}$$

can be computed after defining the injection spectrum of protons with energy E at time t and the distribution of sources at distance r, that provide the CR density profile $w_{\rm CR}(E, r, t)$. Note that for monoenergetic injection at energy E the peak of the photon spectrum $\epsilon^2 dN_\gamma/d\epsilon$[2] is at about $\epsilon = E/10$.

A precise estimate of the injection spectrum is necessary in order to be able to model the expected gamma-ray flux as function of the energy and compare to H.E.S.S. data. A transient monoenergetic injection scenario is considered. Indeed, at each time t, CRs are injected with energy given by Eq. (4.6).

The transient CR flux at the position of the source is obtained from the luminosity defined in Eq. (4.7):

$$\frac{{\rm d}^2 N_{\rm p}}{{\rm d}E {\rm d}t}(E, t) = \frac{9c^2 I}{4ZeBR_*^3} E^{-1} (t + t_{\rm sd})^{-1}. \tag{4.10}$$

A hard injection spectrum $\propto E^{-1}$ is obtained.

Realizations of the MSP parameters are used to consider a variety of MSPs sources in the bulge. The initial spin period distribution is considered to be log-normal [111] with mean 1.5 ms and width 0.58 ms and the magnetic field is modeled as a power-law distribution [112]

[2]The photon spectrum is also referred to as $\epsilon^2 \phi_\gamma$.

with index -1 and constrained between the values 10^8 G and 10^{11} G.
An alternative uniform injection scenario can be considered. It may take place when the monoenergetic injection is reprocessed at a shock front. In this case the injection spectrum can possibly get softer, if the acceleration process is stochastic for instance. The continuous injection rate of accelerated protons is then modeled as a power-law over the time of injection $t_{\rm sd}$ for energies greater than $E_{\rm p,min} = 10^{10}$ eV and smaller than $E_{\rm p,max}(t_{\rm sd}) = E_0(t_{\rm sd})$. With a power-law flux $dN/dE \propto E^{-\beta}$ the injection rate $Q_{\rm p}$ expresses as:

$$\dot{Q}_{\rm p}(E) = \frac{\eta_{\rm p} L_{\rm CR}(t_{\rm sd})(2-\beta)}{1-[E_{\rm p,min}/E_{\rm p,max}(t_{\rm sd})]^{2-\beta}} \Big[\frac{E}{E_{\rm p,max}(t_{\rm sd})}\Big]^{2-\beta} \tag{4.11}$$

The emission can be considered continuous over a timescale $t_{\rm sd}$ if the inverse of the rate of birth of MSP, $\tau_{\rm birth}$, is much lower than the spin-down, *i.e.* $1/\tau_{\rm birth} \ll t_{\rm sd}$. This assumption is satisfied in standard conditions [113], when $t_{\rm sd} \gtrsim 10^6$ yrs and $\tau_{\rm birth} \gtrsim 1/345000$ yrs^{-1}.

4.3.2 Diffusive transport equation

The process of diffusion and interaction of the injected CR in the interstellar medium is described by a diffusive transport equation [110] that defines the density of particles with energy E at a time t and position $\vec{r}$. It includes three terms corresponding to the injection of CRs, their diffusion and the possible loss by spallation:

$$\frac{\partial n(E,\vec{r},t)}{\partial t} = \underbrace{\frac{{\rm d}N(E)}{{\rm d}E}\delta(t-t_{\rm s})\delta^3(\vec{r}-\vec{r_{\rm s}})}_{\text{injection}} + \underbrace{\nabla[D(E)\nabla n(E,vecr,t)]}_{\text{diffusion}} - \underbrace{\Gamma^{\rm sp}(E) n(E,\vec{r},t)}_{\text{spallation}}. \tag{4.12}$$

This equation determines the time dependence of the density n of particles with energy E at time t and position $\vec{r}$. The three terms represent:

- the injection at time $t_{\rm s}$ of CRs with spectrum $\frac{{\rm d}N(E)}{{\rm d}E}$ by a source at position $\vec{r}_{\rm s}$. More information about the injection of protons in MSP is given in Sec. 4.3.1.

- the diffusion of CRs in the interstellar medium with the diffusion coefficient $D(E)$. No spatial dependence of the diffusion coefficient is assumed here (homogeneous medium). The diffusion coefficient of the interstellar medium for a particle with rigidity $R = E({\rm eV})/Z$ is $D(E) = 6\times10^{29}(E/10^{13}\,{\rm eV})^{\delta}$ cm^3 s^{-1}. Assuming a Kolmogorov-type diffusion [114] the energy dependence of the diffusion coefficient has a typical slope $\delta = 1/3$.

- the spallation process, that takes place with spatially uniform rate $\Gamma(E)$. Spallation is the fragmentation of an atomic nucleus due to interaction with an energetic particle. This is the case for an accelerated proton that interacts with the interstellar medium. The rate of spallation depends on the cross section of the interaction, the gas density and the velocity of the particle ($\sim$ light speed).

The general solution $n(E, t, \vec{r})$ of Eq. (4.12) is given by a Green function [110] like

$$\mathcal{G}(\vec{r}, t, \vec{r}_{\rm s}, t_{\rm s}) = \frac{N(E)}{[4\pi D(E)(t-t_{\rm s})]^{3/2}} \exp[-\Gamma_{\rm sp}(E)(t-t_{\rm s})] \exp\left[-\frac{|\vec{r}-\vec{r}_{\rm s}|^2}{4D(E)(t-t_{\rm s})}\right]. \quad (4.13)$$

4.4 Explaining the H.E.S.S. diffuse emission with the Fermi-induced millisecond pulsar population

4.4.1 Expected cosmic-ray density distribution

The CR density at time t, position $\vec{r}$ and energy E due to injection of CRs starting at time $t_{\rm s}$ from a MSP at position $\vec{r}_{\rm s}$ is:

$$w_{\rm CR}(E, \vec{r}, t) = \int_{t'=0}^{t-t_{\rm s}} {\rm d}t' E^2 \frac{{\rm d}^2 N}{{\rm d}E{\rm d}t}(E, t) \mathcal{G}(\vec{r}, t, \vec{r}_{\rm s}, t'). \quad (4.14)$$

In case of continuous injection at constant rate, we define

$$\frac{{\rm d}^2 N}{{\rm d}E{\rm d}t}(E, t) \equiv \dot{Q}_{\rm p}(E). \quad (4.15)$$

Assuming spherical symmetry, continuous injection over a timescale $T \sim t$ and negligible spallation process, the CR distribution can be approximated as

$$w_{\rm CR}(E, r, t) = \frac{\dot{Q}_{\rm p}(E)}{4\pi D(E) r} {\rm erfc}\left(\frac{r}{\sqrt{4D(E)t}}\right), \quad (4.16)$$

as shown in the "H.E.S.S. model" from [39]. The above equation is valid for $t \geq t_{\rm diff}$ ($r < r_{\rm diff}$), meaning that protons diffuse at large distance before interacting with the ISM. In this work we assume that the protons can diffuse at least in $r_{\rm diff} = 200$ pc, the same dimension of the extended TeV emission observed by H.E.S.S., so that they can travel over the distance of the TeV emission.
The CR density obtained by Eqs. (4.14) and (4.15) (dark blue dashed line) and the one by (4.16) (light blue solid line), for a single source for continuous injection time T are compared in Fig. 4.2. From Ref. [39] $\dot{Q}_{\rm p}(E > 10\,{\rm TeV}) = 4 \times 10^{37} (D/10^{30}\ {\rm cm}^2\ {\rm s}^{-1})$ erg s^{-1}. In the left panel, for $T \sim 300$ yrs, the effect of spallation (orange solid line) is negligible and the two solutions match very well. In the right panel, for $T \sim 3$ Gyrs (optimistic for continuous injection), the effect of spallation (orange solid line) becomes significant from the hundred parsec scale.

For an accurate estimate of the total CR density at a given position $\vec{r}$ the spatial distribution of the accelerators situated at position $\vec{r}_{\rm s}$ needs to be properly taken into account.

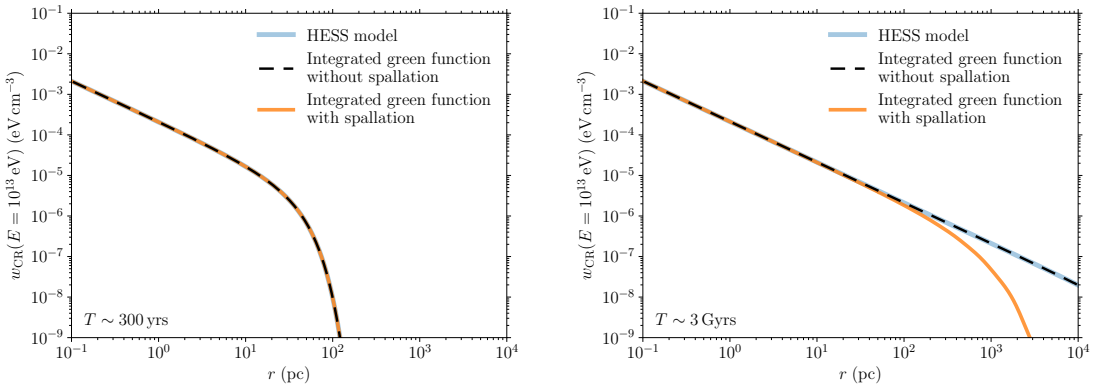

Figure 4.2: Cosmic-ray density $w_{\rm CR}$ in this work for one MSP with (orange) and without (blue) spallation, compared to the one assumed by H.E.S.S. in Ref. [39]. *Left panel:* Continuous injection over 300 yrs. The effect of spallation is negligible. *Right panel:* Continuous injection over 3 Gyrs. The effect of spallation becomes significant above a few hundred pc.

4.4.2 Millisecond pulsars population in the Galactic Center region

The spatial distributions of MSPs in the Galactic disk and the 3 kpc Galactic bulge are taken from Fermi-LAT results [97]. The two populations are assumed to have different spatial distribution, but the same luminosity function.

The Galactic disk population

The spatial distribution $F_{\rm d}$ of MSP [115, 116] in the disk is given in cylindrical coordinates and normalized to the total number of MSPs in the disk, $N_{\rm d}$, by the expression:

$$F_{\rm d}(r_{\rm s}, \theta, z) = \frac{r_{\rm s}^{n} \exp(-r_{\rm s}/\sigma) \exp(-|z_{\rm s}|/z_0) N_{\rm d}}{4\pi z_0 \sigma^{n+2} \Gamma(n+2)}, \tag{4.17}$$

where the parameters of the Lorimer distribution are $n = 2.35$, $\sigma = 1.528 \times 10^3$ pc, and the scale length is $z_0 = 700$ pc. The distribution integrated over θ and z coordinates and normalized to 1 becomes

$$F_{\rm d}(r_{\rm s}) = r_{\rm s}^{n+1} \exp(-r_{\rm s}/\sigma)/\sigma^{n+2}\Gamma(n+2) \tag{4.18}$$

and it is shown in Fig. 4.3 (orange solid line).

The Galactic bulge population

The spatial distribution of MSPs in the Galactic bulge in spherical coordinates is $F_{\rm b}(r_{\rm s}, \theta, \phi) = K_{\rm b} r^{-\alpha_{\rm b}}$. After normalization to the total number of MSPs in the bulge $N_{\rm b}$, it writes as:

$$F_{\rm b}(r_{\rm s},\theta,\phi) = \frac{(3-\alpha_{\rm b})N_{\rm b}}{4\pi r_{\rm max}^{3-\alpha_{\rm b}}} r_{\rm s}^{-\alpha_{\rm b}} \tag{4.19}$$

for $0 < r_{\rm s} < r_{\rm max}$, with bulge dimension $r_{\rm max} = 3$ kpc, and $\alpha_{\rm b} = 2.6$. At small distance the bulge population dominates. The distribution integrated over θ and ϕ and normalized to 1 becomes

$$F_{\rm b}(r_{\rm s}) = (3-\alpha_{\rm b}) r_{\rm s}^{2-\alpha_{\rm b}} / r_{\rm max}^{3-\alpha_{\rm b}}, \tag{4.20}$$

and it is shown in Fig. 4.3 (cyan solid line).

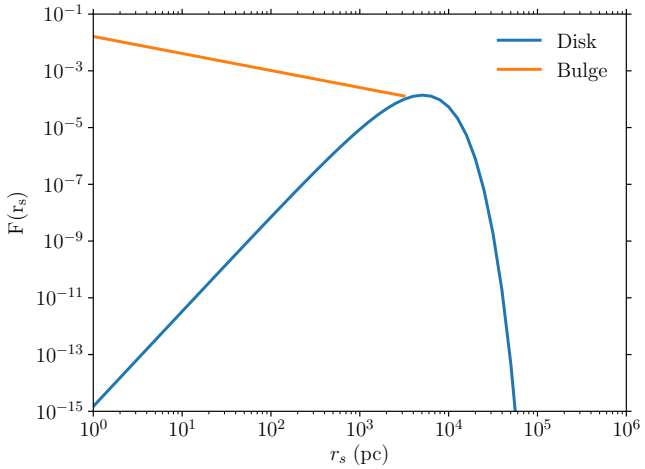

Figure 4.3: Normalized distribution of MSPs in the Galactic bulge (orange line) and in the Galactic disk (blue line) as function of the radial distance $r_{\rm s}$ of the sources from the GC.

4.4.3 Cosmic-ray density distribution from a bulge and disk population of millisecond pulsars

The total CR density, $w^{\rm tot}_{\rm CR,d}(E,r,t)$, at position r and time t due the disk population is computed from the combination of Eqs. (4.14) and (4.17), as:

$$\begin{aligned} w^{\rm tot}_{\rm CR,d}(E,r,t) =& \frac{\dot{Q}_{\rm p}(E) N_{\rm d}}{\pi^2 D(E) z_0 \sigma^{n+2} \Gamma(n+2)} \int_{r_{\rm s}=0}^{\infty} \int_{z_{\rm s}=0}^{\infty} {\rm d}r_{\rm s} {\rm d}z_{\rm s} \\ & \times \frac{r_{\rm s}^{n+1} \exp(-r_{\rm s}/\sigma) \exp(-|z_{\rm s}|/z_0)}{(r-r){\rm s}^2 + z_{\rm s}^2} \mathcal{K}\left(\frac{-4 r r_{\rm s}}{(r-r_{\rm s})^2 + z_{\rm s}^2}\right), \end{aligned} \tag{4.21}$$

with $\mathcal{K}$ a complete elliptic integral of the first kind, which is computed numerically. The integrated cosmic-ray density $w^{\rm tot}_{\rm CR,b}(E,r,t)$ due to the bulge is the convolution of $F_{\rm b}$ for $w_{\rm CR}(E,|\vec{r}-\vec{r}_{\rm s}|,t)$.

For $r < r_{\rm max}$:

$$w^{\rm tot}_{\rm CR,b}(E,r,t) = \frac{\dot{Q}_{\rm p}(E)(3-\alpha_{\rm b})N_{\rm b}}{4\pi D(E)(2-\alpha_{\rm b})r_{\rm max}}\left[1-\frac{1}{3-\alpha_{\rm b}}\left(\frac{r}{r_{\rm max}}\right)^{2-\alpha_{\rm b}}\right]. \tag{4.22}$$

For $r \geq r_{\rm max}$:

$$w_{\rm CR,tot}(E,r,t) = \frac{\dot{Q}_{\rm p}(E)N_{\rm b}}{4\pi D(E)r}. \tag{4.23}$$

The $w_{\rm CR,tot}$ profiles are obtained assuming an observation time $t = T$, a continuous injection of protons over the same time $T \sim 3$ Gyrs and spherical symmetry, as in Eq. (4.16). The parameters of the Fermi-LAT-inferred bulge population of MSPs are assumed. Fig. 4.4 shows the CR density profiles in case the error function in (4.16) is neglected (dashed lines) or not (solid lines). The disk population (solid cyan line) provides a constant radial CR density at small distance from the GC and cannot reproduce alone the CR distribution inferred by H.E.S.S. (orange points). The CR density radial distribution of the bulge population (solid blue line) well describes the H.E.S.S.-inferred one in the GC region.

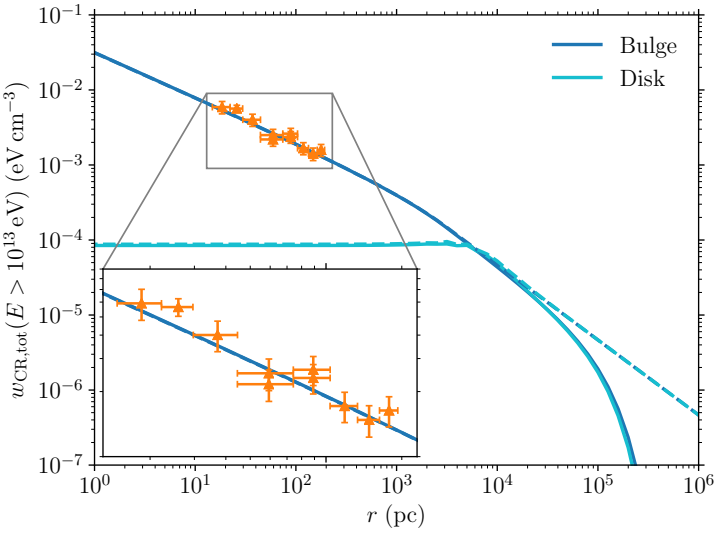

Figure 4.4: Total CR density profile versus radial distance r in the bulge (blue line) and in the disk (cyan line), respectively, neglecting (dashed lines) or not (solid lines) the error function in Eq. (4.16). The H.E.S.S. data points [39] are shown in the inset (orange points).

4.4.4 Millisecond pulsars diffuse gamma-ray spectrum and luminosity

In order to keep the disk contribution sub-dominant with respect to the bulge contribution to the total gamma-ray flux, the ratio between the number of disk and bulge MSPs should

be $N_{\rm d}/N_{\rm b} \lesssim 10$ so that the. In our model the disk population is considered negligible.
The total gamma-ray flux is obtained by integrating Eq. (4.9) over the full bulge population and an injection time of 10^{17} s. The value of the CR density profile for transient injection is derived by inserting Eq. (4.10) in Eq. (4.14).
The parameters used to be in good agreement with the H.E.S.S. gamma-ray luminosity measurements are $\eta_{\rm acc} \sim 0.03$ (moderate efficiency), $\kappa = 10^3$, $\eta_{\rm p} N_{\rm b} \sim 10^6$ and a magnetic field $B = 10^9$ G.
The total gamma-ray spectra for the model of transient monoenergetic injection (right panel) and for uniform injection (left panel) are shown in Fig. 4.5 (solid gray line). Both match well the flux of the TeV diffuse excess measured by H.E.S.S. (orange points) in a region of size 1.4×10^{-4} sr in the vicinity of the GC[3]. The spectrum of the GeV excess by Fermi-LAT are also plotted (blue points). The hadronic model developed in this work cannot reproduce Fermi-LAT data. A joint GeV-TeV model could be achieved with a mixed leptonic and hadronic model, based as well on the presence of a MSPs population with the same characteristics, where the leptonic emission dominates below 100 GeV [97].

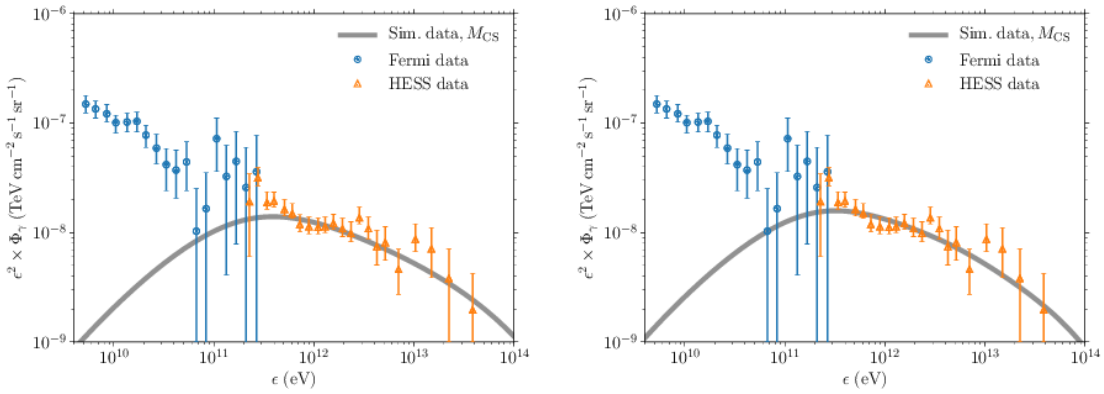

Figure 4.5: Diffuse gamma-ray energy spectrum obtained with this model (gray solid line). H.E.S.S. (orange points) and Fermi-LAT (blue points) measurements are plotted. *Left panel:* for the uniform injection model. *Right panel:* for the transient injection model.

The gamma-ray luminosity as function of the distance from the GC is also computed. It is shown (gray points) for $E \geq 1$ TeV in Fig. 4.6 and compared to H.E.S.S. spectrum (orange points) for transient (right panel) and uniform (left panel) injection. The data alone cannot prefer one scenario over the other.
The CR luminosity distribution in the range $L_{\rm CR} = [10^{32}, 10^{37}]$ erg s^{-1} can be approximated to a power-law with index 0.5 as shown in the Appendix of Ref. [104]. So the MSP with $L_{\rm CR}(t_{\rm sd}) > 10^{33}$ erg s^{-1} are about 10% of the total and those with $L_{\rm CR}(t_{\rm sd}) > 10^{34}$ erg s^{-1} about 3%. So we can estimate that the corresponding sub-population of MSPs count

[3] In Sec. 3.4 the region of detection of the Pevtron in the inner 0.45° of the GC is describe in more details.

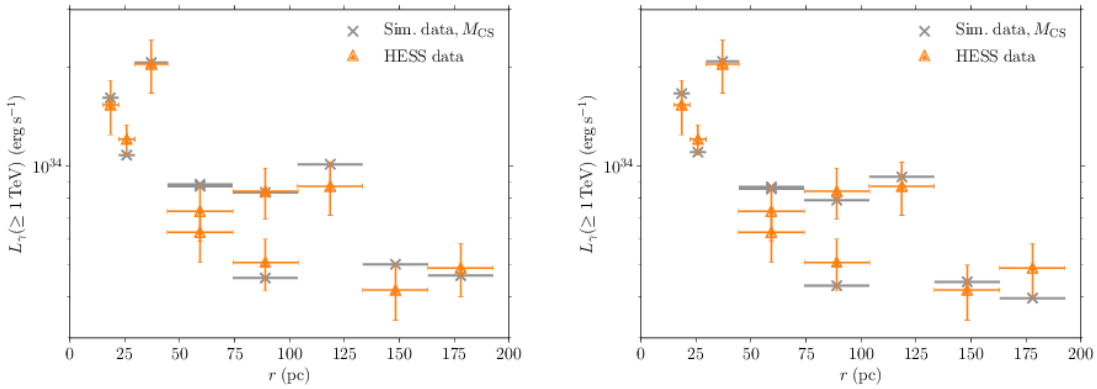

Figure 4.6: Integrated gamma-ray luminosity above 1 TeV versus distance from the GC, obtained with the model developed in this work (gray solid line). H.E.S.S. (orange points) and Fermi-LAT (blue points) measurements are plotted. *Left panel:* for the uniform injection model. *Right panel:* for the transient injection model.

$N_b(L_{CR}(t_{sd}) > 10^{33}$ erg s$^{-1}) \sim 7 \times 10^4$ and $N_b(L_{CR}(t_{sd}) > 10^{34}$ erg s$^{-1}) \sim 2 \times 10^4$. This last value is coherent with results in other studies, like Ref. [117] that predicts a number of MSPs of the order of 10^4.

4.5 Discussion and perspectives

A population of MSP inferred from Fermi-LAT measurements in the Galactic bulge could be able to explain the TeV excess detected by H.E.S.S. in the Galactic Center region. This is not the only possible explanation, but it is a promising scenario. Indeed, such a population of millisecond pulsars it is able to reproduce the Fermi-LAT excess up to 100 GeV invoking leptonic acceleration processes and the TeV measurements by H.E.S.S. through hadronic process. The emission of VHE gamma rays in millisecond pulsars is suggested also in Refs. [118, 119]. Interestingly, an uncertain quantity in the model is the PSR baryon loading η_p, that defines the quantity of accelerated protons with respect to the accelerated electrons. This quantity is not precisely measured, but there are constraints and it is reasonably assumed to be of the order of $10^{-2} - 10^{-3}$ according to measurements [120].

Our study assumes a standard diffusion coefficient. However, in a recent study of HAWC observations of Geminga and PSR B0656+14 a lower diffusion coefficient was deduced in the vicinity of the pulsars [121]. If this condition is valid not only in the vicinity of the investigated objects, but allover the interstellar medium, our model may become incompatible with the H.E.S.S. measurements because the diffusion timescale would become too long to allow the protons to diffuse over the dimension of the measured TeV gamma-ray diffuse emission.

An alternative scenario to millisecond pulsars is the presence of a single *Pevatron* [39]. New

H.E.S.S. observations would increase the statistics at very high energy and constrain the properties of the millisecond pulsar population and the *Pevatron*. Enlarged gamma-ray statistics would possibly show a sharp cutoff attributable to a single source and provide the necessary information to distinguish between the two scenarios. In our model a high-energy cutoff would imply low acceleration efficiency $\eta_{\rm acc}$ or low upper bound on the magnetic field $B_{\rm max}$. In addition, an updated study of the extension and morphology of the H.E.S.S. TeV excess with new data will be crucial to make the distinction between the two scenarii. For instance, the spatial distribution of diffuse emission due to a single *Pevatron* would be more peaked towards the Galactic Center.

Scenarii that include dark matter [94] or steady injection from a population of supernova [122] can also be found in literature. However the dark matter scenario is in contradiction with the absence of measurement of signal in the dwarf galaxies, largely observed by Fermi-LAT with a sensitivity down to the natural scale of dark matter annihilation up to the hundred GeV mass range. In the supernova scenario, at least a dozen of supernovae would be needed to produce the observed diffuse emission, but there is not any evidence of the existence of such a population in the vicinity of the Galactic Center.

Multi-wavelengths observations, *e.g.* in radio with the future Square Kilometer Array (SKA) [123], could also provide the necessary information to confirm or reject the millisecond pulsars hypothesis. These new generation radio telescopes are expected to have the sensitivity to detect and resolve millisecond pulsars in the Galactic Center region.

Chapter 5

The Galactic Center region observations with H.E.S.S. II

Contents

5.1 The Inner Galaxy Survey 68
5.1.1 Main goals of the survey 68
5.1.2 Observational pointing strategy 69
5.2 The H.E.S.S.-II dataset 71
5.2.1 Observation status before the IGS 71
5.2.2 The IGS campaigns 73
5.3 Observation parameters and data taking 2014-2018 75
5.3.1 Zenith angle and offset distributions 75
5.3.2 Sky time exposure maps 77
5.4 Excess and significance sky maps. 77
5.4.1 Comparison with observations at other wavelengths 79
5.5 Energy spectrum of HESS J1745-290 80
5.6 Outlook 82

In this chapter the H.E.S.S.-II strategy for observations of the Galactic Center region is presented together with the main goals and strategy for a survey of the region. The dataset of the long-term campaign are discussed. The first H.E.S.S.-II gamma-ray sky maps in this region are shown and compared to observations at other wavelengths. An update of the spectrum of the central very-high-energy gamma-ray source HESS J1745-290 is done.
Sec. 5.1 introduces the Inner Galaxy Survey strategy and goals, while Sec 5.2 gives a status of the observations until end of 2018. The outcome of the 2014-2018 observations of the Galactic Center region is discussed in Sec. 5.3 and Sec. 5.4. The energy spectrum of the central emitter is computed in Sec. 5.5.
This work has been used during the last three years for internal H.E.S.S. observation proposals that granted each year about 100 hours of observations towards the Galactic Center region.

5.1 The Inner Galaxy Survey

The Inner Galaxy Survey (IGS) is a long-term observation program of the region around the GC with H.E.S.S. II with a new pointing strategy. It started in 2016 and it is still ongoing and it is expected to be pursued until 2021. It is meant to significantly increase the currently available gamma-ray time exposure up to several degrees from the GC. This is one of the key-science projects for the continuation of H.E.S.S.. About 10% of the total yearly H.E.S.S. observation time is dedicated to observations of the GC region. I have been on shift on the H.E.S.S. site in 2017 and 2018 during the IGS data taking.

5.1.1 Main goals of the survey

Among the main goals of the IGS there is the DM search. Indeed, the DM signal is significantly large for several degrees around the GC and the inner part of the halo is the region from which we expect the largest DM annihilation signal detectable on Earth, due to proximity and large DM content. Internal studies have shown that DM search would benefit from extending the region of interest from 1°to few degrees. A similar study is presented in this work in Sec. 11.5. Moving to latitudes of a few degrees above the Galactic plane reduces a bit the signal in case of cuspy DM profile, but it avoids the region with the largest astrophysical background. In addition, observations that extend far from the GC would increase the sensitivity to ≤ 1 kpc DM cores, that otherwise are not contained in the signal region.
Another key-science topic that would benefit from the IGS is the search for GC outflows that have been detected at other wavelengths (see Sec. 3.4). Interestingly, H.E.S.S. has the potential to detect in the VHE energy range the low-latitude Fermi Bubble. Being able to detect the Fermi Bubbles with H.E.S.S. could shed light on the acceleration process that produced them and the astrophysical object at which the underlying process that takes

place.
The increased statistics would also improve the sensitivity to the Pevatron emission in the $E > 10$ TeV energy range, for which H.E.S.S. is the best instruments due to its favorable location with respect to the GC position. In addition, more data would allow H.E.S.S. to improve the knowledge about the diffuse emission from the Galactic plane (see Sec. 3.3), which is an unavoidable background for the search of DM and GC outflows. The pointing positions at a few degrees from the GC together with the larger statistics will also allow to study the morphology of the GC TeV emission and possibly distinguish between different hypothesis of sources and acceleration processes.

5.1.2 Observational pointing strategy

The ultimate goal of the IGS observations is to have a spatially homogeneous exposure as much as possible up to 3° from the GC. Due to the limited visibility window of the GC region and the large spatial extension of the region of interest the survey has been focused on the Northern hemisphere. In the Southern part of the Galactic plane a larger level of NSB in an extended region, up to 400 MHz, has been observed, as shown in Fig. 5.1. Interestingly the Northern part of the Galactic plane is where the peak of low-latitude Fermi Bubbles is expected.
Fourteen pointing positions have been selected in order to best reach the goal and the time requested on each pointing position is revisited every year and adapted to the results from the previous year observations. More information about the year-by-year observations is given in the next section. The 14 IGS pointing positions are shown in Fig. 5.2 and summarized in Tab. 5.1.

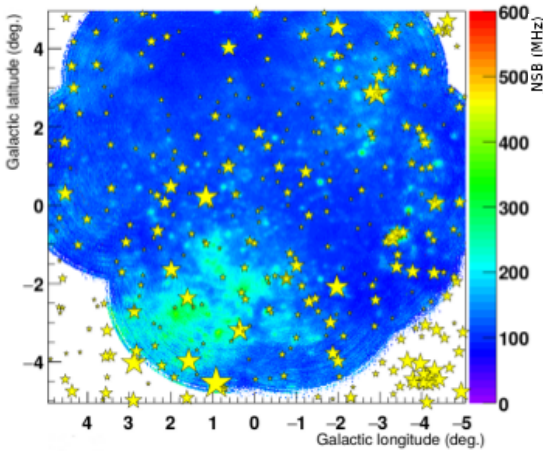

Figure 5.1: H.E.S.S.-II NSB map in MHz of the GC region in Galactic coordinates. An extended NSB region is observed below the Galactic plane. The yellow stars mark the position of point-like bright stars.

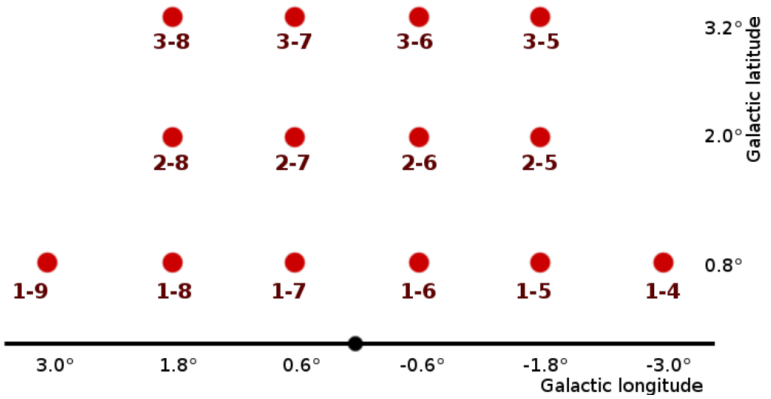

Figure 5.2: Schematic of the 14 pointing positions selected for the Inner Galaxy Survey. These pointing positions are optimal for searches for DM in the extended Galactic halo and GC outflows that are expected to peak at positive latitudes.

Pointing name	1-4	1-5	1-6	1-7	1-8	1-9	2-5	2-6	2-7	2-8	3-5	3-6	3-7	3-8
Gal. Long. [deg.]	-3.0	-1.8	-0.6	0.6	1.8	3.0	-1.8	-0.6	0.6	1.8	-1.8	-0.6	0.6	1.8
Gal. Lat. [deg.]	0.8	0.8	0.8	0.8	0.8	0.8	2.0	2.0	2.0	2.0	3.2	3.2	3.2	3.2

Table 5.1: Galactic longitude and latitude of the 14 pointing positions of the Inner Galaxy Survey.

5.2 The H.E.S.S.-II dataset

The H.E.S.S.-II dataset includes some pre-IGS observations in 2014 and 2015. At that time the extended survey had not started yet and the observations were taken towards the GC with *offset* between 0.4° and 2.3°. The observations taken with the largest *offsets* were aimed to cross-check [124] an analysis of Fermi-LAT data that suggested the presence of a DM line signal in the vicinity of the GC [125], displaced from the center. In this section we present the 2014-2015 and IGS 2016-2018 datasets separately, but in what follows and in Chap. 9 the full 2014-2018 H.E.S.S.-II dataset is considered.
Tab. 5.2 gives the observation live time, mean zenith angle and mean offset for each year from 2014 to 2018 after quality cuts. The observations on a year-by-year basis are discussed in the next sections.

Year	2014	2015	2016	2017	2018	2014-2018
Live time [hours]	60.3	84.5	89.8	68.8	86.6	390.0
Mean zenith angle [deg.]	17.0	15.6	13.0	12.1	18.5	15.6
Mean *offset* [deg.]	1.0	1.5	2.0	3.0	2.7	2.1

Table 5.2: Observation live time, mean zenith angle and mean offset of H.E.S.S.-II data taking in the GC region after quality cuts.

5.2.1 Observation status before the IGS

The H.E.S.S.-II GC observations in 2014 resulted in 60.3 hours of high quality data. The observations were focused near the GC. The mean *offset* was 1.0° and mean zenith angle 17.0°. In 2015 the observations continued in the same region with 84.5 hours, but some observations at larger *offset* began to be taken after Fermi-LAT suggested the detection of a possible DM signal in the vicinity of the GC [125][1]. The mean *offset* was 1.5° and the mean zenith angle 15.6°. Figs. 5.3 and 5.4 show the observation *offset* and zenith angle distributions, respectively, for 2014 (top panel) and 2015 (bottom panel). The pink line marks the position of the mean zenith angle.
Fig. 5.5 shows the gamma-ray sky acceptance in 2014 (left panel) and 2015 (right panel). It is fairly flat within $\sim 1°$, and degrades rapidly at larger latitudes, similarly to H.E.S.S.-I observations of the GC. The IGS is meant to compensate the lack of time exposure at high latitude and extend the observations at a few degree *offset* from the GC.

[1] H.E.S.S. analysis contradicted the detection hypothesis [124].

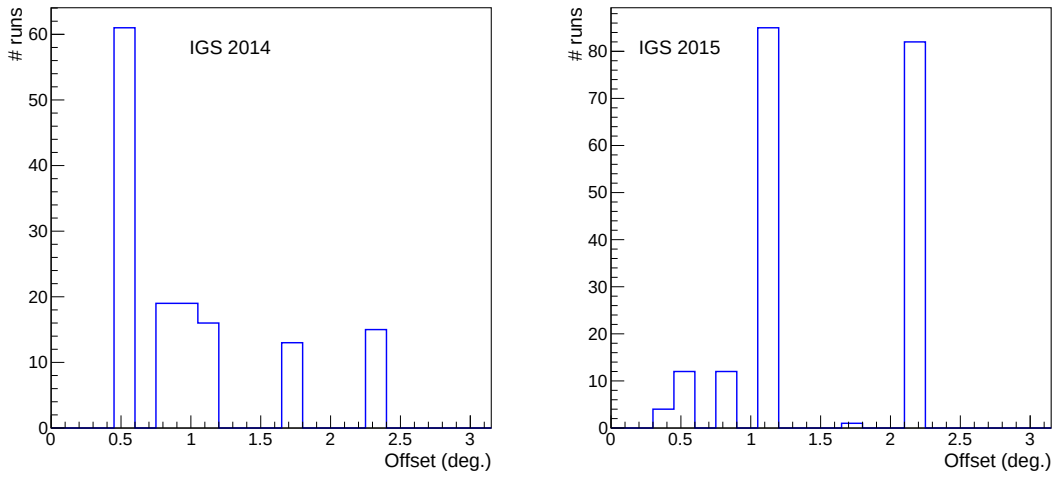

Figure 5.3: Distribution of the *offset* between the GC position and the pointing position for the GC observations taken in 2014 (left panel) and 2015 (right panel).

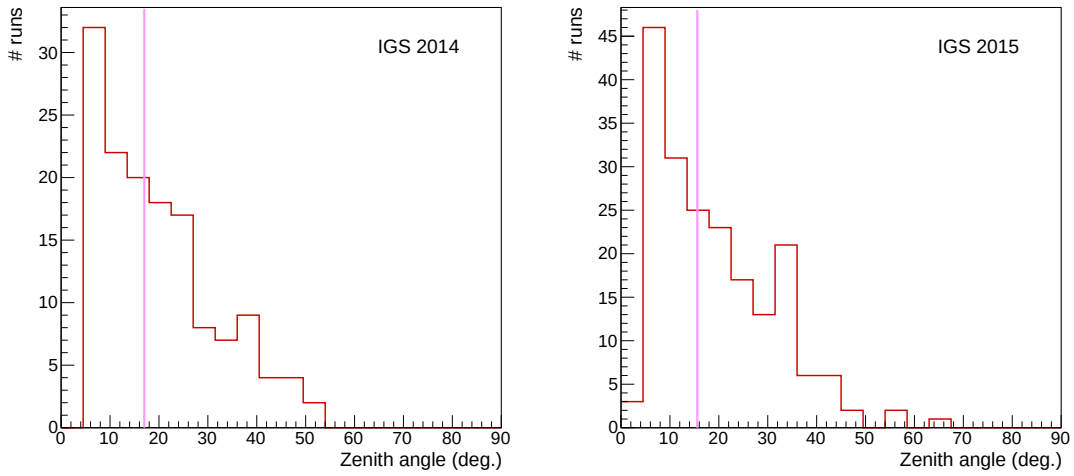

Figure 5.4: Zenith angle distributions for the GC observations taken in 2014 (left panel) and 2015 (right panel). The mean zenith angle is marked by a pink line.

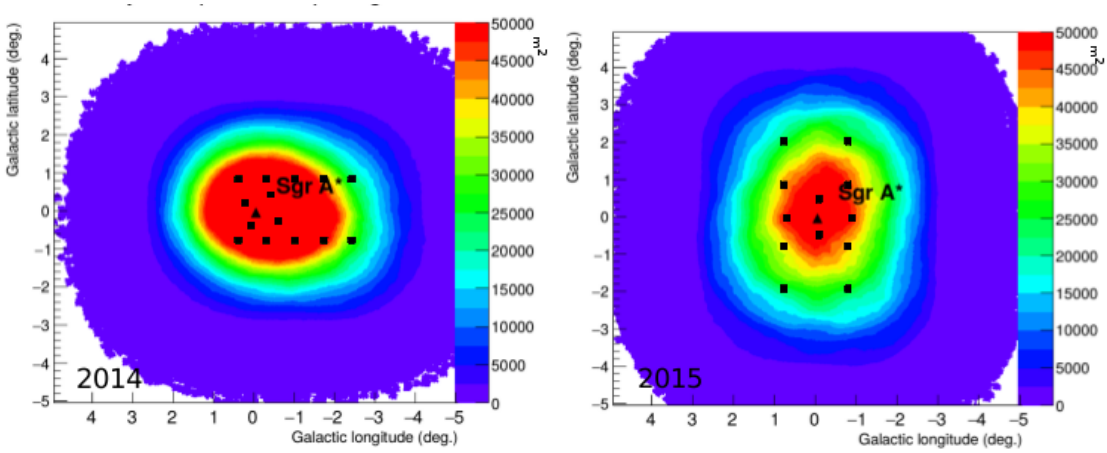

Figure 5.5: Gamma-ray sky acceptance maps in Galactic longitude and latitude for the GC observations taken in 2014 (left panel) and 2015 (right panel). The pointing positions are marked (black squares).

5.2.2 The IGS campaigns

Here the observations of the first three years of IGS are presented. In 2016 the observations have been split almost homogeneously on the 14 pointing positions for a total of 89.8 hours, with a mean *offset* of 2°. Only the pointing positions in the North-Eastern hemisphere were lacking exposure at the end of the first year campaign.
Since previous data were taken at lower latitudes and some pointing positions were under-exposed the 2017 campaign was revisited in order to homogenize the overall exposure. The 68.8 hours of observations covered all the pointings, but focused mainly on the pointing positions 3-6, 3-7 and 3-8 and had a mean *offset* of about 3.0°.
In 2018 the observations amount to 84.7 hours after quality cuts towards selected pointing positions at large latitude (mean *offset* 2.7°) only have been performed in view of the goal of homogenizing the overall exposure up to 3 degrees. The chosen pointing positions were 2-x and 3-x, only a few single *runs* have been taken at lower latitudes for a simultaneous program of observations of Sgr A* with the XMM-Newton telescope. In order to achieve the homogeneous exposure goal the proposal of observations accepted for 2019 and beyond focuses on pointing positions 2-5, 2-8 and 3-x and it will be re-evaluated on an yearly basis. The gamma-ray acceptance maps for every year of IGS and for the total of 2014-2018 H.E.S.S.-II observations are shown in Fig. 5.6. Year-by-year we are getting closer and closer to realizing the goal.

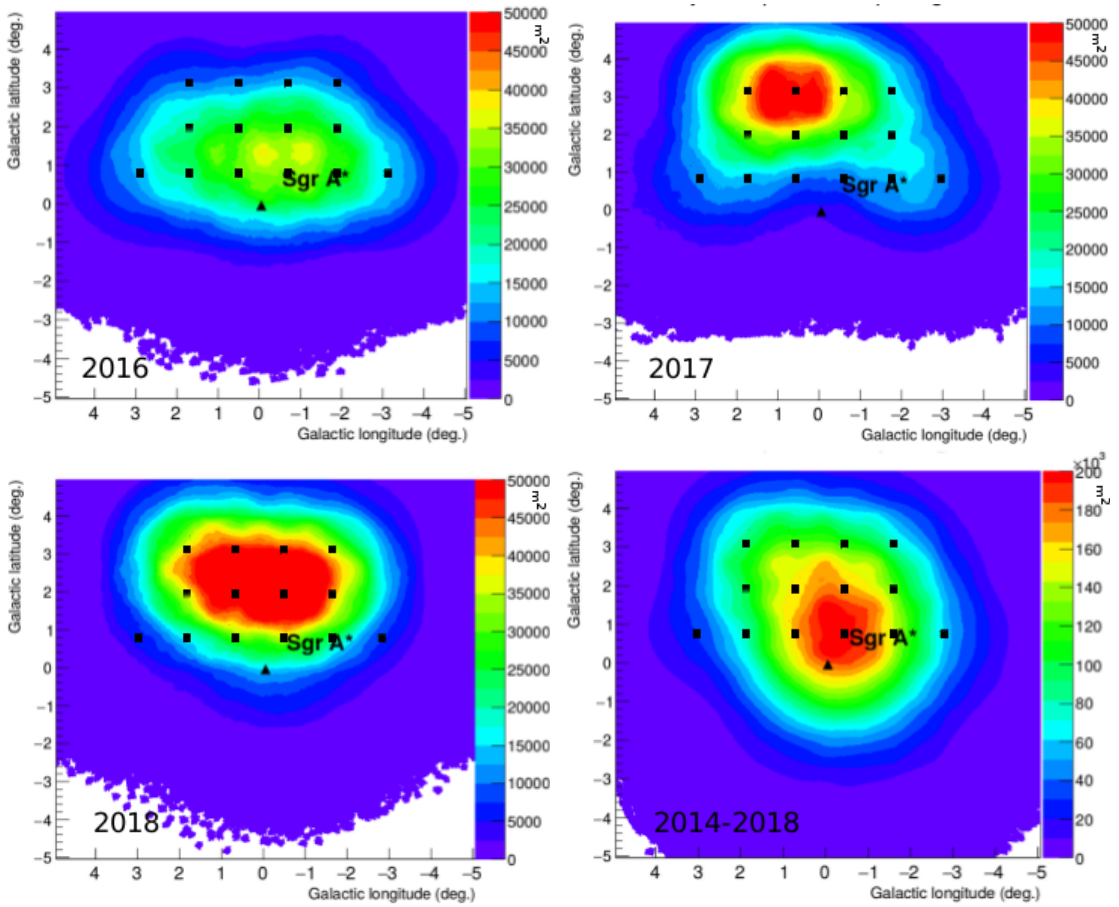

Figure 5.6: Gamma-ray sky acceptance maps in Galactic coordinates for the IGS obervations in 2016 (top left panel), 2017 (top right panel) and 2018 (bottom left panel), and cumulated H.E.S.S.-II acceptance over the full period 2014-2018 (bottom right panel). The pointing positions are marked (black squares).

5.3 Observation parameters and data taking 2014-2018

5.3.1 Zenith angle and offset distributions

The overall 2014-2018 H.E.S.S.-II campaign provided about 390 hours of data in the GC region. Observations with *offset* from 0.4° to 3.2° degrees have been performed, with an overall mean *offset* of 2.1°. Observations at low zenith angle are preferred, but they are not always possible due to the limited observability window competing with observations of other objects in the same RA band. They were taken at zenith from 0° to 65°, with a mean zenith angle of 15.6°. The year-by-year offset and zenith distributions are given in Fig. 5.7 and 5.8. The mean zenith angle is marked by a pink line.

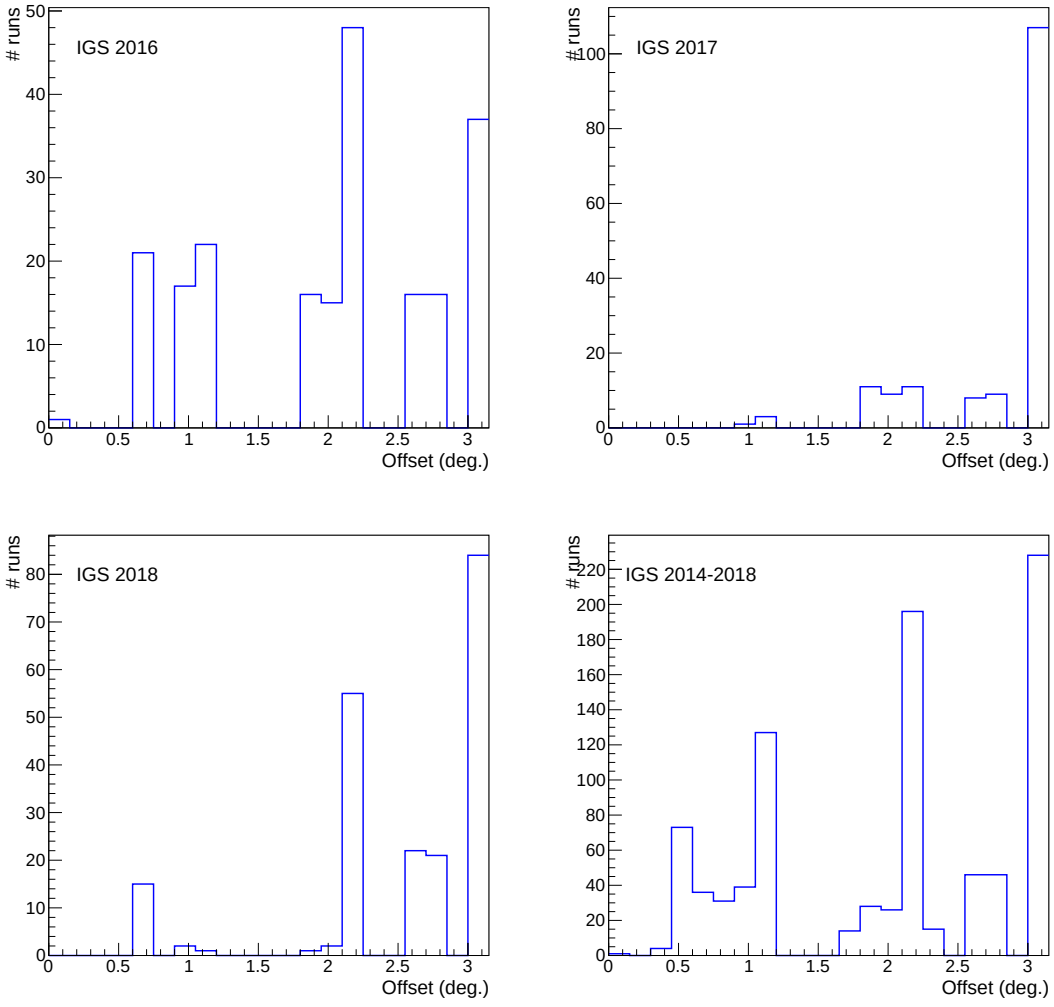

Figure 5.7: Distribution of the *offset* between the GC position and the pointing position for the IGS observations taken in 2016 (top left panel), 2017 (top right panel) and 2018 (bottom left panel), and the overall 2014-2018 campaign (bottom right panel).

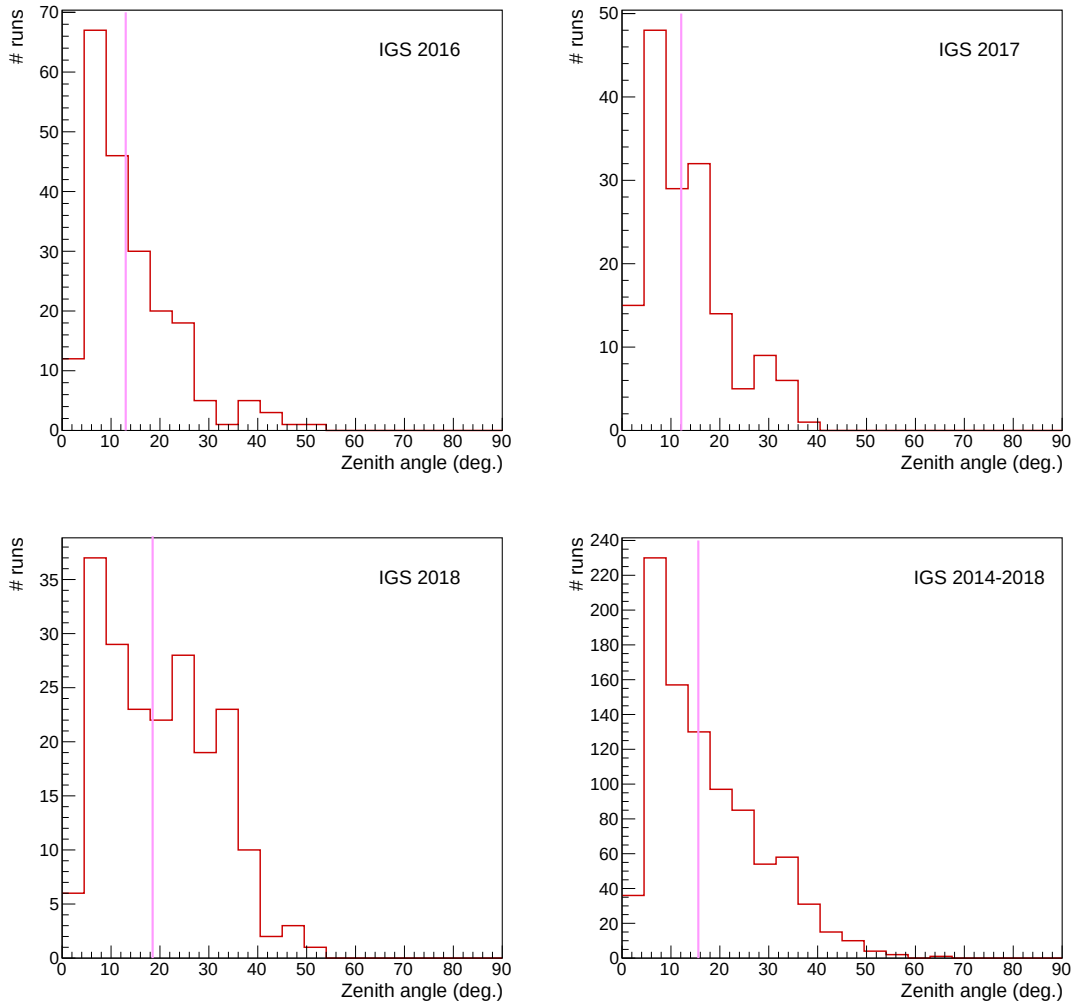

Figure 5.8: Zenith angle distributions for the IGS observations taken in 2016 (top left panel), 2017 (top right panel) and 2018 (bottom left panel), and the overall 2014-2018 campaign (bottom right panel). The mean zenith angle is marked by a pink line.

5.3.2 Sky time exposure maps

The time exposure maps for H.E.S.S.-I GC campaign, H.E.S.S.-II GC campaign, that includes the IGS, and the overall 2004-2018 H.E.S.S. I + H.E.S.S. II dataset are shown in Fig. 5.9. H.E.S.S.-I observations gave about 180 hours hours flat in 1° acceptance corrected [2] and significantly smaller dataset elsewhere. H.E.S.S.-II observations provided only about 120 hours flat in 1°, but provide also about 100 hours between 1° and 2° and 70 hours between 2° and 3°. The cumulated 2004-2018 contains almost 300 hours in the inner 1°, more than 150 between 1° and 2° and about 100 between 2° and 3°.
Fig. 5.10 shows the time exposure sky map projections for the IGS campaign that will be carried out until 2021. The projections are made considering 100 hours of observations each year for the next three years on the same pointing positions chosen for the campaign 2019. The projected time exposure is added to the real 2004-2018 time exposure. The exposure increases with the observation time on each pointing position, but it accounts also for the radial degradation of the exposure at large distance from the center of the camera. If the observations take place as assumed in these projections in 2021 the observations will be fairly homogeneous up to about 3° and the first survey at VHE in the GC region will be achieved before the advent of CTA.

5.4 Excess and significance sky maps.

A standard *Ring Background* analysis in *CT5- Mono* configuration is performed on the 2014-2018 H.E.S.S.-II dataset. The maps of the excess (left panel) of photons above the residual background and its significance (right panel) in terms of standard deviations are shown in Fig. 5.11. The main VHE standard sources in the FoV are HESS J1745-290 (Sgr A*), HESS J1747-281 (G09+01) and HESS J1745-303 and they are marked on the significance map. Now also the TeV emission at Sgr B2 position stands out on the background. The diffuse emission is clearly visible in the significance map, artificially saturated at 13σ. Some significant hot-spots (with significance $> 4\sigma$) are also present in the FoV. Note that no gamma ray is present in some parts of the FoV due to the IGS pointing strategy focused on the Northern hemisphere. Since the VHE diffuse emission is becoming more extended from the Galactic plane this will have consequences on the definition of the exclusion regions for DM search with H.E.S.S.-II (see Chap. 9).

[2] In the H.E.S.S.-I DM search analysis the non-acceptance corrected 254 hours of exposure are considered (see Chap. 8). Then the expected signal is multiplied for an acceptance corrected for the observational *offset*. The same approach will be used for the DM search with H.E.S.S.-II, but additional care is needed due to the larger *offsets* (see Chap. 9).

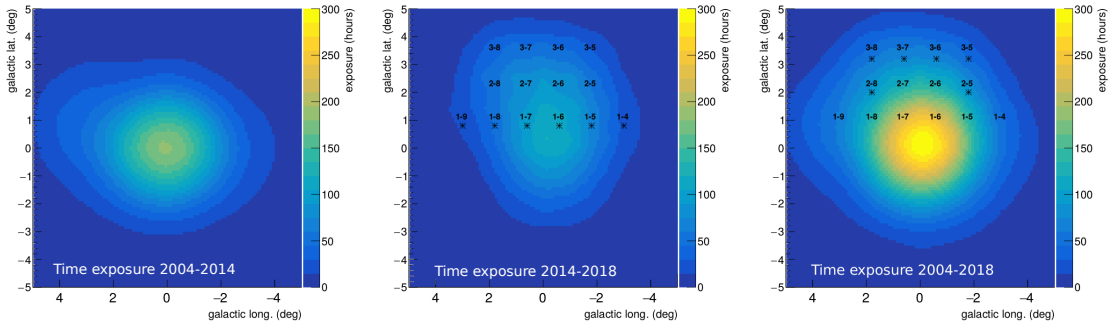

Figure 5.9: Time exposure maps in Galactic coordinates for H.E.S.S.-I (2004-2014, top left panel) , H.E.S.S.-II (2014-2018, top right panel) and cumulated observations (2004-2018, bottom panel) of the GC region. The pointing positions of the IGS are marked on the H.E.S.S.-II map.

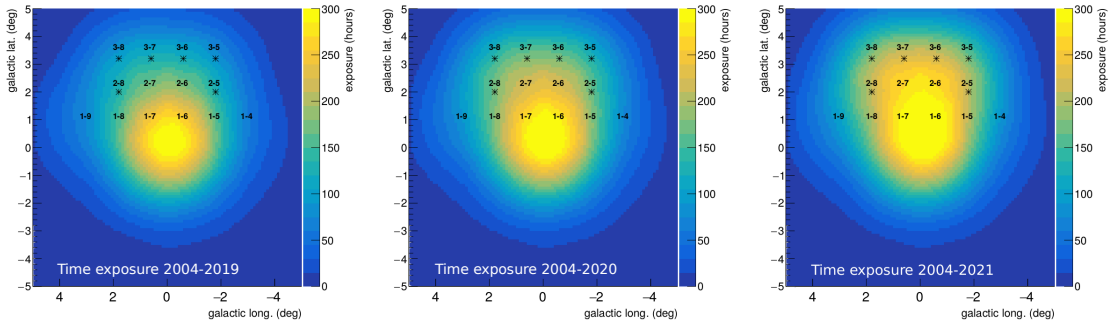

Figure 5.10: Projection of the time exposure maps in Galactic coordinates for H.E.S.S.-I and H.E.S.S.-II observations during the next three years of the IGS. Maps for 100 h/year observations on the pointing positions 2-5, 2-8 and 3-x in 2019 (top left panel), 2020 (top right panel) and 2021 (bottom panel). The IGS pointing positions are drawn on every map. Those that are actually targeted for the campaigns beyond 2019 are marked with an asterisk.

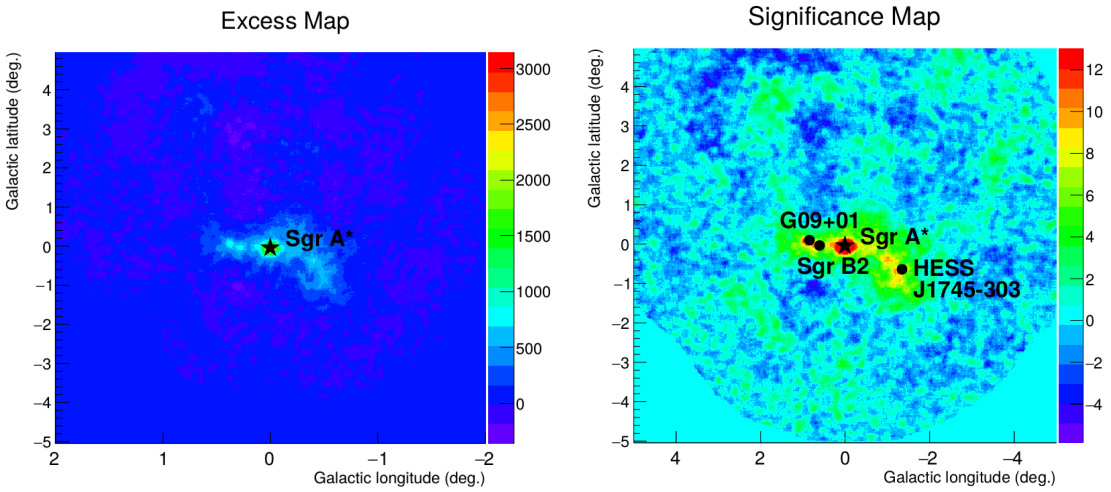

Figure 5.11: Gamma-ray excess (left panel) and significance (right panel) maps for H.E.S.S.-II *CT5 Mono* reconstruction with *Ring Background* analysis in Galactic longitude and latitude with an energy threshold at 100 GeV. The main significant standard VHE gamma-ray sources and diffuse emissions are visible in the maps. The position of HESS J1745-290 (Sgr A*) is marked by a black star, those of G09+01, HESS J1745-303 and Sgr B2 by a black dot.

5.4.1 Comparison with observations at other wavelengths

Comparing observations at different wavelength is a powerful mean to study the nature of the underlying acceleration processes responsible for the detected emissions. With IGS observations we can test if there are hints of extended emission or outflows in the vicinity of the GC in radio and GeV gamma-rays.

Fig. 5.12 shows the correlation between the TeV emission and the gas density along the Galactic plane. The significance contours CS line emission (black contours) that trace the presence of molecular gas [126] (*e.g.* molecular hydrogen) are overlaid to those of H.E.S.S.-II excess significance at 3, 5 and 7σ (white contours). The TeV emission is partially spatially correlated to the distribution of gas clouds along the Galactic plane confirming the hypothesis of hadron like processes initiated by standard accelerators. More extended emission is detected in the North-Western quadrant. It is not correlated with the gas distribution and it may be due to different acceleration processes.

In Fig. 5.13 the contours of emission detected by the Green Bank Telescope in radio at 5 GHz (6 cm) are overlaid to H.E.S.S.-II significance map. In radio a GC lobe (see Sec. 3.4) that extends from from the GC to the Northern part of the Galactic plane has been detected and could be powered by stellar wind has been observed [101]. The radio contours also show a lobe-like feature at about 0.5° in Galactic longitude that extends at positive latitudes for almost 1°. A correlation may exist between the outflows in radio and the TeV emission that is detected in H.E.S.S. data in the North-Western quadrant.

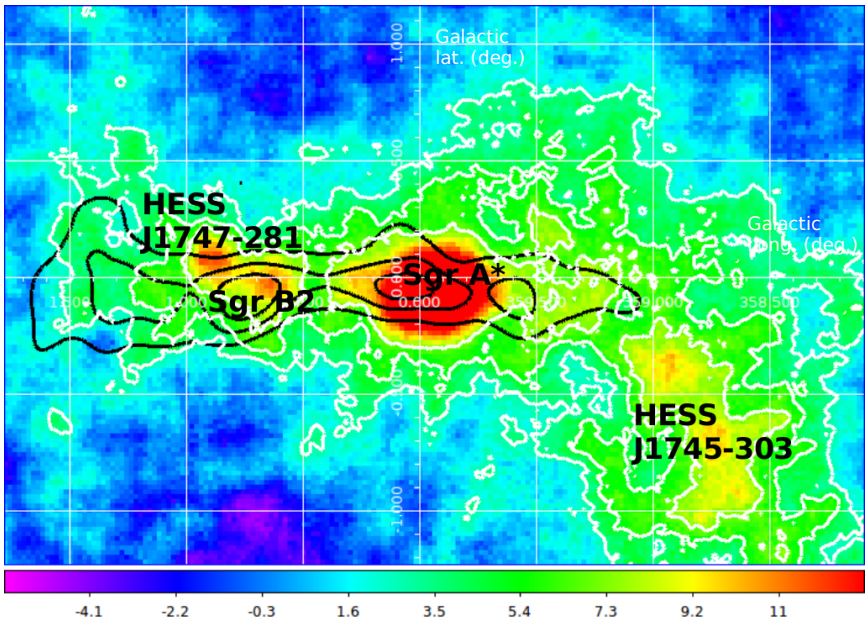

Figure 5.12: Gamma-ray significance H.E.S.S.-II map in Galactic coordinates with overlaid H.E.S.S. (white lines) and CS map [126] (black lines) significance contours at 3σ, 5σ and 7σ. The names of the most visible TeV sources in the FoV are printed: Sgr A*, Sgr B2, HESS J1745-290 and HESS J1745-303.

Part of the excess in the FoV could also be correlated to the Fermi Bubbles (see Sec. 3.4). The 3σ, 5σ and 7σ significant contours from H.E.S.S. are overlaid to the low-latitude Fermi Bubbles [89] in Fig. 5.14. A dedicated task force has been created and a study is ongoing to look for low-latitude Fermi Bubbles emission with H.E.S.S..
TeV emission provides that modt of the gamma rays are produced by hadronic acceleration processes taking place around the GC and the presence of outflows could be related to a continuous activity of the super massive black hole Sgr A* at the center of our galaxy.

5.5 Energy spectrum of HESS J1745-290

The spectrum of the source H.E.S.S. J1745-290, coincident with the super massive black hole Sgr A*, is computed using the 2014-2018 H.E.S.S.-II data and a *Ring Background* method on a *CT5 Mono* analysis. The source region is considered point-like (0.125°) and centered at $(-0.056°, -0.046°)$. The IGS dataset is not optimized for the observation of H.E.S.S. J1745-290 due to the large-latitude pointing positions that underexpose the GC focusing on regions where the DM or Fermi Bubbles signal-to-noise ratio is larger. However 88 live hours are accumulated on the target, providing a detection at 37σ with 3698 excess photons in the source region. The 2014 and 2015 dataset taken at small *offsets* provide most of the statistics at the position of the target.

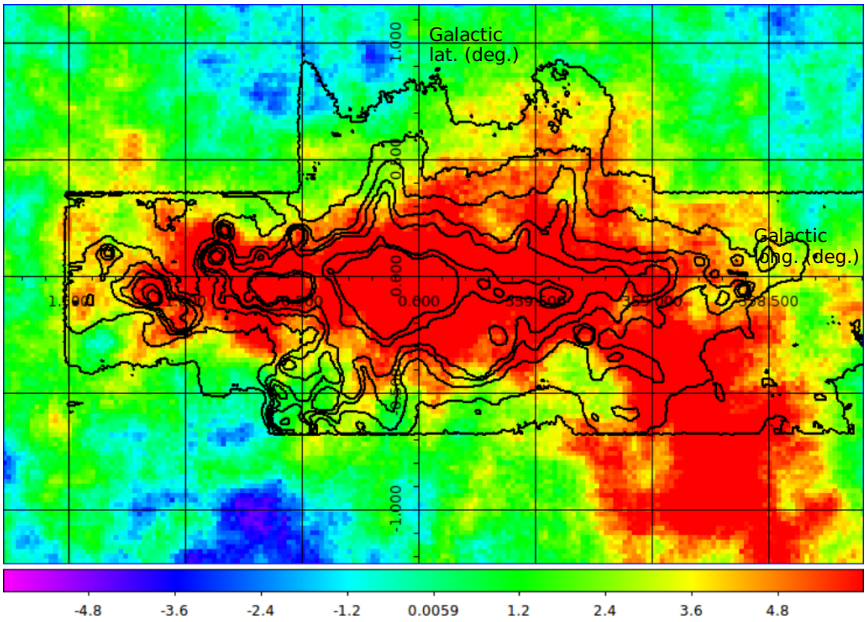

Figure 5.13: H.E.S.S. significance map with overlaid the 5 GHz radio contours by the Green Bank Telescope [101]. The map is saturated at 6σ in order to emphasize the diffuse emissions. There may be hints of correlation between H.E.S.S.-II diffuse emission and radio outflows.

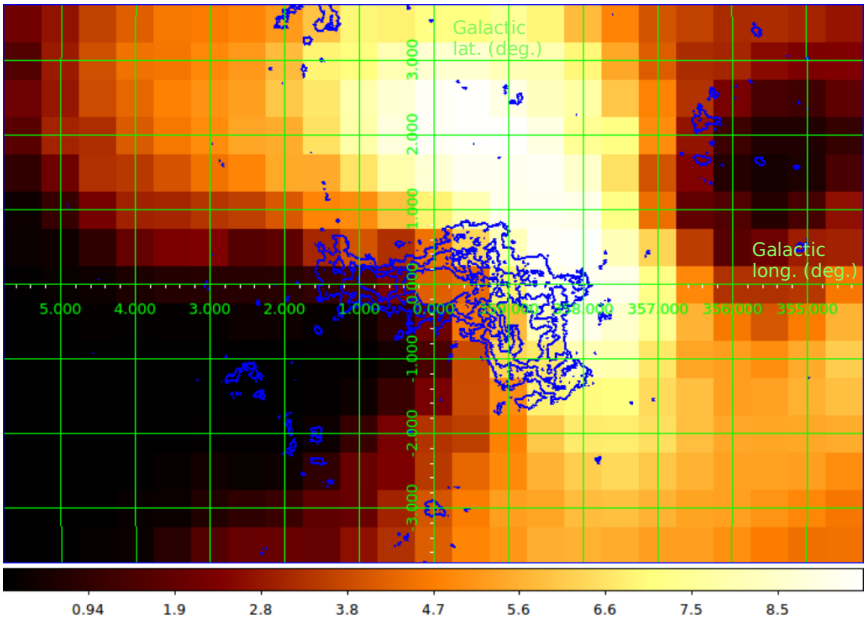

Figure 5.14: Map of low-latitude Fermi Bubble emission detected by Fermi-LAT [89] with overlapped H.E.S.S.-II significance contours at 3σ, 5σ and 7σ. The presence of a VHE asymmetric emission shifted towards the North-West of the GC could be correlated with the Fermi Bubbles. A dedicated analysis is currently carried out in order to search for VHE emission from the Fermi Bubbles with H.E.S.S..

The spectrum scaled for E^2 is given in Fig. 5.15 as function of the reconstructed energy. A fit is performed with a simple power-law (top panel) with index Γ and normalization ϕ_0:

$$\phi(E) = 2\phi_0 \left(\frac{E}{E_0} \right)^{\Gamma} \tag{5.1}$$

and a power-law with exponential cutoff $E_{\rm cut}$ (bottom panel):

$$\phi(E) = 2\phi_0 \left(\frac{E}{E_0} \right)^{\Gamma} \exp\left(-\frac{E}{E_{\rm cut}} \right). \tag{5.2}$$

Parameter	Power-law	Power-law with exp. cutoff
ϕ_0 [TeV^{-1} cm^{-2} s^{-1}]	$(1.88 \pm 0.06) \times 10^{-12}$	$(1.99 \pm 0.07) \times 10^{-12}$
Γ	2.29 ± 0.02	2.21 ± 0.04
E_0 [TeV]	0.46	0.36
$E_{\rm cut}$ [TeV]	–	15.45 ± 7.38
$I(>1\,\text{TeV})$ cm^{-2} s^{-1}	$(1.46 \pm 0.06) \times 10^{-12}$	$(1.45 \pm 0.13) \times 10^{-12}$
χ^2/dof	103.0/55	97.6/54

Table 5.3: Parameters of the simple power-law and power-law with exponential cutoff fits to the H.E.S.S.-II *CT5 Mono* spectrum of Sgr A*. The values of the spectral index Γ, normalization ϕ_0 at the decorrelation energy E_0, the cutoff $E_{\rm cut}$, the integral flux I above 1 TeV and the reduced χ^2 are given.

The parameters of the fits, together with the decorrelation energy E_0, the integral flux I above 1 TeV and the reduced chi-square of the fit are given in Tab. 5.3. This analysis does not allow us to distinguish between the simple power-law and the power-law with exponential cutoff hypotheses. The obtained spectrum is consistent with previous H.E.S.S.-I [70, 39] and preliminary H.E.S.S.-II [127] measurements. The HESS J1745-290 spectrum measured by H.E.S.S. I had been best fitted by a power-law with exponential cutoff with $\Gamma = 2.14 \pm 0.02_{\rm stat} \pm 0.10_{\rm syst}$, $\phi_0 = (2.55 \pm 0.04_{\rm stat} \pm 0.37_{\rm syst}) \times 10^{-12}$ TeV^{-1} cm^{-2} s^{-1} adn $E_{\rm cut} = 10.7 \pm 2.0_{\rm stat} \pm 2.1_{\rm syst}$ TeV. The simple power-law fit of H.E.S.S.-II data from 2013 and early 2014 gave $\Gamma = 2.28 \pm 0.04$ and $\phi_0 = (9.46 \pm 0.31) \times 10^{-12}$ TeV^{-1} cm^{-2} s^{-1}. The full H.E.S.S.-II dataset improves the accuracy of estimation of the parameters of the fit reducing the uncertainties with respect to the 2013-2014 partial H.E.S.S. sample.

5.6 Outlook

The Inner Galaxy Survey is a long-term key-science project. It is expected to give important results in the search for dark matter and for Galactic outflows, like Fermi Bubbles and the

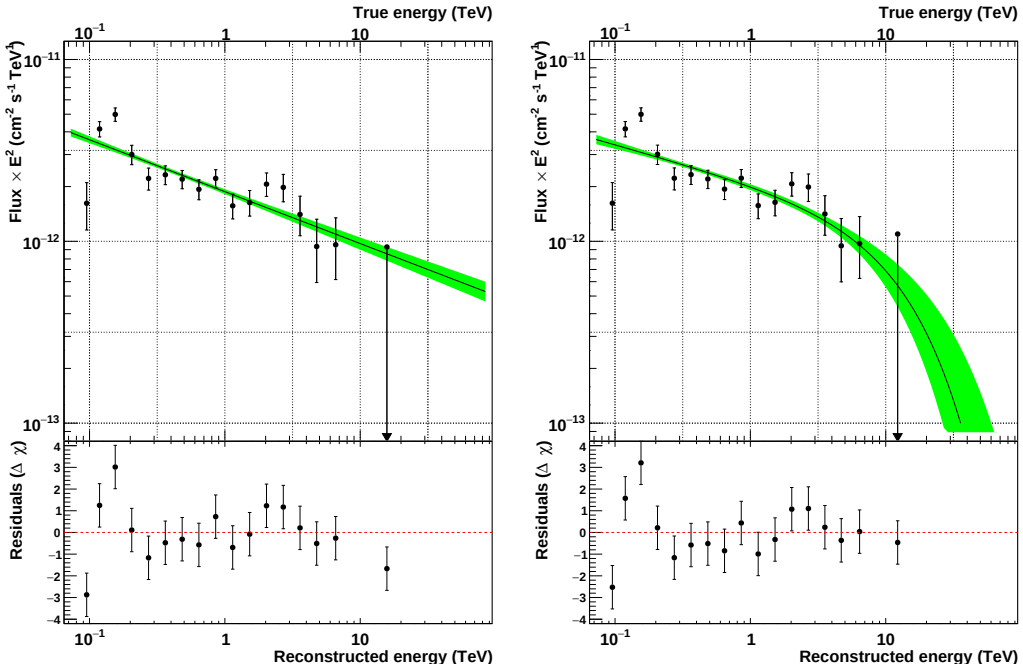

Figure 5.15: Spectrum of Sgr A* with H.E.S.S.-II *CT5 Mono* analysis. The value of the parameters is given in the text.

Galactic Center lobe observed in radio. Improvement in the understanding of the various diffuse emissions in the Galactic Center region is expected thanks to the increased photons statistics, but also thanks to the pointing strategy focused on the large latitudes where Fermi Bubbles are observed up to 1 TeV and where the dark matter Galactic halo extend. Searches for outflows are ongoing in the H.E.S.S. Collaboration. The first H.E.S.S.-II sky maps show a more extended diffuse emission than previously detected with H.E.S.S. I. This emission is only partially correlated to the gas clouds in the Central Molecular Zone. It could be linked to the presence of a Pevatron at the Galactic Center previously detected by H.E.S.S., capable to accelerate non-thermal protons that then escape from the Galactic Center region. An alternative scenario is the presence of a still hypothetical population of millisecond pulsars in the Galactic bulge. A dedicated spectral and morphological study could highlight correlations with other wavelengths observations and reveal faint emissions showing if a TeV outflow correlated with the Galactic Center radio lobe or the low-latitude Fermi Bubbles is present. A deeper study of the diffuse emission could help distinguish the presence of a single PeV protons accelerator or a population of unresolved emitters and on activity in the Galactic Center region that could have caused the ejection of outflows from Sgr A*. A refined spectral and morphological modeling of the standard diffuse emissions in the Galactic Center regions is also expected to increase the H.E.S.S. sensitivity to dark matter in the Galactic Center region as well. The future CTA array foresee to model the background in this region.

Part III

Dark matter quest

Chapter 6

The invisible Universe: Dark Matter

Contents

6.1 From observations to the dark matter paradigm 88
6.1.1 Astrophysical evidences of dark matter 88
6.1.2 The standard cosmological model 90
6.1.3 Cosmological measurements 91
6.1.4 Cosmological parameters and thermal relic density of cold DM particles . 95
6.2 Dark matter candidates 96
6.2.1 MACHOs 96
6.2.2 Non-WIMP particles 97
6.2.3 WIMPs 98
6.3 Issues with ΛCDM and alternative theories 99
6.4 Dark matter detection strategies 99
6.4.1 Direct searches 99
6.4.2 Searches at colliders 101
6.4.3 Indirect searches 102
6.4.4 Complementarity of the detection techniques 104
6.5 Dark matter density distributions at Galactic scale 107
6.6 Astrophysical targets for dark matter search with gamma rays 109
6.7 Gamma-ray flux from dark matter annihilation 111
6.8 Dark matter annihilation spectra in gamma rays 112
6.8.1 Continuum signal 112
6.8.2 Mono-energetic γ line 113
6.8.3 Astrophysical and particle physics signal enhancement 114

This chapter succinctly introduces the dark matter paradigm. Form cosmological measurements, dark matter makes about the 24% of the Universe, and 85% of the total matter content in the Universe. At the galaxy scale, it is required to explain astrophysical measurements such as the rotation curve of galaxies and galaxy cluster dynamics. Interestingly, a new invisible kind of matter can be accommodated by new elementary particles in many extensions of the Standard Model of particle physics as a weakly interacting massive particles (WIMPs). Several techniques have been devised to look for this new particle and the one that covers the range of TeV masses is particularly suited for the indirect search. The strength of a possible dark matter signal depends on the underlying mechanism of the self-annihilation process that gives rise to the gamma-ray spectra and the the DM distribution in the most promising targets.

In Sec. 6.1 we introduce the measurements that lead to the need for dark matter and discuss the implications for the standard model of cosmology, the ΛCDM model. In Sec. 6.2 the main dark matter candidates are presented. The limitations of the ΛCDM and alternative models that do not include dark matter are discussed in Sec. 6.3. In Sec. 6.4 the different techniques for dark matter searches in the form of WIMPs are explained. The expected density distribution of dark matter and the main targets for indirect dark matter search are discussed in Sec. 6.5 and Sec. 6.6. DM annihilation spectra and the expected gamma-ray flux due to dark matter annihilation are presented in Sec. 6.8 and Sec. 6.7.

6.1 From observations to the dark matter paradigm

6.1.1 Astrophysical evidences of dark matter

The "missing mass" problem

The first convincing evidence of the existence of dark matter (DM) is the measurement of the velocity of objects in gravitationally bound systems, that deflects from what is expected assuming only the gravitational interaction of the visible objects. In the '30s Zwicky measured the velocity dispersion of individual galaxies in the Coma cluster [128]. Using the virial theorem he demonstrated that the gravitational potential of the visible galaxies was not enough to explain their rotation curves. He inferred that the mass of the cluster was 400 times larger than the mass obtained from the luminosity of galaxies. This apparent "missing mass" took the name of "dark matter" with the years because associated with invisible, *i.e.* non-luminous, mass. In the '70s measurements of the rotational curves of galaxies by Rubin and Ford confirmed the hypothesis of missing mass [129]. Their measurements of the Andromeda galaxy showed that the velocity of the stars in the galaxy does not behave as $1/\sqrt{r}$ as predicted from Kepler's law, but it stays constant far from the galaxy centre. Assuming the validity of Newtonian gravity this implies that there must be additional invisible matter, a DM halo, centered at the gravitational center of the galaxy

and with mass profile $\propto 1/r^2$. Interestingly, the inner part of galaxy rotation curves is based on measurements of the stellar population, but the outer part can be extended to faint regions beyond the disk at several ten kpc from the center using measurements of the Doppler shift of the 21-cm emission line of neutral hydrogen. An example of the velocity dispersion curve of NGC 3198 [130] as function of the distance from the center of the galaxy is shown in Fig. 6.7. The expected rotation curve based only on the visible matter is marked as "disk". The contribution of the DM halo that reproduces the measurements is labeled as "halo".

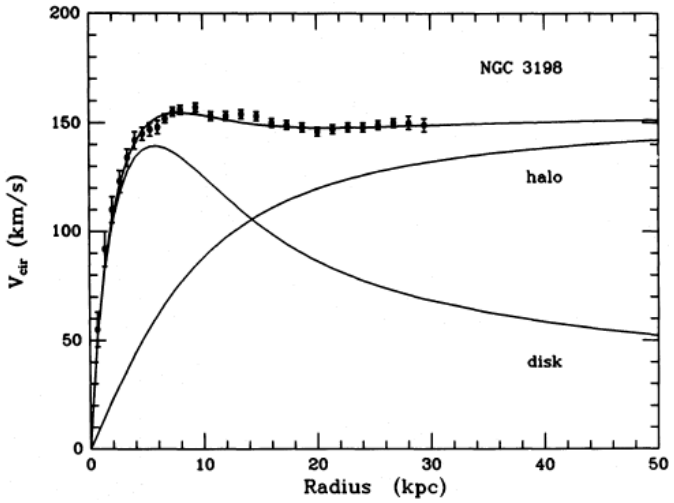

Figure 6.1: Rotation curve of NGC 3198. The measurements (dots) are shown together with the contribution of the visible matter (disk) and the DM halo. Figure extracted from Ref. [130].

Gravitational lensing

Strong lensing Another astrophysical evidence of the existence of DM comes from the gravitational lensing [131] where a distortion of the background light is due to the deformation of the space-time in presence of a gravitating mass, acting as a lens on the background galaxies similarly to optical refraction. This effect is visible in the left panel of Fig. 6.2 in the Hubble observations of the Abel 1689 cluster [132] that distorts the emission of the background objects. The visible mass cannot account for the significant observed bending of light.

Bullet cluster One of the most striking evidences of presence of collisionless DM halos comes from the measurements of the cluster merger E0657-558, known as the Bullet Cluster [133, 134]. The right panel of Fig. 6.2 shows a composite X-ray and optical image of the Bullet Cluster. The hot gas (ordinary matter) is represented in magenta. The mass

Figure 6.2: *Left panel:* Gravitational lensing of the Abel 1689 galaxy cluster produced bu the Hubble telescope. The DM halo of the cluster distort the galaxies in the background. Figure extracted from Ref. [132]. *Right panel:* Composite image of the cluster merger 1E0657-558, known as the Bullet Cluster. Credit: X-ray: NASA/CXC/CfA/ Ref. [133]; Lensing Map: NASA/STScI; ESO WFI; Magellan/U.Arizona/ Ref. [134]; Optical: NASA/STScI; Magellan/U.Arizona/ Ref. [134].

distribution can be estimated thanks to the weak lensing of light that passes close to a massive object. The mass distributions of the clusters reconstructed from weak lensing (dominated by DM) is represented in blue. The composite image shows that the hot gas of the two mergers lags behind the subcluster galaxies and interact, while the two mergers DM component is ahead the collisional gas and coincident with the collisionless galaxies. The Bullet Cluster has been used to constraint the DM self-interaction cross-section down to $\sigma/m < 1$ cm^2 g^{-1} [135].

6.1.2 The standard cosmological model

The standard cosmological model is based on Einstein's equations of general relativity, Friedmann-Lemaître-Robertson-Walker metric [136–139] and Hubble's discovery of the expansion of the Universe. It explains the thermal history of the Universe from the Big Bang, the relic background radiation, the abundance of elements and large scale structures that we observe. Extended reviews of the standard cosmological model can be found for instance in Refs. [140, 141].

Fundamental properties of the geometry of the Universe are homogeneity and isotropy, often referred to as the cosmological principle. The former is confirmed by measurements of the distributions of galaxies on a large scale ($\gtrsim$ 10 Mpc) and the latter from Cosmic Microwave Background (CMB) measurements. Under these hypotheses and the relationship between the geometry of the Universe and its energy content implied by Einstein's

equation [142], Friedmann equations [136, 137] are derived. They write

$$\left(\frac{\dot{a}}{a}\right)^2 + \frac{k}{a^2} = \frac{8\pi G}{3}\rho \tag{6.1}$$

and

$$\frac{\ddot{a}}{a} = -\frac{4\pi G}{3}\left(\rho + \frac{3p}{c^2}\right) + \frac{\Lambda c^2}{3}, \tag{6.2}$$

where G is the Newtonian gravitational constant, k is the curvature of the Universe (-1 for an open hyperbolic space, 0 for a flat space and $+1$ for a closed spherical space), $a(t)$ is the scale factor that parametrizes the expansion of the Universe, Λ is the cosmological constant that represents the vacuum energy that enables an accelerated expansion of the Universe, $\rho = \rho_\mathrm{m} + \rho_\mathrm{r}$ is the sum of the matter and radiation energy densities of the Universe, and p their pressure. The first term takes the name of Hubble parameter $H(t) = \dot{a}(t)/a(t)$[1]. Under the hypothesis of a flat Universe, the total density $\rho_\mathrm{tot} = \rho + \rho_\Lambda$ today equals the critical density $\rho_\mathrm{c} = \frac{3H^2}{8\pi G}$, with $\rho_\Lambda = \Lambda/(8\pi G)$. The total density is the sum of all the kind of matter and radiation that fill the Universe. The density of each component ρ_i is defined as a fraction of the critical density in terms of the density parameter $\Omega_\mathrm{i} = \rho_\mathrm{i}/\rho_\mathrm{c}$. The first Friedmann equation can be rewritten in terms of the present values of the density parameters, *i.e.* the relic density of matter, radiation and vacuum energy, as

$$\frac{H^2(z)}{H_0^2} = \Omega_\mathrm{r}(1+z)^4 + \Omega_\mathrm{m}(1+z)^3 + \Omega_\mathrm{k}(1+z)^2 + \Omega_\Lambda, \tag{6.3}$$

where $\Omega_\mathrm{k} = -k/H_0^2$ and the scale factor is related to the redshift by $a(t) = 1/(1+z)$. Cosmological measurements indicate that most of the matter is not made of baryons but of cold DM, *i.e.* $\Omega_\mathrm{m} = \Omega_\mathrm{b} + \Omega_\chi$ with $\Omega_\chi \gg \Omega_\mathrm{b}$. The fact that the DM density parameter behaves more like $\Omega_\chi a^{-4}$ than a^{-3} tells us that DM is a particle-lie component rather than radiation. The standard cosmological model, including dark energy and DM, takes then the name of Lambda-cold-dark-matter (ΛCDM) model.

6.1.3 Cosmological measurements

Cosmic Microwave Background

In the early Universe photons and baryons formed a plasma in thermal equilibrium and in which free electrons could move. Then at the recombination epoch the Universe cooled down to a temperature (~ 3000 K) such that neutral hydrogen formation was favored. Most of the neutral hydrogen was produced in excited states and photons were emitted during the transition to the bound state. The Universe became transparent and photons started to stream freely. This is called the decoupling era and the liberated photons, fossil light

[1]The value of the Hubble parameter nowadays [143] is $H_0 = H(t_0) = (67.4 \pm 0.5)$ km s^{-1} Mpc^{-1}, measured by Planck.

of the Big Bang, are the so called Cosmic Microwave Background (CMB). The CMB was accidentally detected in 1964 with the radio telescope at Bell Labs [144]. Measurements of CMB today provide the relic temperature of the Universe of T=2.725 K [145]. Measurements performed in the '90s detected anisotropies in the CMB [146] at the level of 16 ± 4 μK. Baryon density is directly related to the CMB temperature. Areas with high density correspond to cold spots in the CMB map and under-densities correspond to warm ones. The power spectrum of CMB temperature as a function of the multipole moment is shown in Fig. 6.3. Odd peaks correspond to compressions determined by radiation pressure and baryon gravitation potential (larger for large masses) while even peaks correspond to decompression driven only by the pressure. This means that in case of large baryon density the odd peaks would increase in height relative to the even peaks. Thus, the relative amplitude of the second peak with respect to the first one provides a measurement of $\Omega_{\rm b}$.

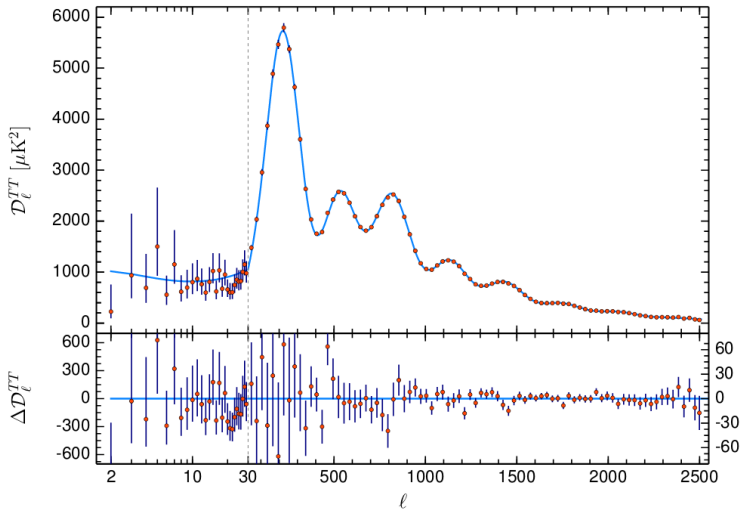

Figure 6.3: Planck 2018 CMB angular power spectra as function of the multipole moment, fitted with the ΛCDM prediction. Figure extracted from Ref. [143].

Baryonic Acoustic Oscillations

The most important features from the anisotropy of the CMB come from the baryon acoustic oscillations (BAOs) in the photon-baryon fluid detectable today. In the early Universe in the primordial plasma, due to the interplay between the baryonic gravitational potential and radiation pressure, relativistic acoustic waves were formed. In fact, under the influence of radiation pressure, at the position of initial overdensities, the baryon-photon fluid propagated outward from the density as an expanding spherical shell at the speed of sound. Then, at the recombination epoch the acoustic waves froze, when the baryons did not feel anymore the radiation pressure and spherical baryonic shells remained standing

around the central DM overdensities. The comoving radius of the spherical shell of baryons is very close to the comoving sound horizon at recombination r_s. This means that BAOs are standard rulers for the horizon size, *i.e.* the geometry of the universe. The baryonic and DM density evolve together, driven by gravity, and nowadays galaxies are more likely to be observed with a separation r_s, corresponding to a peak at r_s in the matter density profile. The BAO scale cannot be obtained by the measurement of a single object in the sky. The density profile is the result of many perturbations, *i.e.* of a statistical measurement of the correlation between the position of large scale structures in the Universe. In absence of DM the perturbations would have been washed out and no characheristic correlation scale would be observed nowadays. A review of BAOs is given in Ref. [147].

Type Ia supernovae

Type Ia supernovae can be used as standard rulers of the distance of objects in the Universe. They are standard candles since at the moment of explosion they have a standard luminosity curve. Their apparent magnitude depends almost exclusively on their distance. Once the distance of their host galaxy is known, the measurement of the redshift due to the expansion of the Universe can be measured [148]. This measurement is used to put constraints on $a(t)$ and consequently the value of the relic densities in the ΛCDM.

Big Bang Nucleosynthesis

The determination of baryons abundance is related to the process of primordial nucleosynthesis [149], or Big Bang nucleosynthesis, that consists in the creation of the chemical elements at early phases of the Universe after the Big Bang. During the first tens of minutes after the Big Bang, when the Universe was still hot, nuclear reactions formed mainly the light elements: ^{4}He, D, ^{3}He and ^{7}Li. Their abundances are widely accepted to measure ^{4}He/H$\sim$ 0.1, ^{3}He/H$\sim$D/H$\sim 10^{-5}$ and ^{7}Li/H$\sim 10^{-10}$. The abundance of the light elements depends on the baryon-to-photon ratio η which is constrained to a range $5.1 \times 10^{-10} < \eta < 6.5 \times 10^{-10}$. The abundance of baryonic matter depends on η and results about five times smaller than the DM abundance. It measures $\Omega_b h^2 = 0.0224 \pm 0.0001$ [143] and it accounts for about the 5% of the critical density. The missing 95% of the Universe is 70% dark energy and 25% DM. The baryon nucleosynthesis is one of the main proofs of the validity of the ΛCDM.

Structure formation

The amplification of primordial density fluctuations due to the expansion of the Universe leads to the hierarchical formation of structures [150]. Experimentally, the measurement of distribution of luminous objects in the Universe can characterize the formation of large scale structures and relate it to the characteristics of the observed objects. Surveys that

combine the measurement of the redshift and the angular position of astronomical objects can map the distribution of matter in a portion of the sky. The 2dF Galaxy Redshift Survey (2dFGRS) [151] at the Anglo-Australian Telescope mapped the optically luminous galaxies in a statistically representative volume of the Universe. More recently the Sloan Digital Sky Survey (SDSS) [152] produced the most detailed three-dimensional map of the Universe ever made that covers one third of the sky, using multi-spectra with deep multi-color images in ultraviolet, green, red and infrared. The comparison between the structure distribution observed nowadays and the simulated one from the growth of cosmic fluctuations in the near-uniform early Universe can be made.

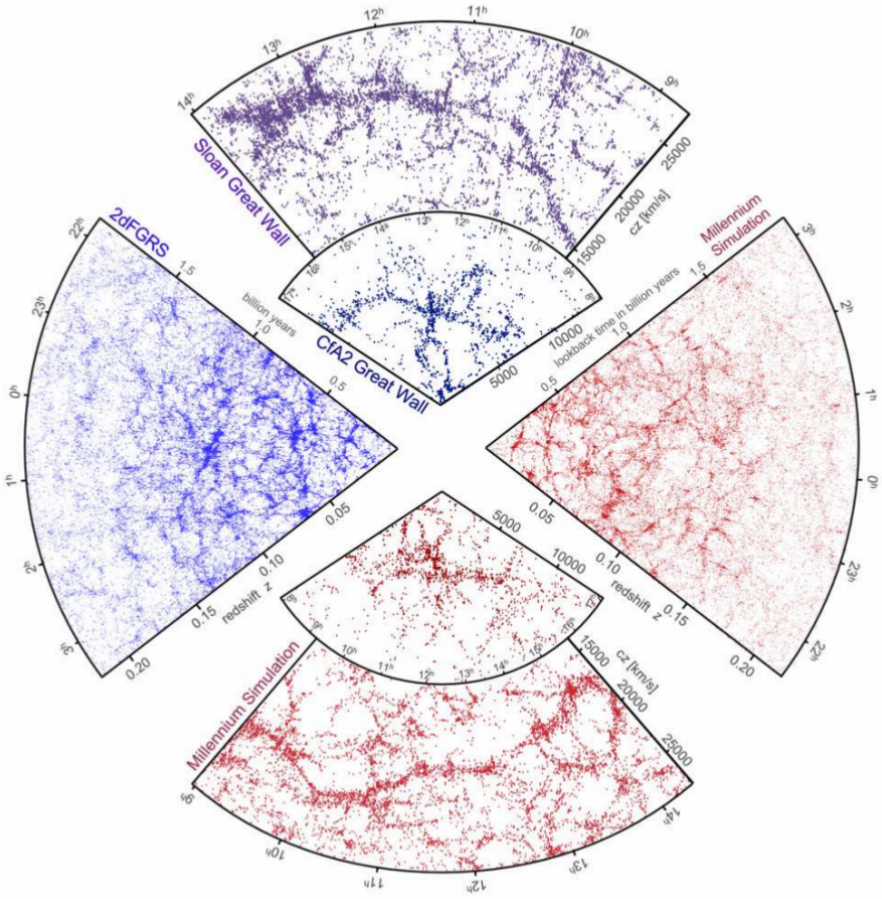

Figure 6.4: Maps of part of the 2dF Galaxy Redshift Survey (left panel) and Sloan Digital Sky Survey (top panel) and maps obtained with the Millennium simulations for the corresponding portions of the sky (right and bottom panels, respectively). Figure extracted from Ref. [153].

In the models gas dynamics, radiative cooling, photoionization, recombination and radiative transfer cannot be treated analytically. Therefore the formation of structures is studied through complex N-bodies numerical simulations in a large box of space. In the initial conditions nearly uniform matter density is set with small inhomogeneities. The

perturbations are simulated accordingly to the measured CMB temperature power spectrum and the equations that govern the Universe expansion, matter (baryon and DM) gravity, baryonic gas pressure forces and dark energy[2] are injected. The system evolves and gravity makes the fluctuations evolve. In the regions with initial high density matter collapses forming DM halos and galaxies. An example of simulations of the formation of large scale structures, clusters and groups of galaxies and their evolution can be found in Ref. [154]. Filaments become more prominent over time, clusters form at intersections of filaments. The growth of structures slows down at redshift below about 1 because gravity becomes subdominant and the acceleration is dominated by the dark energy. Low mass objects are formed first and then merge into bigger ones. The simulations show that hot DM would have not allowed the nowadays observed distribution of galaxy-scale structures. The initial structure simulations included only DM and predicted very cuspy profiles, in tension with some observations at galactic scales. The presence of baryons tends to flatten the inner part of the halos.
Fig. 6.4 shows part of the 2dFGRS and SDSS maps in the left and top panels, respectively. In the opposite panels mock galaxy surveys produced by the Millenium simulations [155] are shown. They are constructed using semi-analytic techniques to simulate the dark matter distribution and the structure formation, and matching the geometry and magnitude limits of the experimental surveys. The simulations and measurements are in striking agreement when a dominant component of non-baryonic dark matter in the matter content is included. Baryon-only induced fluctuations in the early universe would not allow to reproduce the observed structure distribution today. Prominent structures like the observed Sloan Great Wall (visible in the top panel of Fig. 6.4) are found also in the simulations (see bottom panel).

6.1.4 Cosmological parameters and thermal relic density of cold DM particles

In the expanding Universe each particle component is at the beginning in thermal contact with the others and evolve with time [156]. They are in thermal equilibrium until the epoch when their number density n decreases thus reducing the interaction rate $\Gamma = n\sigma v$, dependent on the particle velocity v and its cross section σ, as expected from the Boltzmann decrease. As the universe expands, below scale determined by the Hubble parameter (which has dimension 1/time), the particles cannot efficiently annihilate anymore. This phenomenon of decoupling takes place at the epoch called the freeze-out when the particles do not interact in the time scale of expansion of the Universe $\sim H^{-1}$. After that moment the abundance of the decoupled particles remains constant and takes the name of relic density. The decoupling takes place at different epochs for particles with different mass which undergo different

[2]Only recently baryons are being included in simulations because they make them even more complex. There is so far no consensus on how to include their physical processes in the simulations.

interaction processes. For cold (*i.e.* non-relativistic) weakly interacting DM particles the thermal relic density is approximately [157]

$$\Omega_\chi h^2 \approx \frac{3 \times 10^{-27}\,\mathrm{cm}^3\,\mathrm{s}^{-1}}{\langle \sigma v \rangle}. \tag{6.4}$$

Recent Planck measurements [143] provide the relic density values for each component and are summarized in Tab 6.1.
Following Eq. (6.4), the measured $\Omega_{CDM}h^2$ value implies that the thermal relic cross section, *i.e.* the thermally averaged velocity weighted annihilation cross section of DM thermally produced in the early Universe, measures $\langle \sigma v \rangle \sim 3 \times 10^{-26}$ cm^{3} $^{-1}$.

Parameter	Symbol	Value
Hubble constant	$H_0 = 100h$ [km s^{-1} Mpc^{-1}]	67.4 ± 0.5
Cold DM density	$\Omega_{\mathrm{CDM}}h^2$	0.120 ± 0.001
Baryon density	$\Omega_{\mathrm{b}}h^2$	0.0224 ± 0.0001
Matter density	$\Omega_{\mathrm{m}} = \Omega_{\mathrm{b}} + \Omega_\chi$	0.315 ± 0.007
Curvature	Ω_{k}	0.001 ± 0.002
Vacuum energy density	$\Omega_\Lambda h^2$	0.3107 ± 0.0082
Cosmological constant	Λ [ev^2]	$(4.24 \pm 0.11) \times 10^{-66}$

Table 6.1: Latest values of the cosmological parameters measured by Planck [143].

6.2 Dark matter candidates

The nature of DM is still unknown. There are three main categories of DM candidates: non-luminous astrophysical objects, Weakly Interacting Massive Particles (WIMPs) and non-WIMP particle candidates.

6.2.1 MACHOs

Astrophysical candidates for DM are the massive astrophysical compact halo objects (MACHOs), that are made of standard baryonic matter that emit no or low radiation. Black holes, neutron stars, brown dwarfs and free-floating planets can be MACHOs. However, their density could account only for a small part of DM as longtime argued [158]. Promising candidates of this category are the primordial black holes (PBHs) created in the early Universe [159] in the radiation-dominated era. PBHs with mass between 10^{-7} and 10 solar masses are excluded from providing the DM [160]. The mass ranges at which PBHs can still provide the DM are the asteroid mass range $10^{16} - 10^{17}$ g, the sublunar mass range $10^{20} - 10^{26}$ g and the intermediate mass black hole range $10 - 10^3$ solar masses [161]. These

objects are mainly looked for through gravitational microlensing [131], *i.e.* a transient amplification of the flux from a background star whose light is bended at the passage near a compact object. Interestingly, the possibility that the black-hole binary detected by LIGO could shed light to a new, and till now overlooked, component to DM has been studied [162], since PBH mergers have no optical or neutrino counterpart so far and are expected to be spatially distributed like DM. However, for a satisfiying explanarion of DM nature MACHOs alone are not satisfying. In alternative, numerous particle DM candidates can explaine the totaly of DM present in the Universe.

6.2.2 Non-WIMP particles

Neutrinos

In the late '70s standard left-handed neutrinos with mass up to a few eV came out as a natural hot DM candidate [163]. Hot DM implies a top-down formation scenario with superclusters formed first and fragmented into smaller structures. This scenario is now obsolete because it cannot properly reproduce the measured distribution of galaxies. In a bottom-up formation scenario neutrinos are wiped off before being able to form the large scale structures.

Adding a regular Dirac mass term in the standard model (SM) to account for neutrino oscillations introduces right-handed neutrinos. Sterile neutrinos [164] are hypothetical leptons that interact only gravitationally and not via weak interaction (from which the name "sterile"). Besides the three left-handed SM active neutrinos that interact with the W and Z bosons, there are four (or more) right-handed sterile neutrino states that do not interact with the electroweak bosons. The mass of the sterile neutrinos is not well defined and could be between 1 eV and 10^{15} GeV[3]. Sterile neutrinos with eV masses are used in the context of neutrino oscillation anomalies and dark radiation, GeV-TeV sterile neutrinos are used for tests of baryogenesis theories, while sterile neutrinos in the keV mass range are a good candidate for warm DM [166, 167]. keV neutrinos could explain the formation of large scale structures [168].

Axions and axion-like particles

Axions are particles that have been first introduced to solve the problem of absence of CP violation in strong interaction, predicted in Quantum Chromodynamics (QCD) for non-zero quark masses. They are the pseudo-Nambu–Goldstone bosons that arise from the Peccei-Quinn solution to the strong CP problem [169]. This solution introduces a $U(1)$ approximate global symmetry spontaneously broken at a scale f_{a} roughly located around 10^{12} GeV. Axions coupling to standard matter is $\propto 1/f_{\mathrm{a}}$. Axions are neutral,

[3]For the seesaw mechanism if the left-handed neutrinos have small masses the right-handed ones must have large masses and vice versa [165].

weakly-interacting bosons, so they are a good candidate for DM. They are very light, but a non-relativistic (cold) axions population could be produced out of equilibrium [170]. In addition to axions, the spontaneous high scale breaking of an approximate U(1) symmetry can generate axion-like particles (ALPs). ALPs are not linked to QCD so their mass and coupling to standard matter are independent parameters and are therefore less constrained experimentally. A review of the search for axions and APL can be found in Ref. [171].

6.2.3 WIMPs

DM is likely made out of particles that should have with the following characteristics: non-baryonic, electromagnetically neutral, color neutral(-ish), massive (gravitationally attractive), with a lifetime larger than the age of the Universe, and able to reproduce the measured relic density, and form the observed structures in the present-day universe. Among the most promising DM candidates are the Weakly Interacting Massive Particles (WIMPs).

WIMPs are predicted in a supersymmetric (SUSY) extension of the standard model (SM) [172]. These particles reproduce naturally the relic density[4]. In SUSY for each particle a supersymmetric partner that differs of a half-integer spin exists. Every boson has a supersymmetric fermion partner and vice versa. For example for each quark there is a squark. Candidates for WIMP are the superpartners of the bosons. In SUSY the proton is allowed to decay through the process $p \to e^+\pi_0$ with a timescale rejected by observations. To circumvent this problem a new discrete symmetry is introduced, the R-parity, which is conserved and prevents the proton to decay. It is defined as $R = (-1)^{2S+3B+L}$, where S is the spin, B is the baryon number and L the lepton number of a particle. SM particles have $R = 1$, while SUSY particles have $R = -1$. An important consequence of R-parity is that the lightest supersymmetric particle (LSP) is stable, since it cannot decay into SM particles with opposite R. The LSP makes a good DM candidate, in particular the lightest neutralino. It is the lightest mixture of the fermionic partners of the neutral Higgs boson and neutral electroweak gauge bosons. The superpartner of the Higgs boson is the Higgsino. The superpartners of the electroweak gauge bosons are the Wino, superpartner of the W boson, and the Bino, superpartner of the gauge boson of the U(1) gauge field corresponding to weak hypercharge. The neutralinos are Majorana fermions, so they are identical to their antiparticles and can self-annihilate. They also interact with the weak vector bosons. Heavy neutralinos can decay through Z boson to the lightest neutralino. This decay is then invisible in a detector, it corresponds to a missing momentum in the final state of the interaction. The mass of the WIMP candidates can be constrained by the thermal relic density. The mass needed to reproduce the relic density and thermal relic cross section is usually referred to as thermal mass. For a pure Wino candidate it is expected to be $2.7 - 2.9$ TeV [173],

[4]This characteristics is often referred to as WIMP miracle, since SUSY was not developed in order to explain DM, but the WIMP DM candidate appeared naturally.

while for the pure Higgsino it is 1 TeV [174]. This is the mass range that can be probed by gamma-ray telescopes through indirect DM search as shown in Sec. 6.4.

Alternative DM candidates to SUSY particles are Kaluza-Klein (KK) particles. These elementary particles appear in theories of a multidimensional Universe [175], where the $3+1$-dimension Universe is a *brane* embedded in a $3+\delta+1$-dimension space-time called *bulk*. KK particles are states that propagate between the small extra-dimensions and, like the superpartners in SUSY, are partners of SM particles, but in this case with same spin. Similarly to the case of R-parity in SUSY, a new discrete KK-party is introduced. The Lightest KK Particle (LKP) is a good DM candidate in alternative to the LSP [176].

6.3 Issues with ΛCDM and alternative theories

The ΛCDM gives a satisfying explanation to most of the cosmological and astrophysical measurements that confirmed the existence of DM. However, some issues arise at small scales. For example on a small size scale it may fail to reproduce the measured DM density at the center of galaxies [177]. Including baryons in the simulations may weaken the disagreement, while their impact is still under debate. In addition the N-body simulations predict the formation of small-scale substructures in the DM halos and the presence of many galaxy satellites. This prediction is not in agreement with measurements, that count a number of dwarf galaxies about an order of magnitude smaller than in the simulations [178]. Considering the increasing detection of ultra-faint dwarf galaxies in the last few years it is possible that these small halos exist and are not easy to detect, the lightest being not massive enough to trigger star formation. On the other hand, they could have been destroyed by tides caused by the interaction with more massive halos.

Due to the difficulties encountered by the ΛCDM at the galaxy scale, some theories are developed that do not include DM but can explain some of the observations that lead to the prediction of the existence of DM, in particular the dynamics of stars in galaxies. These theories suggest that the Newton's law of gravity should be modified. They are usually referred to as MOND (Modified Newtonian Dynamics) [179]. MOND can be satisfactory at the Galactic scale, but has limitations at galaxy cluster and cosmological scales. Many modified gravity theories have been ruled out by the precise measurement of the speed of GWs compared to the speed of light [180].

6.4 Dark matter detection strategies

6.4.1 Direct searches

Direct DM search refers to the detection of DM particles χ that directly interact with standard matter particles X in a process of the type $\chi X \to \chi X$. The measured quantity is the recoil of the nucleus of a target material with which galactic WIMP interacts through

elastic scattering. The signal rate depends on the DM mass and the interaction cross section between DM particles and the target, but also on the local density[5] and velocity distribution of DM in the Milky Way, a quantity known with large uncertainties. The nuclear recoil energy spectrum [181] reads $\mathrm{d}R/\mathrm{d}E_\mathrm{R} \approx R_0/(E_0 r)\mathrm{e}^{-E_\mathrm{R}/E_0 r}$, where E_R is recoil energy, E_0 is the kinetic energy of the incoming DM particle, R is the event rate per unit mass, R_0 is the total event rate and r is the kinematic factor $r = 4m_\mathrm{DM}m_\mathrm{T}/(m_\mathrm{DM}+m_\mathrm{T})^2$ for a nucleus of mass m_T and a DM particle of mass m_DM. By measuring R at E_R the DM signal rate (contained in R_0) can be constrained and for a fixed m_DM this translates into limits on the elastic-scattering cross section of DM off nucleons. Assuming a Galactic velocity of the order of $10^{-3}c$ and DM with mass between 10 GeV and 1 TeV, the expected recoil energy would be in the range 1-100 keV.

The expected differential rate at Earth is about 1 event keV^{-1} kg^{-1} d^{-1} [181]. Since the recoil event is very rare, a major difficulty of direct detection is background rejection, the second challenge is to lower the threshold in order to gain sensitivity to low-mass DM. Reducible background that can be discriminated from DM recoil is the electron recoil from gamma-ray background external to target, contamination inside the detector or elastic scattering of solar neutrinos off electrons. This kind of background can usually be discriminated based on the pulse shape. An additional background, more difficult to distinguish from DM recoil and sometimes irreducible is the nuclear recoil from fission, alpha particles recoil, interaction with neutron from atmospheric muon spallation or coherent neutrino-nucleus scattering. The external radiogenic and cosmogenic backgrounds are partially rejected using shields and locating the detectors underground. The choice of low-background materials is also crucial.

The requirement of large mass targets, low E_R threshold, low background and good discrimination between nuclear recoil and electron recoil is challenging. Numerous detectors have been built that use different materials and detection technique and are sensitive to different DM mass ranges. For example liquid noble targets are large target with low background while cryogenic crystal targets have low E_R threshold and high energy resolution.

Most of the experiments of direct detection are based on scintillation, ionization or low temperature phonon techniques or a combination of them. Examples are the liquid argon and xenon detectors like Darkside and XENON that use both ionization and scintillation techniques, the NaI(Tl) scintillator DAMA/LIBRA, the cryogenic germanium and silicon detectors SuperCDMS and EDELWEISS and the tellurium bolometer CUORE. There are experiences like DAMA/LIBRA that look for an annual modulation of the count rate, due to the variation of the distance between the detector and the center of the Wilky Way, depending on the motion of the Earth around the Sun. Peaks of counts are expected in correspondence of peaks of relative velocity, in June. A significant signal observed by DAMA [183] has been strongly constrained by other experiments.

[5] Give the value and comment to GAIA results on the local densitey value, see pMSSM paper references.

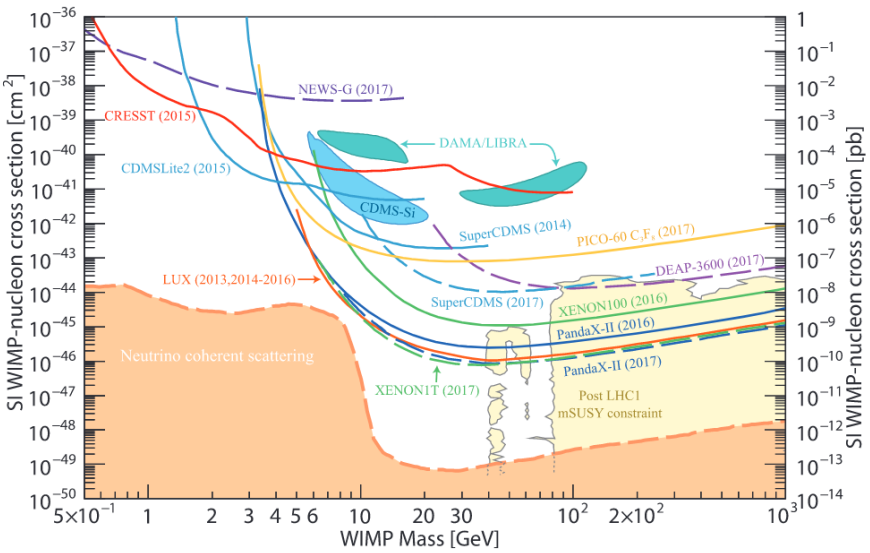

Figure 6.5: Summary of direct detection constraints on the spin-independent WIMP-nucleon elastic cross section. The orange line represents the neutrino floor corresponding to the neutrino-nucleus elastic cross section. Figure extracted from [182].

Fig. 6.7 summarizes the actual constraints on the spin-independent WIMP-nucleon cross section from direct DM search. The observed constraints are getting closer to the coherent elastic neutrino-nucleus scattering cross section, called the neutrino floor [184]. This is an irreducible background for direct DM detection, but some models below the neutrino floor can be probed by indirect detection (see Sec. 12.3). A review of direct DM searches can be found in Ref. [182].

6.4.2 Searches at colliders

The collider DM searches refer to the production of DM particles through interaction of accelerated SM particles, in a process $XX \to \chi\chi$. The LHC with Run 2 and proton-proton (pp) collisions at center of mass energy of 13 TeV had the statistics and luminosity to lead very constraining DM searches. No DM particle candidate was detected so far and stringent limits have been set on specific DM models. If a DM particle is produced in the *pp* collision it cannot be observed directly, its most straightforward signature will be missing energy [185]. In beyond the Standard Model (BSM) theories that include a single DM particle and no additional BSM particle, the mediators of the SM-DM interaction can be the Z boson or the Higgs boson (portal models). Models that include a new BSM particle also as a mediator, like a heavier version of SM particles, are more complex. If the mediator is heavy compared to the collision energy, the interaction between DM and SM matter is a contact interaction and simplified models can be used, through effective field theories (EFTs) [186] that reduce the assumptions on the DM particle and its properties, like its

coupling to the SM. Otherwise, knowing that the mediator will likely decay into the SM partons that created it, some simplified model scenanrii can be developed, that describe the visible physics in the final state and not the additional invisible physics at energies higher than the collider scale [187]. Less simplified models are used to describe specific channels adding the information about their specific features and signatures.

Some benchmark channels for DM search at LHC are:

- the production via the Z boson and invisible decay that has for signature very large missing transverse momentum and eventually a single photon from initial state radiation (ISR),
- the production via the Higgs boson and decay into a couple of Z boson that then decay invisibly,
- more general heavy-invisible-particles decays mediated by the Z or Higgs boson with signature missing energy and ISR, like the mono-jet or the mono-Higgs,
- in addition mediators can be produced together with two top or bottom quarks producing multi-jets besides missing energy,
- more complex specific channels of production of SUSY particles as well as missing transverse momentum,
- displaced decay vertexes produced by the decay of long-lived particles (LLP) or more complex signatures due to LLP that decay only in the external subdetectors (calorimeters and muon spectrometers).

To be noted that colliders themselves cannot fully claim discovery of DM without confirmation from direct or indirect searches, but they can discover the existence of new particles beyond the SM.
Fig. 6.6 shows a summary of a selection of constraints obtained by ATLAS and CMS on specific DM models. Constraints from direct DM search are shown for comparison. A review of DM searches at colliders can be found in Ref. [188].

6.4.3 Indirect searches

Indirect DM model independent search refers to the detection of the secondary SM particles produced by DM self-annihilation[6] in a process $\chi\chi \to XX$, where X could be a photon, a neutrino, a hadron or a lepton. Depending on the final state different instruments have been built to detect it.

The advantage of gamma rays as probe for DM annihilation is that they are not deviated by the magnetic fields. Thus they point back to their source and gamma-ray telescopes

[6]SM particles can be produced also by DM decay on a cosmological times scale through the process is etc.

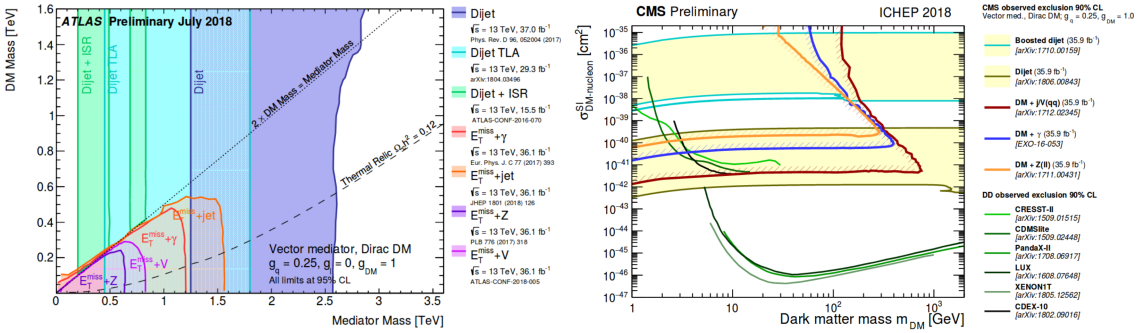

Figure 6.6: Summary of collider DM searches with ATLAS and CMS in specific models. *Left panel:* 95% C.L. ATLAS constraints in the DM mass vs mediator mass region. The dashed line indicates the mass combinations that are consistent with the relic DM density measurements for a standard history of the Universe. *Right panel:* 95% C.L. CMS constraints on the spin-independent DM-nucleus cross section as function of DM mass. Constraints from direct searches are also shown. Figures extracted from [188].

can be used to points towards the most DM-dense regions of the Universe. However, they suffer from the large astrophysical background. In addition the gamma-ray spectrum is attenuated by interaction with the EBL that limits the distance that can be probed with gamma rays to about z=1. Indirect DM search with gamma-ray telescopes is described more in details in what follows.

Like gamma rays neutrinos do not deviate from the direction of their source. In additon, they do not interact much during the travel, reaching far distances. They interact only weakly with matter so indirect search with neutrino telescopes are performed by under-water and under-ice large-size experiments such as ANTARES and IceCube. This ensures that the detected muons are actually produced by cosmic neutrinos and not by background sources. Neutrinos can be produced in prompt DM annihilation, but can also be obtained as secondary product from the decay of leptons (an antileptons) in the final state. In addition DM can annihilate into couples of gauge bosons, that decay into leptons and subsequently into neutrinos. In case of the neutral Z gauge boson the decay can directly take place into neutrinos. A clean channel for indirect DM search with neutrinos is also the multiple scattering of DM with solar nuclei when traversing the Sun and eventually captured inside. The DM particles annihilates inside the Sun producing SM particles that decay into neutrinos. The neutrinos are them able to escape the Sun and reach Earth [189, 190]. A disadvantage is the low detectability of neutrinos.

Indirect searches with charged CRs are performed by experiments like the satellite detectors AMS and PAMELA, through measurements of the flux of electrons, protons and their antiparticles. Unlike neutrinos and photons, charged CRs are bent in Galactic magnetic fields at GeV energies. So they are isotropically distributed and do not give information about the direction of their source, excepted for the very local ones. Thus,

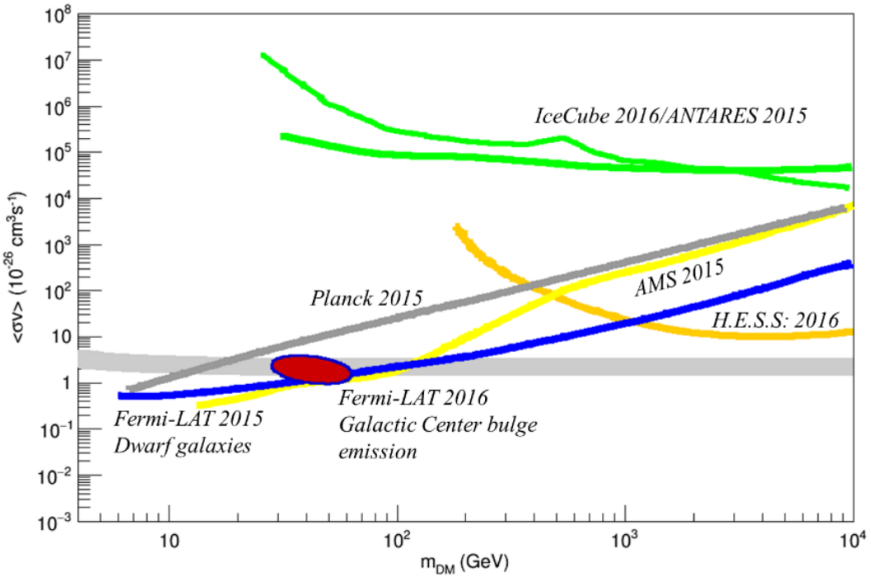

Figure 6.7: Summary of indirect detection constraints on WIMP self-annihilation cross section. The gray line is the thermal relic cross section, which represents the natural annihilation scale for thermally produced WIMPs. Figure extracted from [191].

they are not searched by pointing towards the region of largest DM density, but looking for an overall excess of positrons and antiprotons with respect to those expected by standard astrophysical processes. An advantage of antimatter is the low background. An excess of positrons have been measured by PAMELA [192] and later confirmed by AMS-02 [193] with higher precision and in a wider energy range. Their measurements are in agreement with a DM interpretation [194] while they could also be very likely explained by standard astrophysical processes like acceleration of CRs in pulsars [195]. A possible DM scenario should be confirmed by other experiments and measurements of the flux of antiprotons and gamma rays. An excess of antiprotons has been observed in AMS data [196]. This could be a hint of DM with mass of $40 - 130$ GeV and thermal annihilation cross section. However, the results are strongly affected by systematic uncertainties on the CR propagation in the ISM. Fig. 6.7 summarizes the constraints from indirect DM search with different secondary SM particles. A review of indirect DM searches can be found in Ref. [191].

6.4.4 Complementarity of the detection techniques

Now that each different detection technique is improving significantly and tightly constraining the dark matter parameter space in the hundred GeV mass range, the complementarity about the different detection techniques is becoming more and more important. TeV DM masses cannot be easily reached by colliders due to limited center-of-mass energy as well as

by direct detection because of the lower number density of DM particles that correspond to larger DM masses. This further motivates the indirect detection that can probe the TeV mass regime.

Direct detection constraints are now approaching the challenging region of the neutrino floor. On the other hand, indirect detection faces challenges with the contamination from standard astrophysical emissions. While the local DM density is known within a factor of two, indirect detection is affected by the limited knowledge of the DM density distribution in the targets. Production of DM particles at collider can provide measurement of the fundamental properties like the spin and the couplings that are not accessible to indirect detection. However, the discovery of a new particle DM candidate at a collider needs a confirmation with direct/indirect detection techniques to assess that the new particle is actually the DM in the Universe.

In order to compare direct, indirect and collider search results the physics of the underlying DM interaction must be known to some extent. This is done in a model-dependent way through effective field theories (EFTs) and simplified models [197]. The EFT framework can be used when the center-of-mass energy of the interaction is small with respect to the mass of the mediator which is integrated out leaving the DM particle as the only degree of freedom. When the EFT framework cannot be applied, as it is often the case at LHC, approaches based on simplified models are used, that introduce also the mediator properties in the calculations. Simplified models make use of specific Feynman diagrams making assumptions on the nature of the mediator and its couplings to DM and SM particles. Constraints are set at colliders in the parameter space of the mediator mass vs DM mass and can be translated into constraints on the DM annihilation cross section or DM-nucleon scattering cross section [198] without additional assumption. Fig. 6.8 shows results obtained by CMS with 13 TeV proton-proton collisions. The simplified model used for the interpretation includes a pair of Dirac fermion DM particles in the final state that couple to a mediator that can be vector, axial-vector, scalar or pseudoscalar. The left panel compares direct detection and collider searches assuming a scalar mediator. Below about 10 GeV, the collider contraints surpass the direct detection ones by orders of magnitude. The right panel compares indirect detection and collider searches assuming a pseudoscalar mediator. Here, the collider constraints vanishes above about 200 GeV and the indirect detection constraints become relevant.

With EFTs, the constraints on the DM annihilation cross section $\langle \sigma v \rangle$ can be translated into constraints on the EFT scale M_* [197], a scale that describes the strength of the interaction, as function of the DM mass. Four cases are considered depending on the nature of the mediator: scalar ($\mathcal{O}_S$), pseudo-scalar ($\mathcal{O}_P$), vector ($\mathcal{O}_V$) or axial-vector ($\mathcal{O}_A$) operator. The operators $\mathcal{O}_P$ and $\mathcal{O}_A$ are suppressed by the spin of the target nucleus or the scattering momentum exchange. The operators $\mathcal{O}_S$ and $\mathcal{O}_P$ are suppressed by a Yukawa coupling for consistency with the principle of minimal flavor violation. Indeed, $\mathcal{O}_S$ suppresses the indirect

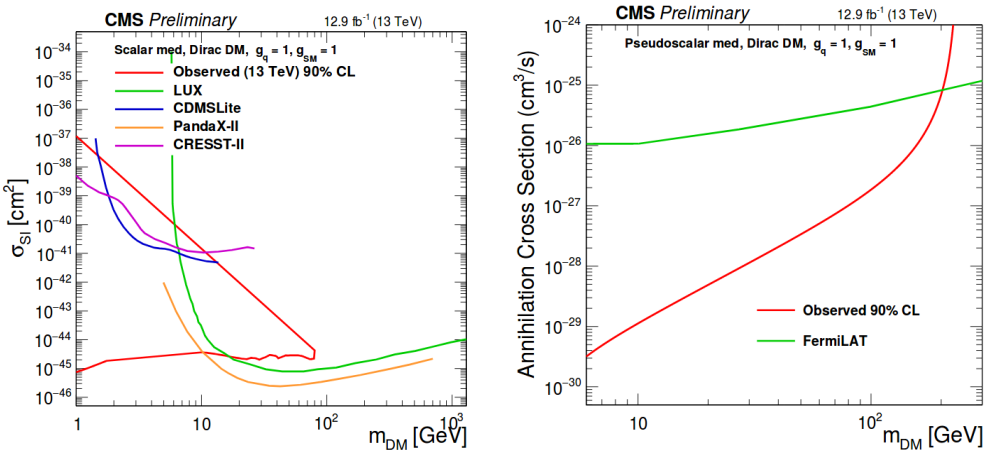

Figure 6.8: Comparison of DM techniques through simplified models. *Left panel:* comparison of direct detection and collider searches assuming scalar mediator. Constraints on the spin-independent DM-nucleon scattering cross section versus DM mass. *Right panel:* comparison of indirect detection and collider searches assuming pseudoscalar mediator. Constraints on the DM annihilation cross section versus DM mass. Figure extracted from [198].

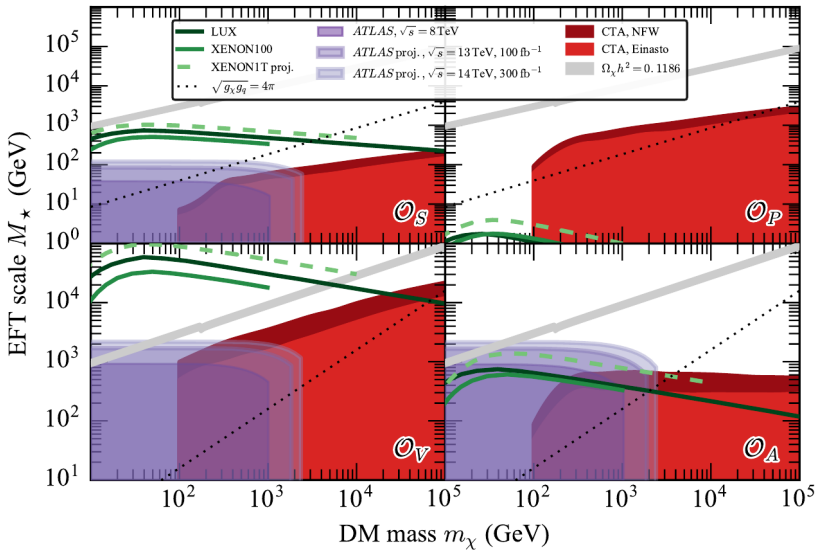

Figure 6.9: Lower limits on the EFT scale M_* as function of the DM mass, compared for indirect, direct and collider searches. Figure extracted from [197].

detection constraints, $\mathcal{O}_P$ suppresses the direct detection constraints and $\mathcal{O}_A$ suppresses both, while in case of $\mathcal{O}_V$ there is no suppression of the interaction. Operators $\mathcal{O}_S$ and $\mathcal{O}_V$ also weaken collider constraints.
Fig. 6.9 shows the complementarity between indirect, direct and collider searches by comparing CTA forecast limits on M_* as function of the DM mass at the GC [197], together with LUX [199] and XENON [200], and ATLAS [201] constraints for the different operators. The different techniques probe overlapping regions of the parameter space and combining them together enable to cover a larger region than in the case of a single technique used. In the scalar case the direct constraints are the strongest in the full mass range. Independently on the assumed mediator the indirect searches extend to higher masses than the collider searches. In the axial-vector case the indirect searches outcome the other techniques in the TeV mass range. The indirect searches provide the overall strongest results in the pseudo-scalar scale, but without reaching the value predicted for the relic density.

6.5 Dark matter density distributions at Galactic scale

DM signal is proportional to DM density, so it is crucial to estimate the DM density profile around the target of interest. DM halos can be modeled with different parameterizations and they are split in two macro categories: cuspy profiles and cored profiles.
Cuspy profiles are common in the most massive galaxies. They can rise in places like the Milky Way center due to the strong gravitational potential of the central supermassive black hole Sgr A*. The two main cuspy profile models are the Einasto [202] and the NFW [91] profiles, parametrized as

$$\rho_{\rm E}(r) = \rho_{\rm s} \exp\left[-\frac{2}{\alpha_{\rm s}}\left(\left(\frac{r}{r_{\rm s}}\right)^{\alpha_{\rm s}} - 1\right)\right] \quad \text{and} \quad \rho_{\rm NFW}(r) = \rho_{\rm s}\left(\frac{r}{r_{\rm s}}\left(1+\frac{r}{r_{\rm s}}\right)^2\right)^{-1}, \tag{6.5}$$

where r is the distance from the center of the galaxy, $\rho_{\rm s}$ is the critical density at the position of the Sun, $r_{\rm s}$ is the scale radius at which the profile changes slope and $\alpha_{\rm s}$ determines the steepness of the profile. The NFW profile is degenerate in $r = 0$, while $\rho_{\rm E}(0)$ is finite.
The observation of the rotation curves of many galaxies suggests that the central DM halo is flat. Especially small mass galaxies can have a cored profile. The main models of cored profiles are the Burkert [203] and the isothermal [204] profiles, parametrized as

$$\rho_{\rm B}(r) = \rho_0 \frac{r_{\rm c}^3}{(r+r_{\rm c})(r^2+r_{\rm c}^2)} \quad \text{and} \quad \rho_{\rm Iso}(r) = \rho_0\left(1+\left(\frac{r}{r_{\rm c}}\right)^2\right)^{-1}. \tag{6.6}$$

Simple cored profiles can also be modeled starting from cuspy profiles as

$$\rho_{\mathrm{E,core}}(r) = \begin{cases} \rho_{\mathrm{E}}(r) & \text{for } r > r_{\mathrm{c}} \\ \rho_{\mathrm{E}}(r_{\mathrm{c}}) & \text{for } r \leq r_{\mathrm{c}} \end{cases} \quad \text{and} \quad \rho_{\mathrm{NFW,core}}(r) = \begin{cases} \rho_{\mathrm{NFW}}(r) & \text{for } r > r_{\mathrm{c}} \\ \rho_{\mathrm{NFW}}(r_{\mathrm{c}}) & \text{for } r \leq r_{\mathrm{c}} \end{cases} . \tag{6.7}$$

These parametrizations are derived from constraints due to N-body cosmological simulations and observations of stellar and gas kinematic. These profiles do not include the baryonic component that would require more sophisticated N-body simulations with this additional component [205]. The DM density profiles can also be altered by the interaction with other halos, that produce tidal stripping or eventual disruption of the smallest halo [206].
Examples of NFW (black solid lines), Einasto (red and blue solid lines) and Burkert (orange solid line) DM density profiles of the Milky Way halo are shown in Fig. 6.10. Near the GC the cuspy profiles are 3 to 4 orders of magnitude larger than cored profiles. The references for the normalization of the parameters that reproduce GC measurements and simulations are given in the caption. Several DM profiles can reproduce the GC dynamics because its

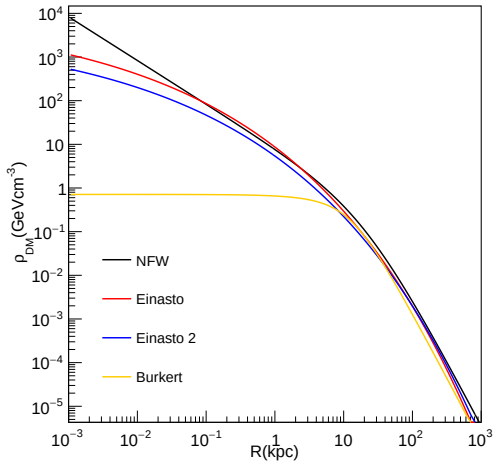

Figure 6.10: DM density profiles of the Milky Way as function of the distance from the GC. An Einasto [207] (red solid line), a second parametrization of the Einasto profile [208] (blue solid line), an NFW profile [207] (black solid line) and a Burkert profile [209] (orange solid line) are shown.

gravitational potential is dominated by stars and gas. The large uncertainty on the Galactic halo profile strongly affects the DM search and the obtained constraints on the annihilation cross section, that can change of several orders of magnitude depending on the assumed DM density distribution.
A tridimensional model of the Einasto profile at the GC obtained with the normalization from Ref. [207] is shown in Fig. 6.11.

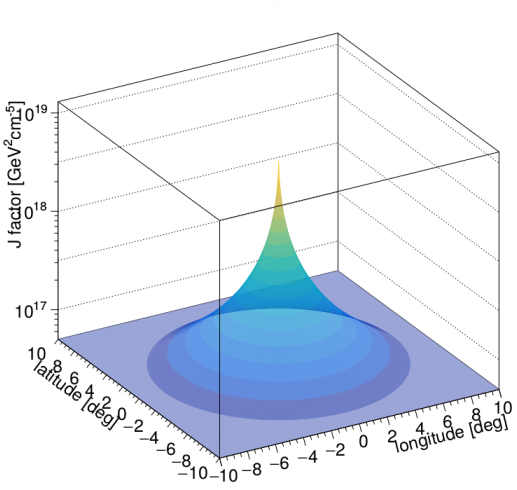

Figure 6.11: Tridimensional model of the Galactic halo in Galactic coordinates assuming an Einasto profile.

6.6 Astrophysical targets for dark matter search with gamma rays

In gamma-ray astrophysics the targets that are observed in order to look for DM are environments that host very dense DM halos or clumps. In these DM dense regions the relic DM particles can interact and annihilate or decay giving a detectable gamma-ray signal. More details on the types of expected DM annihilation signals is given in the next section. DM dense regions are:

- The **Galactic Center (GC)**. Being situated at about 8.5 kpc from the Sun the GC is the closest DM target. As shown in Sec. 6.5, it is expected to harbor a very large amount of DM. Assuming a NFW profile, the J-factor at the GC integrated in a region of 1° is $\log_{10}(J/\mathrm{GeV}^2\,\mathrm{cm}^{-5}) = 21.0$. For these reasons it is the object that could provide the largest DM signal in gamma rays. However, many standard astrophysical emitters in VHE gamma rays are present in this region (see Chap. 3) and represent a background for DM search. This region has been widely observed by H.E.S.S. and Fermi-LAT and it gives the strongest constraints on DM annihilation. Details on the DM search towards the Inner Galactic halo with H.E.S.S. are given in Chap. 8 and Chap. 9. The GC excess of GeV gamma rays measured by Fermi-LAT in the GC region could be interpreted as signal of DM annihilation [210], but standard astrophysical explanations are more plausible in absence of DM detection towards other cleaner environments, *e.g.* dwarf galaxies. In addition, some studies relate the H.E.S.S. TeV gamma-ray flux observed towards Sgr A* to DM signal [211]. A hint of

DM signal was found by Fermi-LAT compatible with DM of mass 130 GeV near the GC [125], but this hypothesis was rejected by H.E.S.S. [124].

- The **Galactic halo** further from the inner part of the Milky Way is a cleaner environment. Moving towards the external part of the halo reduces the intensity of the expected signal, especially under the assumption of a cuspy DM density profile peaked at the GC. At the same time it avoids the VHE gamma-ray crowded region where several diffuse emissions are detected in the GeV-TeV energy range. The annihilation signal is significantly smaller than in the few-degrees region around the GC, but the uncertainty on the DM profile, *i.e.* the impact of the underlying assumption on DM distribution, is reduced because the different halo models start to converge beyond the several kpc distance from the GC.

- **Dwarf galaxies** of the Local Group satellites of the Milky Way (dSphs) are the most DM-dominated objects of the Universe and they are located at a relatively small distance from Earth, about $25 - 250$ kpc. 56 dSph satellites of the Milky Way (dSph candidates) have been detected so far [212] and a factor $3 - 4$ times more is expected with upcoming optical surveys [213]. Since dSphs mostly do not host star formation regions and are almost gas-free, they provide a clean environment in gamma rays and an eventual gamma-ray emission could be easily associated to DM annihilation. In addition, due to their proximity and large DM content large signal is expected with respect to other targets like galaxy clusters. DSphs have a J-factor integrated in a region of 0.5° of the order of $\log_{10}(J/\mathrm{GeV^2\,cm^{-5}}) = 18 - 19$. Thus, dSphs are the very promising targets for unambiguous DM detection. They are primary observation target for IACTs. More information about DM search towards these objects with H.E.S.S. is given in Chap. 10.

- **Galaxy clusters** are the largest gravitationally bounded systems dominated by DM, which constitutes about 80% of their mass [214], but they are very distant from the solar system.Galaxy clusters have a J-factor integrated in a region of 1° of the order of $\log_{10}(J/\mathrm{GeV^2\,cm^{-5}}) = 16 - 17$. For this reason, despite the small standard astrophysical gamma-ray emission compared to the GC, they have been used to set constraints a few orders of magnitude fainter than towards the GC. However, thanks to their large mass $10^{14} - 10^{15}$ times larger than the Sun, they are promising targets for search for decay of DM [215] for which the searches become more efficient when large volumes are considered. Electrons and positrons produced in the decay undergo ICS and loose energy much faster than they can diffuse out of the system, producing gamma rays before escaping.

- **DM clumps** and subhalos of various size could have formed in the main DM halos. Those that are inside the Milky Way DM halo are potentially detectable from Earth.

However they are very difficult to localize. In fact, small halos do not have large enough gravitational potential to accrete star formation, *i.e.* they do no shine in gamma rays, unless DM annihilation takes place. Some of these subhalos could be close to Earth and have a relevant DM density, but their position is completely unknown so they are not suitable for pointed observations. Some bright sources detected by the wide-field Fermi-LAT telescope without counterparts at other wavelengths, called UFOs (unidentified Fermi objects), are favorable candidates for DM clumps [216] and can be targeted by IACTs.

In order to be able to detect a signal it must be strong and distinguishable from the background. So the best targets for DM search are those that have large DM content, are relatively close to Earth (large signal), and have low standard astrophysical background. The most promising target is the GC, being the closest to the observer, *i.e.* the one that provides the largest signal. Alternatively the dwarf galaxies satellites of the Milky way are promising targets for an unambiguous detection since they are the regions with lowest background at a relatively small distance from the observer.

6.7 Gamma-ray flux from dark matter annihilation

In VHE gamma rays the IACTs can detect a flux of photons coming from dense DM environments where DM annihilation takes place, but it depends on the assumptions on the annihilation process and the DM distribution. The gamma-ray flux can be estimated as

$$\frac{\mathrm{d}\phi_\gamma}{\mathrm{d}E}(E,\Delta\Omega) = \underbrace{\frac{1}{4\pi}\frac{\langle\sigma v\rangle}{m_{\mathrm{DM}}^2}\sum_{\mathrm{i}} Br_{\mathrm{i}}\frac{\mathrm{d}N_{\mathrm{i}}}{\mathrm{d}E}(E)}_{particle\,physics} \times \underbrace{J(\Delta\Omega)}_{astrophysics} . \tag{6.8}$$

The first term of Eq. (6.8) contains the particle physics information about DM properties: its mass m_{DM}, its thermally averaged velocity weighted annihilation cross section $\langle\sigma v\rangle$, its annihilation spectrum $\mathrm{d}N_{\mathrm{i}}/\mathrm{d}E$ in a specific channel i and the corresponding branching ratio Br_{i}. The second term of the equation contains the astrophysics information about the DM distribution around the target. It is also known as J-factor an it is the integral of the square of the DM density over the line of sight *los* and the solid angle $\Delta\Omega$, which reads

$$J(\Delta\Omega) = \int_{\Delta\Omega}\int_{\mathrm{los}} \rho^2(r(s,\theta))\mathrm{d}s\mathrm{d}\Omega. \tag{6.9}$$

In the searches for decay the J-factor is substituted by the D-factor $D = \int_\Omega \int_{\rm los} \rho(r(s,\theta))\mathrm{d}s\mathrm{d}\Omega$. The average J-factor $J(\Delta\Omega)$ over an integration region $\Delta\Omega$ is computed as

$$J = \frac{2\pi}{\Delta\Omega}\int \mathrm{d}\theta \sin\theta J(\theta) \quad \text{for a disk} \quad \Delta\Omega = 2\pi\int_0^{\theta_{\rm max}} \mathrm{d}\theta\sin\theta, \tag{6.10}$$

$$J = \frac{4}{\Delta\Omega}\int \mathrm{d}\theta \sin\theta J(\theta) \quad \text{for an annulus} \quad \Delta\Omega = 2\pi\int_{\theta_{\rm min}}^{\theta_{\rm max}} \mathrm{d}\theta\sin\theta, \tag{6.11}$$

$$J = \frac{2\pi}{\Delta\Omega}\int\int \mathrm{d}b\mathrm{d}\ell \cos b J(\theta,b,\ell) \quad \text{for a } b\times\ell \text{ region} \quad \Delta\Omega = 4\int_{b_{\rm min}}^{b_{\rm max}}\int_{\ell_{\rm min}}^{\ell_{\rm max}} \mathrm{d}b\mathrm{d}\ell\cos b, \tag{6.12}$$

where θ is an annular radius and ℓ and b are longitude and latitude.
While $\frac{\mathrm{d}\phi_\gamma}{\mathrm{d}E}$ is the actual flux of gamma rays produced in the self-annihilation process, in order to estimate the number of gamma rays observed with a telescope the characteristics of the detector and the information about the observations must be taken into account. The expected number of counts is obtained by convolving the differential flux for the gamma-ray effective area of the detector $A^\gamma_{\rm eff}$, its energy resolution $\mathcal{G}(E)$ and integrating over the energy range ΔE of interest and the observation time $T_{\rm obs}$. The gamma-ray event count number reads

$$N^\gamma_{\rm S} = T_{\rm obs}\int_{\Delta E}\frac{\mathrm{d}\phi_\gamma}{\mathrm{d}E}(E,\Delta\Omega)A^\gamma_{\rm eff}(E)\mathcal{G}(E)\mathrm{d}E. \tag{6.13}$$

The effective area and energy resolution depend on the observation conditions (*e.g.* observations zenith angle and *offset*), as well as on the energy, as explained in Sec 2.5.

6.8 Dark matter annihilation spectra in gamma rays

6.8.1 Continuum signal

DM, in the context of particle physics, can annihilate and several final states are allowed. The products of a tree-level annihilation can be leptons, quarks or bosons, assuming that the mass of the DM particle is large enough to produce them. The particles in the final state can then produce gamma rays through decay or hadronization. The obtained gamma-ray spectrum is referred to as the *continuum*. The annihilation of cold DM is considered at rest, so its spectrum will have a cut-off at $m_{\rm DM}$. The behavior of the spectrum at lower energies depends on the final state particle. Fig. 6.12 shows the *continuum* spectrum for annihilation in the W^+W^- (green solid line), ZZ (orange solid line), $b\bar{b}$ (black solid line), $t\bar{t}$ (violet solid line), e^+e^- (cyan solid line), $\mu^+\mu^-$ (red solid line) and $\tau^+\tau^-$ (blue solid line) annihilation channels, for DM with mass 1 TeV. They are obtained from Ref. [208]. These spectra assume annihilation at rest so they all have a sharp cutoff at $m_{\rm DM}$. The leptonic channels are the sharpest at the end of the spectrum, meaning that their maximum is close to $m_{\rm DM}$, while the bosonic and quark channels have a maximum at about $m_{\rm DM}/10$. The $\tau^+\tau^-$ channel shows both hadronic and leptonic features. It is peaked at about $m_{\rm DM}/3$ and

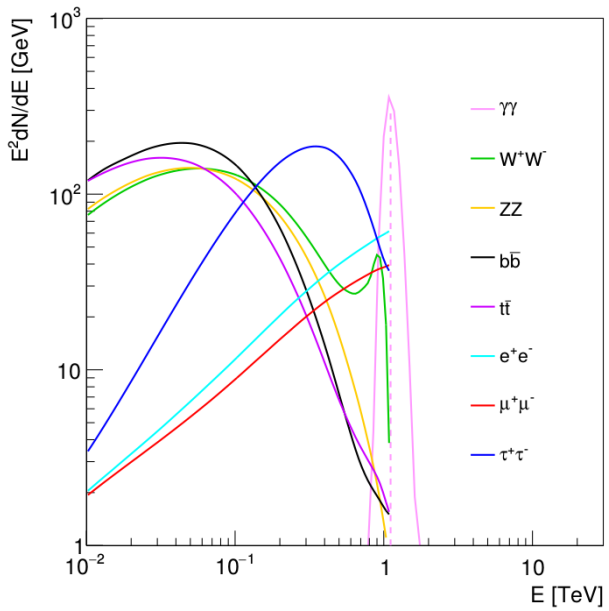

Figure 6.12: Gamma-ray spectra from annihilation of DM with mass 1 TeV. Several *continuum* channels [208] and a *gamma line* (rescaled of two orders of magnitude) are shown. The *gamma line* is spread by a 10% Gaussian energy resolution.

it produces the strongest signal at the peak. In what follows, when we refer to XX channel (with $X = W, Z, b, t, e, \mu, \tau, \gamma$) we assume 100% branching ratio in that single channel, unless differently specified.

6.8.2 Mono-energetic γ line

Direct annihilation into photons can also take place, but not at the tree-level. Two photons can be directly produced through loops. The cross section of this suppressed process scales with the square of the electroweak coupling $\alpha^2_{\rm EW}$, *i.e.* in the WIMP mass range it is $10^2 - 10^4$ times smaller than the *continuum* [217, 218]. The spectrum obtained from prompt photons annihilation is referred to as *gamma line*. It is indeed a monoenergetic line, as a Dirac delta function at the DM mass $\delta(E - m_{\rm DM})$. In a realistic case, for an instrument that has finite resolution, the line is spread and it can be modeled as a Gaussian function with width equal to the energy resolution. In Fig. 6.12 the *gamma line* is shown spread for a 10% energy resolution. This is the sharpest and clearest DM signal. It is the most difficult to detect due to its small expected cross section and its strong sensitivity to fluctuations in the dataset. At the same time it is the channel that would give the most unambiguous DM detection, since no standard astrophysical process could reasonably produce a similar signal.

6.8.3 Astrophysical and particle physics signal enhancement

There are some processes that can enhance the DM signal producing additional photons. From a particle physics point of view the main contributions are from the so called electroweak (EW) corrections and the Sommerfeld enhancement. The EW corrections are included in the spectra from Ref. [208] used in the analyses in this work. In the channels that contain light leptons in the final state ICS can take place with the ambient radiation in the stellar medium (*e.g.* the CMB) [219]. The ICS photons are not included in the spectra from Ref. [208]. From the astrophysical point of view the DM signal can be enhanced by the presence of sub-halos.

Sub-halos

The presence of substructure inside the main DM halo is predicted by the simulations and could boost the expected signal from the smooth distribution of DM in the host halo [220]. The density of the central cusp of sub-halos is much steeper in these halos than in larger halos. The total J-factor is the sum of the smoother distribution of the host halo and sub-halos distributions. The contribution of the substructures is sub-dominant in the inner part of the main halo, but it becomes more significant in the outskirts. Whether or not an actual boost of the gamma-ray signal due to sub-halos exists is still debated in the literature [221].

Electroweak corrections

When DM of mass larger than the EW scale ($\gtrsim 100$ GeV) annihilates into a couple of charged particles the process is likely do be accompanied by production of additional radiation [222]. We talk about final state radiation (FSR) when an additional photon is produced by one of the particles external to the interaction vertex. We talk, instead, of virtual internal bremsstrahlung (VIB) when the photon is produced by the virtual exchanged particle. The intensity of these emissions increases with the DM mass. Their effect is the addition of a sharp line-like feature at the end of the spectrum, near $m_{\rm DM}$. The EW corrections are especially important for the W boson and their effects are visible at the end of its spectrum in Fig. 6.12.

The Sommerfeld effect

The Sommerfeld effect [223] is a classical quantum effect that takes place in low velocity regime, when the two initial state DM particles can exchange the mediator of the interaction several times before the annihilation occurs. This process is non-relativistic and takes place in DM halos where the relative velocity between DM particles is of the order of $\beta = v/c = 10^{-5}$ ($v = 10$ km s^{-1}). Particles interact through a Yukawa-like potential $V(r) = -(\alpha/r)\exp(-m_{\rm V} r)$, exchanging a vector boson of mass $m_{\rm V}$, where α is the coupling

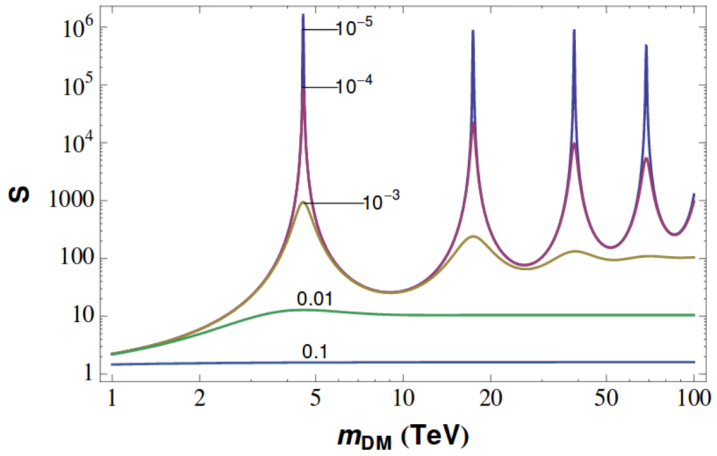

Figure 6.13: Intensity of the Sommerfeld effect for DM annihilation into W^+W^- mediated by a Z boson as function of the DM mass. The effect is shown for relative DM velocity between 10^{-1} and 10^{-5}. Figure extracted from [224].

constant. The initial thermal relic cross section $\langle\sigma v\rangle_0$ is enhanced by a factor $S(\beta, m_{\rm DM}, m_{\rm V})$, such that $\langle\sigma v\rangle = S(\beta, m_{\rm DM}, m_{\rm V})\langle\sigma v\rangle_0$. Depending on the relative velocity β three regimes can be defined [224], as shown in Fig. 6.13. When $\beta \gg \alpha$ (large velocity) there is no enhancement and $S(\beta, m_{\rm DM}, m_{\rm V}) = 1$. This regime is shown by the blue line for $\beta = 10^{-1}$. When $\sqrt{\alpha m_{\rm V}/m_{\rm DM}} \ll \beta \ll \alpha$ (intermediate velocity) the enhancement scales as $1/v$ and $S(\beta, m_{\rm DM}, m_{\rm V}) \simeq \pi\alpha/\beta$ independently on the masses. This enhanced non-resonant regime is shown by the green line for $\beta = 10^{-2}$. When $\beta \ll \sqrt{\alpha m_{\rm V}/m_{\rm DM}}$ (small velocity) some resonances arise due to the presence of bound states, as shown by the yellow, magenta and purple lines ($\beta = 10^{-3} - 10^{-5}$). The enhancement scales with $1/\beta^2$ and strongly depends on the particle mass. For very small relative velocities, like those expected in DM halos, the resonances can increase the thermal relic cross section up to a factor 10^5. The position of the resonances is determined by the DM mass and the mediator mass $m_{\rm V}$, *i.e.* the coupling between DM and the mediator. The largest resonances are obtained for small DM masses. Large $m_{\rm V}$ shift the resonances to larger $m_{\rm DM}$.

Chapter 7

Likelihood analysis technique for the search for dark matter signatures

Contents

7.1 The likelihood method . . . 118
7.1.1 Definition of the likelihood function . . . 118
7.1.2 The log-likelihood ratio test statistic . . . 119
7.2 Application to dark matter search . . . 119
7.2.1 The likelihood function for a counting experiment . . . 119
7.2.2 Monte Carlo setup . . . 120
7.2.3 Significance of an excess . . . 120
7.2.4 Definition of observed and expected limits . . . 121
7.2.5 Size of the background region . . . 123
7.2.6 Performarces of 1D and 2D-binned versus integrated likelihood . . . 124
7.3 Impact of uncertainties on the limits . . . 125
7.3.1 Statistical uncertainty on the J-factor . . . 125
7.3.2 Systematic uncertainties . . . 126
7.3.3 Impact of the energy resolution . . . 127
7.3.4 Uncertainty on the background residual background determination . . . 129
7.4 Exclusion versus modeling of background components . . . 129
7.5 The profiling likelihood technique . . . 131
7.6 Summary . . . 133

Treating random processes requires a statistical description of the observed events in terms of probability density functions. One of the statistical approaches mostly used in high energy physics to look for a weak signal in an observed dataset over a measured or modeled background is the likelihood technique. In this chapter we define the likelihood function and the log-likelihood ratio test statistics, and their application to indirect dark matter searches that end up with constraints or measurements of the dark matter properties. We apply the latest likelihood methods and make original tests on the parameters of the likelihood function and their impact on the test statistics. We study the effect on the limits of the binning of the likelihood, the profiling of the likelihood, the systematic uncertainty on the measurements, the energy resolution of the detector and the statistical uncertainty on the J-factor. Examples are given on limits computed using mock data of H.E.S.S. I-like observations. These observations are assumed to provide 250 hours of exposure flat in 1° around the Galactic Center and the searched signal is due to annihilation into $b\bar{b}$, unless otherwise stated. The Einasto profile is chosen to describe the J-factor distribution. The aim of this chapter is to study the behavior of the likelihood ratio test statistics and the impact of uncertainty on the parameters relevant for dark matter searches, and it is not to derive proper constraints.
The likelihood function and log-likelihood ratio test statistics are presented in Sec. 7.1. Their application to the search for dark matter is described in Sec. 7.2. In Sec. 7.3 the effect on the dark matter limits of the uncertainties on the likelihood parameters is studied. Alternative treatments of the standard astrophysical background are discussed in Sec. 7.4 and the likelihood profiling technique is discussed in Sec. 7.5.

7.1 The likelihood method

7.1.1 Definition of the likelihood function

The likelihood is a function of the parameters of a model given an observed dataset. Indeed, given a set of observations $\boldsymbol{\mathcal{D}}$ they follow a probability distribution with probability density function $f(\boldsymbol{\mathcal{D}}|\boldsymbol{\theta})$, that is determined by a set of parameters $\boldsymbol{\theta}$. For independent homogeneously distributed data $\boldsymbol{\mathcal{D}} = \{x_i\}_{i=1}^{n}$, their likelihood function is

$$\mathcal{L}(\boldsymbol{\theta}|\boldsymbol{\mathcal{D}}) = \prod_{i=1}^{n} f(x_i|\boldsymbol{\theta}). \tag{7.1}$$

In practice, the log-likelihood function is used instead:

$$\ln \mathcal{L}(\boldsymbol{\theta}|\boldsymbol{\mathcal{D}}) = \sum_{i=1}^{n} \ln f(x_i|\boldsymbol{\theta}). \tag{7.2}$$

The likelihood gives the probability, as function of a parameter θ, that x_i is observed for a model that depends on a variable θ.

7.1.2 The log-likelihood ratio test statistic

In order to search for a new phenomenon an hypothesis $H_1(\theta_1)$, that includes a new signal, is compared to a null-hypothesis $H_0(\theta_0)$, representing the absence of the new signal besides background and already known signals. Two likelihood functions for the two different hypotheses are compared to estimate the probability that $H_1(\theta_1)$ is more likely than $H_0(\theta_0)$. To determine which hypothesis is more compatible with the data a variable called test statistics, TS, is defined. The log-likelihood ratio test statistics (LLRTS) is defined as

$$TS = -2\ln\lambda(\boldsymbol{\theta}) = -2\ln\frac{\mathcal{L}(\boldsymbol{x}|\boldsymbol{\theta_1})}{\mathcal{L}(\boldsymbol{x}|\boldsymbol{\theta_0})}. \tag{7.3}$$

For a large count distribution TS behaves like a χ^2 distribution [225]. Thus, for a one-sided[1] likelihood and one degree of freedom the value $TS = 2.71$ allows us to set 95% confidence level (C.L.) limits on the model varying parameter. In the same way, $TS = 3.84$ corresponds to limits at 99% C.L..

7.2 Application to dark matter search

7.2.1 The likelihood function for a counting experiment

In dark matter searches with IACTs we define a region of interest were the signal is looked for and a control region where the background is measured and used to estimate the background in the signal region. The number of gamma-like events is a measured in these two regions and these are two independent random measurements. In this kind of counting problem, often referred to as *ON/OFF problem*, we deal with Poisson distributions of counts x_i. The number of photons measured in the signal region are referred to as $N_{\rm ON}$ and in a background region as $N_{\rm OFF}$. In the signal region, in presence of DM, we expect a signal $N_{\rm S}$ and a background $N_{\rm B}$. The photons $N_{\rm ON}$ are then distributed as a Poisson function with mean $N_{\rm S} + N_{\rm B}$. The photons $N_{\rm OFF}$ are distributed as a Poisson function as well with mean $\alpha N_{\rm B}$. The normalization $\alpha = \Delta\Omega_{\rm OFF}/\Delta\Omega_{\rm ON}$ is the ratio between the solid angle size of the regions in the sky where $N_{\rm OFF}$ and $N_{\rm ON}$ are measured[2].
The likelihood function for DM search applied with H.E.S.S. reads

$$\mathcal{L}(N_{\rm S}, N_{\rm B}|N_{\rm ON}, N_{\rm OFF}, \alpha) = \frac{(N_{\rm S}+N_{\rm B})^{N_{\rm ON}}}{N_{\rm ON}!}e^{-(N_{\rm S}+N_{\rm B})}\frac{(\alpha N_{\rm B})^{N_{\rm OFF}}}{N_{\rm OFF}!}e^{-(\alpha N_{\rm B})}. \tag{7.4}$$

[1] Only positive values of the TS are allowed, scanning $\boldsymbol{\theta} > 0$.

[2] $N_{\rm ON}$, $N_{\rm OFF}$, $N_{\rm S}$ and $N_{\rm B}$ are built as histograms of measured or expected gamma ray counts versus energy.

In case a small signal N'_S is present also in the background region, the mean of the Poisson function of the background region becomes $N_B \rightarrow N'_S + \alpha N_B$.

7.2.2 Monte Carlo setup

Examples of the event distributions used in this chapter are shown in Fig. 7.1. They mimic 250 h of homogeneous observation in the inner 1° around the GC with the H.E.S.S.-I array. They are used here to to study the application and performances of the LLRTS on a H.E.S.S.-like DM search, assuming annihilation in the $b\bar{b}$ channel and Einasto DM density profile, unless specified otherwise. The inner 0.3° around the GC are excluded because in the actual H.E.S.S. observation this region is dominated by standard astrophysical VHE gamma-ray emission. When applying a binned analysis the region of interest is split in seven rings of width 0.1° with inner radius between 0.3° and 0.9°. The N_{ON} (red line) distribution is built as a Poisson realization of the N_{OFF} (blue line) distribution in order to fake two independent random measurements in absence of signal.

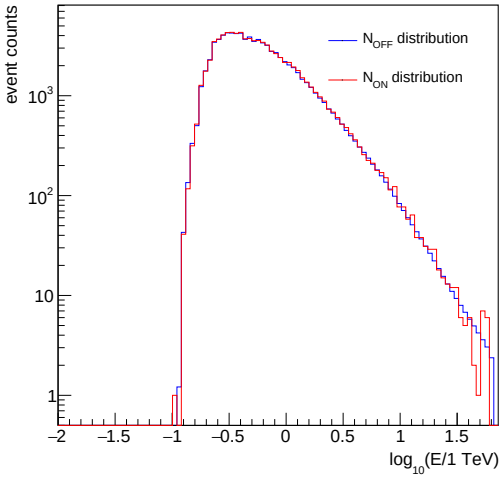

Figure 7.1: Event distributions of mock observations of the inner 1° of the GC for 250 h. The distributions of the N_{ON} counts is a Poisson realization of the distribution of the N_{OFF} counts in order to mimic two independent measurements in absence of signal.

7.2.3 Significance of an excess

The measurements in the signal and background regions are compared, eventually in spectral and spatial bins (see Sec. 7.2.6), looking for an excess in the signal region with respect to the background expectation.
In case an excess is observed, its significance can be first approximated in terms of σ as the

number of excess counts above its standard deviation :

$$S = \frac{N_{\rm ON} - N_{\rm OFF}}{\sqrt{\alpha(N_{\rm ON} + N_{\rm OFF})}}. \tag{7.5}$$

A more refined computation of S is given by [226] and it is used in this work:

$$S = \sqrt{2}\left\{ N_{\rm ON} \ln\left[\frac{1+\alpha}{\alpha}\left(\frac{N_{\rm ON}}{N_{\rm ON}+N_{\rm OFF}}\right)\right] + N_{\rm OFF} \ln\left[(1+\alpha)\left(\frac{N_{\rm OFF}}{N_{\rm ON}+N_{\rm OFF}}\right)\right]\right\}^{1/2}. \tag{7.6}$$

In gamma-ray astronomy, a signal excess is considered significant if its significance is above 5σ.

7.2.4 Definition of observed and expected limits

The expected signal depends on the annihilation cross section $\langle\sigma v\rangle$, as shown in Eq. (6.8) in the Chap. 6 and its value is let free in the DM model, the mass, annihilation channel and DM distribution being fixed. So $\langle\sigma v\rangle$ is a free parameter in Eq. (7.4). For a particle of mass $m_{\rm DM}$, an annihilation spectrum dN/dE and a J-factor J, the value of $\langle\sigma v\rangle$ can be constrained through a LLRTS. The obtained 95% C.L. upper limits on $\langle\sigma v\rangle$ as a function of $m_{\rm DM}$ are called observed limits. Expected limits can be first computed setting $N_{\rm ON} \equiv N_{\rm OFF}$ in Eq. (7.4)[3], giving the sensibility of the experiment to DM in an annihilation channel. Examples of observed (red solid line) and expected (blue solid line) limits on $\langle\sigma v\rangle$ as function of $m_{\rm DM}$ are given in Fig. 7.2 (left). The observed limits in case of presence of a DM-like signal with $m_{\rm DM} = 1$ TeV and $\langle\sigma v\rangle = 5 \times 10^{-24}$ cm^3 s^{-1} for annihilation into $b\bar{b}$ are also shown (red dashed line). In this case a bump in the $\langle\sigma v\rangle$ curve is visible at the position of $m_{\rm DM}$.

A refined estimate of the sensitivity is given by the mean expected limits which are computed by making several Poisson realizations of the background and the signal counts. For each observation *run* and region of interest the distribution of counts measured in the signal and background regions are recomputed several times as independent measurements. For each realization of $N_{\rm OFF}$ and $N_{\rm OFF}/\alpha$ the new events distribution is computed by filling each bin with a random number following a Poisson probability function with mean equal to the number of counts measured in the same bin. The LLRTS analysis is repeated for all the realizations. The mean of the distribution of the cross section values provides the mean expected limits. The standard deviation of the same distribution gives the containment bands at 1σ and 2σ. Fig. 7.3 shows a distribution of the log-values of $\langle\sigma v\rangle$ obtained through the Poisson realizations, with mean $\log_{10}(\langle\sigma v\rangle/{\rm cm}^3\,{\rm s}^{-1}) = -24.81$ and standard deviation 0.4. Fig. 7.2 (right) shows the mean expected limits (black solid line) and the 1σ (green box) and 2σ (yellow box) containment bands, obtained by means of 100 Poisson realizations.

[3]This is a good approximation of the mean expected limits and is used for the studies in this chapter.

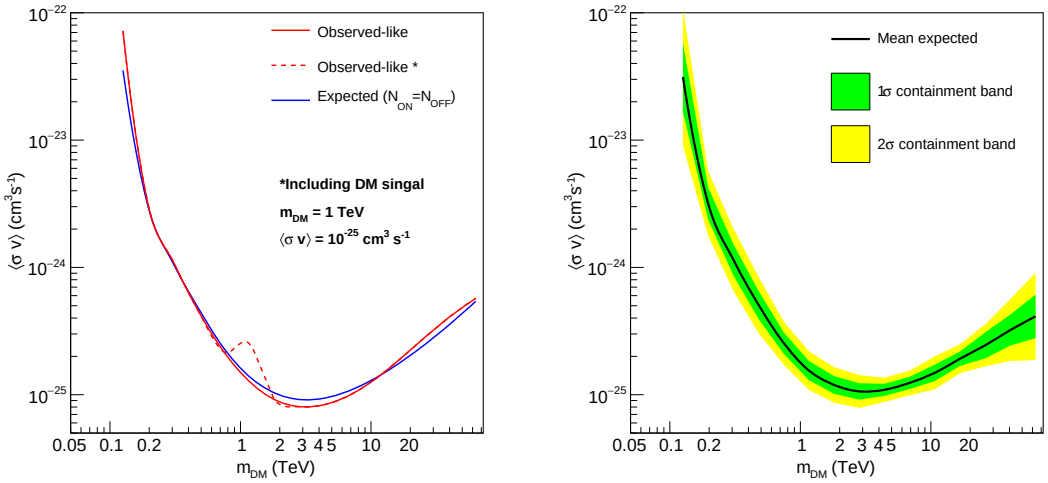

Figure 7.2: Example of limits with mock H.E.S.S. I-like event distributions for a DM signal due to annihilation in the $b\bar{b}$ channel. *Left:* Observed (red solid line) and expected (blue solid line) limits. Observed limits in presence of a DM-like signal for $m_{\mathrm{DM}} = 1$ TeV are also shown (red dashed line). *Right:* Mean expected limits (solid black line) and containment bands at 1σ (green box) and 2σ (yellow box). The bands become larger where the statistics is smaller.

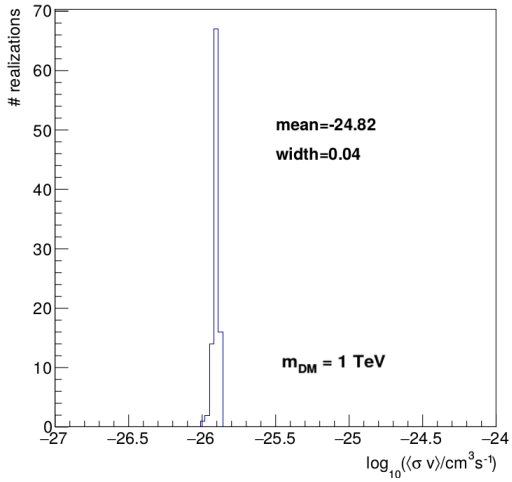

Figure 7.3: Distribution of the log-values of $\langle\sigma v\rangle$ obtained through 100 realizations of background and signal measurements. The mean of $\log_{10}(\langle\sigma v\rangle/\mathrm{cm}^3\,\mathrm{s}^{-1})$ is -24.81 and its standard deviation is 0.04.

An alternative method to compute the mean expected limits and containment bands is the Asimov dataset [225]. The Asimov dataset is an artificial dataset built in a way such that it reproduces the real parameter values when evaluating the estimators for the parameters of the LLRTS. The estimators are found by setting to 0 the partial derivatives with respect to the parameters themselves. The Asimov data counts are defined as the mean expectation of the corresponding actual measurements, *i.e.* they coincide with the outcome of a very-large-statistics Monte Carlo. Let us consider a simplified likelihood $\mathcal{L}(\lambda|d) = \frac{\lambda^d}{d!}e(-\lambda)$. In practice, using the Asimov dataset means that rather than making several realizations of d and calculating $\bar{\lambda}_{95\%}$ for each one and then taking the mean, we can just set d equal to the mean λ, and then calculate the limit from that. With this procedure we obtain $\bar{\lambda}_{95\%}$ as well by applying the LLRTS only once. This is equivalent to saying that we compute the TS as $TS = (\Phi^{-1}(0.95) \pm N)^2$. Here, Φ is the cumulative distribution function of a standard normal distribution with mean $\mu = 0$ and width $\sigma 1$. N is added in order to compute the N-sigma containment band. For $N = 0$ we recover the usual LLRTS for $TS = 2.71$ that provides the mean expected limits.

7.2.5 Size of the background region

The *multiple OFF* technique (see Sec. 2.4.2), when applicable, improves the precision of the residual background determination in the signal region with respect to a measurement in a single background region. Averaging the residual background measurement on more than

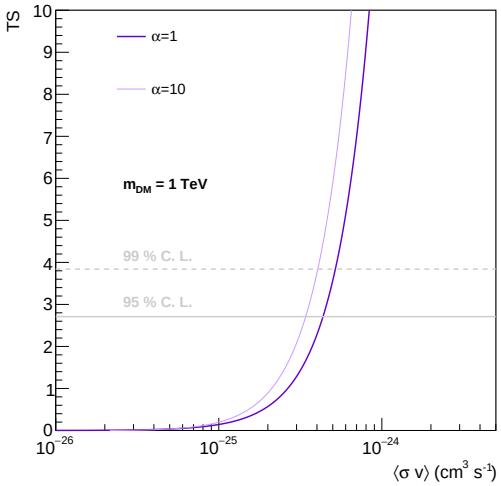

Figure 7.4: TS versus $\langle\sigma v\rangle$ for $\alpha = 1$ (purple solid line) and $\alpha = 10$ (lilac solid line) for a DM particle of mass 1 TeV and annihilation in the $b\bar{b}$ channel. The 95% C.L. and 99% C.L. upper limits on $\langle\sigma v\rangle$ are given by the gray solid line and the gray dashed line, respectively.

one region, *i.e.* $\alpha > 1$ in Eq. (7.4), improves the sensitivity to a weak signal, increasing its significance. The effect of α is more important for small statistics datasets, so a dataset

10 times smaller than in the other plots is chosen for this study. The typical value of α in H.E.S.S. analyses for example towards dwarf galaxies is about 10. Fig. 7.4 shows the TS versus $\langle\sigma v\rangle$ value in the case for $\alpha = 1$ (purple solid line) and $\alpha = 10$ (lilac solid line) at mass of 1 TeV. An improvement of 20% is observed.
In a region where many VHE gamma-ray sources and diffuse emission are detected it may not be possible to apply the *multiple OFF* background measurement, and $\alpha = 1$ is chosen to avoid any possible leakage in the control regions.

7.2.6 Performarces of 1D and 2D-binned versus integrated likelihood

As explained in Sec. 6.8 a DM signal is characterized by peculiar spectral features such as bumps and energy cutoffs close to the DM mass. This information can be used to improve the discrimination of the searched signal against the smooth power-law-like residual background by binning the likelihood in energy bins (i). This technique is referred to as the one-dimension (1D-) likelihood in what follows. The 1D-likelihood function reads:

$$\mathcal{L}_{\rm i}(\boldsymbol{N_S}, \boldsymbol{N_B}|\boldsymbol{N_{ON}}, \boldsymbol{N_{OFF}}, \alpha) = \frac{(N_{\rm S,i} + N_{\rm B,i})^{N_{\rm ON,i}}}{N_{\rm ON,i}!} e^{-(N_{\rm S,i}+N_{\rm B,i})} \frac{(\alpha N_{\rm B,i})^{N_{\rm OFF,i}}}{N_{\rm OFF,i}!} e^{-(\alpha N_{\rm B,i})}. \tag{7.7}$$

In addition, the peaked distribution of the searched DM signal (see Sec. 6.5) makes DM stand out on the isotropic residual background. The information on the spatial distribution of the signal can also improve the discriminating power of the test statistics by binning in spatial bins (j). This is referred to as the two-dimension (2D-) likelihood approach:

$$\mathcal{L}_{\rm i,j}(\boldsymbol{N_S}, \boldsymbol{N_B}|\boldsymbol{N_{ON}}, \boldsymbol{N_{OFF}}, \boldsymbol{\alpha}) = \frac{(N_{\rm S,i,j} + N_{\rm B,i,j})^{N_{\rm ON,i,j}}}{N_{\rm ON,i,j}!} e^{-(N_{\rm S,i,j}+N_{\rm B,i,j})} \frac{(\alpha_{\rm j} N_{\rm B,i,j})^{N_{\rm OFF,i,j}}}{N_{\rm OFF,i,j}!} e^{-(\alpha_{\rm j} N_{\rm B,i,j})}. \tag{7.8}$$

The total likelihood reads as the product of the individual likelihoods:

$$\mathcal{L} = \prod_{i,j} \mathcal{L}_{i,j} \tag{7.9}$$

or equivalently the sum of the log-likelihood functions over the indexes (i, j).
Fig. 7.5 shows the TS as function of $\langle\sigma v\rangle$ for the integrated (black), 1D- (blue) and 2D-likelihood (red) computed for a DM particle of mass 1 TeV. Lines that allow to find the 95% (solid gray line) and 99% (dashed gray line) are marked on the plots. There is a factor improvement up to 30% moving from the 1D- to the 2D-likelihood and up to a factor 2.5 from the integrated to the 2D-likelihood. An unbinned, *i.e.* event-by-event, likelihood approach is not suitable with a large dataset of $\mathcal{O}(10^6)$ events.

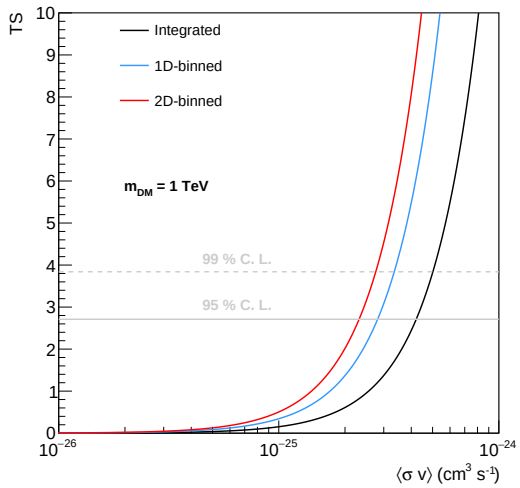

Figure 7.5: TS value versus $\langle\sigma v\rangle$ for 2D- (red), 1D-binned (blue) and integrated (black) likelihood at mass 1 TeV. Lines at TS values 2.71 and 3.84, corresponding to 95% (solid gray line) and 99% (dashed gray line) C.L. constraints respectively, are also shown.

7.3 Impact of uncertainties on the limits

7.3.1 Statistical uncertainty on the J-factor

The measured J-factors $J_{\rm obs}$ have statistical and systematic uncertainties. The statistical uncertainty on J can be treated as a nuisance parameter in the likelihood. The results shown in Chap. 10 do not include the systematic uncertainty but they account for the statistical one. The J-factor values follow a log-normal distribution with mean $\log_{10}\bar{J}$ and width equal to its 1σ RMS, σ_J:

$$\mathcal{J}(J|\bar{J},\sigma_J) = \frac{1}{\sqrt{2\pi}\sigma_J \log(10) J} e^{-\frac{(\log_{10} J - \log_{10}\bar{J})^2}{2\sigma_J^2}}. \tag{7.10}$$

The measured J-factor is one Gaussian realization that follows the $\mathcal{J}$ distribution. The best value of J is obtained through maximization of $\mathcal{J}$. The expected value is $\hat{J} = \bar{J}e^{-\sigma_J^2 \log^2(10)}$. Fig. 7.6 shows the TS versus $\langle\sigma v\rangle$ curves without (solid line) and with (dashed line) the likelihood term corresponding to the statistical uncertainty on the J-factor, for $\sigma_J = 0.4$. The 95% C.L. mean upper limits are given by the solid gray line. They degrade of a factor 2.3 when including the statistical uncertainty σ_J.

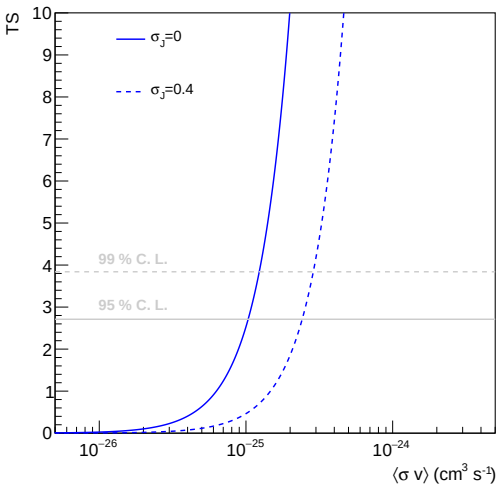

Figure 7.6: Profile of TS versus $\langle\sigma v\rangle$ with (dashed line) and without (solid line) including a statistical uncertainty $\sigma_J = 0.4$ on the J-factor, for a fixed DM mass.

In case of combination of targets or experiments k the likelihood in Eq. (7.4)[4] reads

$$\mathcal{L}_{\rm k}(N_{\rm S,k}, N_{\rm B,k}|N_{\rm ON,k}, N_{\rm OFF,k}, \alpha_{\rm k}) = \frac{(N_{\rm S,k}+N_{\rm B,k})^{N_{\rm ON,k}}}{N_{\rm ON,k}!}e^{-(N_{\rm S,k}+N_{\rm B,k})}\frac{(\alpha_{\rm k}N_{\rm B,k})^{N_{\rm OFF,k}}}{N_{\rm OFF,k}!}e^{-(\alpha_{\rm k}N_{\rm B,k})}. \tag{7.11}$$

The computation of the likelihood with J-factor uncertainty can be simplified by considering that $N_{\rm S,k}$ depends on $\langle\sigma v\rangle\, J_{\rm k}$ and that we know values of $\mathcal{L}_{\rm k}$ versus $\langle\sigma v\rangle$. The likelihood then writes

$$\mathcal{L}_{\rm k}(N_{\rm S,k}, N_{\rm B,k}|N_{\rm ON,k}, N_{\rm OFF,k}, \alpha_{\rm k}) = \mathcal{L}_{\rm k}\Big(N_{\rm S,k}\frac{J_{\rm k}}{J_{\rm obs}}, N_{\rm B,k}|N_{\rm ON,k}, N_{\rm OFF,k}, \alpha_{\rm k}\Big). \tag{7.12}$$

In practice, following this procedure, values of $\mathcal{L}_{\rm k}$ for different $J_{\rm k}$, possibly obtained with different binning or profiling techniques, can be shared among different experiments without releasing the data[5].

7.3.2 Systematic uncertainties

Systematic errors may be present in the photon count measurements. They can be due, for example, to acceptance inhomogeneities in the camera, variations of the observation conditions and differences of the energy scale in different parts of the camera. This ends up to a count number of events measured with a accuracy of a few percent or better in

[4] For simplicity we give the example for the integrated likelihood to avoid additional indexes in the formula, but the same approach is applicable to the 1D- and 2-D likelihoods.

[5] Note that this procedure is exactly valid in case there is one single region of interest. If the signal region is split in sub-regions of interest the uncertainty on the J-factor in each region may not be same and may need to be treated separately.

H.E.S.S.[6].

The presence of systematics limits the instrument sensitivity. Indeed, despite the increase of events statistics, that weakens the statistical uncertainty, at a certain point the observations will be dominated by systematic uncertainties. Understanding the behavior of the limits on the annihilation cross section in presence of systematics is crucial, especially for future array of telescopes like CTA that are expected to collect an huge statistical dataset with reduced statistical uncertainties compared to current IACTs.

The systematics can be accounted for in the likelihood function as nuisance parameters $\beta_{\mathrm{i,j}}$ distributed as a Gaussian with mean σ_β. Following [227] the 2D-likelihood is redefined as:

$$\mathcal{L}_{\mathrm{i,j}}(\boldsymbol{N_S}, \boldsymbol{N_B}, \beta_{\mathrm{i,j}} | \boldsymbol{N_{ON}}, \boldsymbol{N_{OFF}}, \boldsymbol{\alpha}) = \frac{[\beta_{\mathrm{i,j}}(N_{\mathrm{S,i,j}} + N_{\mathrm{B,i,j}})]^{N_{\mathrm{ON,i,j}}}}{N_{\mathrm{ON,i,j}}!} e^{-\beta_{\mathrm{i,j}}(N_{\mathrm{S,i,j}}+N_{\mathrm{B,i,j}})} \times \frac{[\beta_{\mathrm{i,j}}(\alpha_{\mathrm{j}} N_{\mathrm{B,i,j}})]^{N_{\mathrm{OFF,i,j}}}}{N_{\mathrm{OFF,i,j}}!} e^{-\beta_{\mathrm{i,j}}(\alpha_{\mathrm{j}} N_{\mathrm{B,i,j}})} \times \mathrm{e}^{-\frac{(1-\beta_{\mathrm{i,j}})^2}{2\sigma_\beta^2}}. \tag{7.13}$$

The best value of $\beta_{\mathrm{i,j}}$ is found by maximizing

$$\frac{\mathrm{d}\mathcal{L}_{\mathrm{i,j}}(\boldsymbol{N_S}, \boldsymbol{N_B}, \beta_{\mathrm{i,j}} | \boldsymbol{N_{ON}}, \boldsymbol{N_{OFF}}, \boldsymbol{\alpha})}{\mathrm{d}\beta_{\mathrm{i,j}}} = 0. \tag{7.14}$$

In the left panel of Fig. 7.7 β is given as function of σ_β in a specific bin $(i, j) = (1, 39)$, with the energy bin (j) selected to be at the peak of the events distribution (about 300 GeV) for $m_{\mathrm{DM}} = 1$ TeV. The cyan dashed line points to the value $\beta \sim 0.998$ corresponding to a typical value $\sigma_\beta = 0.03$. In the right panel of Fig. 7.7 the TS versus $\langle\sigma v\rangle$ with (green dashed line) and without (green solid line) bin-by-bin systematic uncertainty corresponding to $\sigma_\beta = 0.03$ is given for $m_{\mathrm{DM}} = 1$ TeV. The limits degrade of about 50%.

7.3.3 Impact of the energy resolution

The energy resolution of the experiment spreads the narrow signal and it is a factor of degradation of the sensitivity to signals like the DM monoenergetic *gamma lines*.

The left panel of Fig. 7.8 shows the Gaussian function spread for 5% (orange solid line), 10% (black solid line) and 20% (green solid line) width[7] around a mean of 3 TeV. The right panel of Fig. 7.8 shows the TS versus $\langle\sigma v\rangle$ for 5% (orange solid line), 10% (black solid line) and 20% (green solid line) energy resolution for a DM mass of 3 TeV. An improvement (degradation) of about 30% is observed on the 95% C.L. upper limits on the DM annihilation cross section by increasing (decreasing) the energy resolution from 10% to 5% (20%). However, this estimate does not account for a loss (gain) of events due to the different reconstruction cuts necessary to get a better (worse) energy resolution.

[6] Systematic uncertainty of 1% is usually quoted in H.E.S.S..

[7] The H.E.S.S. uncertainty is know better than at a factor 2.

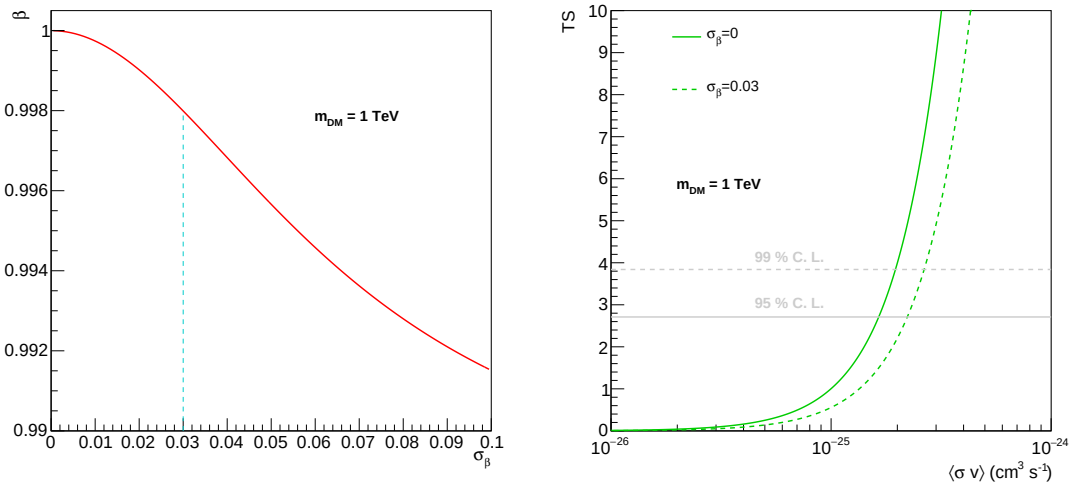

Figure 7.7: Test of the systematic uncertainties on the measurements. *Left panel:* β as function of σ_β in a specific bin for $m_{\rm DM} = 1$ TeV. *Right panel:* corresponding curve of TS versus $\langle\sigma v\rangle$ with (dashed line) and without (solid line) the parameter $\beta_{i,j}$.

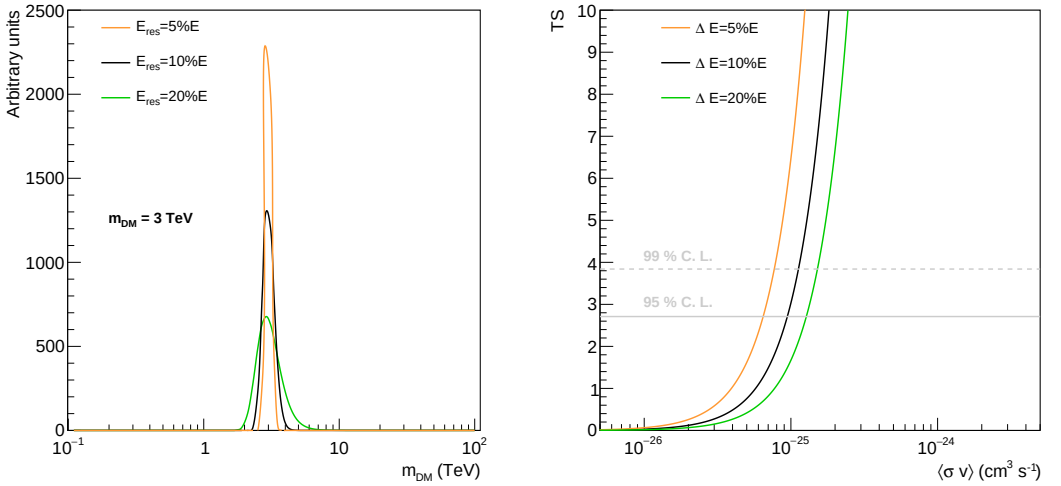

Figure 7.8: Impact of the energy resolution on a *gamma line*. *Left:* Gaussian functions of with 5% (orange solid line), 10% (black solid line) and 20% (green solid line) of the energy, for a DM mass of 3 TeV. *Right:* Curves of TS versus $\langle\sigma v\rangle$ at $m_{\rm DM} = 3$ TeV for 5% (orange solid line), 10% (black solid line) and 20% (green solid line) energy resolution. The 95% C.L. upper limits on $\langle\sigma v\rangle$ are given by the gray solid line.

7.3.4 Uncertainty on the background residual background determination

In this section we consider, as an example, the possibility that the event distribution in the residual background varies of 4% in the FoV due to a gamma-ray contamination that affects the measurement of the residual background but not the signal. We show a conservative way to treat this uncertainty estimating the impact on the limits. So, the expected and observed limits on $\langle\sigma v\rangle$ are recomputed for a background multiplied by a factor 1.04. The effect on the expected limits is of the percent level, *i.e.* negligible, but a 4% uncertainty on the residual background count number can strongly affect the observed limits, up to a factor 80% , as shown in Fig. 7.9.
The effect of a systematic uncertainty on the background measurement depends strongly on the available dataset and the presence of standard gamma-ray background components in the measurements, so a check must be made on a case-by-case basis on the real dataset.

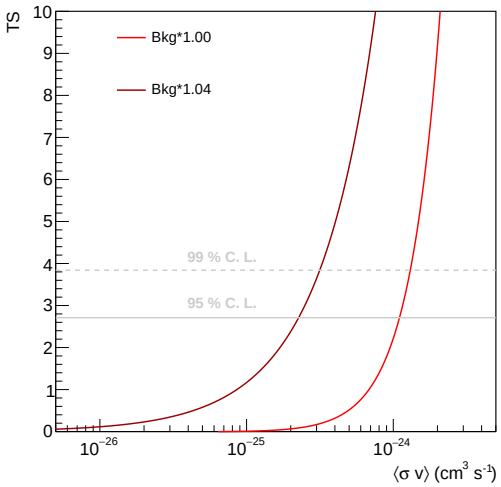

Figure 7.9: TS versus $\langle\sigma v\rangle$ for the residual background adding (burgundy solid line) or not (red solid line) 4% events. The 95% and 99% C.L. upper limits on $\langle\sigma v\rangle$ are given by the solid and dashed gray lines respectively.

7.4 Exclusion versus modeling of background components

Part of relevant regions of interest for DM search may harbor standard astrophysical VHE gamma-ray emissions. These are additional backgrounds for the DM search and should be identified for further rejection. This is the case for the GC, where, in the region where the DM density profile peaks, several standard astrophysical emitters and VHE gamma-ray diffuse emission are detected. However, in this region we have large gamma-ray statistics due to the observation campaign strategy and resulting high time exposure.

An example of the experimental analysis approaches that can be carried out in regions with diffuse emission in addition to the residual background is made for the GC. The region of interest is assumed to extend up to 2° in radius around the GC and the impact of the spatial extent of a standard diffuse emission from 0.3° to 1° on the dark matter sensitivity is studied. The region around the Galactic plane, that hosts TeV emission correlated with the CMZ and the several TeV sources, is difficult to model and therfore is excluded through a patch of latitude ±0.3°. If other standard astrophysical emissions are detected near the GC beyond that, the options are the following:

1. Exclude the region where the VHE gamma-ray diffuse emission is detected; or
2. Look for DM signal above the VHE gamma-ray astrophysical background $N_{\rm bkg}$ by modeling the background and including it in the likelihood function as $N_{\rm S} + N_{\rm B} \rightarrow N_{\rm S} + N_{\rm B} + N_{\rm bkg}$.

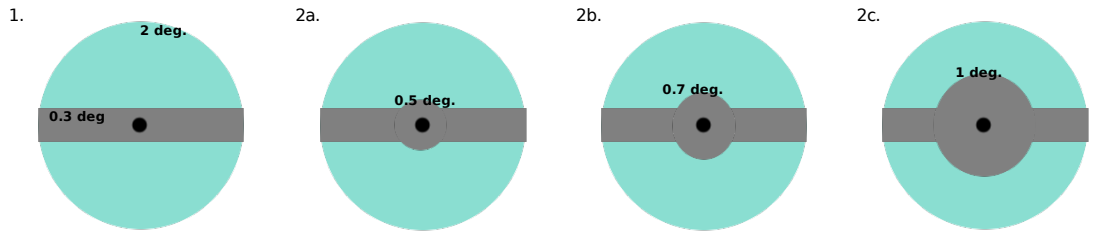

Figure 7.10: Schematic of the "exclusion" or "modeling" techniques that can be applied to DM search in a gamma-ray crowded region. A circular region of interest (teal area) of 2° around the GC (black dot) is considered here. In all the scenarios a band of ±0.3° is excluded (gray area) along the Galactic plane. In the sub-plot *1.* no other diffuse emission is detected so no additional exclusion is added. In the sub-plot *2.a* an additional circular region of 0.5° centered at the GC contains standard diffuse emission that may be modeled or excluded. In the sub-plot *2.b* the diffuse emission extends up to 0.7° from the GC. In the sub-plot *2.c* it extends up to 1° from the GC.

A schematic of these possibilities, for diffuse emission extending up to 1° in radius from the GC is shown in Fig. 7.10. The gamma-ray astrophysical background injected in the mock observations is modeled as a pure power-law with spectral index -2 and normalization at 1 TeV of 10^{-11} TeV^{-1} cm^{-2} s^{-1}, considered to be homogeneous in the region up to $r_{\rm bkg}$. A dark matter line signal at $m_{\rm DM} = 3$ TeV is injected following an Einasto profile. The LLRTS is applied for the line search for different cases: while including (strategy 2) a standard gamma-ray emission of variable radial extent from 0.3° up to 1° in radius from the GC, and while excluding (strategy 1) regions of dimension $r_{\rm bkg} = 0.3°$, $r_{\rm bkg} = 0.5°$, $r_{\rm bkg} = 0.7°$ and $r_{\rm bkg} = 1°$, respectively, in order to reject the astrophysical background. Fig. 7.11 shows how the TS profile vs $\langle\sigma v\rangle$ behaves for the above mentioned cases. The 95% C.L. upper

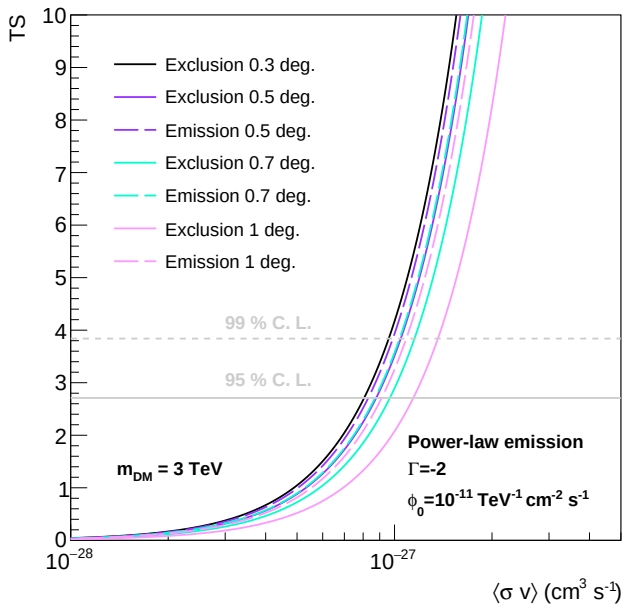

Figure 7.11: TS versus $\langle\sigma v\rangle$ in case of no standard gamma-ray emission beyond the Galactic plane and central emitter (black solid line) and in case of additional astrophysical diffuse emission around the GC up to 0.5° (violet lines), 0.7° (teal lines) and 1° (pink lines), respectively. Different approaches are compared: 1) excluding the region that hosts the astrophysical diffuse emission (solid lines), 2) modeling and including the diffuse emission in the likelihood (dashed lines). A power-law background with spectral index -2 and a flux normalization at 1 TeV of 10^{-11} TeV^{-1} cm^{-2} s^{-1} is injected in the mock observations to perform this study. In case we are able to perfectly model and subtract the astrophysical background we fall back to the ideal case of residual-background only an no additional exclusion region (black solid line).

limits on $\langle\sigma v\rangle$ are given by a gray solid line. The capability to model the astrophysical background would improve the sensibility to DM with respect to fully exclude it from the analysis. Indeed, excluding a region of 0.5°, 0.7° and 1° degrades the sensitivity of 9%, 20% and 40%, respectively, with respect to a residual background-only scenario, while including $N_{\rm bkg}$ in the likelihood would degrades them by 4%, 9% and 16%, respectively.
In H.E.S.S. the astrophysical background is so far entirely excluded from the region of interest, while the foreseen strategy for CTA is to model it.

7.5 The profiling likelihood technique

The LLRTS is not defined in a unique way. Different frequentist and hybrid approaches are possible. Some are described in this section:

1. An *hybrid profiling* approach, assuming $N_S = 0$ in the no-DM hypothesis, is based on:

$$\lambda(N_S) = \frac{\mathcal{L}(N_S, \hat{\hat{N}}_B(N_S))}{\mathcal{L}(0, \hat{\hat{B}}(0))}, \tag{7.15}$$

where $\hat{\hat{N}}_B$ is obtained through a conditional maximization, *i.e.* it depends on N_S as given by:

$$\hat{\hat{N}}_B = \frac{N_{ON} + N_{OFF} - (\alpha+1)N_S + \Lambda}{2(\alpha+1)} \tag{7.16}$$

with

$$\Lambda = \sqrt{\Big(N_{ON} + N_{OFF} - (\alpha+1)N_S\Big)^2 + 4(\alpha+1)N_{OFF}N_S}. \tag{7.17}$$

2. A *full profiling* approach [225], with no assumption about $\hat{N}_S$, is based on:

$$\tilde{\lambda}(N_S) = \frac{\mathcal{L}(N_S, \hat{\hat{N}}_B(N_S))}{\mathcal{L}(\hat{N}_S, \hat{N}_B)}, \tag{7.18}$$

valid for $0 \leq \hat{N}_S \leq N_S$.
In this approach $\hat{N}_B$ is a non-conditional maximization so it does not depend on N_S, which is also maximized independently:

$$\hat{N}_B = N_{OFF}/\alpha \qquad \text{and} \qquad \hat{N}_S = N_{ON} - N_{OFF}/\alpha. \tag{7.19}$$

If $\hat{N}_S < 0$ it falls back to the *hybrid profiling* approach. If $\hat{N}_S > N_S$, $TS \equiv 0$.
This approach may be problematic if the residual background is difficult to measure or model or if it is contaminated by a photons signal that can affect $\hat{N}_S$ and $\hat{N}_B$.

3. A *simplified* approach, that does not include the profiling of the likelihood, is based on:

$$\lambda(N_S) = \frac{\mathcal{L}(N_S, \tilde{N}_B)}{\mathcal{L}(0, \tilde{N}_B)}, \tag{7.20}$$

where $\tilde{N}_B = N_{OFF}/\alpha$ is extracted from measurements.

4. In case of *discovery* the TS becomes:

$$TS = -\ln \lambda(0), \tag{7.21}$$

where the discovery is defined based on the significance of an excess in the signal region, as described in Sec. 7.2.3.

The *full profiling* approach is the more robust and gives the best limits, but the hypothesis $0 < \hat{N}_S < N_S$ may not be easily satisfied when looking for a very small signal in a region,

like the GC, where the residual background can be slightly contaminated and difficult to estimate, or low statistics and therefore high fluctuations are present. In that case, the *hybrid profiling* approach is also a reasonable conservative choice.

7.6 Summary

The log-likelihood ratio test statistics is an optimal method to search for small signals due to new phenomena in high energy astroparticle physics. It can be straightforwardly applied to dark matter searches and in this case a 2-dimensional approach provides the highest sensitivity. It is used in Part IV and Part V of this work to set upper limits on the dark matter annihilation cross section, in absence of significant gamma-ray excess. Observed and expected limits have been defined and the technique to obtain mean expected limits and their containment bands has been explained. This section showed the improvement or degradation of the DM constraints while varying the parameters of the likelihood. As explained, nuisance parameters can be included in the likelihood to account for statistical and systematic uncertainties. Whether the systematic uncertainty can be modeled as a Gaussian nuisance parameter or not is not obvious and the Gaussian choice is taken for simplicity.

Part IV

Searches for dark matter with H.E.S.S. data

Chapter 8

Dark matter gamma-line search in the Galactic Center region with H.E.S.S. I

Contents

8.1 Observations and data set . . . 138
8.1.1 H.E.S.S. observation strategy of the GC . . . 138
8.1.2 Gamma-ray excess and significance sky maps . . . 138
8.2 Construction of the gamma-ray-like event PDFs . . . 139
8.2.1 Choice of the regions of interest . . . 139
8.2.2 Definition of the exclusion regions . . . 142
8.2.3 Energy-dependent event distributions . . . 142
8.3 Residual background measurement in the Galactic Center region . . . 143
8.3.1 The *Reflected Background* method . . . 143
8.3.2 Construction of the energy-dependent background PDFs . . . 145
8.3.3 Expected residual background PDF from blank-field observations . . . 146
8.4 Search for a gamma-ray signal excess . . . 146
8.4.1 Excess significance in each ROI . . . 146
8.4.2 Expected dark matter *gamma line* signal . . . 149
8.5 Constraining the annihilation cross section . . . 150
8.5.1 Expected and observed limits . . . 150
8.5.2 Comparison with other experiments . . . 151
8.5.3 Impact of cuspy dark matter profiles . . . 153
8.6 Study of the sources of systematics uncertainties . . . 154
8.6.1 Energy scale and energy resolution . . . 154
8.6.2 Test of azimuthal symmetry . . . 154
8.6.3 Impact of the Night Sky Background morphology . . . 156
8.7 Discussion and perspectives . . . 157

The Galactic Center is arguably one of the major targets for indirect dark matter search in gamma-rays. In this chapter we present H.E.S.S.-I dataset from 10 years of observations towards this promising region. The technique to measure the residual background and compare it to the events in the signal region is explained. Then the hypothesis of presence of a monoenergetic *gamma line* from dark matter annihilation is tested against a no signal hypothesis on the data. In absence of significant excess of photons, constraints are derived on the photon flux and the dark matter annihilation cross section. Statistical and systematic uncertainties are studied.
The dataset and the construction of the events distributions are presented in Sec. 8.1 and Sec. 8.2, respectively. In Sec. 8.3 and Sec. 8.4 the measurement of the residual background and the definition of the expected signal are explained. Constraints on dark matter annihilation cross section are derived in Sec. 8.5 and a study of the systematic uncertainties is presented in Sec. 8.6 This work has been published in Ref. [228].

8.1 Observations and data set

8.1.1 H.E.S.S. observation strategy of the GC

During the first phase of H.E.S.S., observations have been carried out for 10 years towards the region around the GC. The *wobble* observation technique (see Sec. 2.4) is applied with *offsets* up to 1.5° from the GC. The average *offset* is about 0.7°. This technique is preferred to the *ON-OFF* strategy (see Sec. 2.4.2) because it needs half the observation time and covers uniformly the ROI, provided it is not too extended. In addition it allows us to define signal and background regions in the same observational conditions, same *offset*, size and live time, *i.e.* contained in the same FoV, as explained in details in Sec. 2.4. The total data set over 10 years represents 254 live hours from 610 *runs*. Observations are selected for zenith angles up to 50°, but low zenith is preferred in order to achieve the lowest possible energy threshold. The average zenith angle is 19° and the distribution of zenith angles is shown in the left panel of Fig. 8.1. The mean zenith angle is marked with a pink line.
In order to give an estimate of the observation exposure of these 10 years of observations with the 610 cumulated *runs*, a map of the time exposure in the sky is shown in the right panel of Fig. 8.1, expressed in hours.

8.1.2 Gamma-ray excess and significance sky maps

First, a standard *Ring Background* analysis has been performed to measure the background and look for a signal excess in all the sky map. Sky maps of the excess of photons and its significance in the GC region are shown in the left and right panel of Fig. 8.2, respectively. The significance is computed with Eq. (7.6). The maps are given in bins of $0.02° \times 0.02°$, but they are covoluted for a Gaussian kernel with width chosen according to the H.E.S.S.

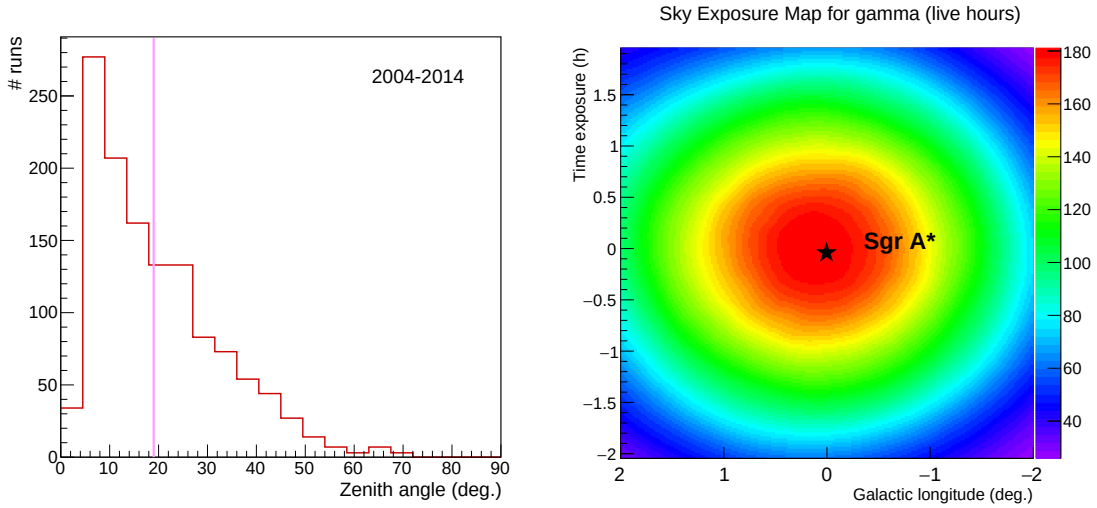

Figure 8.1: *Left panel:* Distribution of the observational zenith angle over 10 years of data taking towards the GC with H.E.S.S. I. About 60% of the observations have been taken at less than 20°. The mean zenith angle (pink line) is 19°. *Right panel:* Time exposure map from the analysis of 10 years of H.E.S.S. I observations towards the GC. The map is plotted in Galactic longitude and latitude and the time exposure is given in hours.

point spread function (PSF) of about 0.1°. The significance map is given in terms of σ. Both the maps are in Galactic coordinates. The position of Sgr A* is indicated as a black star in all the maps. The brightest emissions due to Sgr A* (HESS J1745-290) and G09+01 (HESS J1747-281) are visible on the plots yellow areas. The VHE diffuse emission and the extended source HESS J1745-303 are also visible.
A more sophisticated background measurement technique is applied for DM search and it is explained in Sec. 8.3.1

8.2 Construction of the gamma-ray-like event PDFs

8.2.1 Choice of the regions of interest

The region of interest, referred to as the *ON region*, is where the DM signal is searched for. It is defined based on the available photons statistic distribution in the sky, *i.e.* depending on the pointing strategy, and the expected DM density profile. The signal-to-noise ratio varies like the J-factor over the integration region θ. The J-factor Einasto profile integrated in θ divided by θ at the GC peaks around $\theta = 1°$, then flattens and decreases slowly and smoothly, as shown in Fig. 8.3 (red solid line). This is not true for a cored profile, for example with core size 1 kpc (cyan solid line), that keep increasing for large integration radii.

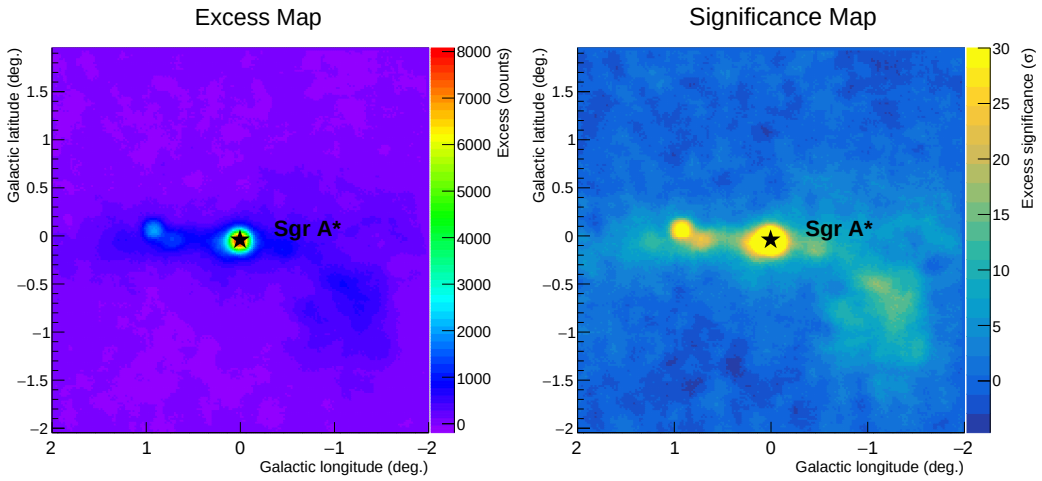

Figure 8.2: Excess and significance sky maps obtained from a *Ring Background* analysis of 10 years of H.E.S.S. I observations towards the GC. The maps are computed in bins of $0.02° \times 0.02°$ and they are convoluted for a Gaussian with width chosen according to the H.E.S.S. PSF. The maps are plotted in Galactic longitude and latitude. *Left panel:* Excess map. *Right panel:* Significance map.

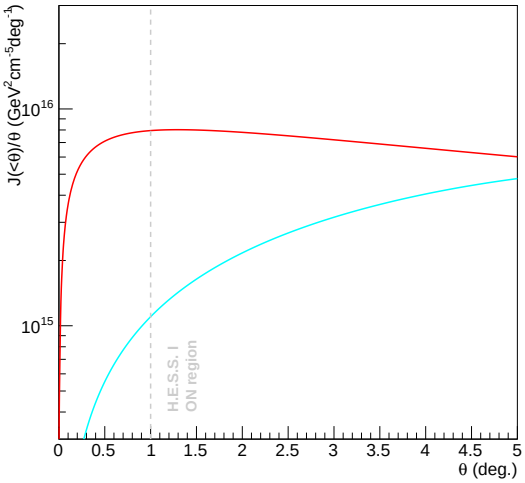

Figure 8.3: Integrated J-factor over θ as a function of θ for the Einasto profile (red solid line) and a 1 kpc cored profile (cyan solid line). The size of the *ON region* is marked by a gray dashed line. At about 1° the Einasto profile flattens while the cored profile grows.

The *ON region* is defined as a circle of 1° centered at (0°,0°), around the GC. It is then divided in seven sub-regions of interest (ROIs), defined as rings of width 0.1°, with inner radius from 0.3° to 0.9°.
The DM distribution is expected to be more dense, and eventually peaked, towards the GC and to degrade with the distance. This is one of the regions that hosts the largest amount of DM and the closest to us. On the other hands, as explained in details in Sec. 3.2, several point-like, extended and diffused sources of VHE gamma rays have been detected in the inner 300 pc of the Milky Way. These emissions constitute an important background for DM search and they cannot be easily modeled and subtracted, so they are excluded from the analysis region. Masks are put on the Galactic plane and other bright TeV gamma-ray standard emissions in the FoV (see Chap. 3).

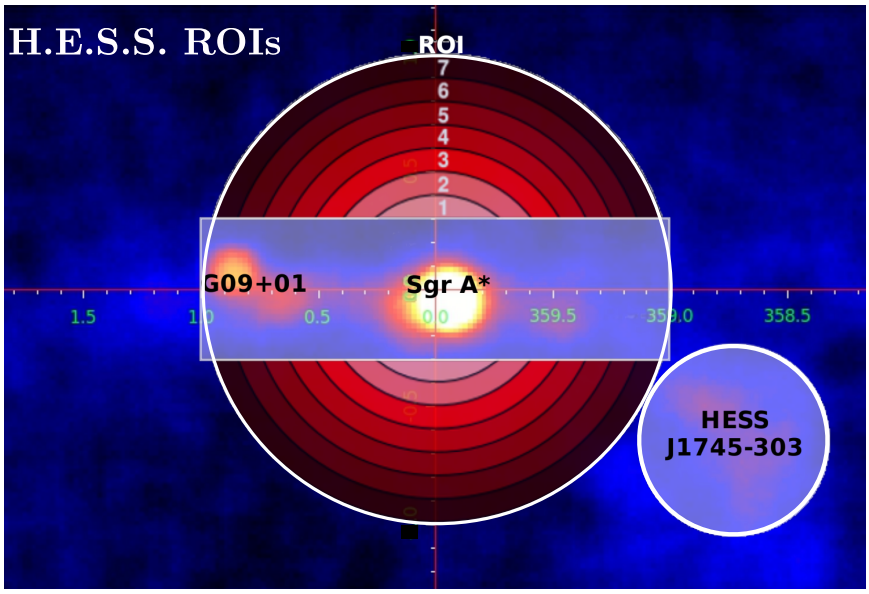

Figure 8.4: Schematic of the seven H.E.S.S. ROIs (red rings) in Galactic longitude and latitude with overlaid the exclusion regions (gray-shaded box and disk). The standard VHE gamma ray sources Sgr A* (HESS J1745-290), G09+01 (HESS J1747-281) and HESS J1745-303 are shown in the FoV.

8.2.2 Definition of the exclusion regions

In order to perform the residual background measurement, a set of masks is selected in several regions of the FoV to discard from the ROIs the areas dominated by standard astrophysical background. A band of $\pm 1^\circ$ in Galactic longitude and $\pm 0.3^\circ$ in Galactic latitude is excluded in order to cover most of the diffuse emission along the Galactic plane, Sgr A* and G09+01. A disk of radius 0.4° centered at $(-1.26^\circ, -0.64^\circ)$ masks HESS J1745-303.
The dimension of each ROI after adding these exclusions and the corresponding J-factor integrated in the ROIs, truncated by the exclusion regions, for an Einasto profile are shown in Tab. 8.1.

ROI #	$\theta_{\mathbf{min}}$ **(deg.)**	$\theta_{\mathbf{max}}$ **(deg.)**	$\mathbf{\Delta\Omega_{ROI}}$ **($\times 10^5$ sr)**	$\mathbf{J_{ROI}}$ **Einasto ($\times 10^{20}$ GeV^2 cm^{-5})**
1	0.3	0.4	3.1	3.8
2	0.4	0.5	5.0	5.2
3	0.5	0.6	6.9	6.2
4	0.6	0.7	8.8	6.9
5	0.7	0.8	10.8	7.5
6	0.8	0.9	12.7	7.9
7	0.9	1.0	14.6	8.2

Table 8.1: Inner and outer radii of each ROI are given together with the solid angle and the J-factor integrated in the ROI assuming the Einasto profile. These values are computed when removing the exclusion regions as described in the text.

The sky map in Galactic coordinates in Fig. 8.4 shows the 7 ROIs as rings of different shades of red. The excluded regions are represented as gray shaded patches. The H.E.S.S. emission positions of Sgr A*, G09+01 and the center of the extended emission HESS J1745-303 are marked on the map.

8.2.3 Energy-dependent event distributions

For each event selected as gamma-ray like the information about the energy and the position in the sky is reconstructed. The events are gathered depending on the ROI in which they fall. The distribution of these events as function of their energy is the *ON* probability density function (*PDF*). Fig. 8.5 shows the number of events in the *ON PDFs* in 1° (Z-axis) versus reconstructed energy in TeV (X-axis) and distance θ from the GC (Y-axis).

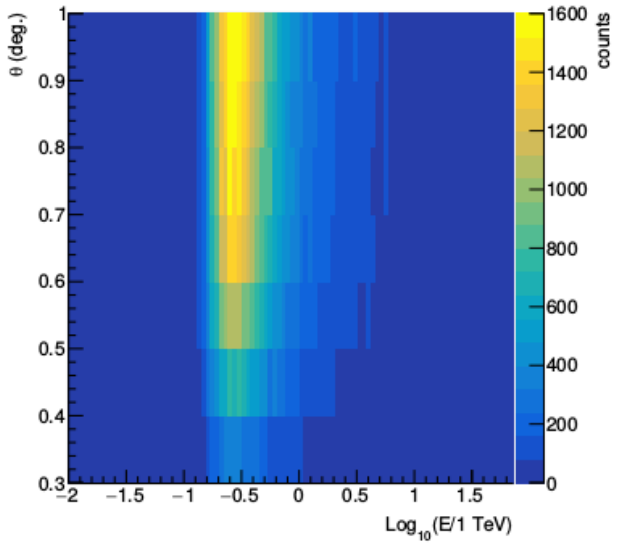

Figure 8.5: *ON PDFs* mapped as a function of the energy and the distance θ from the GC in degrees.

8.3 Residual background measurement in the Galactic Center region

8.3.1 The *Reflected Background* method

As explained in Sec. 2.4.2 different approaches are used to estimate the residual background. In parallel, there are modeling techniques that are being developed, like the run-wise simulations (RWS) [229], but they are not optimized yet for searching a signal in an extended region, with variable Night Sky Background (NSB) and possible multiple sources of diffuse emission. The dimension of the region and the presence of complex exclusion regions would not allow us to exploit the benefits of the *Multiple OFF* because a large α[1] would be difficult to achieve in this very crowded region in VHE gamma-rays.

The technique called *Reflected Background* is at the moment the best available option for DM search with H.E.S.S. in the GC region. It consists in measuring the residual background in the same FoV of the *ON region* but in another area called *OFF region* where there is low or null expected signal with respect to the *ON region*. The *OFF region* is defined on a *run*-by-*run* basis, *i.e.* for each observation *run*, and for each ROI. It is symmetric to the *ON region* with respect to the telescope pointing position. Thus, the signal and the background regions have the same shape and solid angle size. In addition, they are observed under the same conditions (weather, humidity, zenith angle, etc.). There is also azimuthal symmetry in the camera since the radial acceptance is the same in each direction at the same distance from the center. Indeed, the acceptance is the same in the *ON* and *OFF regions* without

[1] A standard value for α when measuring the residual background with the *Multiple OFF* technique is 10.

adding further offline correction, that would be otherwise needed when considering regions at a different radial distance from the center of the camera or with different shape and size. The same procedure is repeated for each *run* and each ROI. The left panel of Fig. 8.6

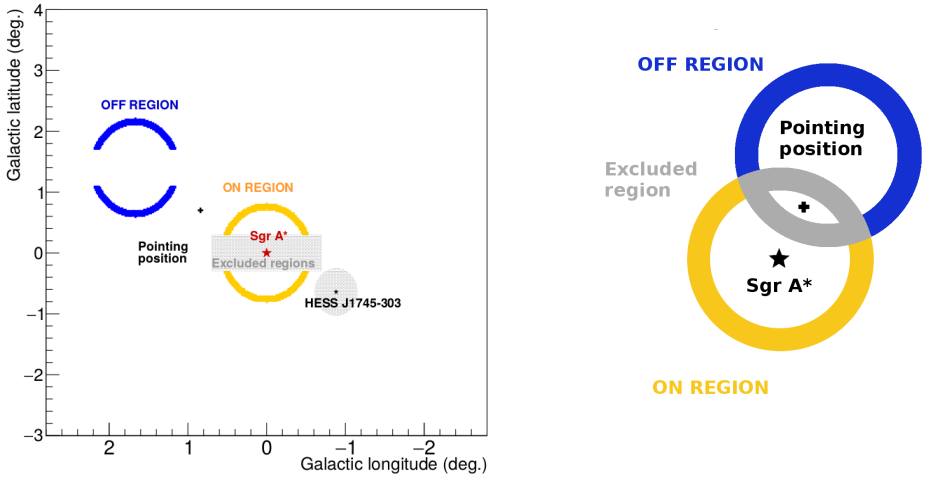

Figure 8.6: *Left panel:* Schematic representation in Galactic coordinates of an *ON* (orange) and a *OFF region* (blue) for a pointing position with the *Reflected Background* method. The excluded regions are a gray band and disk. The pointing position is marked with a black cross, the position of the center of the extended source HESS J1745-303 with a black star and Sgr A* with a red star. *Right panel:* Schematic representation of the additional exclusion regions (gray) due to overlapping of the *ON* (orange) and *OFF regions* (blue) or in regions where the *OFF region* is closer to the GC (marked as a star at the position of Sgr A*) than the *ON region*. This happens when the pointing position (black cross) is in the *ON region* or close to the GC.

shows a schematic of one ROI (orange area) and the corresponding *OFF region* (blue area) for a specific pointing position marked as a black cross. The gray patches represent the exclusion regions defined in Sec. 8.2.2. These regions are symmetrically excluded also in the *OFF region*. Following the same principle, if an *OFF region* falls in an excluded region, the corresponding symmetric area in the *ON region* is discarded as well in order to maintain same shape and size.

However, the *OFF region* is not far enough from the GC to be completely DM signal-free. It contains a substantial amount of DM, although always smaller than the *ON region*. This can be noticed in Fig. 8.7 where intensity maps of the expected DM signal, given in terms of J-factor, in the *ON* and *OFF regions* in Galactic coordinates for specific ROIs and pointing positions are represented. In the left panel of Fig. 8.7 ROI 2 is shown together with its corresponding *OFF regions* for two pointing positions:P (0.89°, 0.12°) and P(−0.42°, 0.55°). In the right panel of Fig. 8.7 ROI 5 is shown together with its *OFF regions* for the pointing

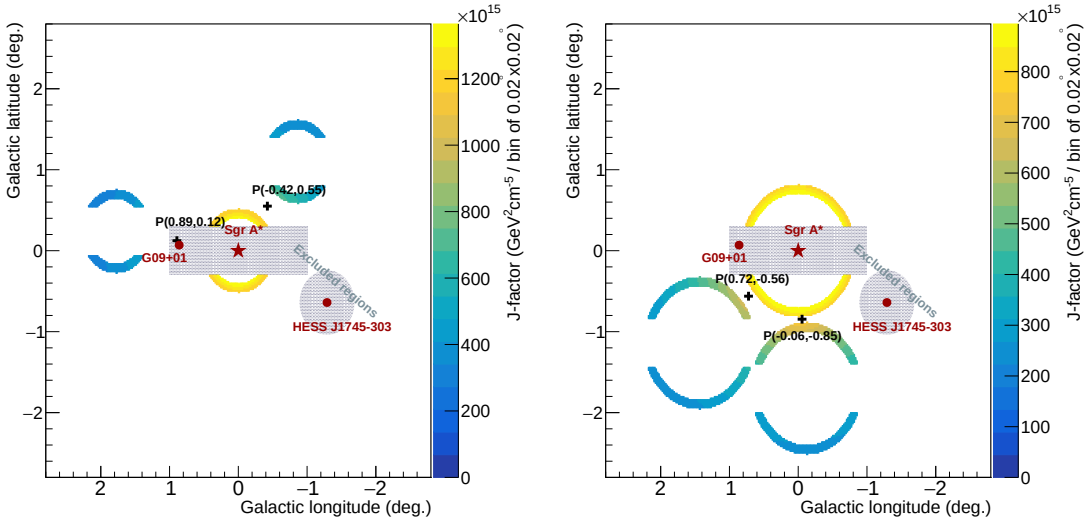

Figure 8.7: J-factor maps in Galactic coordinates of some *ON* (yellow/orange) and *OFF regions* (blue/green) that represent intensity of the expected DM signal in the regions. The map is binned with pixels of size 0.02° both in Galactic longitude and latitude. The excluded regions are gray patches. *Left:* map for ROI 2 (radius from 0.4° to 0.5°) and its *OFF regions* for observations at pointing positions P(0.89°, 0.12°) and P(−0.42°, 0.55°). *Right:* map for ROI 5 (radius from 0.7° to 0.8°) and its *OFF regions* for observations at pointing positions P(0.72°, −0.56°) and P(−0.06°, −0.85°).

positions P(0.72°, −0.56°) and P(−0.06°, −0.85°). In the right panel of Fig. 8.7 the *OFF regions* get closer to the *ON region* and the DM signal in the background region increases. In an extreme case, for large regions and pointing positions close to the GC, the two rings can overlap or the *OFF region* can get closer to the GC than the *ON*, *i.e.* hosts more DM. To avoid such configuration and maintain a significant positive DM gradient between the *ON* and the *OFF regions*, the overlapping and the areas where the *OFF* falls inside the *ON region* is excluded, as shown in the right panel of Fig. 8.6. As explained previously, the exclusion must take place symmetrically in the *ON* and in the *OFF regions* to keep the same size, therefore $\alpha = 1$. The full procedure is repeated for the 610 runs and 7 RoIs. The total J-factor, averaged over the time of each run, is computed for each ROI. The DM gradient obtained between the *ON* and *OFF region* decreases with increasing distance from the GC. It degrades from a factor 4.1 in the inner ROI to a factor 2.2 in the outer ROI, as the DM density fades out with the distance and the *OFF regions* get closer to the *ON*.

8.3.2 Construction of the energy-dependent background PDFs

The distribution of events detected in the *OFF regions* in each ROI is built as a function of the energy and called *measured OFF PDF* or for simplicity *OFF PDFs*. At a later stage these distributions are compared to the *ON PDFs*, looking for an excess in the *ON region*

with respect to the *OFF region*. The seven *OFF PDFs* are shown (red histograms) in Fig. 8.8, with respect to the *ON PDF* (blue histograms). The *PDFs* count 25 bins per decade and cover a $\log_{10}(E/1\,\mathrm{TeV})$ range from -1 to 1.68.

8.3.3 Expected residual background PDF from blank-field observations

Besides the residual background measured in the *OFF regions*, the energy-dependent distribution of misidentified hadrons can also be estimated from blank field observations. This is done using H.E.S.S. extragalactic observations far from the Galactic plane, at latitudes $|b| > 10°$. In this environment the NSB is isotropic and no diffuse emission is detected, thus it is ideal for a good estimate of residual background without contamination from VHE gamma-ray emissions. I built a script that selects extragalactic *runs* in the same observational conditions of the *runs* performed at the GC. The obtained event distributions are called *expected OFF PDFs*. Then they must be properly normalized to the live time and dimension of the *OFF regions* after cuts from an analysis performed on the Galactic plane. This method is expected to be accurate at about 20% [81].
The *expected OFF PDFs* (green histograms) are compared to the *measured OFF PDFs* (red histograms) in Fig. 8.9. The countings for the two *OFF PDFs* are given in Tab. 8.2. The *expected OFF PDFs* reproduce the *measured OFF PDFs* at the 10% level or better. Tab. 8.2 list the counts in the *measured* and *expected OFF PDFs* for each ROI and the percentage of agreement between the two.

ROI #	$\mathbf{N}_{\mathrm{OFF}}^{\mathrm{measured}}$	$\mathbf{N}_{\mathrm{OFF}}^{\mathrm{expected}}$	$\frac{\lvert\mathbf{N}_{\mathrm{OFF}}^{\mathrm{measured}}-\mathbf{N}_{\mathrm{OFF}}^{\mathrm{expected}}\rvert}{\mathbf{N}_{\mathrm{OFF}}^{\mathrm{measured}}}$
1	5500	6060	0.1
2	11091	11823	0.07
3	16289	16254	<0.01
4	21216	20726	0.02
5	22817	22893	<0.01
6	23645	24658	0.04
7	25079	27091	0.08

Table 8.2: Number of counts in the *measured OFF* and *expected OFF PDFs* and relative difference between the counts for each ROI.

8.4 Search for a gamma-ray signal excess

8.4.1 Excess significance in each ROI

The *ON* and *measured OFF PDFs* are compared on a ROI-by-ROI basis in order to search for significant signal. The excess significance can be evaluated in terms of standard deviations, σ, using Eq. (7.6). Tab. 8.3 lists the number of measured photons in the *ON* and *OFF*

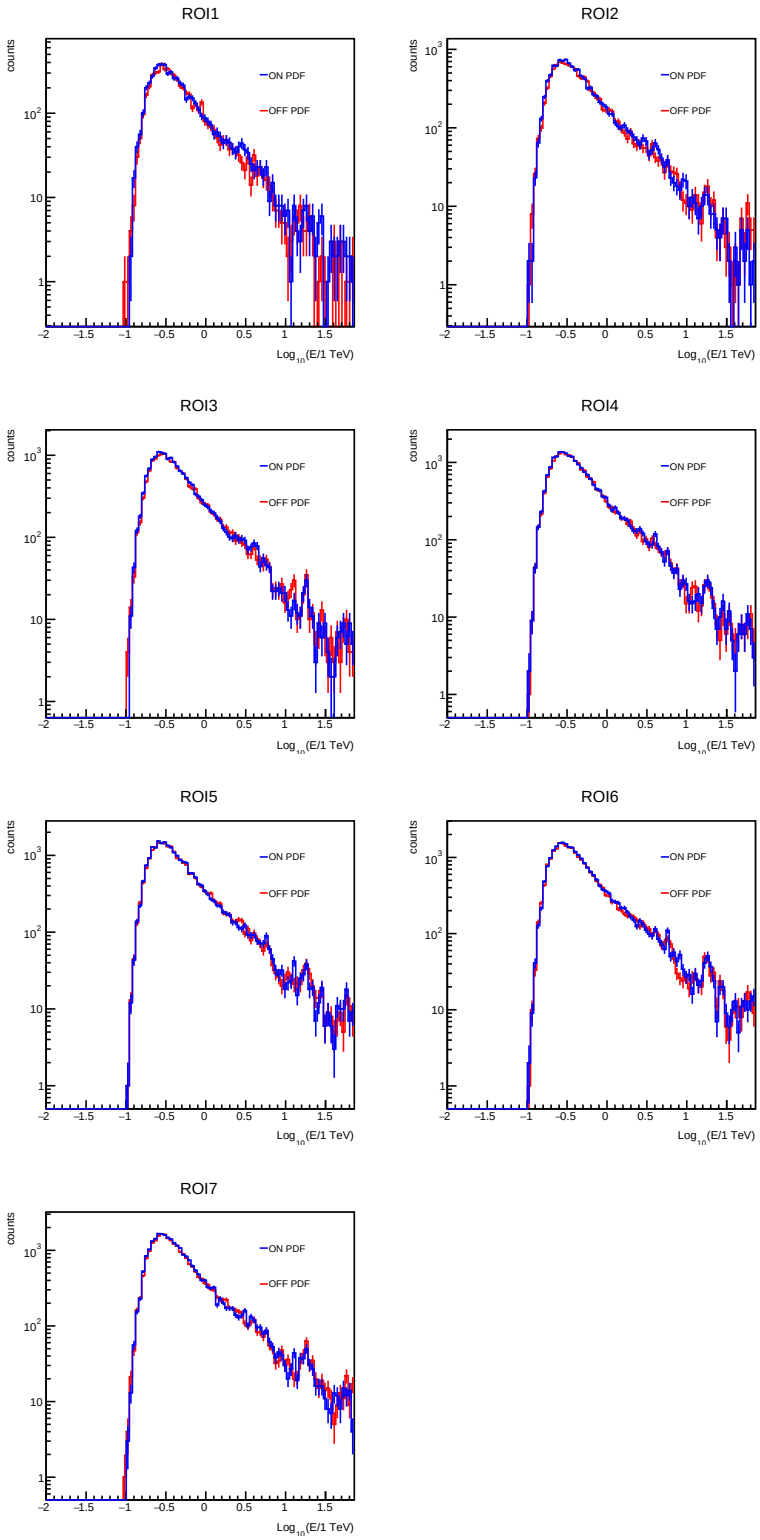

Figure 8.8: *ON* (blue) and *OFF PDFs* (red) overlaid, in blue and red respectively, as a function of the energy.

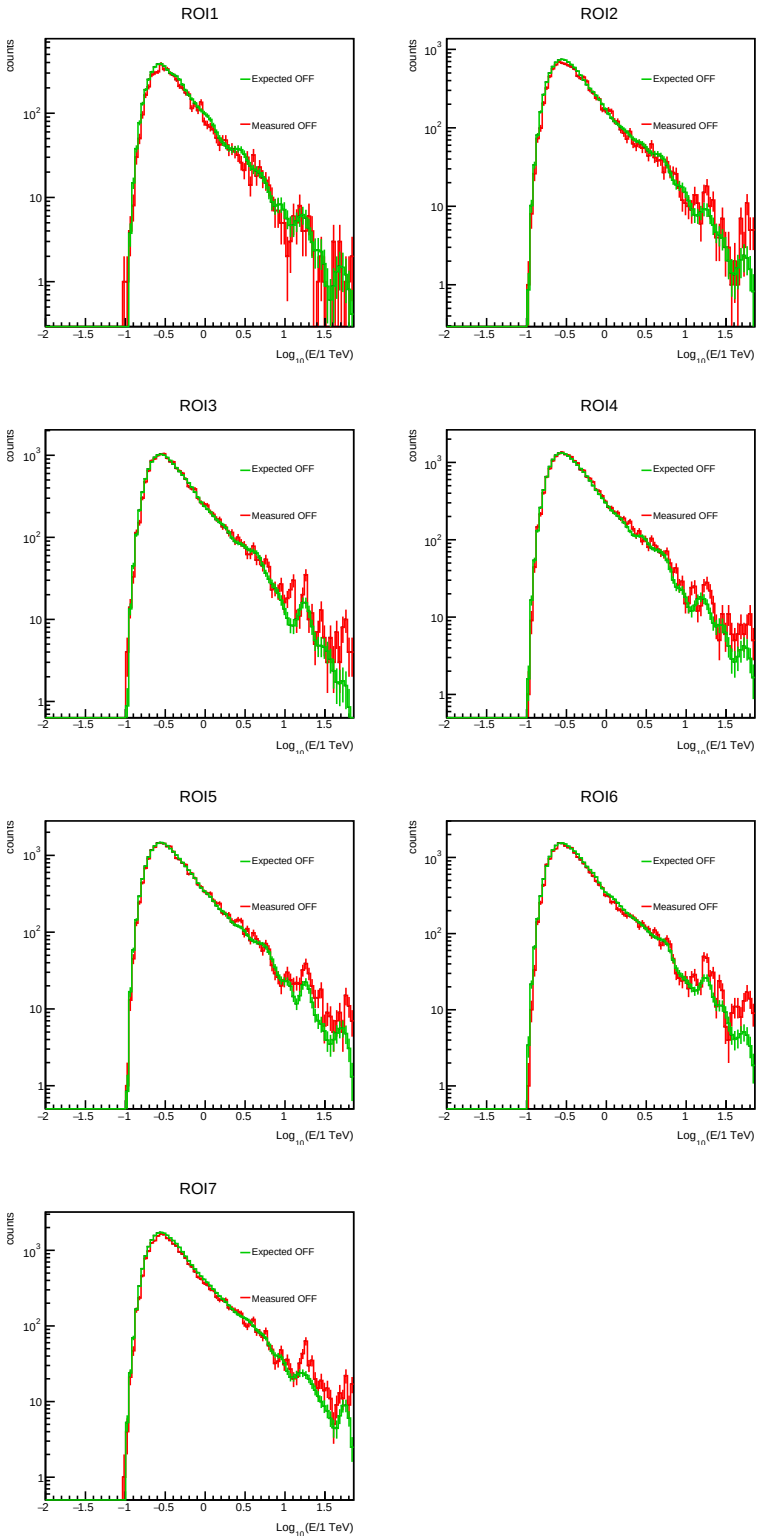

Figure 8.9: *Measured OFF* (red) and *expected OFF PDFs* (green) overlaid, in red and green, respectively, as a function of the energy.

PDFs and the significance, in terms of σ, of the excess above 300 GeV. No significant excess is detected in any of the ROIs.

ROI #	ON counts	OFF counts	Excess significance (σ)
1	5794	5500	1.2
2	11616	11091	2.3
3	16916	16289	1.5
4	21581	21216	0.6
5	23175	22817	0.5
6	24255	23645	2.7
7	25868	25079	1.9

Table 8.3: Counts of measured events in the *ON* and *OFF regions* and significance of the excess in the *ON region*, ROI-by-ROI.

8.4.2 Expected dark matter *gamma line* signal

Once an annihilation channel and a DM density profile are chosen the expected signal from DM annihilation in the previously defined ROIs can be computed.
The energy-differential flux per spectral and spatial bin $\frac{d\phi_\gamma}{dE}(E,\Omega)$ as defined in Eq. (6.8) can be converted to the expected number of photons by using the information about the observations and the experiment contained in the IRFs, *i.e.* the observation live time, the effective area and the energy resolution.
The DM *gamma line* spectrum of the process $\chi\chi \to \gamma\gamma$ is a Dirac delta function (see Sec. 6.8.2) at an energy equal to the DM mass. The finite energy resolution of the detector is taken into account. So the theoretical spectrum $\frac{dN_\gamma}{dE}(E)$ is convolved with a Gaussian of width equal to the energy resolution $\Delta E = 0.1E$ and mean m_{DM}, written as:

$$G(E) = \frac{1}{\sqrt{2\pi}\Delta E} e^{-\frac{(E-m_{\mathrm{DM}})^2}{2\Delta E^2}}. \tag{8.1}$$

The expected number of photons from DM annihilation per bin (i,j), $N_{\gamma,\mathrm{i,j}}$, is obtained from the differential flux by including the J-factor J_j integrated on the ROI of size $\Delta\Omega_j$, the energy-dependent effective area of the instrument $A_{\mathrm{eff}}(E)$ averaged over the zenith angle and *offset* and the observation live time T_{obs}[2]:

$$N_{\gamma,i,j} = T_{\mathrm{obs}} \int_{\Delta E_i} dE \int_{\Delta\Omega_j} d\Omega \frac{d\phi_\gamma}{dE}(E,\Omega) G(E) A_{\mathrm{eff}}(E) \tag{8.2}$$

[2]In the analysis histograms are used instead of continuous functions, so the integral becomes a sum over the energy bins.

The observations are considered homogeneous over the *ON region* up to 1°. The weight due to the different time length of each observation is already included in the integrated J-factor. The effective area is computed for the *run*-by-*run* actual zenith angle and offset, then averaged over the full dataset by weighting for the *run* live time over the total live time.
In Fig. 8.10 a DM *gamma line* (cyan), expected for $m_{\rm DM} = 1$ TeV and $\langle\sigma v\rangle = 10^{-26}$ cm^3 s^{-1}, is overlaid to the *ON* (blue) and *OFF PDFs* (red) measured in ROI 1.

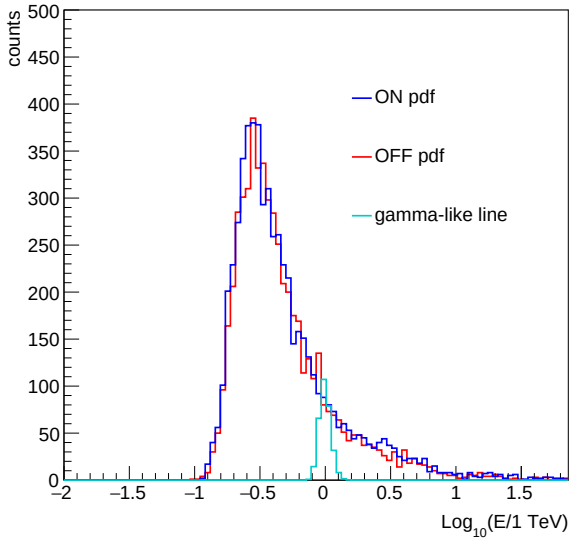

Figure 8.10: Expected DM line events distribution (cyan) for $m_{SM} = 1$ TeV and $\langle\sigma v\rangle = 10^{-26}$ cm^3 s^{-1},. Overlaid are the *ON* (blue) and *OFF PDFs* (red) for ROI 1.

8.5 Constraining the annihilation cross section

8.5.1 Expected and observed limits

In absence of significant excess in the *ON region* with respect to the *OFF region*, constraints can be derived on the thermally-averaged velocity-weighed annihilation cross section. In the LLRTS in Eq. (7.3), once the DM distribution and the annihilation channel are chosen and one specific $m_{\rm DM}$ is tested, the only free parameter is $\langle\sigma v\rangle$.
The 2D-likelihood described in Chap. 7 is computed under two hypotheses: in presence of DM and for a signal equals zero. The LLRTS is applied and the upper limits (U.L) at 95% confidence level (C.L.) are computed. They are referred to as the observed limits, that reflect excess in the *ON region*. With a narrow signal of width comparable to the bin size the observed limits reflect the fluctuations between the *ON* and *OFF PDFs* in a given energy bin.

The mean expected limits are computed by making several Poisson realizations of the background and the signal. For each run and ROI the *PDFs* are recomputed several times as independent measurements. For each realization the new *PDF* is computed by filling each energy bin with a random number following a Poisson probability function with mean equal to the measured value in the same bin. The LLRTS procedure is then performed in each realizations. The mean of the distribution of the $\langle\sigma v\rangle$ values corresponds to the mean expected limits. The standard deviation of the same distribution provides the containment bands at 1σ and 2σ.

For the DM search with 10 years of H.E.S.S. I data towards the GC the Einasto profile is assumed and a monoenergetic line signal from prompt annihilation of DM into two photons is looked for. The 95% C.L. observed upper limits on $\langle\sigma v\rangle$ and on the flux as a function of the DM mass are shown in Fig. 8.11 (red dots) [228]. These are upper limits, *i.e.* all the $\langle\sigma v\rangle$ values above them are excluded. The mean expected limits are shown (black solid line) together with the containment bands at 1σ (green band) and 2σ (yellow band) level obtained from 100 Poisson realizations. The thermal relic cross section for the process $\chi\chi \to \gamma\gamma$ from [230] is represented as a gray shaded area.
The previous H.E.S.S. I observed (blue squares) and expected (blue solid line) constraints from 2013 (112 h live time) [231] are overlaid. The 68% containment band from 2013 is shown on the flux[3]. At about 1 TeV the new limits presented in this work improve the previous H.E.S.S. limits by a factor about 6. The improvement comes from the new background measurement technique, the 2D-likelihood approach, the doubled gamma-ray statistics and the improved raw data analysis with *Model ++* (instead of *HAP*) that provides better efficiency of gamma-ray selection and hadron rejection.

8.5.2 Comparison with other experiments

The new H.E.S.S. limits on $\langle\sigma v\rangle$ reach 4×10^{-28} cm^3 s^{-1} at 1 TeV. They are the most constraining ever obtained so far in the TeV DM mass range, assuming an Einasto profile. The constraints obtained in this work are compared to those from other experiments in the left panel of Fig. 8.12.
The limits by MAGIC (green solid line) are computed from about 160 hours of observations on Segue 1 [232]. They assumed a J-factor $\log_{10}[J(< \theta_{\rm ROI})/{\rm GeV}^2\ {\rm cm}^{-5}] = 19.5$ in their ROI, value that could be overestimated up to a factor 100 [233]. The constraints by VERITAS (orange solid line) are obtained by stacking observations on 19 dwarf galaxies, including Segue 1 (with $\log_{10}[J(< \theta_{\rm ROI})/{\rm GeV}^2\ {\rm cm}^{-5}] = 19.2$ in their ROI), for a total observation time of about 230 hours [234].
These limits towards dwarf galaxies are 2 to 3 orders of magnitude smaller than those obtained by H.E.S.S. (red dots) towards the GC because these objects are further from

[3]The systematic error was estimated to be about 50 % on previous H.E.S.S.-I flux upper limits.

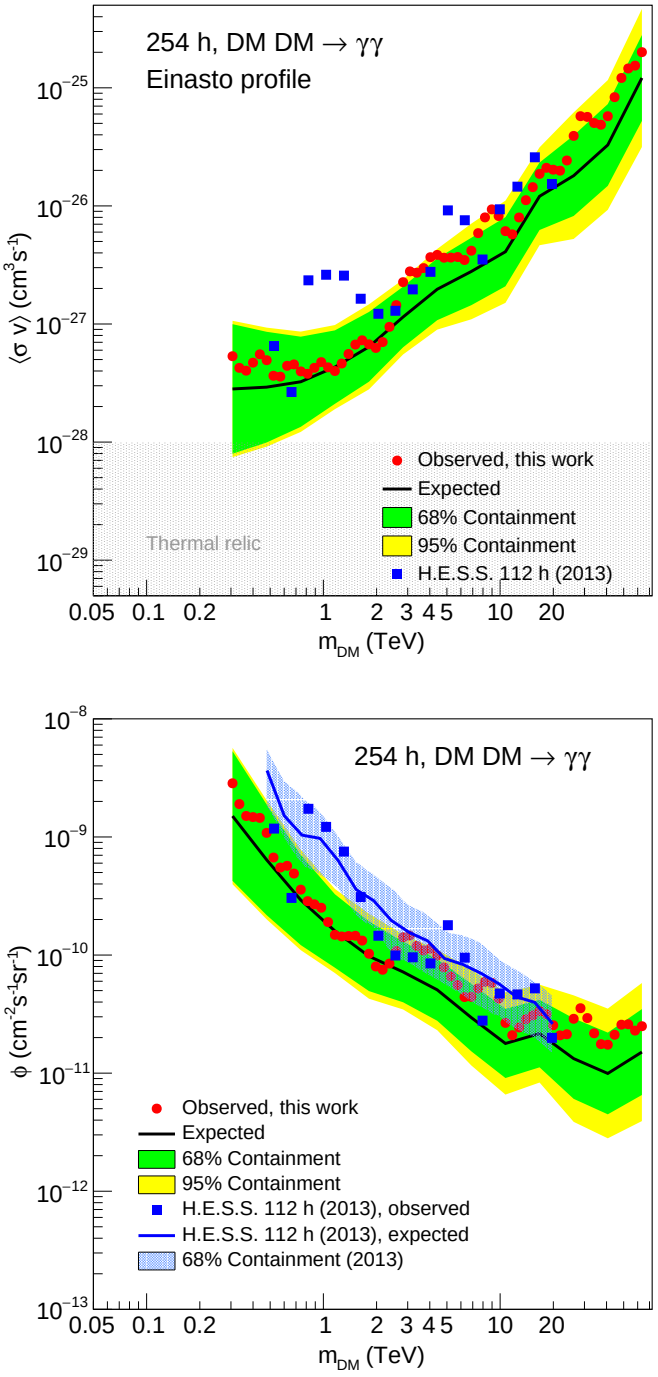

Figure 8.11: 95% C.L. U.L. on photons flux (bottom) and DM annihilation cross section (top) from 10 years of observation of the GC region with H.E.S.S. I. Observed (red dots) and mean expected (black solid line) limits are shown together with 1σ (green band) and 2σ (yellow band) containment bands. Previous H.E.S.S. results from 2013 are shown (blue) together with 1σ containment bands (blue shaded area).

the Sun and host less DM, i.e. they have smaller J-factor, and the event statistics is reduced (smaller $T_{\rm obs}$). From this point of view H.E.S.S. is advantaged by its position in the Southern hemisphere, a unique location among the current existing IACTs. Advantages and disadvantages of the dwarf galaxies as targets for DM search are discussed in Sec. 6.6. The constraints by Fermi-LAT from 5.6 years of data taking with *PASS 8* analysis and Einasto profile[4] [95] are also shown (black solid line). Fermi-LAT limits are more constraining at lower energies that cannot be reached by IACTs and degrade in the hundred-GeV mass range. H.E.S.S. limits are competitive with those from Fermi-LAT in the lower part of H.E.S.S. energy range. They overlap at 300-500 GeV. At 500 GeV H.E.S.S. is 7 times more constraining than Fermi-LAT. Fermi-LAT and H.E.S.S. together put the strongest constraints on DM annihilation in the GeV to tens TeV mass range, *i.e.* in the WIMP mass range.

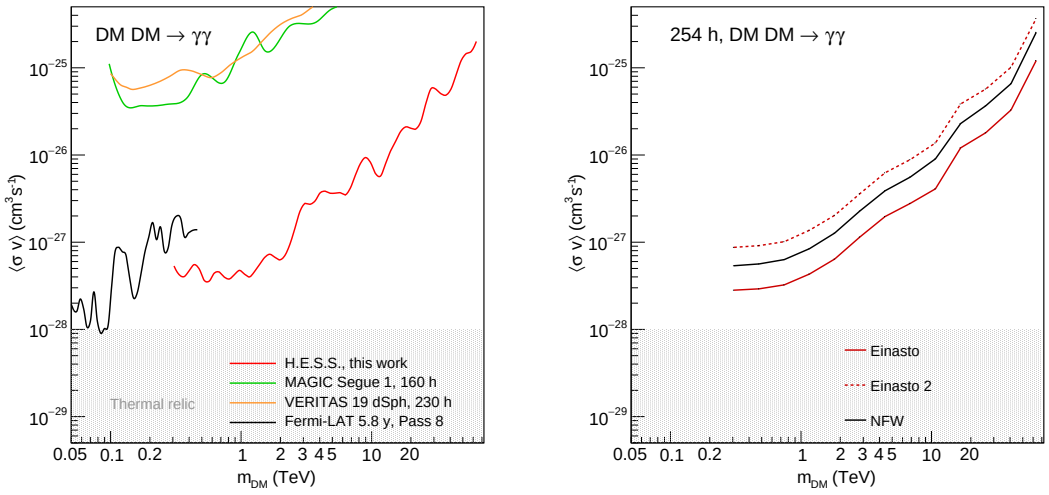

Figure 8.12: *Left panel:* Observed limits on $\langle\sigma v\rangle$ by H.E.S.S. (this work, red solid line) and Fermi-LAT (black solid line) towards the GC, MAGIC (green solid line) and VERITAS (orange solid line) towards dSph. H.E.S.S. and Fermi-LAT limits overlap at a few hundred GeV and together they set the most stringent limits so far on DM annihilation cross section in the GeV-TeV mass range. *Right panel:* H.E.S.S.-I mean expected limits on $\langle\sigma v\rangle$ computed at 95% C.L. assuming different DM profiles: Einasto profile with the parametrization chosen for the main analysis (red solid line), Einasto with different parameter values (red dashed line) and NFW profile (black solid line), with parameters given in Tab. 8.4.

8.5.3 Impact of cuspy dark matter profiles

The impact of different cuspy DM density profiles on H.E.S.S. I sensitivity to DM *gamma lines* is studied. Einasto and NFW profiles are compared. For more details on their

[4]Referred to as *R16* analysis in the Fermi-LAT paper.

parametrization see Sec. 6.5. The parameter values used here are summarized in Tab. 8.4. The mean expected limits are shown in the right panel of Fig. 8.12. The Einasto profile with the parametrization chosen for the main analysis (red solid line) gives the more constraining limits. Note that DM profiles with large cores are allowed but cannot be used in combination with the *Residual Background* method because the *OFF regions* would fall inside the core.

Profile	Einasto [207]	NFW [207]	Einasto [208]
ρ_0 **(GeV cm^{-3})** [235]	0.39	0.39	0.39
ρ_S **(GeV cm^{-3})**	0.079	0.307	0.033
r_S **(kpc)**	20.0	21.0	28.4
α_S	0.17	/	0.17

Table 8.4: Parameter values for different DM profiles used in this work. The Einasto profile with parameters taken from [207] is the one used in the main analysis.

8.6 Study of the sources of systematics uncertainties

8.6.1 Energy scale and energy resolution

Due to their dependency on the zenith angle and *offset*, there is an uncertainty on the energy-dependent quantities like the energy scale and the energy resolution, which may also vary from one energy bin to the other. Systematic uncertainties on these quantity can degrade the DM limits. The impact of the uncertainty on the energy scale and the energy resolution has been studied.

First, as standard in H.E.S.S., a 5% uncertainty on the energy scale is assumed. The energy reconstructed for each photon is biased by 5% and the limits on the annihilation cross section are recomputed. An effect on the $\langle\sigma v\rangle$ constraints up to 15% shift is derived, with a slight energy dependence.

Second, the energy resolution has been artificially deteriorated of a factor 2, testing the effect of an extreme energy resolution degradation. The expected signal in the *ON region* is recomputed for a Gaussian of width 20% of the energy instead of 10%. The constraints on $\langle\sigma v\rangle$ for the new signal are affected up to a 25%.

The effect of the systematics on the energy reconstruction are accounted for together: in order to be conservative and avoiding double counting of uncertainties, the largest of the two shifts on the limits is chose. A systematic of 25% is included in the containment bands shown in Fig. 8.11.

8.6.2 Test of azimuthal symmetry

Besides the radial variation of the acceptance, the telescope effective area is considered azimuthally symmetric, *i.e.* without significant inhomogeneous response in the cameras.

If radial-only variation of the acceptance is a good description of the CR background, the map of recorded events at different angles would be constant within the statistical errors. A test is made to validate the assumption of azimuthal symmetry. The hadron-like events are used here since they are isotropically distributed and a large statistics is expected. 27 runs at the same pointing position $(-0.7°, -0.4°)$ are stacked. First, the isotropy assumption is tested by comparing the acceptance-corrected number of counts $x_{\rm i}$ in a 0.5° radius disk taken in each of the four quadrants. d.o.f is the number of degrees of freedom, *i.e.* the number of tested regions -1: $d.o.f. = 3$. The reduced χ square $\chi^2 = \frac{1}{\rm d.o.f}\sum_{i=1}^{n_{\rm pixel}s}\frac{(x_i-\bar{x})^2}{x_i}$ is 0.88, *i.e.* no important anisotropy is observed in hadron-like events.

Then, an annular region centered at (-0.7°,-0.4°) is chosen to test azimuthal symmetry, with inner and outer radii 0.5° and 0.6°, respectively. The ring is split in small squared pixels of size 0.02° × 0.02° and the number of hadron-like events in each pixel is measured. The left panel of Fig. 8.13 shows the considered region, plotted in Galactic coordinates with the number of counts in the Z-axis. The distribution of the hadron-like events as

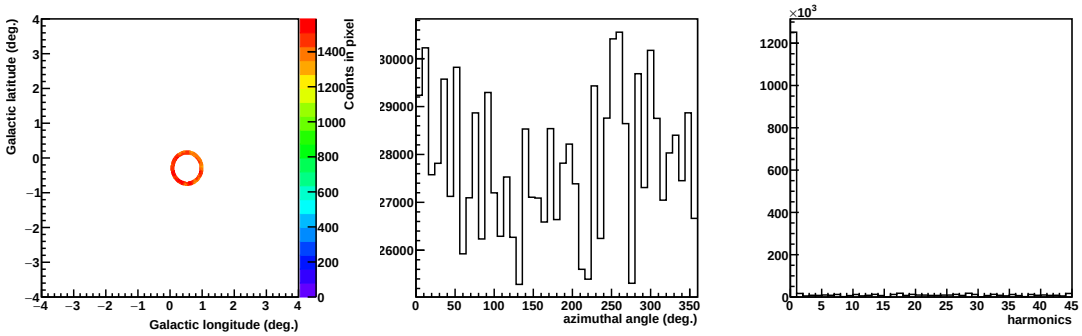

Figure 8.13: Test of azimuthal symmetry. *Left panel:* Region of the sky, in Galactic coordinates, chosen for the test. The Z-axis represents the number of hadron-like events per pixel of dimension 0.02° × 0.02°. *Central panel:* distribution of the number of counts at different azimuthal angles around the pointing position. *Right panel:* harmonic of the fast Fourier transform of the distribution of counts with respect to the azimuth. No significant harmonic beyond the 0=th. No periodicity is observed in the variation of the number of events.

function of the azimuthal angle is shown in the central panel of Fig. 8.13. It does not show any significant specific behavior beyond a constant. This is confirmed by the plot of the magnitude of the first fast Fourier transform in the right panel of Fig. 8.13, where no significant harmonic is observed beyond the 0-th one. No systematic uncertainty on the azimuthal symmetry is therefore added in the expected containment bands shown Fig. 8.11.

8.6.3 Impact of the Night Sky Background morphology

The NSB, described in Sec. 2.3.3 is the optical photons detected by the cameras from stars or diffuse light in the sky. The NSB can be estimated during calibration. The *Model ++* analysis chain is able to account for the NSB contribution in every pixel and partially take it into account [53]. A map of the NSB in the GC region is shown in the left panel of Fig. 8.14 in Galactic coordinates with the NSB rate in MHz in the Z-axis. The NSB is not uniform in the FoV of the GC. It varies from one quadrant to another, ranging from 100 up to 300 MHz. The brightest localized regions correspond to bright stars, and an extended high-NSB region is observed in the third quadrant. The right panel of Fig. 8.14 shows the

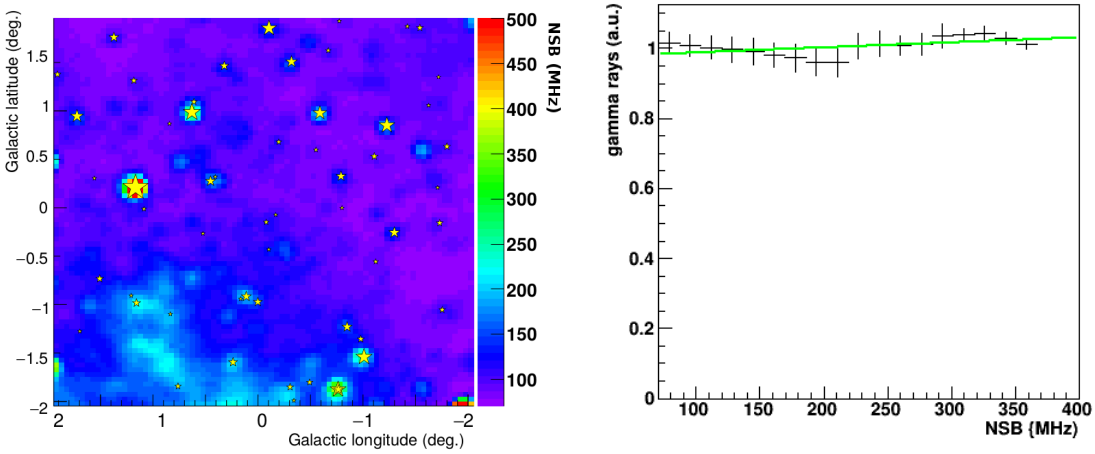

Figure 8.14: *Left:* Night Sky Background intensity map (MHz) in Galactic coordinates in the GC region. *Right:* Distribution of the gamma-like rate (residual background) as function of the NSB (MHz), normalized to 1. The standard deviation in the Y-axis is 0.036.

reconstructed gamma-ray-like rate versus NSB rate in the whole FoV, normalized to one. The distribution is compatible with 1 with a 4% systematic uncertainty.

An additional test is made to check this systematic error which should be reflected in an uncertainty on the count number of gamma rays in different regions of the sky. All the runs are stacked together in order to average on possible small effects of inhomogeneities in the FoV. The number of gamma-like events, normalized for the same time exposure, is measured in four regions, one in each quadrant. These regions are defined as disks of radius 0.5° centered in $(-0.8°, -0.8°)$, $(0.8°, -0.8°)$, $(0.8°, 0.8°)$ and $(-0.8°, 0.8°)$ in Galactic longitude and latitude, respectively. In the first quadrant the number of counts per pixel is 13640 with RMS 423. In the second quadrant the number of counts per pixel is 14284 with RMS 550. In the third quadrant the number of counts per pixel is 13820 with RMS 499. In the fourth quadrant the number of counts per pixel is 13099 with RMS 458. The RMS is larger than what is expected from statistical fluctuations. Therefore, these measurements show a

3% systematic uncertainty in the first quadrant, 3.8% in the second, 3.5% in the third and 3.4% in the fourth. A conservative value 4% is taken for the overall systematic uncertainty. The count number in different quadrants varies mainly due to NSB, but also due to other faint gamma-ray diffuse emissions that may leak into the ROIs, and both contribute to this systematic uncertainty.

The effect of the NSB variation and other gamma-ray standard non-isotropic emissions is accounted for as an overall 4% variation on the number of measured photons.The *OFF PDFs* are rescaled of a factor 1.04 and the limits on $\langle \sigma v \rangle$ are recomputed. A shift in the constraints is observed, ranging from the percent level (at high energies) to 60% (at low energies). This systematic uncertainty is added in the expected containment bands in Fig. 8.11. Alternatively, the variation of the background in the *OFF region* and the uncertainty on the azimuthal symmetry could be interpreted as an uncertainty of the normalization $\alpha = 1.00 \pm 0.04$ of the residual background between the *ON* and *OFF regions* in the likelihood.

8.7 Discussion and perspectives

The analysis of the full H.E.S.S.-I dataset towards the Galactic Center looking for monoenergetic *gamma lines* from dark matter annihilation shows the power of the most efficient analysis techniques, *Model++*, applied for the selection and reconstruction of gamma rays used in indirect dark matter search with Cherenkov telescopes. Previous results of dark matter search with H.E.S.S. in the same annihilation channel had been published in 2013. The full 10-years dataset used in this work double the available photon statistics. In addition, the *Model ++* photon reconstruction and selection improves H.E.S.S. sensitivity at low energy with respect to the previously used *HAP* raw-data analysis. A 2D-likelihood approach is now standard in the Galactic Center region since H.E.S.S. results of *continuum* dark matter signal search in 2016. Including the bin-by-bin spatial and spectral information specific to expected dark matter signals improves the sensitivity as well. An event-by-event analysis is not optimal for a dataset as large as $\sim$ 1.5 million gamma-ray like events. The *reflected background* technique is also specifically developed for dark matter search in a complex region where other standard astrophysical gamma-ray emissions are present. Attention is paid to the presence of a dark matter signal also in the background regions and to its effect on the likelihood function.

All the above mentioned improvements allowed us to set with this work the most stringent limits so far on the annihilation cross section in the TeV mass range for dark matter prompt annihilation into two photons. The strongest limit of 4×10^{-28} cm^3 s^{-1} is obtained at 1 TeV. The thermal relic cross section is not probed yet, if no further enhancement like the Sommerfeld effect (see Sec. 6.8.3) is considered on the line signal.

With the full H.E.S.S.-II telescope array and new strategy of survey of the Galactic Center

region our sensitivity to dark matter is expected to increase. First results including CT5 are shown in Chap. 9.

Chapter 9

Dark matter signal search with the Inner Galaxy Survey

Contents

9.1 2014-2018 observational datasets 160
9.1.1 Definition of the regions of interest 160
9.1.2 Exclusion regions for dark matter search with H.E.S.S. II 161
9.2 *Mono* analysis of the IGS data 162
9.2.1 *Mono* effective area 162
9.2.2 Construction of the *ON* and *OFF* event *PDFs* 164
9.2.3 Data unblinding and expected signal 167
9.2.4 Observed and expected constraints on the annihilation cross section . . . 169
9.2.5 Comparison with previous H.E.S.S.-I limits and other experiments 171
9.3 Towards an *hybrid* analysis of IGS data 172
9.3.1 *Combined* reconstruction 172
9.3.2 Definition of the PDFs in *combined* reconstruction 174
9.4 Outlook and perspectives 176

The H.E.S.S.-II dataset accumulated in 2014-2018 has been used for DM searches in *continuum* annihilation channels including observations carried out with the Inner Galaxy Survey. The regions of interest have been updated and extended thanks to the Inner Galaxy Survey pointing strategy and significant statistics at $|b| > 1°$. Acceptance corrections in the computation of the measured counts and expected signal are introduced in order to account for the large *offsets*. In addition, updated exclusion regions are chosen with respect to H.E.S.S.-I analysis. The first constraints on the dark matter annihilation cross section with CT5 are computed. The strategy for a CT1-5 dark matter search is discussed at the end of the chapter.
The dataset, the definition of the region of interest and the exclusion regions for H.E.S.S. II are described in Sec. 9.1. The *CT5 Mono* analysis of H.E.S.S.-II data for which the Inner Galaxy Survey provides the most significant part, is presented in Sec. 9.2. The construction of the *ON* and *OFF PDFs* is explained. The first H.E.S.S.-II constraints on the dark matter annihilation cross section are computed in *Mono* and compared to other studies. The framework for an upcoming *Combined* analysis is then discussed in Sec. 9.3. This work will be presented at ICRC19 and it will possibly be subject of an upcoming paper.

9.1 2014-2018 observational datasets

In this analysis the 2014-2018 dataset is used including the IGS observations. A description of the observations is given in Chap. 5. The overall five-year dataset counts 970 observation *runs* for a total of about 390 hours for the full 14-pointing-position campaign after quality cuts. The time exposure is not completely homogeneous on 3° in radius around the GC as aimed, but enough photon statistics is accumulated at large latitudes to significantly enlarge the signal region with respect to H.E.S.S.-I analysis presented in Chap. 8.
These data have been taken with the full CT1-5 H.E.S.S.-II array, thus, analyses can be performed both in *Combined* and in *Mono* modes. The *Mono* analysis in Sec. 9.2 is used for the moment for the DM search because the pipeline for a *Combined* analysis is still preliminary. Anyway, some information about the strategy to adopt with a *Combined* analysis is given in Sec. 9.3. A *Combined* analysis is expected to give better results. Increased CT1-5 stereo trigger rate and larger camera effective FoV are expected, thanks to the stereoscopy.

9.1.1 Definition of the regions of interest

Thanks to the observations at latitudes up to 3.2° from the GC position the *ON region* size for DM search can be extended from 1° to 4° in radius. Following H.E.S.S.-I analysis the ROIs are defined as rings centered at the GC with width 0.1°. Fig. 9.1 shows the *ON region* together with the exclusion regions from the H.E.S.S.-I analysis and the IGS pointing positions. New exclusion regions are chosen for the H.E.S.S.-II analysis in order to exclude

the more extended VHE diffuse emission. The number of ROIs is now 27 instead of 7 with inner radii from 0.3° to 2.9°. The definition of the ROIs is the same for a *Mono* and a *Combined* analysis.

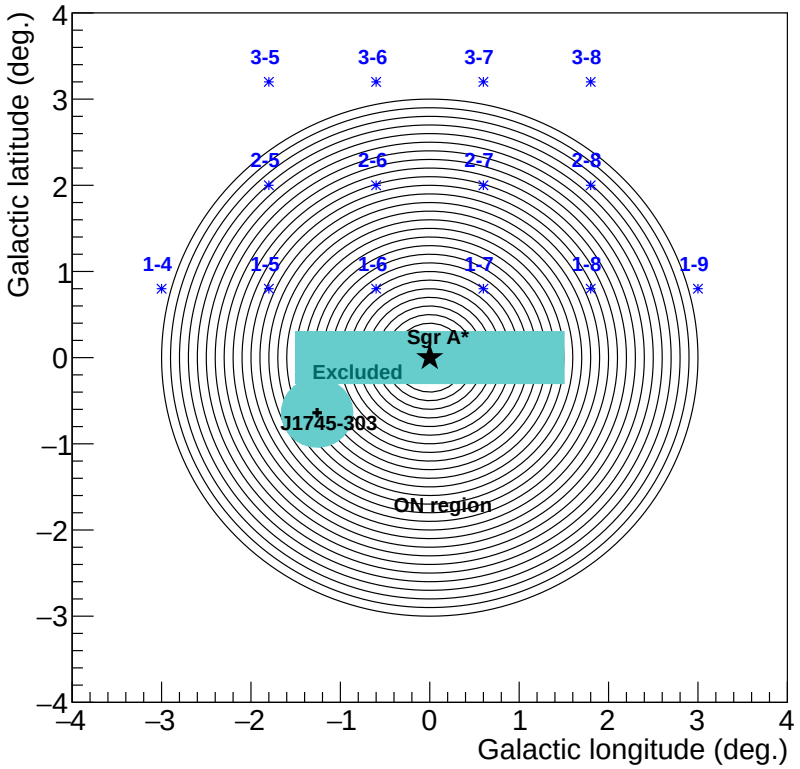

Figure 9.1: Schematic of the ROIs up to 3° with H.E.S.S.-I exclusion regions (azure boxe and disk). The pointing positions of the IGS are marked by asterisk markers and their names 1-x, 2-x and 3-x. The main standard VHE gamma-ray sources in the FoV are HESS J1745-290 (Sgr A*, black star) and J1745-303 (black cross).[1]

9.1.2 Exclusion regions for dark matter search with H.E.S.S. II

As shown in Fig. 9.2 the H.E.S.S.-I exclusion regions (gray lines) are not sufficient to reject most of the diffuse emission and to prevent from its leakage into the signal region. Updated exclusion regions for DM search with H.E.S.S. II are chosen and listed in Tab. 9.1 with their name, their position and the dimension of the disk-shaped patch that masks them. The 'GC X' exclusions are masks included in the H.E.S.S. standard GC analyses in order to reject emissions along the Galactic plane correlated to molecular clouds and most of diffuse emissions. The other exclusions are taken from the Galactic Plane Survey (GPS) [81] (see Sec. 3.2). All the GPS sources up to about ±8° in longitude or latitude

from the GC are excluded[2]. The additional hot-spots labeled 'New' are other new emissions wit significance $> 4\sigma$ observed in the whole FoV. These additional patches are added on emissions compatible with H.E.S.S. PSF $\sim 0.1°$ or larger. Fig. 9.2 shows the updated exclusion regions (white lines) including the 'New' patches (pink lines), overlaid to the H.E.S.S.-II excess significance map, artificially saturated at 6σ.
The updated exclusions reject the two inner ROIs reducing them to 25 broken rings with inner radii from 0.5° to 2.9°.

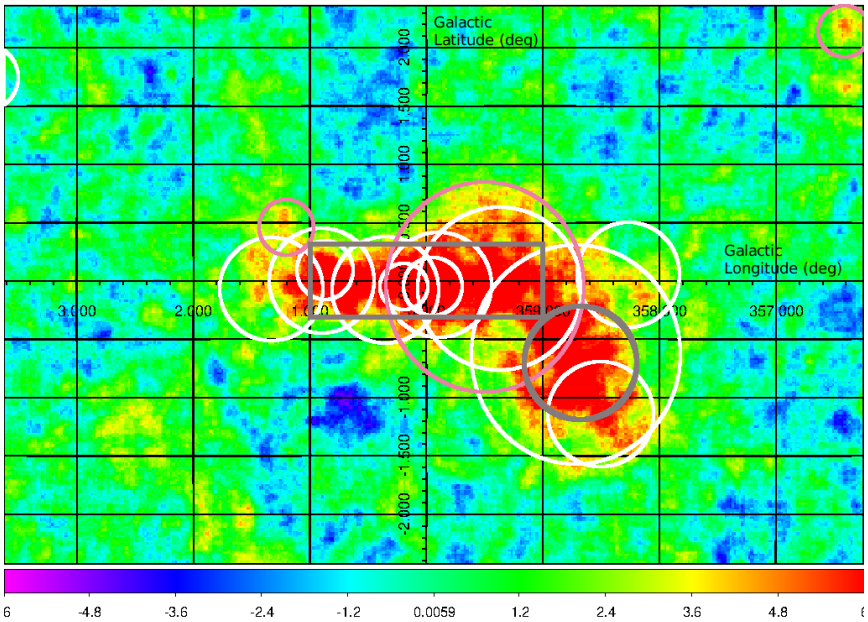

Figure 9.2: H.E.S.S.-II *Mono* significance map with overlaid exclusion regions for DM search. H.E.S.S.-I analysis exclusion regions are shown (gray lines), but must be updated in order to avoid the leakage of the extended diffuse emission into the signal region. Updated exclusion regions in correspondence of known VHE gamma-ray emissions are shown (white lines) together with additional patches (pink lines) at the position of hot-spots without known counterparts.

9.2 *Mono* analysis of the IGS data

9.2.1 *Mono* effective area

In Chap. 5 we presented the *Mono* analysis of the H.E.S.S.-II data towards the GC and showed the gamma-ray acceptance, excess and significance sky maps. The same dataset is used for DM searches. However, here the *Reflected Background* method (see Sec. 8.3) is applied on *CT5 Mono* analysis on a *run*-by-*run* basis, as done for H.E.S.S.-I analysis. For

[2]These ranges are chosen under the conservative hypothesis that the photon statistics is negligible beyond: $\sim 3.2°$ (largest pointing position) + 3.5° (largest FoV) +0.9° (dimension of a very extended source.)

Source name	Gal. long. (deg.)	Gal. lat. (deg.)	Radius (deg.)
GC A	1.326	-0.08	0.45
GC B	0.906	-0.	0.45
GC C	0.36	-0.07	0.45
GC D	-0.09	-0.04	0.45
GD E	-0.62	-0.07	0.45
HESS J1741-302	-1.737	0.05	0.45
HESS J1745-303	-1.289	-0.64	0.9
HESS J1747-248	3.81	1.74	0.3
HESS J1746-285	0.14	-0.11	0.25
HESS J1746-308	-1.55	-1.11	0.4
HESS J1804-216	8.4	-0.028	0.8
HESS J1801-240	6.61	-0.24	0.3
HESS J1800-240	5.95	-0.33	0.6
HESS J1729-345	-6.61	-0.02	0.45
HESS J1731-347	-6.46	-0.67	0.5
HESS J1801-233	6.66	-0.27	0.4
New 1	-0.5	0.1	0.95
New 2	1.7	3.7	0.4

Table 9.1: List of excluded regions that are masked in the DM analysis. Their name, the position in Galactic coordinates and the radius of the disk mask are given.

H.E.S.S. II additional selection cuts are introduced in order to account for the IGS pointing positions at variable distance from the GC and the decrease of the photons statistics with the distance from the center of the camera. The mean acceptance averaged on the zenith angle, the muon efficiency and the *offset* is not accurate enough for the new dataset where a large range of *offsets* between the pointing position and the events that fall in each ROI is present. The effective area is then averaged only on the muon efficiency and the zenith angle of the observations which is fairly stable from one year to the other since the data taking is performed in the same way every year. The dependency on the *offset* is accounted for explicitly. The mean acceptance is binned in *offset* ranges at $(0.0°, 0.5°)$, $(0.5°, 1.0°)$, $(1.0°, 1.5°)$, $(1.5°, 2.0°)$, $(2.0°, 2.5°)$, $(2.5°, 3.0°)$ and $(3.0°, 3.5°)$. A cut in *offset* is set to 3.5°. Fig. 9.3 compares the acceptances computed for the same dataset, but fixing different *offsets*. The energy threshold for events selection is chosen for each gamma-like event at 10% of the maximum acceptance[3] and it varies with the chosen *offset* range. For small *offsets* d the acceptance is overall larger and it peaks about 1 TeV. For large *offsets* it degrades and it shifts towards larger energies. At 3° *offset* the effective area degrades of a few orders of magnitude at low energies. For example, at about 600 GeV the acceptance is 10^{13} m^2 for $d > 3°$ and 3×10^{14} m^2 for $d < 0.5°$.

[3]This is a standard procedure, see Sec. 2.5.

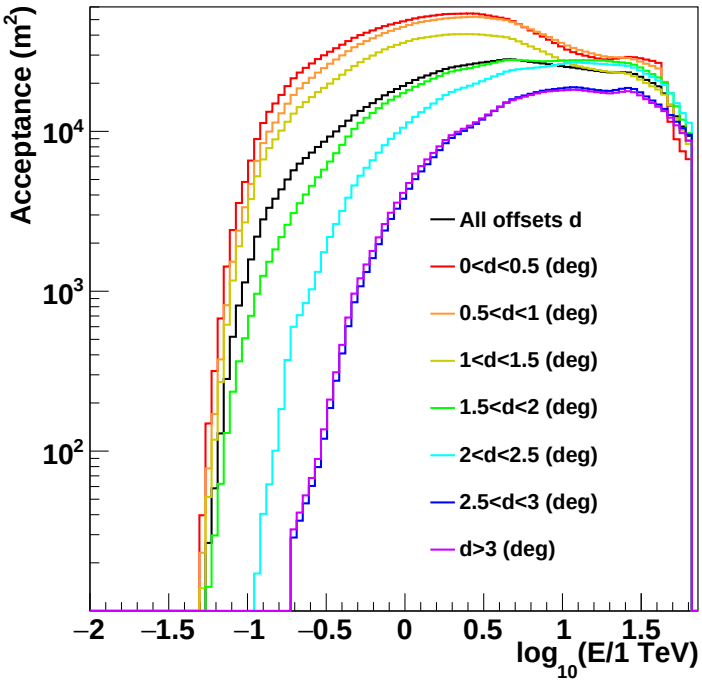

Figure 9.3: H.E.S.S.-II *Mono* effective area for different ranges of *offset*. The acceptance is averaged on the zenith angle and muon efficiency and computed in a selection of *offset* ranges: $(0.0°, 0.5°)$ (red solid line), $(0.5°, 1.0°)$ (orange solid line), $(1.0°, 1.5°)$ (yellow solid line), $(1.5°, 2.0°)$ (green solid line), $(2.0°, 2.5°)$ (cyan solid line), $(2.5°, 3.0°)$ (blue solid line) and above 3° (violet solid line). The acceptance averaged on the *offset* (black solid line) is also shown.

9.2.2 Construction of the *ON* and *OFF* event *PDFs*

The *ON* (red histograms) and *OFF PDFs* (black histograms) as function of the gamma-ray energy in Figs. 9.4 and 9.5 are built following the *Residual Background* method applied in the H.E.S.S.-I analysis. Since the high-latitude IGS pointing positions and larger *ON regions* allow for large offsets, the acceptance behavior at different *offsets* is taken into account in the *PDFs* contruction. Indeed, events at *offset* larger than 3.5° are excluded because beyond this value the *Mono* acceptance degrades significantly and it is subject to strong uncertainties. For events at *offset* $< 3.5°$ a hard threshold is set according to the acceptance criteria and it depends on the observation *offset*.
Since the *ON* and *OFF regions* are build with the *Reflected Background* method their dimension is the same, *i.e.* $\alpha \equiv 1$ in the likelihood function given in Eq. (7.8).

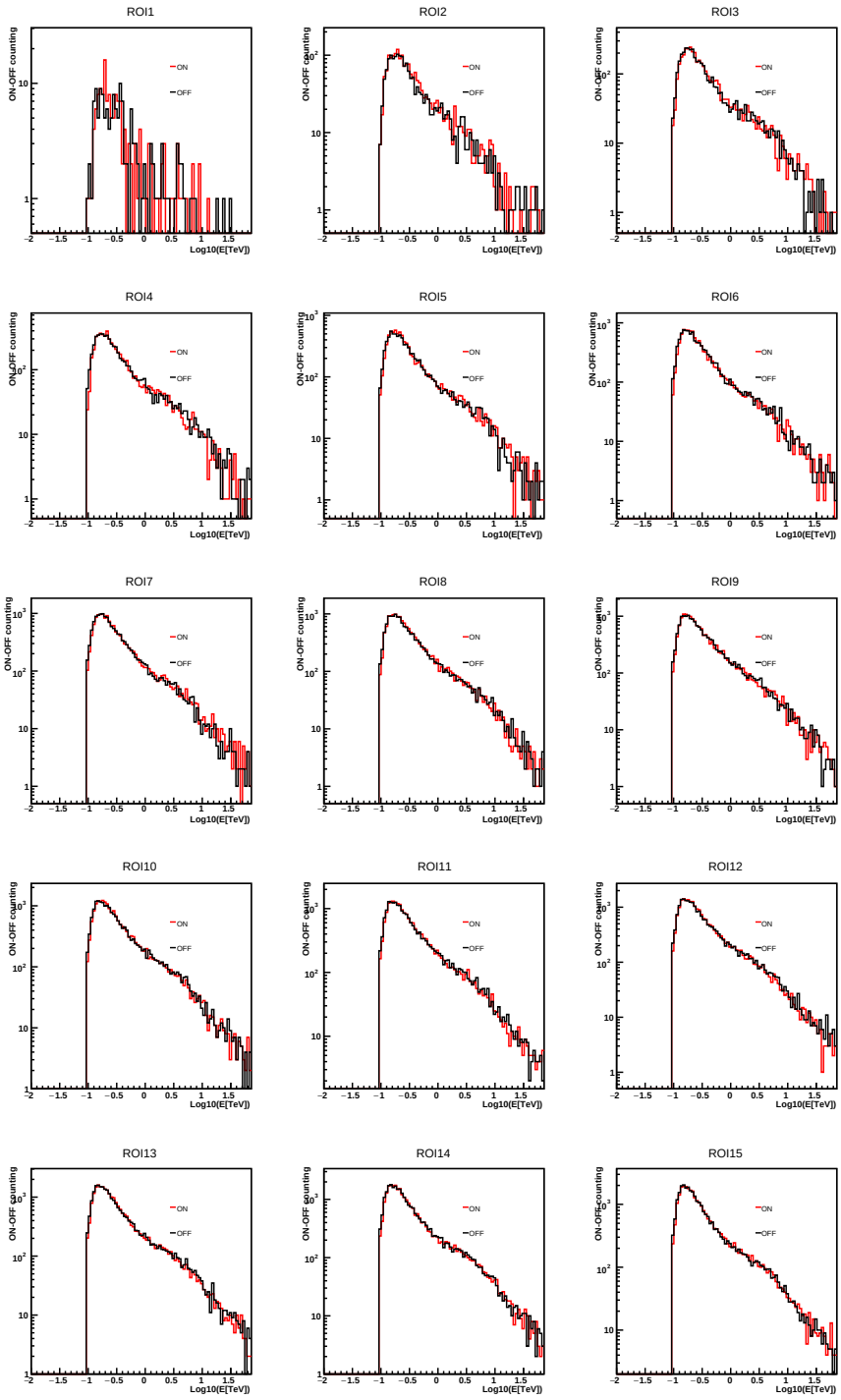

Figure 9.4: *ON* (red) and *OFF PDFs* (black) for ROIs 1 to 15.

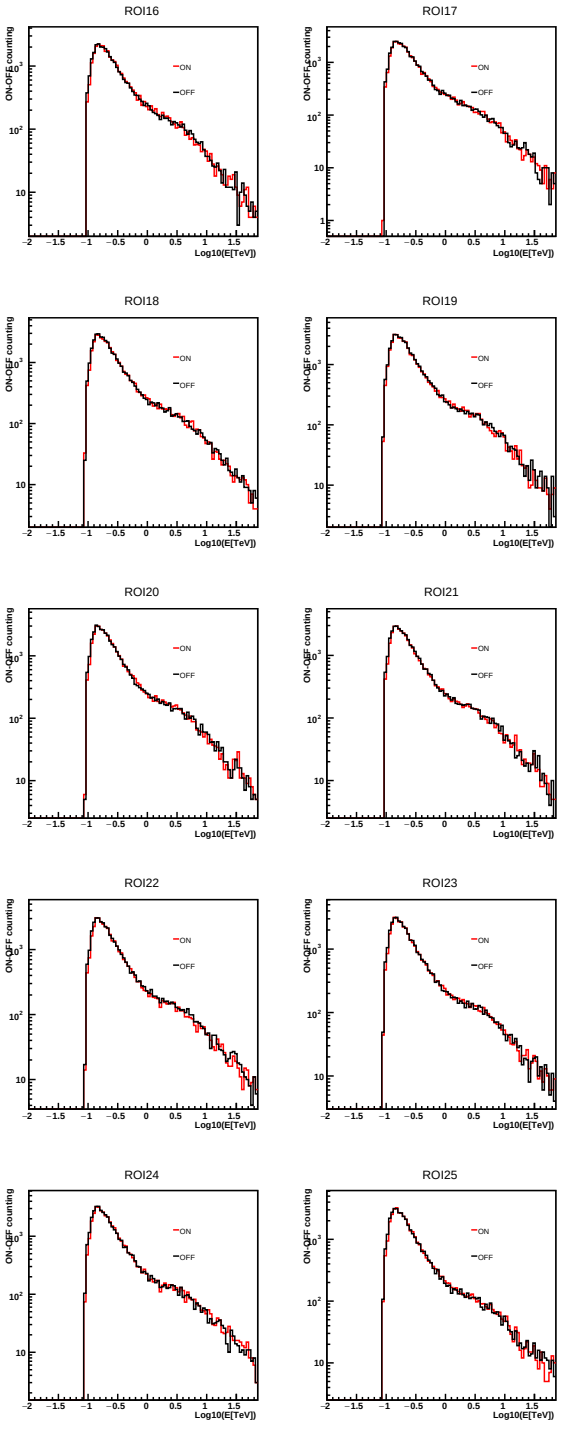

Figure 9.5: *ON* (red) and *OFF PDFs* (black) for ROIs 16 to 25.

9.2.3 Data unblinding and expected signal

The *ON* and *OFF PFDs* are compared and the overall excess significance in the 3° *ON region* is compatible with zero. A slightly positive excess is observed in the inner regions in the several hundreds GeV energy range. This could be due to a small leakage of diffuse emission in the ROIs. A study of the diffuse emissions is beyond the scope of this work and due to our current knowledge we are obliged to look for a DM signal above other gamma-ray signal with a different spectral and spatial behavior. The significance of the

ROI number	ON counts	OFF counts	Significance (σ)
1	141	138	0.2
2	1678	1555	2.2
3	3411	3366	0.6
4	5301	5243	0.6
5	7547	7235	2.6
6	10041	10032	0.1
7	12726	12626	0.7
8	13575	13146	2.6
9	14630	14474	0.9
10	16805	16501	1.7
11	18048	17857	1.0
12	19099	18763	1.7
13	20650	20640	0.1
14	22627	22547	0.4
15	24254	24260	0.0
16	26204	26007	0.9
17	28488	28746	-1.1
18	31368	31793	-1.7
19	33531	33966	-1.7
20	32280	32186	0.4
21	31253	31726	-1.9
22	31215	31810	-2.4
23	31334	31485	-0.6
24	31643	31573	0.3
25	31064	30754	1.2

Table 9.2: Number of counts in the *ON* and *OFF PDFs* and significance of the photons excess in the signal region for each ROI. No significance excess is observed with respect to the background. Excess between -2.4σ and 2.6σ is observed in each region and an excess compatible with 0 is measured in the whole 3° signal region.

excess, computed following the formula in Eq. (7.6), is given for each ROI in Tab. 9.2 and it fluctuates between $\pm 2.5\sigma$. An overall energy threshold at 140 GeV is set in order to avoid the problematic energy region near the energy threshold where systematic effects can

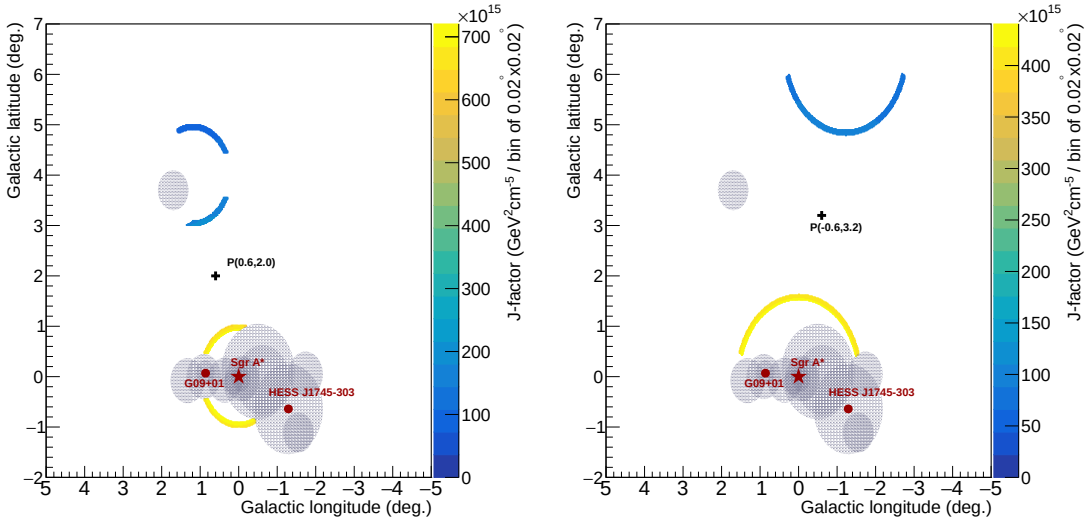

Figure 9.6: H.E.S.S.-II maps of the GC region in Galactic coordinates of some *ON* (yellow) and *OFF regions* (blue), expressed in terms of J-factor, *i.e.* intensity of the expected DM signal. The map is binned with pixels of dimension 0.02° in Galactic longitude and latitude. The excluded regions are gray patches. *Left:* map for ROI 5 (radius from 0.9° to 1.0°) and its *OFF regions* for observations at pointing position P(0.6°, 2.0°). *Right:* map for ROI 11 (radius from 1.5° to 1.6°) and its *OFF regions* for observations at pointing position P(−0.6°, 3.2°). The effect of the cut in *offset* at 3.5° is visible from the absence of expected signal in $b < 0.$ for this pointing position.

arise. The excess increases at intermediate energies and becomes smaller at higher energies. A 'plateau' effect is expected in the limits that reflect the integration of the excess, that increases up to several hundreds GeV, then becomes stable. The total excess significance above the whole *ON region* up to 3° is compatible with 0.

Following Eq. (6.13) the expected signal is computed by applying the same energy and *offset* cutoffs as the *PDFs*. It cannot be constructed event-by-event, but the percentage p_{mn} of events in each considered *offset* range is known on a *run*-by-*run* basis. Thus, the signal in each ROI for each *run* m is weighted not only for the *run* live time, but also for the proper acceptance from Fig. 9.3 in the *offset* range n. The signal in the energy bin i and ROI j is computed as

$$N_{\mathrm{S,\,ij}} = \sum_{\mathrm{m}}^{N_{\mathrm{runs}}} \frac{T_{\mathrm{obs,m}}}{T_{\mathrm{obs,\,tot}}} \int_{\Delta E_i} \frac{\mathrm{d}\phi_\gamma}{\mathrm{d}E}(E, \Delta\Omega_{\mathrm{jm}}) \sum_n (A^\gamma_{\mathrm{eff,\,n}}(E) p_{\mathrm{mn}}) \mathcal{G}(E) \mathrm{d}E. \tag{9.1}$$

Fig. 9.6 shows examples of *ON* and *OFF regions* in Galactic coordinates in terms of J-factor, *i.e.* intensity of the expected signal. The left panel shows ROI 5 for pointing position $\mathrm{P}(0.6°, 2.0°)$ and right panel ROI 11 for pointing position $\mathrm{P}(-0.6°, 3.2°)$. The excluded regions are masked (gray patches) and the position of the main VHE gamma-ray sources are

marked. Some expected DM signal is present both in the *ON* and in the *OFF region*. For these two specific cases the DM gradient is a factor larger than 4. When integrating over all the observations the J-factor gradient is between 9 (inner ROIs) and 1.5 (outer ROIs) depending on the ROI. For large pointing positions and outer ROIs the distance between the *ON* and *OFF regions* decreases, so the DM gradient decreases as well.

9.2.4 Observed and expected constraints on the annihilation cross section

In absence of any significant gamma-ray excess in any ROI, a 2D-likelihood analysis is performed in order to constrain the DM properties. The same likelihood approach is used, as applied to H.E.S.S.-I dataset looking for monoenergetic *gamma lines* (see Chap. 8). Here, we focus on the *continnum* annihilation channels W^+W^-, $\tau^+\tau^-$, $b\bar{b}$ and $t\bar{t}$. A H.E.S.S.-I DM search in the GC region in the *continuum* has been published in [236]. In both studies the DM density distribution is assumed to follow an Einasto profile [207], because the *Residual Background* method is not suited for DM cores as large as the FoV or larger.
The 95% C.L. observed upper limits on the DM annihilation cross section $\langle\sigma v\rangle$ are computed using the 2D-likelihood function in Eq. (7.8) and the LLRTS in Eq. (7.18). The mean expected limits and their containment bands are computed via 100 independent Poisson realisations of the counts in the *ON* and *OFF regions*. The containment bands include the effect of the systematic uncertainty on the reconstructed energy. An uncertainty of 5% on the energy scale can shift the limits up to 15%. The effect of the energy resolution is subdominant in the *continuum* channels where the smooth expected signals are not strongly affected by the energy resolution. Even in the W^+W^- channels that presents a sharp feature due to EW contributions near the DM mass at the end of the spectrum the effect of the energy resolution is mitigated by the integration over the full spectrum, *i.e.* the uncertainty on the energy resolution has a negligible effect on the limits. Thus. no uncertainty on the energy resolution is considered here.
The top left, top right and bottom panels of Fig. 9.7 show the 95% C.L. upper upper limits on DM annihilation cross section as function of the DM mass $m_{\rm DM}$ for the W^+W^-, $\tau^+\tau^-$ and $b\bar{b}$ channels respectively. The observed limits (red dots) are shown together with the mean expected limits (solid black line) and the 1σ (green area) and 2σ (yellow area) containment bands[4], including the systematic uncertainty on the energy scale. The best H.E.S.S.-II limits for Einasto profile reach $\sim 4.8 \times 10^{-26}$ cm^3 s^{-1} at about 1 TeV in the W^+W^+ channel, $\sim 1.8 \times 10^{-26}$ cm^3 s^{-1} at 1 Tev in the $\tau^+\tau^-$ channel and $\sim 8.3 \times 10^{-26}$ cm^3 s^{-1} at 4 TeV in the $b\bar{b}$ channel. The corresponding mean expected limits reach $\sim 2.6 \times 10^{-26}$ cm^3 s^{-1} at about 2 TeV in the W^+W^+ channel, $\sim 1.0 \times 10^{-26}$ cm^3 s^{-1} at 1 Tev in the $\tau^+\tau^-$ channel and $\sim 4.4 \times 10^{-26}$ cm^3 s^{-1} at 4 TeV in the $b\bar{b}$ channel.

[4]The bands are obtained through Poisson realizations of the measurements in the GC region and not in blank field observations.

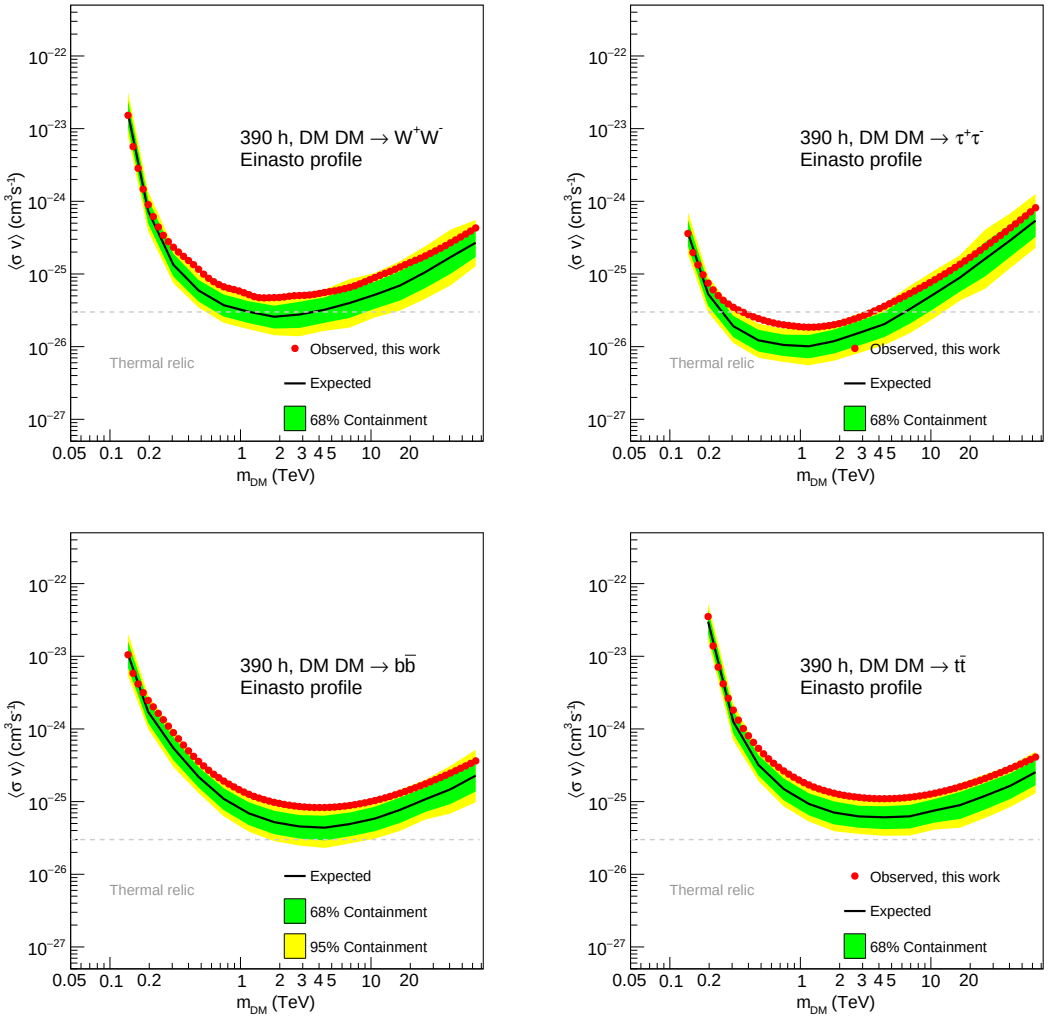

Figure 9.7: 95% C.L. H.E.S.S.-II *Mono* upper limits on the DM annihilation cross section in *continuum* channels as function of the DM mass for about 390 h of observations and assuming an Einasto DM density profile. The observed (red dots) and mean expected (solid black line) limits are given with the 1σ (green area) and 2σ (yellow area) containment bands. The bands include a 15% systematic error due to the uncertainty on the reconstructed energy. *Top left panel:* for the W^+W^- channel. *Top right panel:* for the $\tau^+\tau^-$ channel. *Bottom left panel:* for the $b\bar{b}$ channel. *Bottom right panel:* for the $t\bar{t}$ channel.

The observed limits probe the thermal relic cross section only in the $\tau^+\tau^-$ channel. The H.E.S.S.-II *Mono* sensitivity reaches the thermal relic cross section also in the W^+W^- channel, but the observed limits do not due to an overall slightly positive excess in the inner part of the signal region. This is also the region that hosts the largest amount of DM, hence, has a bigger impact on the observed limits.
The observed limits are within the $+2\sigma$ containment band in most of the mass range. They only exceed the 2σ band slightly at $400 - 800$ GeV, probably due to a small leakage of the diffuse emission in the *ON region*. The gamma-ray excess ($< 3\sigma$) is mainly in the few-hundreds GeV range in the inner ROIs, then it propagates to the limits at higher masses due to the integration effect of the *continuum* annihilation channels, but it is compensated by the null excess in multi-TeV range. The significance of this signal exceeds 2σ in some of the inner ROIs where higher DM signal is host, *i.e.* it has a larger impact on the observed limits than the negative fluctuations in the outer ROIs. The slight excess in the low energies is not compatible with a DM signal, otherwise a bump-like feature would be expected in the observed limits in correspondence of the DM particle mass.

9.2.5 Comparison with previous H.E.S.S.-I limits and other experiments

In the left plot of Fig. 9.8 H.E.S.S.-II *Mono* observed upper limits on $\langle\sigma v\rangle$ are compared to H.E.S.S.-I constraints [236] in the three channels. The new limits are more sensitive especially at low masses due to CT5 better sensitivity to hundreds-GeV gamma rays that lowers the energy threshold compared to CT1-4. The improvement with H.E.S.S. II is also due to the larger statistics thanks to the 390 hours of observations and to the large *offsets* for which the best sensitivity shifts at larger energies, especially important to obtain strong limits at high masses. At about 300 GeV the new limits are $5-7$ times stronger than H.E.S.S. I, and above 10 TeV where the integrated excess significance is compatible with 0 they are about 3 times more constraining compared to H.E.S.S. I. In the 800 GeV-4 TeV mass range, where the best limits lie, the improvement is only $20 - 60\%$. The improvement on observed limits in the intermediate mass range is smaller than expected from the computation of expected limits because of standard gamma-ray background in the ROIs. The *Mono* H.E.S.S.-II mean expected limits would be almost 3 times better than H.E.S.S. I at about 1 TeV, but the presence of a slight diffuse emission in the *ON region* degrades the observed limits with respect to the mean expected ones. Further improvement would be achieved thanks to the CT1-5 spectroscopy, which is not exploited in the *Mono* analysis.
In the right plot of Fig. 9.8 H.E.S.S.-II *Mono* limits in the $\tau^+\tau^-$ annihilation channel in the GC region are compared to other experiments. VERITAS constraints are taken from the combination of five dSph for a total of 230 hours and are about two orders of magnitude above the thermal relic cross section due to the smaller expected DM annihilation signal towards dSph with respect to the GC. Fermi-LAT accumulated in six years observations towards 45 dSph and set stringent constraints on $\langle\sigma v\rangle$ in the GeV mass range, probing the

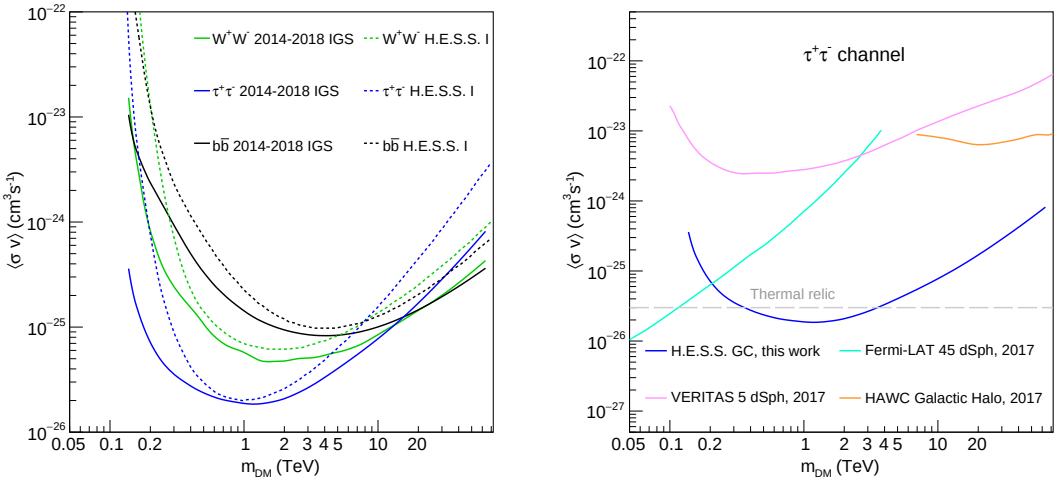

Figure 9.8: H.E.S.S.-II 95% C.L. observed upper limits on $\langle\sigma v\rangle$ vs $m_{\rm DM}$ compared to other previous results. *Left panel:* comparison of H.E.S.S.-I (dotted lines) and H.E.S.S.-II (solid lines) limits in the W^+W^-(*greenlines*), $\tau^+\tau^-$ (blue lines) and $b\bar{b}$ (black lines) annihilation channels. *Right panel:* H.E.S.S.-II constraints (blue solid line) on $\langle\sigma v\rangle$ towards the GC in the $\tau^+\tau^-$ annihilation channel are compared to those by Fermi-LAT [237] (teal solid line) from the combination of 45 dSph, those by VERITAS [234] (pink solid line) from the combination of 5 dSph and those from HAWC [238] (orange solid line) in the Galactic halo. The thermal relic cross section (gray dashed line) is printed on the plot. Fermi-LAT probes the theral relic cross section below ~ 100 GeV and H.E.S.S. II in the mass range $\sim 0.4 - 4$ TeV.

thermal relic cross section below about 100 GeV. The H.E.S.S.-II IGS observations allow us to probe the thermal relic cross section, in the mass range between about 400 GeV and 4 TeV. HAWC is sensitive at high energies with respect to IACTs, with an energy threshold at about 2 TeV, but its constraints from less than two years of data taking towards the Galactic halo lie a few orders of magnitude above than the natural scale for DM annihilation.

9.3 Towards an *hybrid* analysis of IGS data

9.3.1 *Combined* reconstruction

In case of the *Combined* analysis that best exploits the hybrid nature of the H.E.S.S. array, the analysis becomes more complicated. The acceptance and its energy and radial dependencies are strongly affected not only by the *offset*, but also by the reconstruction type. In the *Combined* analysis three kind of events are possible:

1. *CT1-4* or *H.E.S.S.-I* events that are reconstructed only with at least two of the four small telescopes. This happens mainly if CT5 is excluded by the array during the

observations or for pointing positions at large *offset* from the target and very energetic gamma rays. In case of large *offset* only very energetic events from the target region can travel far enough to be detected and CT5 is less sensitive to this kind of large showers.

2. *Stereo* (or *Hybrid*) events that are reconstructed with CT5 together with at least one among CT1-4. This is usually the most powerful reconstruction when dealing with emission that covers a large range of energies.

3. *Mono* events that are reconstructed only with CT5.

The difference between the reconstructions described here for a *Combined* analysis and the observations mode defined in Sec. 2.6 is that with a combined analysis an event can be observed with CT5 and another telescope (*Stereo - CT1-5*), but be reconstructed in *Mono* because the best-fit to the model template is obtained in *Mono* and not in *Stereo - CT1-5*. The number of telescopes that are triggered by events reconstructed as gamma rays is homogeneous with respect to the involved telescopes. Fig. 9.9 shows a slightly smaller involvement of CT1 in the observations, but overall all the telescopes contributed in the same way to the data taking. As expected, most of the single-telescope reconstructed event are not lost because the single telescope is CT5 that can be used in *Mono* mode.

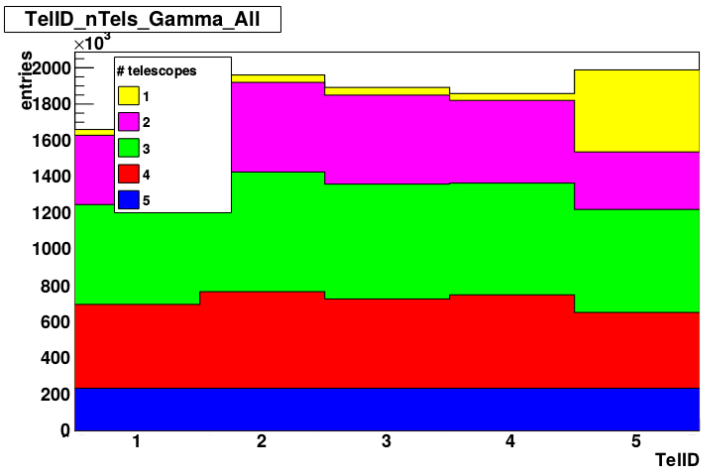

Figure 9.9: Number of events reconstructed as gamma rays versus identification number of the telescope for different multiplicities in the GC dataset. Single telescope reconstructions (yellow) are mainly with CT5 only. These events are reconstructed in *Mono*, while the few percentage of events reconstructed by a single telescope other than CT5 are lost because they do not fullfill the requirement for the stereoscopy trigger.

Not only all the telescopes were involved homogeneously in the observations, but due to the peculiar IGS *offset* choice the photons are reconstructed about 1/3 in every reconstruction type, while towards other standard H.E.S.S. targets *Stereo* events dominate and *CT1-4*

events are almost absent. In Tab. 9.3 a list of the number of events that pass each step on the *Combined* reconstruction is given, depending on the reconstruction type.

Step in reconstruction chain	*Stereo* [events]	*Mono* [events]	*CT1-4* [events]
Reconstructed	172 321 238	704 341 398	79 407 203
Pass shape cuts	144 966 509	593 215 816	76 604 664
Classified	18 256 893	6 787 276	13 953 844
Gamma-like	2 444 348	2 104 882	1 811 653

Table 9.3: Number of events for reconstruction type at different steps of the reconstruction chain.

9.3.2 Definition of the PDFs in *combined* reconstruction

In the *Combined* analysis framework the event distributions for each reconstruction type can be built. Indeed, each reconstructed photon has a flag that allows us to know if it has been reconstructed in *CT1-4*, *Stereo* or *Mono* mode. Splitting the *PDFs* accordingly to the reconstruction class is necessary in order to account for the different spectral and spatial degradation of the sensitivity of the different reconstruction types. Fig. 9.10 shows the overall *Combined PDFs* (dark blue) and its *Mono* (cyan), *Stereo* (orange) and *CT1-4* (magenta) sub-*PDFs*.

Knowing the chosen reconstruction type of each photon explains the behavior of the overall *PDFs* that show a 'shoulder' while moving to high energies. Indeed, this behavior reflects the effect of the *offset*. When observing a certain point in the sky from a large *offset* only the highest energy photons reach the observer. The 'shoulder' appears at high energies due to a large fraction of large *offset* events that are preferably reconstructed in *Stereo*. The shoulder gets more and more pronounced for the large ROIs. Since the pointing positions do not coincide with the center of the *ROI* the gradient of sensitivity inside the ROI is strong. For the same pointing position photons that cover a wide range of *offsets* are detected. When summing the effect of the sensitivity at low *offset* and at high *offset* that we already underlined for the *Mono* analysis and the fact that different reconstructions have different sensitivity in different energy ranges, we understand why the 'shoulder' appears for large ROIs. The effect is significantly smaller in the *Mono* analysis because CT5 sensitivity decreases rapidly at high energies, while this is not the case for the *Stereo* reconstruction that dominates the 'shoulder'. As expected, in the *Combined* analysis *Mono* is important at low energies and degrades where the CT5 sensitivity decreases. The presence of CT5 in *Mono* and *Stereo* reconstructions shifts the peak of the overall *Combined PDFs* at lower energy with respect to H.E.S.S. I.

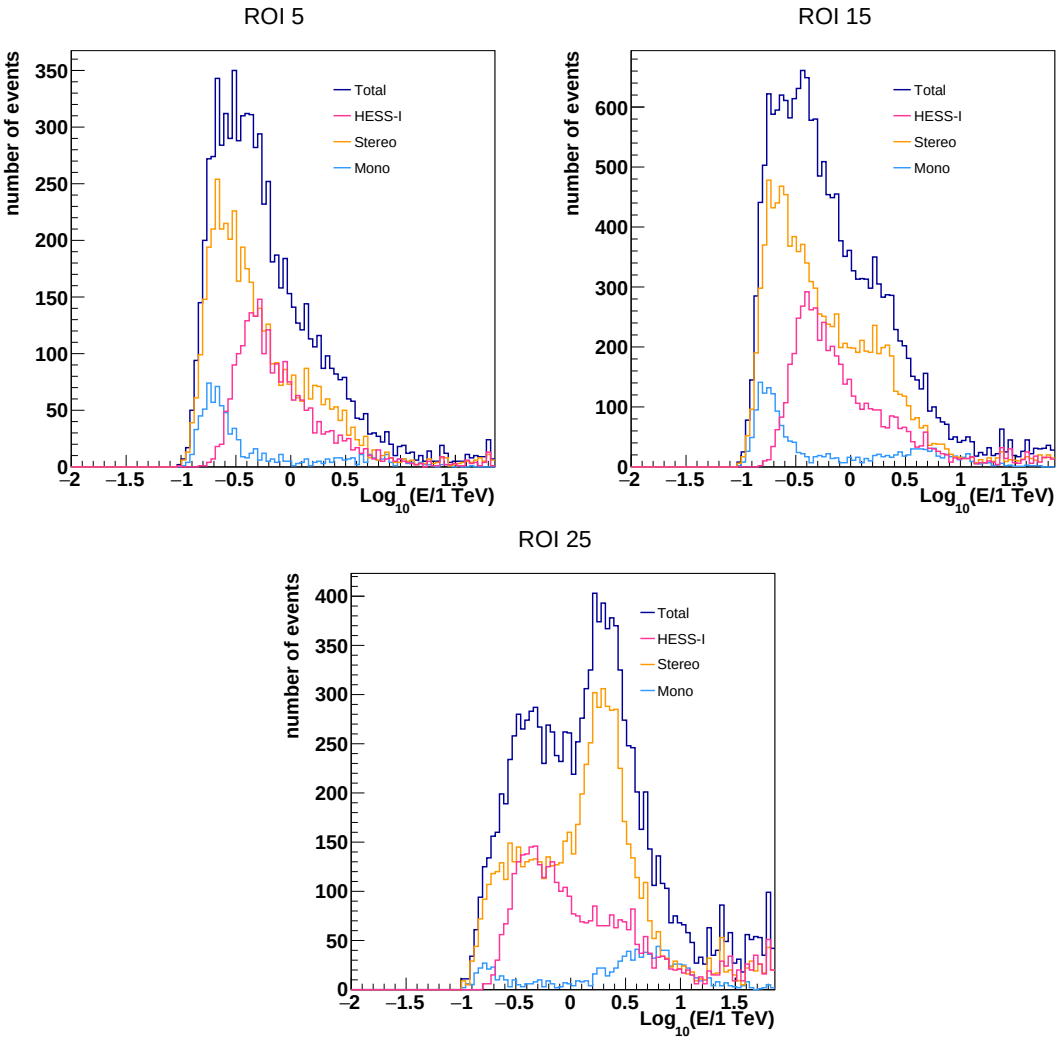

Figure 9.10: *Mono* (cyan), *Stereo* (orange), *CT1-4* (magenta) and overall *Combined PDFs* (dark blue) for DM search in a region of 3° around the GC. The *ON PDFs* are shown for ROI 5, 15 and 25. A 'shoulder' appears at high energies in the *PDFs* ou the outer ROIs due to the large *offsets*.

9.4 Outlook and perspectives

The first study for dark matter made with H.E.S.S.-II including Inner Galaxy Survey observations has been performed. The *Mono* events reconstruction and the presence of a slight excess of diffuse standard emission in the region of interest somehow limit the possibility to probe the thermal annihilation cross section in most of the channels. The excess on the 3° region of interest is compatible with zero, but the integration effect over the regions where most of the expected signal and the observed diffuse emission appear degrades a bit the observed limits with respect to the sensitivity. The natural scale is reached by the observed H.E.S.S.-II *Mono* limits on the annihilation cross section only in the $\tau^+\tau^-$ channel. Despite the sensitivity below 3×10^{-26} cm^3 s^{-1} in the W^+W^- channel the observed limits did not probe the thermal relic cross section. A small diffuse gamma-ray excess is observed, that may come from more extended Pevatron emission, Fermi Bubbles or other fainter emissions. If more extended or more intense diffuse emission will be detected in the region of interest for dark matter search with the future observations, it will be crucial in to have a better understanding of the spectrum and morphology of this emission in the Galactic Center and model it in order to fully exploit H.E.S.S.-II sensitivity.

This study showed both that there are promising prospects for dark matter search and that there is a limitation. H.E.S.S.-II *Combined* analysis which is being developed is expected to increase the statistics thanks to the contribution of all the five telescopes, then improve the sensitivity to DM, probably at the point where other annihilation channels could be probed. On the other hand, the new observations contain more standard gamma-ray background that cannot be completely rejected from the analysis because it covers a large part of the region that hosts the largest amount of dark matter. The degradation of the observed limits due to this small background with respect to the promising sensitivity points out the necessity to make dedicated accurate studies of these emissions and try to model them in order to take them properly into account when looking for a faint dark matter signal in the very-high-energy gamma-ray crowded region of the Galactic Center.

Chapter 10

Dark matter searches towards newly detected ultra-faint DES dwarf galaxies

Contents

10.1 Ultra-faint dwarf galaxies recently detected by DES 178
10.2 H.E.S.S. observations and datasets 179
10.2.1 Selection of targets among DES dSph 179
10.2.2 Gamma-ray excess and significance sky maps 180
10.3 Dark matter density profiles 180
10.3.1 Measured J-factors 180
10.3.2 J-factor statistical and systematic uncertainties 182
10.3.3 Predicting J-factors 183
10.4 ON and OFF PDF measurements 184
10.4.1 Definition of the regions of interest and background measurement 184
10.4.2 ON and OFF energy-dependent event PDFs 185
10.5 Constraints on the annihilation cross section 187
10.5.1 Expected and observed limits in different channels 187
10.5.2 Individual versus combined limits 195
10.5.3 Effect of the statistical uncertainty on the J-factor 195
10.5.4 Comparison with other experiments 197
10.6 Outlook and perspectives 198

A selection of the Milky Way satellites discovered by DES has been observed by H.E.S.S., using the full five-telescopes array. H.E.S.S. has been the first among the Imaging Atmospheric Cherenkov telescopes that started an observation campaign towards these objects. Dark matter searches in several annihilation channels have been performed towards these satellites. The targets, their observations and the measurement or estimate of their J-factor are described at the beginning of the chapter. Limits on the annihilation cross section as function of the mass are then given for *continuum* and *gamma lines*. The results are discussed and compared to other limits from other experiments.
The targets and datasets are introduced in Sec. 10.1 and Sec. 10.2. The J-factors in this analysis are taken from the latest determination available in the literature, and some J-factor measurements and prediction techniques and their uncertainties are discussed in Sec. 10.3. In Sec. 10.4 the *ON* and *OFF* regions are discussed and in Sec. 10.5 the constraints on dark matter annihilation cross section are derived in several annihilation channels for each target as well as a combination of them. The results are compared to other studies.
The observations of these objects are the results of the internal proposals that I have led for two years, including predictions of the possible outcome for dark matter searches. This work will be presented at ICRC19 and it will be published as Ref. [239].

10.1 Ultra-faint dwarf galaxies recently detected by DES

The Dark Energy Survey (DES) is a wide-field optical imaging survey, that covered 5000 deg^2 (1800 deg^2 during the first year) of the Southern Galactic hemisphere. This survey has been able to detect ultra-faint satellites of the Milky Way up to a distance about 120 kpc from the Sun. During the first year of observation 9 objects compatible with DM-dominated dSph were discovered by DES [240, 241] and during the second year of data 8 more ultra-faint satellites were detected [242]. a recent DM search towards these candidates and other dSph for a total of 45 targets has been performed by Fermi-LAT [237].
DES dSph candidates are selected as over-densities corresponding to individually resolved stars that match the typical characteristics of the stellar population of ultra-faint dSph, based on their age, metallicity and distance. The main uncertainty is due to the fact that when looking for ultra-faint objects some over-densities may be wrongly identified as part of the galaxy, while they are foreground or background stars. The morphology (tides, asphericity) of the galaxies was also studied by DES. The knowledge of the luminosity function of the dSph is a necessary input of the Jean equation used for determining the DM content of a galaxy (see Sec. 10.3). First the mass versus half-light-radius tells us if a system is DM dominated. In addition, spectroscopic measurements are used to discriminate between ultra-faint dSph (highly DM-dominated systems) and globular clusters (baryon-dominated systems). In particular, they provide the velocity of the stars and its dispersion (large for globular clusters). Dynamical hints of presence of DM halo or chemical signatures like

the presence of heavy elements help determining the nature of the object. For example, globular clusters contain mainly old stars with low metallicity [243], while dwarf galaxies also contain younger metal-rich stars showing a significant dispersion in stellar metallicities due to multiple generations of star formation. More details on the J-factor measurement are given in Sec. 10.3.

10.2 H.E.S.S. observations and datasets

10.2.1 Selection of targets among DES dSph

The targets have been ranked according to the following criteria:

- large measured or predicted J-factor, close to $\log_{10}[J(< 0.5^\circ)/\mathrm{GeV}^5\mathrm{cm}^{-2}] = 19$ in a region of 0.5° centered at the nominal position of the target,
- good visibility during darktime from the H.E.S.S. site location for observations at zenith angle below 50°,
- distribution of the visibility window over a large period of the year,
- likelihood that the target is a dwarf spheroidal galaxy and not a globular cluster,
- interest shown by the DM community for the targets Reticulum II and Tucana II, visible only from the Southern hemisphere,
- best visibility from the Southern hemisphere,
- previous H.E.S.S. observations.

Three main targets have been selected: Reticulum II (Ret II, DES J0335.6-5403), Tucana II (Tuc II, DES J2251.2-5836) and Tucana III (Tuc III, DES J2356-5935). In addition, Tucana IV (Tuc IV, DES J0002-6051) is found to be in the same FoV of Tuc III and Grus II (Gru II, DES J2204-4626) was observed by chance in 2009 in the FoV of observations of NGC 7213. Additional observations have been performed on Gru II with the full H.E.S.S. array to extend the dataset.
A campaign towards DES satellites of the Milky Way have been performed by H.E.S.S. during 2017 and 2018 and about 80 hours of observations have been collected. In Tab. 10.1 the position of the five targets in Galactic longitude and latitude, their heliocentric distance, the observation live time and mean zenith angle of the observations are listed. Note that the actual live time on Tuc IV is halved due to the radial degradation of the radial acceptance and the large offset of the target with respect to the pointing positions optimized for Tuc III. For the same reason the live time on Gru II is reduced to 2/3 of the initial value.

Source name	Heliocentric distance [kpc]	Longitude [degrees]	Latitude [degrees]	Confirmed dSph?	Live time [hours]	Mean zenith angle [degrees]
Reticulum II	32	266.30	-49.74	Yes	18.3	43.5
Tucana II	58	328.04	-52.35	Yes	16.8	36.1
Tucana III	25	315.38	-56.18	No	25.3	39.1
Tucana IV	48	313.29	-55.29	No	12.2	39.1
Grus II	53	351.14	-51.94	No	12.4	29.2

Table 10.1: DES satellite of the Milky Way observations with H.E.S.S.. Heliocentric distance, position and confirmation of the nature of the targets is given together with the observational live time and mean zenith angle.

10.2.2 Gamma-ray excess and significance sky maps

Gamma-ray excess and significance maps are produced in the standard analysis chain for each of the five selected targets. It is among the first analysis made with the full CT1-5 H.E.S.S. telescope array. Here the background is measured with the *Multiple OFF* method and the targets are treated as point-like sources. No significant excess is observed on any target, as well as anywhere in the FoV. The five excess maps are given in Fig. 10.1 in Galactic coordinates. A specific multi-ROI analysis is made for DM search and details on the significance of the excess in every ROI of every target is given in Sec. 10.4.

10.3 Dark matter density profiles

10.3.1 Measured J-factors

Spectroscopic measurements provide information on the chemical abundance and the internal kinematics of the dSph, that are used to measure the DM content. The kinematics of the stellar population of a system traces its gravitational potential which is highly dominated by DM. The J-factor distribution can be inferred from the stellar kinematic of the system, the stellar kinematics being dictated by the gravitational potential of the system.
Under the assumption of collisionless system at equilibrium, negligible rotational support and spherical symmetry the Jeans analysis is applied [204, 244]. The Jeans equation reads

$$\frac{1}{\nu}\frac{\mathrm{d}}{\mathrm{d}r}(\nu\bar{v}_r^2) + 2\frac{\beta(r)\bar{v}_r^2}{r} = -\frac{GM(r)}{r^2}, \tag{10.1}$$

where $\nu(r)$ is the tridimensional stellar density, $\bar{v}_r^2(r)$ the radial velocity dispersion and $\beta(r) = (1 - v_\theta^2/v_\mathrm{r}^2)$ the velocity anisotropy between the tangential and radial velocities of the stars in the system. $M(r)$ is the enclosed mass in the galaxy. The solution of the Jeans equation depends on the line of sight $\sigma_\mathrm{los}(R)$ that can be measured and is related to the quantity of interest which is the mass content of the system. A problem with the Jean's equation is that there is degeneracy between the assumed mass density and the second order velocity moments that define $\beta(r)$, the so called "mass-anisotropy degeneracy". Indeed,

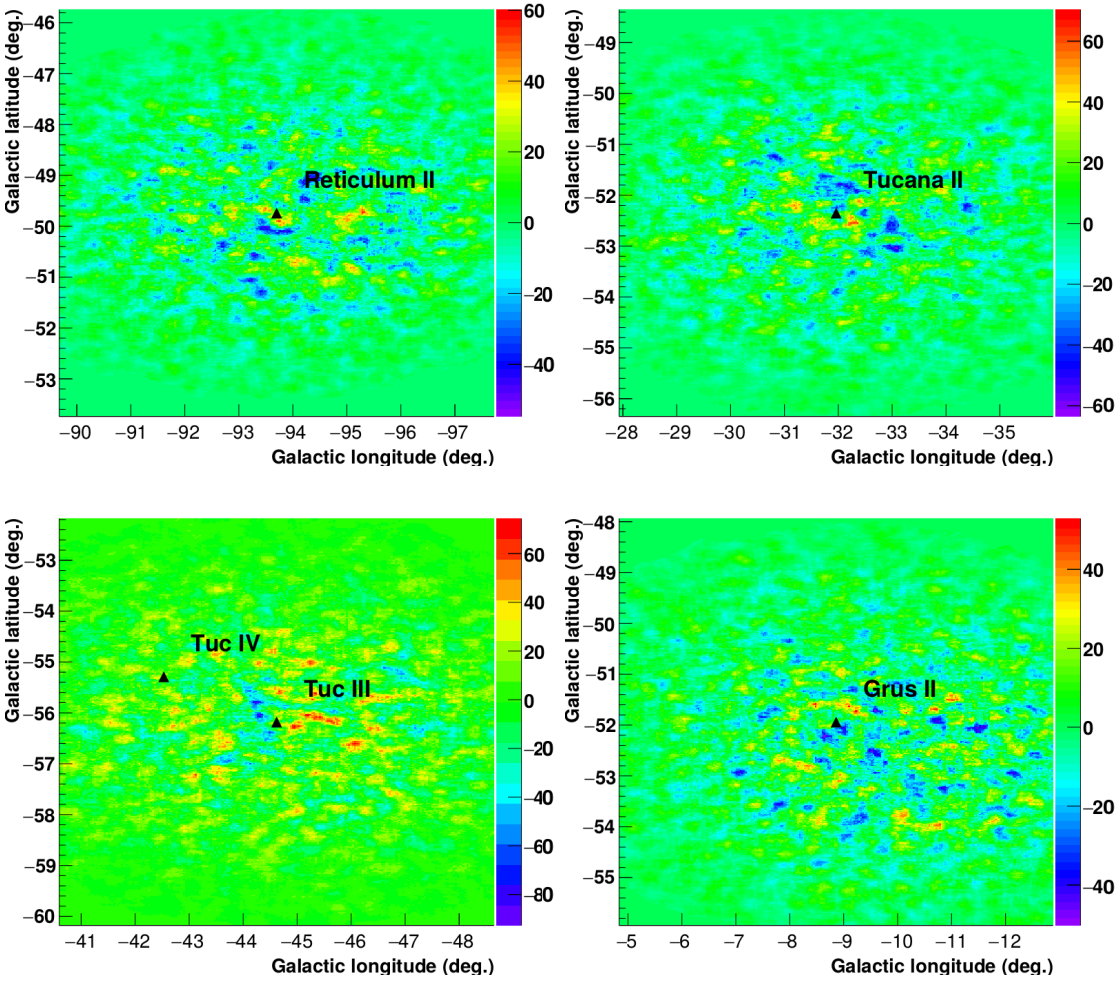

Figure 10.1: Gamma-ray excess maps for the five DES satellites of the Milky Way in Galactic coordinates obtained for point-like sources and the *Multiple OFF* background technique. No significant excess is observed in the FoV of any target.

both $M(r)$ and β are unknown and parameters of Eq. (10.1) and this can lead to very different estimates of the DM content of a system depending on the assumptions made to relate $\sigma_{\rm los}$ to β and $v_{\rm r}$. Parametric models are used instead of the parameters that are not constrained and the best-fit on data is performed in order to reproduce the measured $\sigma_{\rm los}$. Other methods to measure the DM density profile are reviewed in [245]. There are several sources of systematics [246] on the J-factor measurement and some are discussed later in this section.

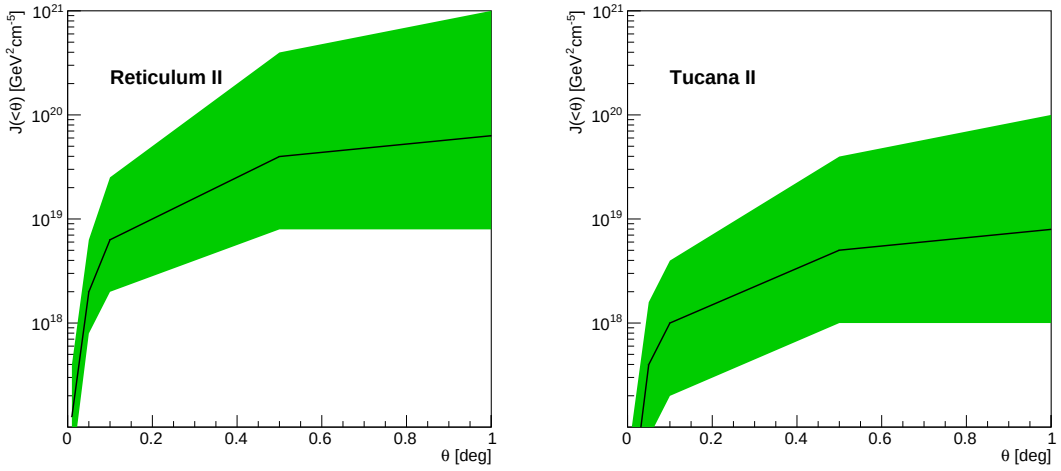

Figure 10.2: Integrated measured J-factor in a region of dimension θ for Ret II (left panel) and Tuc II (right panel) as function of the angular distance θ from the nominal position of the target, together with its 1σ statistical uncertainty (green band).

The J-factors used in this work are extracted from literature. The J-factors in a region of 0.5° and in the *ON region* are given for each dSph in Tab. 10.2 together with their statistical uncertainty, the dimension of the *ON region*, and the reference for the J-factor measurement. For the satellites marked with an asterisk there is no spectroscopic measurement, so they do not have a measured J-factor, but a prediction of the DM profile can be made. A discussion about the definition of the ROIs and their dimension is given in Sec. 10.4. The integrated J-factor $J(<\theta)$ profiles of Ret II [247] (left panel) and Tuc II [248] (right panel) are shown in Fig. 10.2 as function of the dimension θ of the integration region. The green bands correspond to the 1σ statistical uncertainty.

10.3.2 J-factor statistical and systematic uncertainties

Statistical and systematic uncertainties on the J-factor of dSph depend on the conditions of observations and quality of the photometric and kinematic data set and the assumptions made for the computation of the J-factor.

Source name	$\overline{\log_{10} J_{<0.5^\circ}}$ [$\log_{10}$ (GeV^{5}cm^{-2})]	$\sigma_{J_{<0.5^\circ}}$ [$\log_{10}$ (GeV^{5}cm^{-2})]	$\overline{\log_{10} J_{ON}}$ [$\log_{10}$ (GeV^{5}cm^{-2})]	$\sigma_{J_{ON}}$ [$\log_{10}$ (GeV^{5}cm^{-2})]	Ref.
Reticulum II	19.6	0.85	19.2	0.63	[247]
Tucana II	18.7	0.80	18.35	0.71	[248]
Tucana III*	19.4	-	18.8	-	[249]
Tucana IV*	18.7	-	18.1	-	[237]
Grus II*	18.7	-	18.1	-	[237]

Table 10.2: J-factors for DES dwarf spheroidal galaxies satellites of the Milky Way. The J-factor value together with its 1σ statistical uncertainty is given in the ON region and in a region of 0.5° around the center of the target. The objects marked with an * do not have stellar kinematic measurements, *i.e.* the J-factor can not be measured through the Jean's modeling. For these targets different methods for prediction of J-factor are used, but the statistical uncertainty cannot be properly evaluated. References on the J-factors determination or prediction are given in the references in the last column.

The estimate of the enclosed mass and J-factor depends on the measurement of the projected velocities of resolved member stars and the $\sigma_{\rm los}(r)$. These measurements are subject to uncertainties, especially for ultra-faint dSphs that have a reduced detected stellar population ($\sim 10-60$ stars). Indeed, on these targets large statistical uncertainty $\sigma_{\rm J}$ on the DM astrophysical factor is due to the small data sample. Smaller $\sigma_{\rm J}$ are measured in classical dSphs with hundreds of member stars [250]. The statistical uncertainty on the J-factor is included in the computation of the limits as explained in Sec. 7.3.1.
Systematic uncertainty is due to asphericity [251, 250] of both the DM and the stellar components of the dSph, contamination of foreground and background stars mis-attributed to the system, and it affects the parameters of Eq. (10.1). Stars with ambiguous membership can largely affect the J-factor measurement and give possible overestimates of orders of magnitude like in the case of Segue 1 [252]. The presence of stellar streams due to tidal effects from the interaction with the Milky Way [253] may also introduce systematics. Also the error on the estimate of the gravitational center[1] of the galaxy can introduce an error on the evaluation of the DM density profile.
Systematic uncertainty is not included in the computation of the limits in this work. In general it is of the order of $\sigma_{\rm syst} \approx 1$ [246].

10.3.3 Predicting J-factors

If spectroscopic studies are not available the J-factor cannot be measured, but it can be estimated from empirical estimate of the mass. Several techniques can be used to predict the J-factor.
An empirical formula for spherical cusps that relates enclosed mass to the velocity dispersion

[1]The position of the gravitational center of DES dSphs is known with 10% uncertainty [240, 241].

and half-light radius $r_{\rm h}$ is given in [254]:

$$J(<\theta) = \frac{25\sigma_{\rm los}^4\theta}{8G^2dr_{\rm h}^2}. \tag{10.2}$$

In cases like Tuc III, when an upper limit on the velocity dispersion of the stars in the galaxy is provided [249] despite the lack of precise kinematic measurements, this formula can be used to get an upper limit on the J-factor. From Eq. (10.2) and the 95% C.L. upper limit on the velocity dispersion $\sigma_{\rm los} = 1.5$ km s^{-1}, $\log_{10}[J(<0.5^\circ)/{\rm GeV}^2\ {\rm cm}^{-5}] = 17.8$ in an integration region of $\theta = 0.5^\circ$. The same formula applied on Ret II in $\theta = 0.5^\circ$ gives $\log_{10}[J(<0.5^\circ)/{\rm GeV}^2\ {\rm cm}^{-5}] = 19.5$, in good agreement with the value 19.60 ± 0.85 derived in [247].
In total absence of any dynamical information a poor scaling law with the distance D has been developed in the framework of Fermi-LAT observations [237]. The scaling law reads:

$$\log_{10}\left(\frac{J}{J_0}\right) = -2\log_{10}\left(\frac{D}{100\,{\rm kpc}}\right) \tag{10.3}$$

with nominal scale factor taken as $\log_{10}[J_0/{\rm GeV}^2\ {\rm cm}^{-5}] = 18.1$. For Tuc III it gives $\log_{10}[J(<0.5^\circ)/{\rm GeV}^2\ {\rm cm}^{-5}] = 19.4$ in 0.5°. The scaling law applied to Ret II in the same integration angle gives a value of $\log_{10}[J(<0.5^\circ)/{\rm GeV}^2\ {\rm cm}^{-5}] = 19.1$, in agreement with the measurements in [247].
Fermi-LAT scaling law is used in this work for Tuc IV, Gru II and the largest estimate of Tuc III J-factor, since spectroscopic studies on these targets are absent or not sufficiently accurate to provide an actual J-factor measurement. For Tuc III also the smallest J-factor value obtained with Eq. 10.2 is discussed. The rescaling for the dimension of the *ON region* is made considering a DM density slope of 1, *i.e.* a rescaling with the dimension θ of the considered region.
The statistical uncertainty is not available for the targets that lack of sufficiently large kinematic data sample. The value of 0.6 used by Fermi-LAT in [237] could be underestimated considering the σ_J determined in better known targets of the same family, like the measured uncertainty of 0.8 for Tuc II. In this work we will not discuss an uncertainty that cannot be measured. Indeed, the treatment of the J-factor as a log-normal statistical variable is a good approximation for systems with high-quality kinematic data [245].

10.4 ON and OFF PDF measurements

10.4.1 Definition of the regions of interest and background measurement

The region of interest for DM search towards the confirmed galaxies Ret II and Tuc II has been defined as a disk of 0.2° around the target, split in an inner region up to 0.1° and a ring from 0.1° to 0.2° in order to exploit the spatial behavior of the DM profile versus

background. This dimension is chosen in order to have a good signal to noise ratio. The other targets that are not confirmed galaxies or that could show tidal disruption are treated as point-like sources, *i.e.* the region of interest is a disk up to 0.125°, as used in the *Model++* analysis configuration.
The background has been measured using the *Multiple OFF* technique described in Sec. 2.4.2. Examples of *Multiple OFF* regions are shown in Fig. 10.3 as maps in Galactic coordinates of number of reconstructed photons. The onverall *ON region* is circled in red. The left panel shows the regions for Ret II, targeted and with ROIs up to 0.2°. The right panel shows the regions for Tuc IV, which was not directly targeted (the target was Tuc III) and is treated like a point-like object with a single ROI up to 0.125°. The number of *OFF regions* depends on the dimension of the *ON region* and the observation *offset*. In the case of Tuc IV, where the pointing positions (black crosses) are chosen for another target the *OFF regions* lie on larger rings and increase α. Observations with *offset* larger than 1.5° are discarded due to the extremely low statistics and possible strong systematic effects.

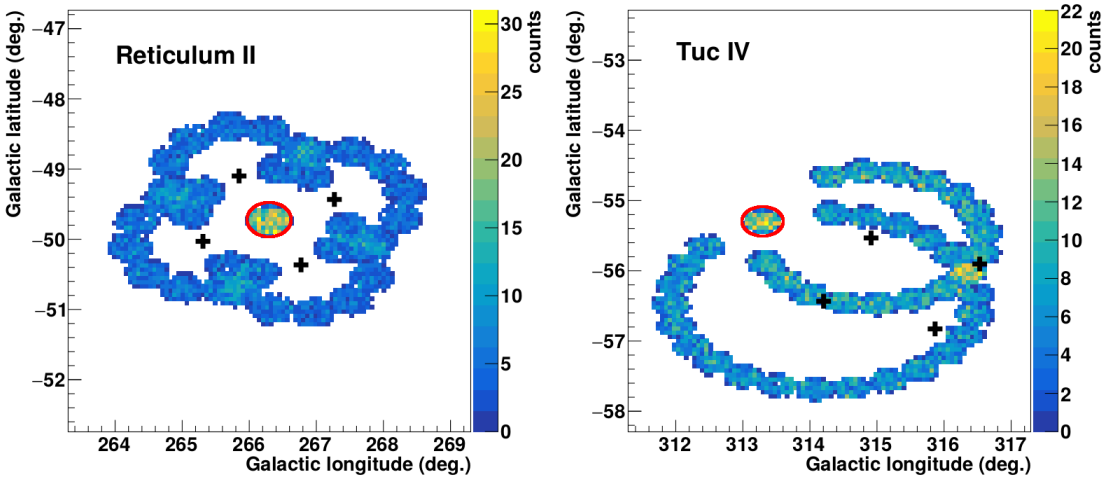

Figure 10.3: *Multiple OFF* regions of Ret II (left panel) and Tuc IV (right panel) in Galactic coordinates. The *ON region* is marked by a red circle. The pointing positions are marked as black crosses.

10.4.2 ON and OFF energy-dependent event PDFs

The *ON* and *OFF PDFs* have been built as function of the energy for each ROI. The PDFs for each target are shown in Fig. 10.4. The bin-by-bin excess fluctuates mainly between about $+1.5\sigma$ and -1.5σ. Tab. 10.3 gives the number of counts in the overall *ON* and *OFF regions*, the ratio α between the dimension of the two regions and the significance of the excess in the *ON region*. No significant excess is observed on any of the five targets. Therefore constraints can derived put on DM properties, *i.e.* $\langle\sigma v\rangle$ versus m_{DM}.

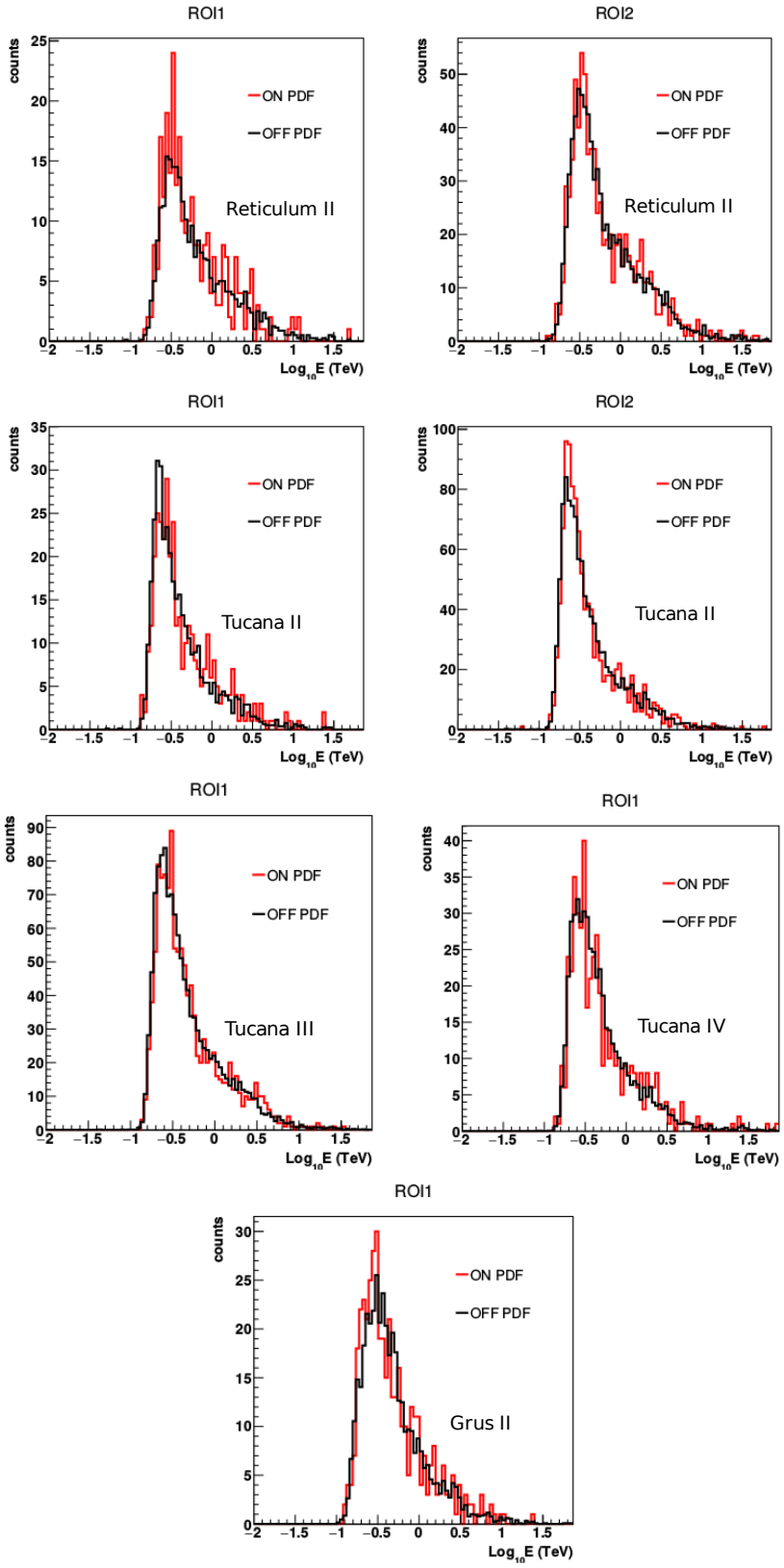

Figure 10.4: *ON* (red) and *OFF PDFs* (black) for each ROI for each target. No significant gamma-ray excess is observed on any target between the *ON* and *OFF* regions.

Source name	ON region size [degrees]	N_{ON} [counts]	N_{OFF} [counts]	$\overline{\alpha}$	Significance [σ]
Reticulum II	0.2	1091	8534	8	0.4
Tucana II	0.2	1447	11567	8	-0.2
Tucana III*	0.125	1206	14970	12	-0.8
Tucana IV*	0.125	485	9713	19.5	-0.4
Grus II*	0.125	434	5396	12.9	0.5

Table 10.3: Counts measurement in DES satellites observed by H.E.S.S.. The counts in the overall *ON* and *OFF regions* are given together with the ratio $\bar{\alpha}$ between the size of the *ON* and *OFF regions* averaged over the *runs*, and the significance of the excess in the *ON region*. The value $\bar{\alpha}$ is determined by the dimension and number of ROI and the *offset* of the object with respect to the pointing position for each *run*.

10.5 Constraints on the annihilation cross section

10.5.1 Expected and observed limits in different channels

Observed (black solid line) and mean expected 95% C.L. upper limits (black dashed line) and 1σ (green band) and 2σ (yellow band) containment bands are computed following the LLRTS procedure in Sec. 7.2.4, that was applied also to the GC analysis in Chap. 8. The containment bands are obtained from 100 Poisson realizations of N_{OFF} and N_{OFF}/α. The 95% C.L. upper limits on $\langle\sigma v\rangle$ are computed in the following channels W^+W^-, ZZ, $b\bar{b}$, $t\bar{t}$, e^+e^-, $\mu^+\mu^-$, $\tau^+\tau^-$ and $\gamma\gamma$.

In Fig. 10.5 the constraints in W^+W^- on the different targets are compared. The best limit of 8.3×10^{-24} cm^3 s^{-1} at 1 TeV is obtained for Ret II, followed by Tuc III with 1.1×10^{-23} cm^3 s^{-1}, since these are the satellites with the largest J-factor. Tuc II follows with 2.4×10^{-23} cm^3 s^{-1} at 1 TeV. Gru II reaches 5.8×10^{-23} cm^3 s^{-1} and Tuc IV with same predicted J-factor and similar live time reaches 9.2×10^{-23} cm^3 s^{-1}. On these last two targets with similar characteristics the mean zenith angle for Gru II observations is lower, therefore it lowers the energy threshold and improves the limits at 1 TeV.
The constraints on *gamma lines* for the five targets are compared in Fig. 10.6. They reach 1.1×10^{-25} cm^3 s^{-1} for Ret II, 8.5×10^{-25} cm^3 s^{-1} for Tuc II, 1.4×10^{-25} cm^3 s^{-1} for Tuc III, 2.2×10^{-24} cm^3 s^{-1} for Tuc IV and 8.9×10^{-25} cm^3 s^{-1} for Gru II at 1 TeV. Fluctuations up to $\pm 3\sigma$ are observed, but they are expected in small data sets and are not significant.
Limits on the other annihilation channels are shown in Fig. 10.7, 10.8, 10.9, 10.10 and 10.11 for Ret II, Tuc II, Tuc III, Tuc IV and Gru II, respectively, on the other above mentioned channels. The best sensitivity is obtained for the $\tau+\tau-$ channel, that have branching ratios in both leptonic and hadronic channels.

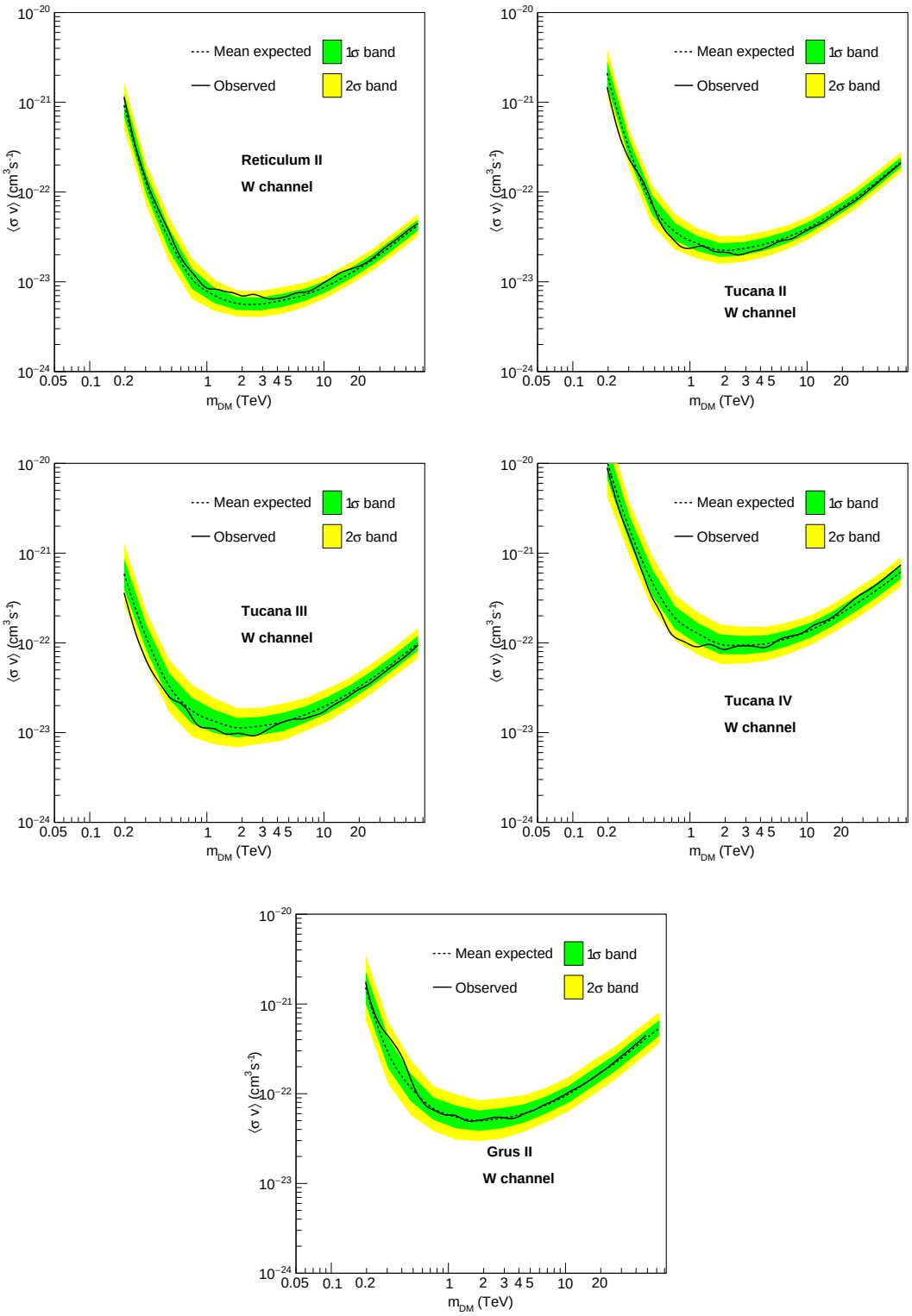

Figure 10.5: 95% C.L. observed (black solid line) and mean expected (black dashed line) upper limits on $\langle \sigma v \rangle$ as function of the DM mass in the W^+W^- annihilation channel on Ret II, Tuc II, Tuc III, Tuc IV and Gru II. The 1σ (green band) and 2σ (yellow band) expected containment bands are shown.

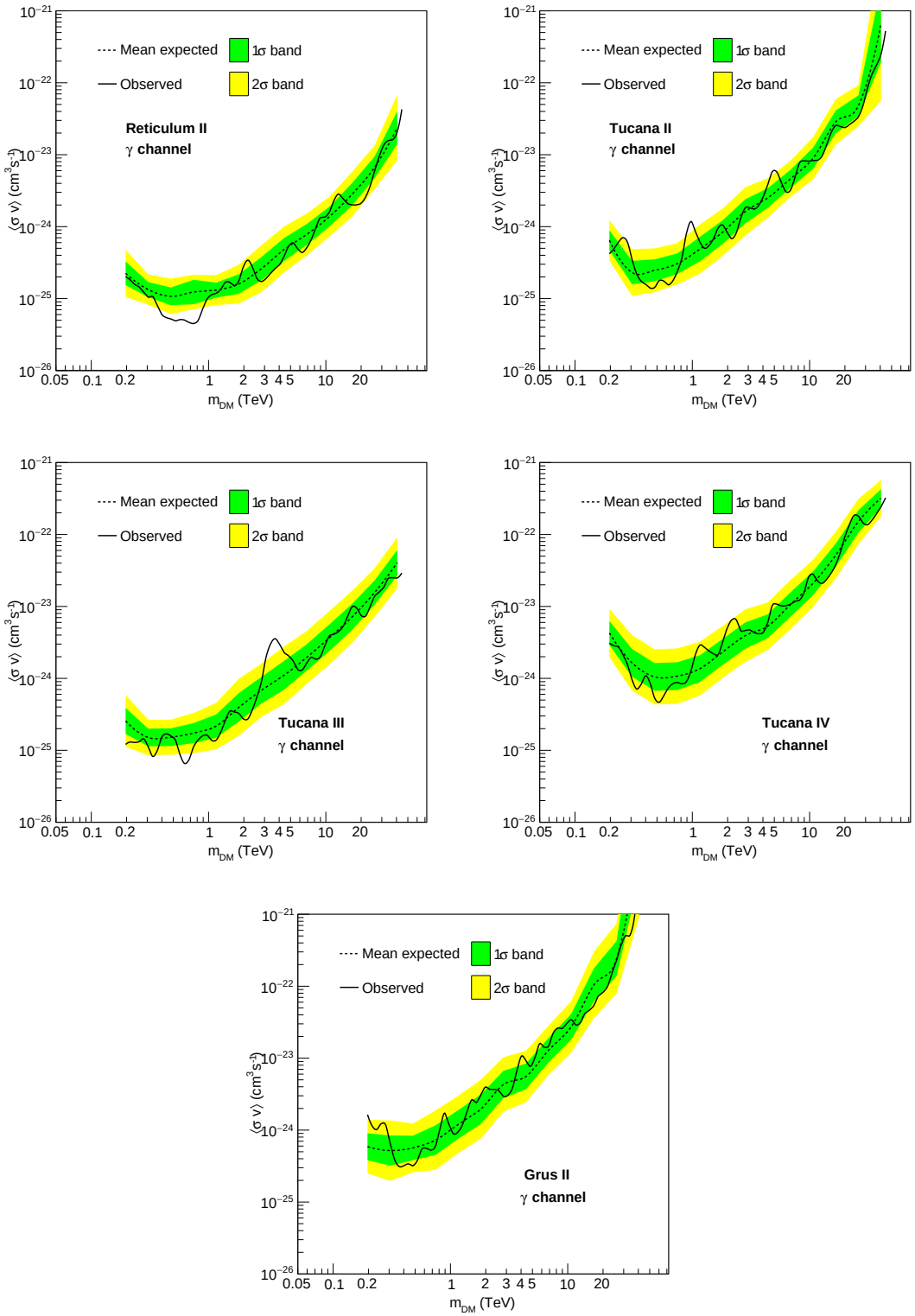

Figure 10.6: 95% C.L. observed (black solid line) and mean expected (black dashed line) upper limits on $\langle \sigma v \rangle$ as function of the DM mass in the $\gamma\gamma$ annihilation channel on Ret II, Tuc II, Tuc III, Tuc IV and Gru II.. The 1σ (green band) and 2σ (yellow band) expected containment bands are shown.

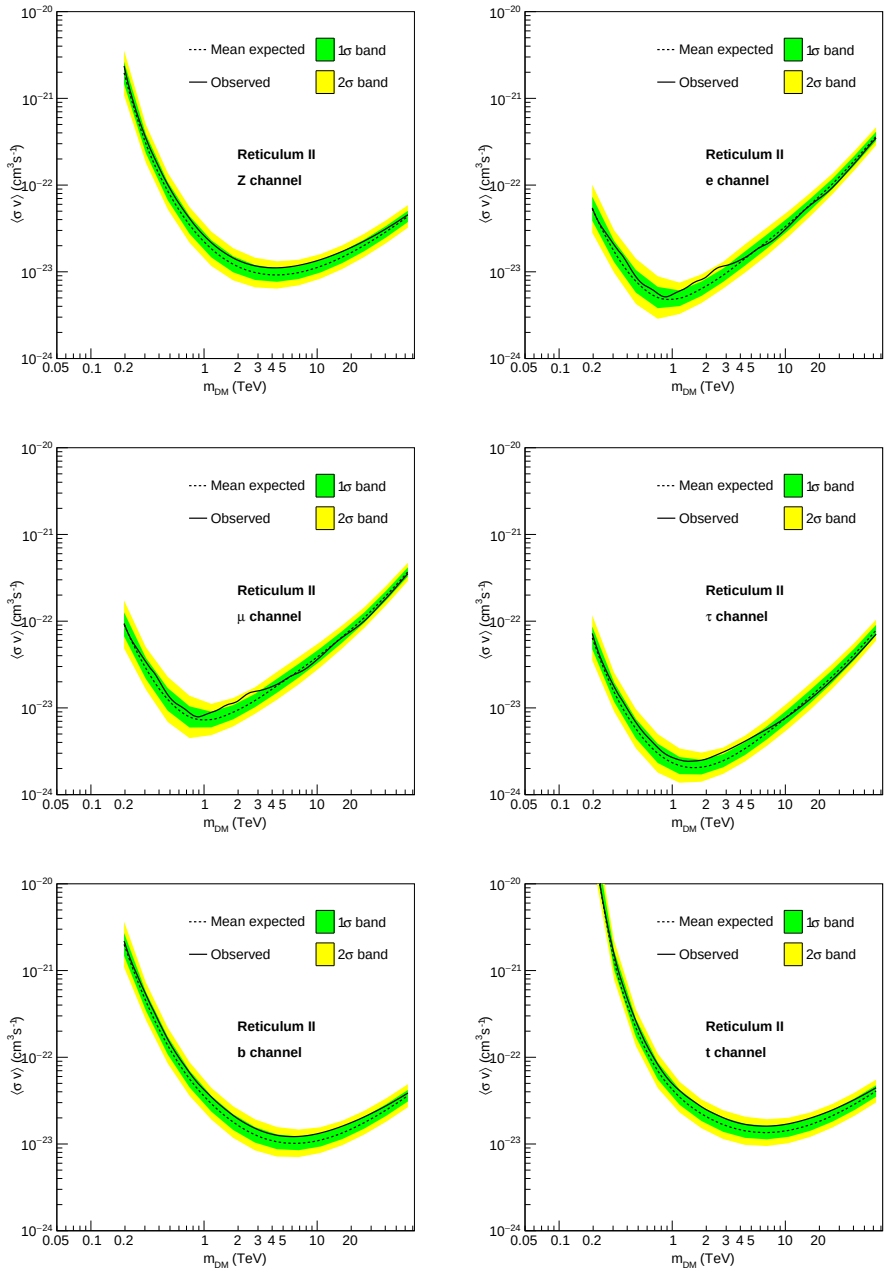

Figure 10.7: 95% C.L. observed (black solid line) and mean expected (black dashed line) upper limits on $\langle\sigma v\rangle$ as function of the DM mass in the ZZ, e^+e^-, $\mu^+\mu^-$, $\tau^+\tau^-$, $b\bar{b}$ and $t\bar{t}$ annihilation channels on Ret II. The 1σ (green band) and 2σ (yellow band) expected containment bands are shown.

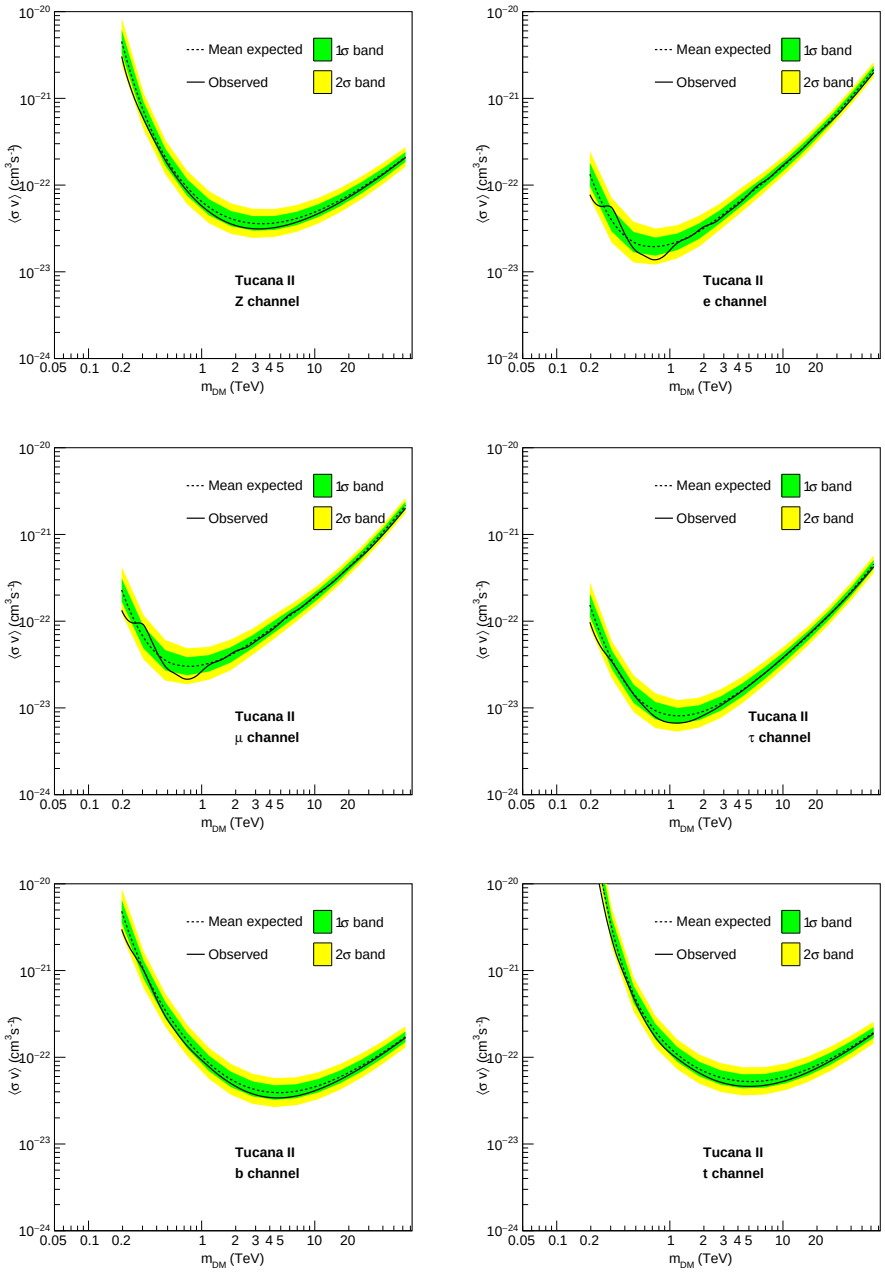

Figure 10.8: 95% C.L. observed (black solid line) and mean expected (black dashed line) upper limits on $\langle\sigma v\rangle$ as function of the DM mass in the ZZ, e^+e^-, $\mu^+\mu^-$, $\tau^+\tau^-$, $b\bar{b}$ and $t\bar{t}$ annihilation channels on Tuc II. The 1σ (green band) and 2σ (yellow band) expected containment bands are shown.

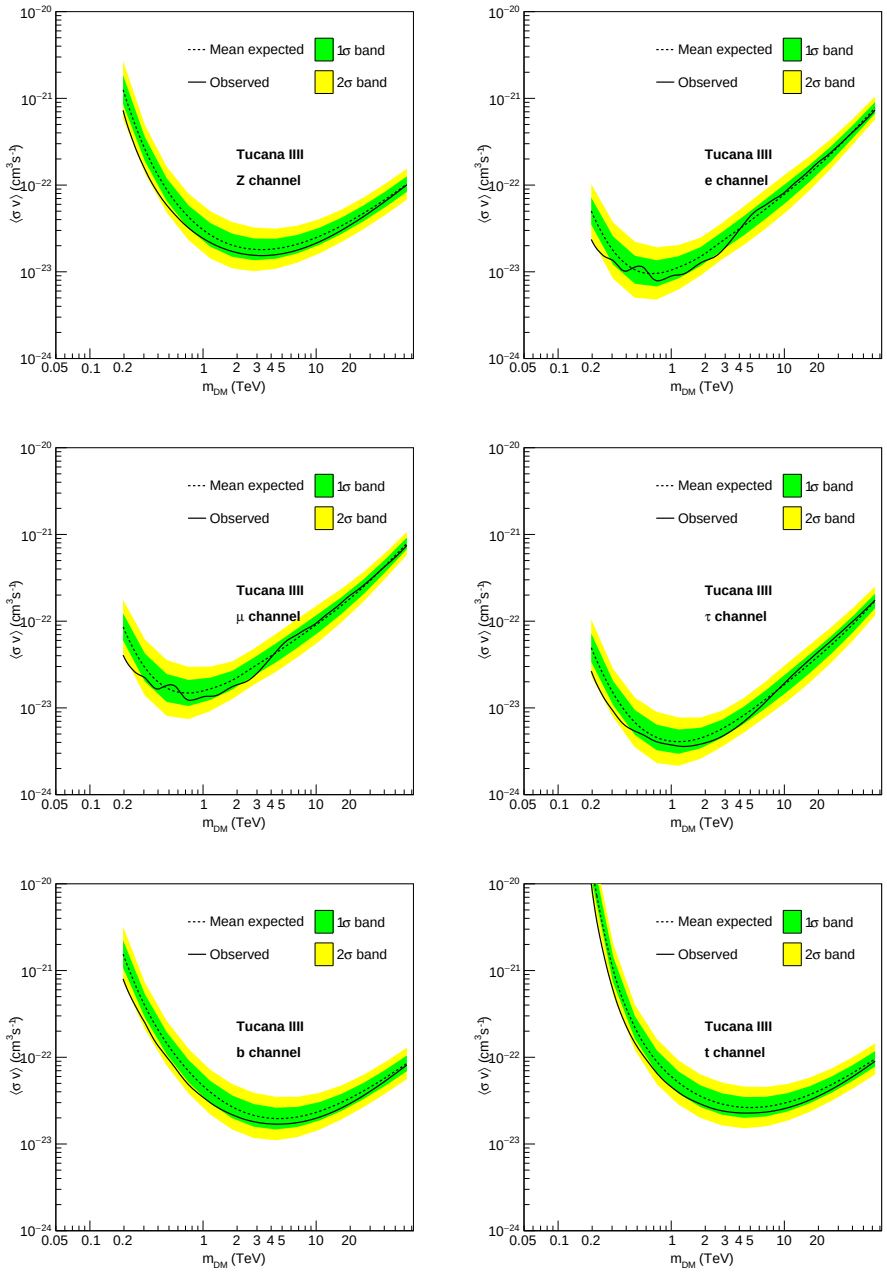

Figure 10.9: 95% C.L. observed (black solid line) and mean expected (black dashed line) upper limits on $\langle\sigma v\rangle$ as function of the DM mass in the ZZ, e^+e^-, $\mu^+\mu^-$, $\tau^+\tau^-$, $b\bar{b}$ and $t\bar{t}$ annihilation channels on Tuc III. The 1σ (green band) and 2σ (yellow band) expected containment bands are shown.

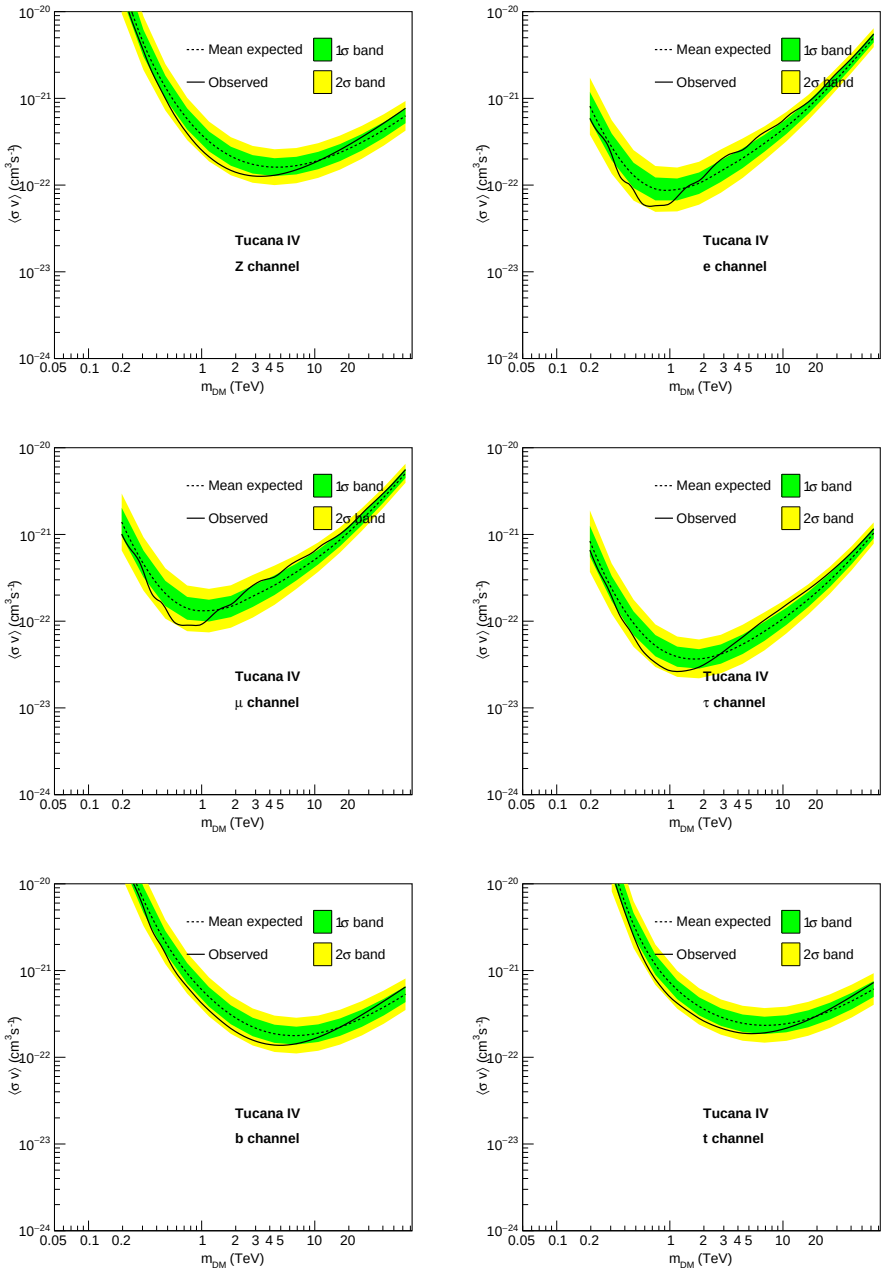

Figure 10.10: 95% C.L. observed (black solid line) and mean expected (black dashed line) upper limits on $\langle\sigma v\rangle$ as function of the DM mass in the ZZ, e^+e^-, $\mu^+\mu^-$, $\tau^+\tau^-$, $b\bar{b}$ and $t\bar{t}$ annihilation channels on Tuc IV. The 1σ (green band) and 2σ (yellow band) expected containment bands are shown.

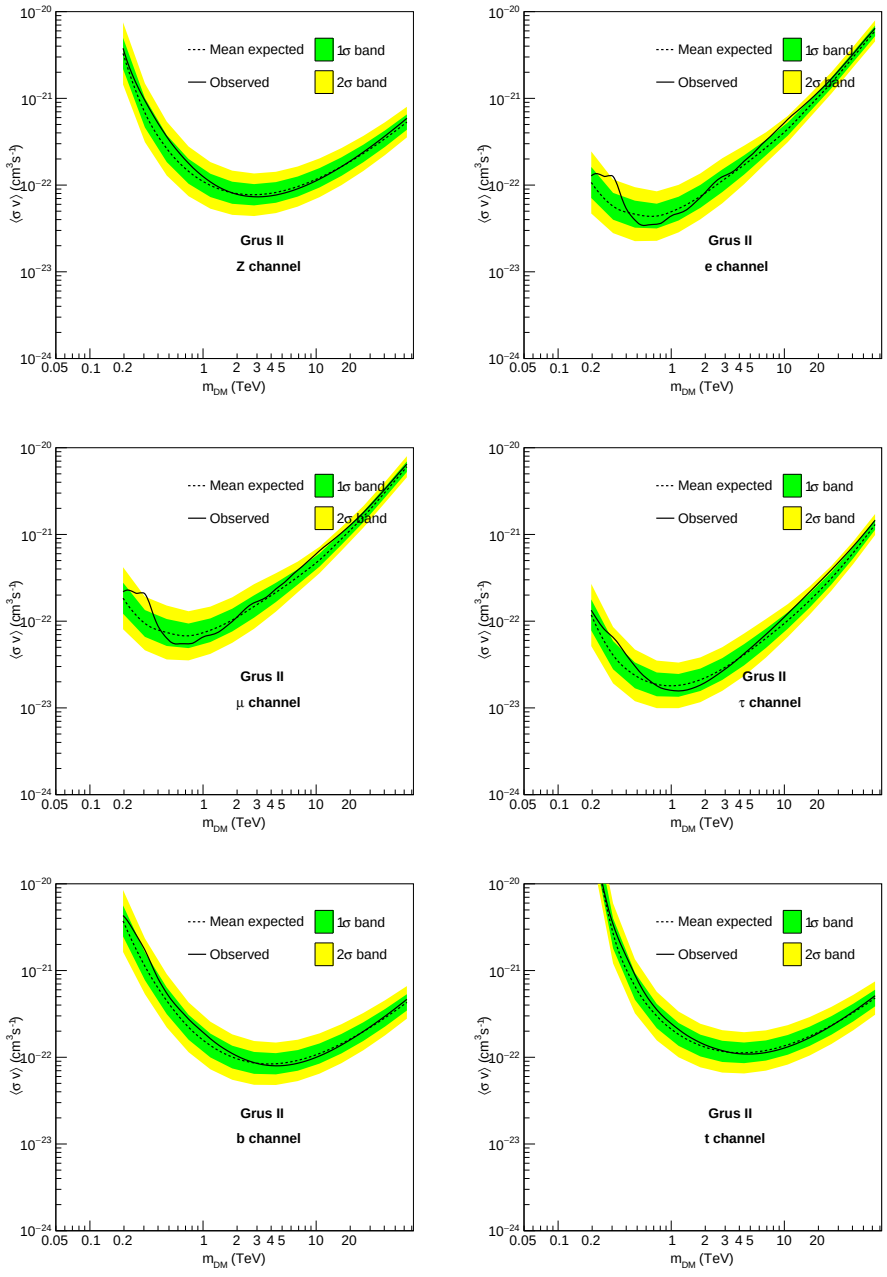

Figure 10.11: 95% C.L. observed (black solid line) and mean expected (black dashed line) upper limits on $\langle\sigma v\rangle$ as function of the DM mass in the ZZ, e^+e^-, $\mu^+\mu^-$, $\tau^+\tau^-$, $b\bar{b}$ and $t\bar{t}$ annihilation channels on Gru II. The 1σ (green band) and 2σ (yellow band) expected containment bands are shown.

10.5.2 Individual versus combined limits

The limits on the different targets can be combined at a likelihood level. The total likelihood is the product of the individual likelihoods $\mathcal{L}_{\rm k}$ for each target:

$$\mathcal{L}_{\rm tot} = \prod_{k=1}^{n_{\rm targets}} \mathcal{L}_{\rm k}. \tag{10.4}$$

Thus the LLRTS for the total sample, being logarithmic, is the sum of the test statistics computed for each target. Fig. 10.12 compares the combined limits to those obtained for the single targets in the W^+W^- (top left panel) and $\gamma\gamma$ (top right panel) channels. It also shows the combined limits in every channel (bottom panel). The combination has been performed on the confirmed galaxies Ret II and Tuc II (gray solid line) and on all the five objects (black solid line). The combined limits are dominated by Ret II and Tuc III. The limits from the combination of all the targets reach 3.7×10^{-24} cm^3 s^{-1} and 6.2×10^{-26} cm^3 s^{-1} at 1 TeV for the W^+W^- and $\gamma\gamma$ channels, respectively, giving a 55% and 45% improvement with respect to Ret II individual limits, respectively. Those from the combination of Ret II and Tuc II are strongly dominated by Ret II and reach 6.3×10^{-24} cm^3 s^{-1} and 1.1×10^{-25} cm^3 s^{-1} at 1 TeV in W^+W^- and $\gamma\gamma$, respectively, giving a 25% and < 1% level improvement with respect to Ret II individual limits.
The improvement of the limits due to the combination of targets opens the path also to the possibility of combining different experiments.

10.5.3 Effect of the statistical uncertainty on the J-factor

The uncertainty on the J-factor can be included in the computation of the limits on $\langle\sigma v\rangle$ by treating the J-factor as a log-normal statistical variable, as explained in Sec. 7.3.1. This technique is conservative and shows a degradation of the limits proportional to $\exp\left(-\sigma_{\rm J}^2 \log^2(10)\right)$. Other approaches are possible, for instance VERITAS showed the uncertainty on J as bands around the limits [234], obtained from many realizations of halo J-factor profiles consistent with kinematic data.
Fig. 10.13 shows the degradation of Ret II and Tuc II limits while adding the uncertainty σ_J corresponding to a $\log_{10} J_{\rm ON,max}$ of 18.4 and 17.4, respectively. The limits deteriorated by the uncertainty on J are ~ 6.5 and 12 times larger than those that do not include σ_J for Ret II and Tuc II, respectively.
On Tucana III the smallest J-factor value found in literature [249], rescaled for the dimension of the *ON region*, $\log_{10}[J(< 0.125^\circ)/{\rm GeV^2 cm^{-5}}] = 17.2$ has been tested. The limits are almost 40 times worse than for the J-factor value given in Tab. 10.2. They are obtained through a simple rescaling with the new J-factor value, as relevant in the case of a single ROI.
Improving the knowledge about the stellar kinematic of ultra-faint dSph, *i.e.* about their DM

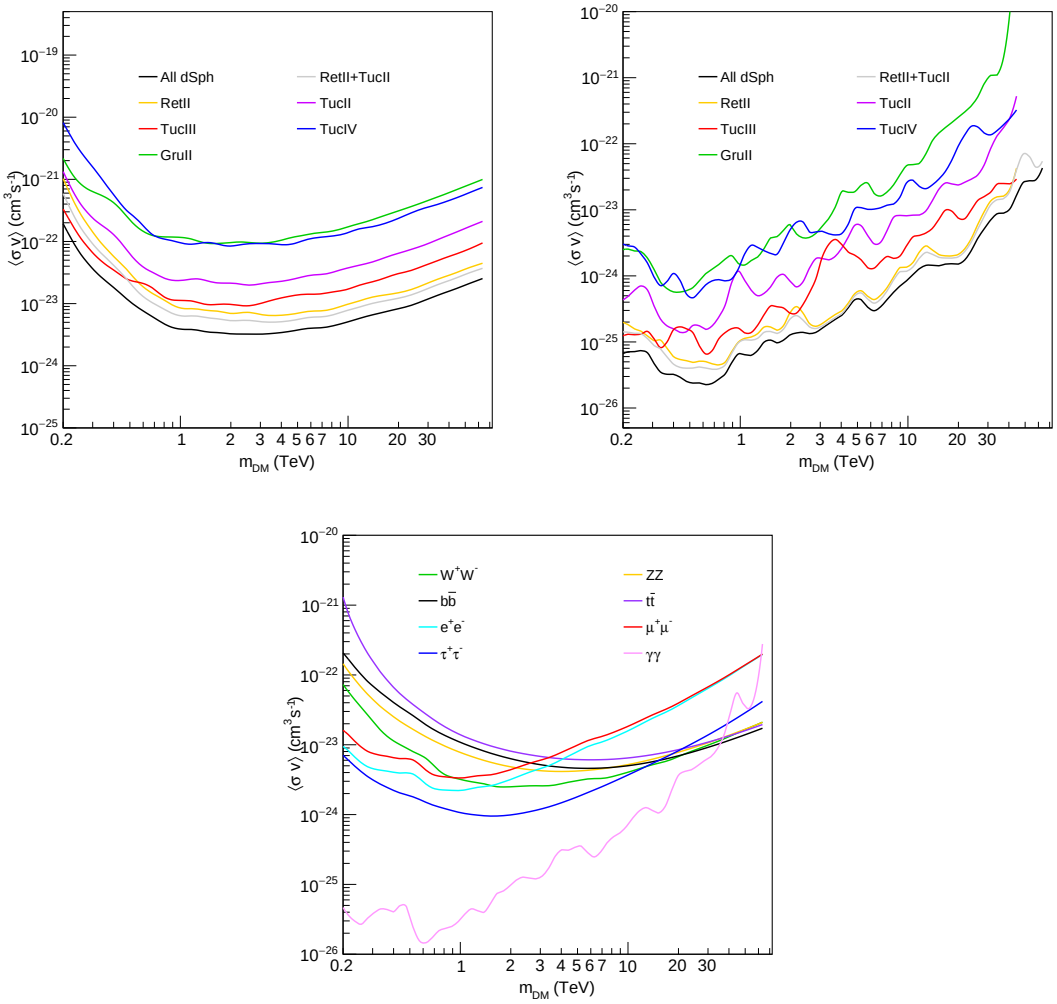

Figure 10.12: Combined 95% C.L. observed (black solid line) and mean expected (black dashed line) upper limits on $\langle\sigma v\rangle$ as function of the DM mass. The combination of all the targets (black solid line) and of Ret II and Tuc II only (gray solid line) is shown in W^+W^- (top left panel) and $\gamma\gamma$ (top right panel). The limits from the combination of all targets are compared in all the channels (bottom plot). No statistical uncertainty is considered here.

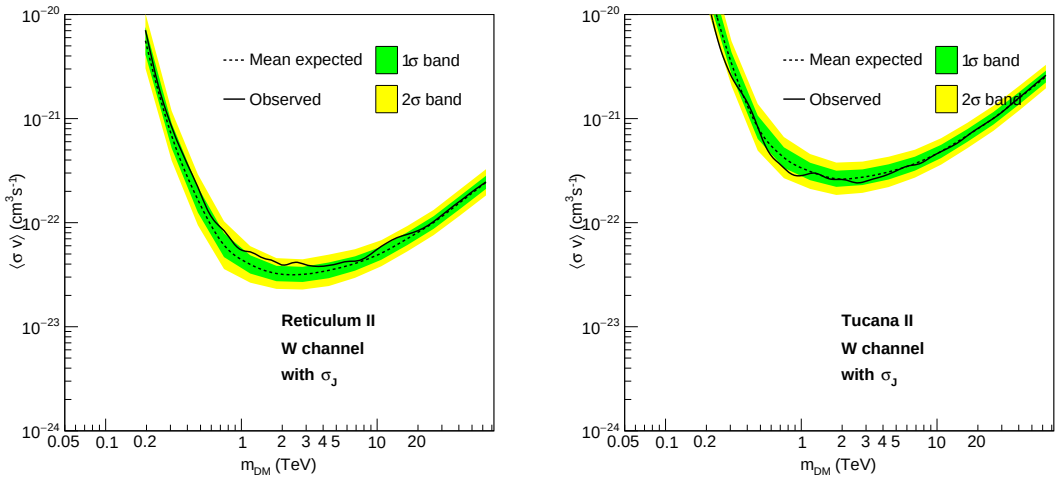

Figure 10.13: Combined 95% C.L. upper limits on $\langle \sigma v \rangle$ as function of the DM mass including the uncertainty on the J-factor. Limits for Ret II (left panel) and Tuc II (right panel) including the statistical uncertainty on the J-factor are shown.

content and spatial distribution, is a challenge for the future that would have a significant impact on the indirect DM searches. Dedicated observations with facilities like Keck or SKA are needed on the basis of specific observations proposals.

10.5.4 Comparison with other experiments

In Fig. 10.14 H.E.S.S. combined limits on DES satellites are compared to previous H.E.S.S. limits on the combination of dSphs [255], MAGIC limits on Segue 1 computed[2] during the combined analysis with Fermi-LAT [256], VERITAS limits on the combination of 5 dSph [234], HAWC limits on 15 targets [257] and Fermi-LAT constraints on 15[3] objects [256]. The limits marked with a * contains the J-factor uncertainty, but the technique used to include it in the LLRTS may not be strictly the same from one collaboration to another. In addition, classical dSph have σ_J significant smaller that ultra-faint ones.

H.E.S.S. limits are the most stringent among IACTs above several TeV. They are stronger than HAWC constraints and are competitive with Fermi-LAT in the few-TeV mass range. Note that Fermi-LAT can show limits on W^+W^- up to a few ten TeV despite the low sensitivity at high energies. Even if there are very few detected gamma rays above hundred GeV in their dataset the *continuum* spectrum is broad in energy and also the low-energy

[2]MAGIC DM limits towards Segue 1 have first been computed in 2013 [232]. A second computation [256] has given more stringent results. The latest constraints have been improved by the collaboration among MAGIC and Fermi-LAT and a change in the likelihood approach applied by MAGIC in their analysis.

[3]A Fermi-LAT DM search performed on 45 targets, including DES dSph, has been published [237], but the combined limits in the W^+W^- channel is not provided.

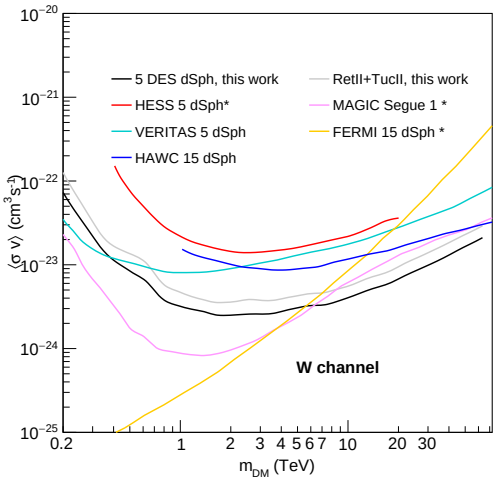

Figure 10.14: 95% C.L. combined upper limits from this work on W^+W^+ compared to previous H.E.S.S. [255], MAGIC [256], VERITAS [234], HAWC [257] and Fermi-LAT [256] DM searches towards dSph. The results marked with an asterisk include the systematic uncertainty of the J-factor, but its value varies significantly from one target to another and the way it is treated in the analysis changes as well from a collaboration to another.

DM photons play a role. This is not the case for *gamma lines*, that are very narrow features at the position of the DM mass.

10.6 Outlook and perspectives

H.E.S.S. has proved to be competitive in the search for dark matter towards dwarf spheroidal galaxies with the full H.E.S.S.-II array. Specifically, this latest analysis of recently discovered ultra-faint dwarf satellites of the Milky Way produces the strongest limits on the DM annihilation cross section in several channels above about several TeV. H.E.S.S. has been the first Cherenkov telescope that observed a selection of DES dSph candidates, exploiting its position in the Southern hemisphere from which most of these objects can be best observed. The constraints derived by ground-based Cherenkov telescopes are particularly interesting for the search of *gamma lines*, that in the multi-TeV range could be enhanced, for example by the Sommerfeld effect, and are not at reach for Fermi-LAT at such large masses.
Since the present experiments target objects in different parts of the sky and use different techniques to detect gamma-rays, in the future a promising method to improve the actual dark matter searches is to combine the efforts. A project is ongoing in order to combine the effort of the different high-energy gamma-ray detectors in order to improve the sensitivity to dark matter annihilation towards dSph. The project includes the IACTs H.E.S.S., MAGIC and VERITAS, and Fermi-LAT and HAWC. Each experiment will provide the TS value

versus $\langle \sigma v \rangle$ at several $m_{\rm DM}$ for targets already used for publications by the single collaborations and agreed J-factors. The results will be then combined together at the likelihood level without sharing the raw datasets. The joint limits will cover a DM mass range from 1 GeV to 100 TeV, scanning cross section values between about 10^{-21} cm^3 s^{-1} and 10^{-27} cm^3 s^{-1}. Compared to the Galactic Center the dwarf galaxies are low standard background regions and the detection of a dark matter signal towards one of them would be unambiguous. In addition, if the dark matter profile of the Galactic halo is cored and of large size the limits computed towards dwarf galaxies become competitive with those at the Galactic Center.

Part V

Prospects for dark matter searches with Cherenkov telescope arrays

Chapter 11

Search for Wino dark matter towards the Galactic Center with H.E.S.S.

Contents

11.1 The Wino model : a prototype dark matter candidate 204
11.2 Expected annihilation signal 205
11.2.1 Definition of the regions of interest 205
11.2.2 Total spectrum: line, *endpoint* and *continuum* contributions 206
11.2.3 Cored dark matter profiles 207
11.3 Analysis of mock H.E.S.S.-I-like observations 208
11.3.1 Cosmic-ray background 208
11.3.2 Expected residual background rate in the regions of interest 209
11.4 Forecast limits on Wino annihilation in H.E.S.S.-I-like observations . 210
11.4.1 Limits on the annihilation cross section 210
11.4.2 DM distribution at the Galactic Center for pure Wino DM 212
11.5 Prospects for DM search with IGS-like observation strategy. 214
11.5.1 IGS-like region of interest 214
11.5.2 Expected limits for different cored DM profiles 214
11.6 Discussion and perspectives 216

In this chapter forecast limits on dark matter annihilation cross section are computed for a H.E.S.S.-I-like analysis of mock observations towards the Galactic Center and a specific heavy weakly interacting dark matter model. The Wino dark matter candidate and the framework for the computation of its spectrum are described. The modeling of the expected background and signal in H.E.S.S.-I-like observations is presented. Forecast constraints on dark matter properties are shown and discussed. Several dark matter density profiles at the Galactic Center are tested. A H.E.S.S.-II IGS-like observation strategy is also tested.
Sec. 11.1 introduces the Wino dark matter candidate and its spectrum. The analysis framework and the expected signal and background in the Galactic Center region are explained in Sec. 11.2 and Sec. 11.3. Forecast constraints on the Wino annihilation cross section are computed for H.E.S.S.-I like analysis in Sec. 11.4 and an Inner-Galaxy-Survey-like observation strategy in Sec. 11.5. This work has been published in [258].

11.1 The Wino model : a prototype dark matter candidate

The Wino is a DM candidate that naturally appears as the LSP in a supersymmetric extension of the SM. It is the neutral component of a $SU(2)_{\mathrm{W}}$ triplet with zero hypercharge [259, 260]. The latest calculations of the Wino annihilation spectrum into photons [261] are used in this work. The computation is performed in an effective field theory (EFT) framework developed in [262] and extends to the next-to-next-to-logarithmic (NLL) order. Due to the small particle velocity ($v/c \sim 10^{-3}$), a non-relativistic EFT can be used and the Sommerfeld effect is included being non-negligible in this mass regime. The spectrum includes non-tree level contributions in the region where $z = \frac{E_\gamma}{m_{\mathrm{DM}}} \to 1$, referred to as the *endpoint*, for DM χ annihilating into a hard photon and additional final state radiation $\chi\chi \to \gamma X$. For example, Z and γ can be produced in a 1-loop process by exchanging a W boson. Note that this framework is valid in the regime where the DM mass is much larger than the mass of the exchanged boson, $m_{\mathrm{DM}} \gg m_{\mathrm{W}}$ GeV. For this reason spectra and limits in this chapter are shown only for masses above 1 TeV.

In the ideal case with $z = 1$ only two bosons can be produced and this case is relevant for an ideal experiment with infinite resolution. In a realistic case, with finite energy resolution, the contribution of additional photons in the final state must be considered for $z \to 1$. Fig. 11.1 shows a schematic of the initial and final state contributions to the gamma-ray spectrum. The two initial state DM particles (blue) undergo Sommerfeld effect (lilac). In the final state, beside the hard photon (red), radiation collimated with the direction of recoil of the boson against the photon is observed (dark blue). The collimated recoiling jet together with the final state radiation gives what we call the *endpoint* contribution. Low energy radiation (green) is present both in the initial and final state.

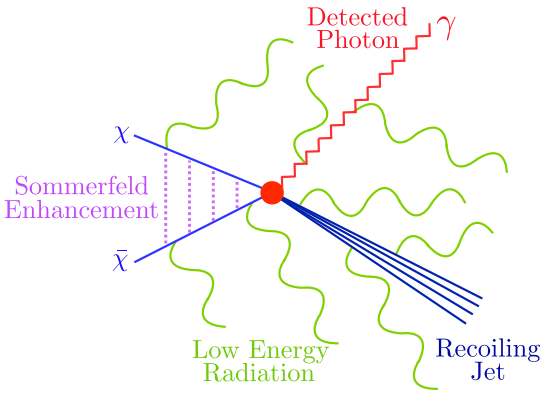

Figure 11.1: Diagram of the annihilation $\chi\chi \to \gamma X$. The DM particles (blue) annihilate into a hard photon (red) that recoils against a collimated jet of electroweak radiation (dark blue). Sommerfeld effect (lilac) takes place in the initial state. Soft isotropic radiation (green) is also emitted.

The NLL annihilation cross section reads

$$\left(\frac{\mathrm{d}\sigma}{\mathrm{d}E}\right)^{NLL} = \sigma_{\mathrm{line}}\left[2\delta(E - m_{\mathrm{DM}}) + \left(\frac{\mathrm{d}\mathcal{N}_\gamma}{\mathrm{d}E}\right)^{\mathrm{endpoint}} + \left(\frac{\mathrm{d}\mathcal{N}_\gamma}{\mathrm{d}E}\right)^{\mathrm{continuum}}\right], \tag{11.1}$$

where $\left(\frac{\mathrm{d}\mathcal{N}_\gamma}{\mathrm{d}E}\right)^{\mathrm{endpoint}}$ is the *endpoint* contribution and $\left(\frac{\mathrm{d}\mathcal{N}_\gamma}{\mathrm{d}E}\right)^{\mathrm{continuum}}$ is the contribution of $W^\pm$ that then decay into photons. These additional contributions to the spectrum are normalized to the line cross section σ_{line}. Fig. 11.2 compares a simple line (colored dashed line, Dirac delta function) to the additional spectral component in the *endpoint* region (colored solid line) for Wino DM with masses between 2 and 44 TeV. This is the theoretical *endpoint + continuum* spectrum that does not account for the energy resolution of the experiment.

11.2 Expected annihilation signal

11.2.1 Definition of the regions of interest

As for the H.E.S.S.-I GC analysis in Sec. 8.2 the regions of interest (ROIs) are defined as rings of width 0.1° around the GC. The overall *ON region* covers from 0.3° up to 1.0° in radial distance from the GC. A band of width ±0.3° in latitude is excluded around the Galactic plane, as well as a disk of radius 0.4° centered at the position of HESS J1745-303. The possibility to build a larger *ON region* up to 4° is discussed in Sec. 11.5.
In the analysis with mock observations there is no reflected *OFF region* for background measurement. The residual background is here modeled from the CR flux spectrum at

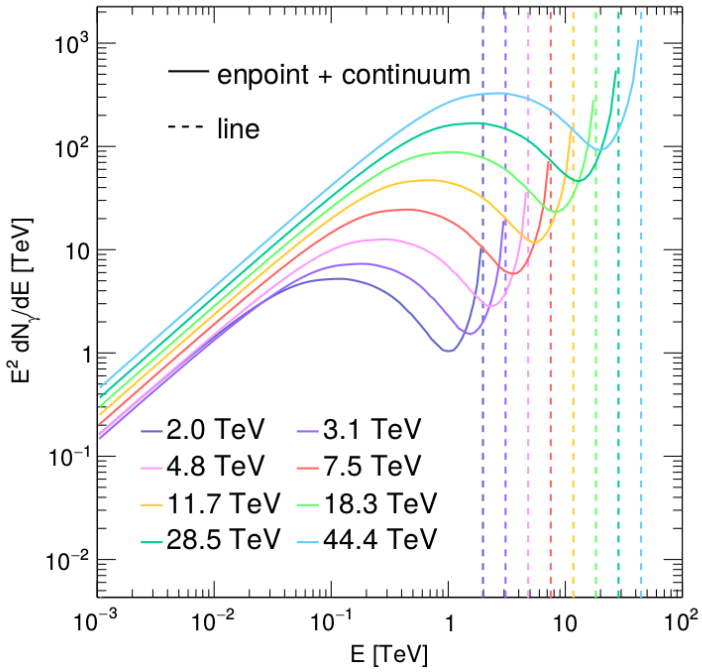

Figure 11.2: Theoretical Wino annihilation spectrum into gamma rays. The *endpoint* and *continuum* (solid lines) components give an additional contribution to the line spectrum (dashed line), shown for different m_{DM} between 2 TeV and 44.4 TeV.

Earth and H.E.S.S.-I IRFs. Thus, no additional exclusion region is added. The observations time is assumed to be 250 hours flat in the *ON region* accordingly to the real H.E.S.S.-I exposure at the GC.
Tab. 11.1 summarizes the properties of the ROIs up to 4° considered here. The 1°-*ON region* stops at ROI 7. The inner radius θ_{i} and solid angle size $\Delta\Omega_{\mathrm{i}}$ for each ROI is given. The integrated J-factor $J(\Delta\Omega_{\mathrm{i}})$ is provided for different DM density profiles.

11.2.2 Total spectrum: line, *endpoint* and *continuum* contributions

In what follows the expected signal is modeled for three different cases, including some or all the spectral contributions to the total spectrum from Eq. (11.1):

1. *line only* (first term),
2. *line + endpoint* (first + second term),
3. *line + endpoint + continuum* (all the three terms), also referred to as the full spectrum.

The impact of each component on the DM limits is tested in Sec. 11.4.
The theoretical spectrum is converted into gamma-ray flux with Eq. (6.8), for the chosen

i-th ROI	$\Delta\Omega_i$	$J_i(\Delta\Omega_i)\,[10^{20}\ \mathrm{GeV^2\ cm^{-5}}]$					
	$[10^{-4}\ \mathrm{sr}]$	Einasto	$r_\mathrm{c} = 0.3$ kpc	$r_\mathrm{c} = 0.5$ kpc	$r_\mathrm{c} = 1$ kpc	$r_\mathrm{c} = 3$ kpc	$r_\mathrm{c} = 5$ kpc
1: $\bar{\theta}_1 = 0.3°$	0.31	3.76	1.08	0.60	0.23	0.035	0.012
2: $\bar{\theta}_2 = 0.4°$	0.50	5.16	1.14	0.97	0.38	0.056	0.019
3: $\bar{\theta}_3 = 0.5°$	0.69	6.15	2.40	1.34	0.52	0.078	0.026
4: $\bar{\theta}_4 = 0.6°$	0.88	6.89	3.04	1.71	0.66	0.099	0.033
5: $\bar{\theta}_5 = 0.7°$	1.08	7.45	3.67	2.07	0.81	0.12	0.040
6: $\bar{\theta}_6 = 0.8°$	1.27	7.88	4.29	2.43	0.95	0.14	0.047
7: $\bar{\theta}_7 = 0.9°$	1.46	8.20	4.90	2.79	1.09	0.16	0.055
⋮	⋮	⋮	⋮	⋮	⋮	⋮	⋮
37: $\bar{\theta}_{37} = 3.9°$	7.55	8.78	8.78	8.78	5.23	0.88	0.28

Table 11.1: Definition of the ROIs and their J-factor The number of the ROI, its inner radius and solid angle size and the J-factor for different DM profiles integrated in the ROI are given, respectively.

DM density profile. Then, the expected number of photons for the H.E.S.S.-I-like mock analysis is computed as in Chap. 8 following Eq. (8.2), including the H.E.S.S.-I IRFs and the observation time. An energy resolution of $\Delta E = 10\%$ and a H.E.S.S.-I-like mean acceptance for a zenith angle of 20° are used.

11.2.3 Cored dark matter profiles

First, an Einasto profile, with the parameters in Tab. 8.4, is used, as in the H.E.S.S.-I analysis at the GC. Then, various cored DM profiles are tested. In this framework it is possible to include large cores because the residual background is modeled, while in the data analysis carried out with the true observations dedicated *OFF runs*[1] would be needed since the DM core size would extend over the whole FoV or more.

The cored profiles are empirically parametrized as a cored Einasto profile as in Eq. (6.7) in order to recover the initial Einasto profile for $r_\mathrm{c} \to 0$. Cores as large as 5 kpc [263] are considered[2].

In the left panel of Fig. 11.3 the differential J-factor as function of the distance from the GC is shown for the cuspy Einasto profile and cores of size 300 pc, 1 kpc, 3 kpc and 5 kpc. In the right panel of Fig. 11.3 the value of the J-factor integrated in the ROIs, computed

[1] See background measurements in Sec. 2.4.2.

[2] Note, however, that some studies disfavor 5-kpc sized flat-density cores [264].

according to Eq. (6.12), is shown for the same profiles as function of the region number. 37 ROIs, corresponding to an overall *ON region* of 4° are considered.

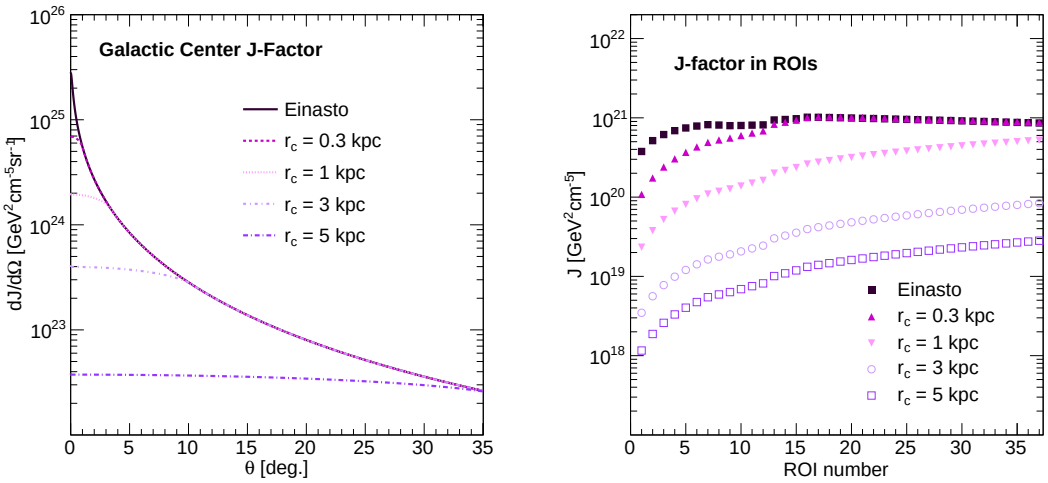

Figure 11.3: Dark matter core profiles considered here for forecast H.E.S.S.-I-like limits on the Wino annihilation cross section. *Left panel:* differential J-factor curves for several DM core sizes as function of the distance from the GC from Eq. (6.9). *Right panel:* integrated J-factor in ROIs from Eq. (6.12) up to 4.0° for several DM core sizes.

11.3 Analysis of mock H.E.S.S.-I-like observations

11.3.1 Cosmic-ray background

The residual background is modeled from the protons, helium and electrons flux spectra modeled in [265]. The protons and helium spectra are power-laws $\mathrm{d}\phi(E)/\mathrm{d}E = N \times (E/1\ \mathrm{TeV})^k$. The electron one follows a more complex function: $\mathrm{d}\phi(E)/\mathrm{d}E = N \times (E/1\ \mathrm{TeV})^k + L/(Ew\sqrt{2\pi})\exp(-(\ln(E/E_\mathrm{p}))^2/2w^2)$. The parameters of the spectra given in Tab. 11.2 are obtained from measurements of BESS, PAMELA, Fermi-LAT and H.E.S.S..

Particle type	N [1/(m^2 s sr TeV)]	k	L	E_p [TeV]	w
p	0.096	-2.70			
He	0.0719	-2.64			
e	6.85×10^{-5}	-3.21	3.19×10^{-3}	0.107	0.776

Table 11.2: Parametrization of the CR spectra of protons, helium and electrons taken from Ref. [265].

Differential fluxes of the CR hadrons (black solid line) and electrons (black dashed line), the Pevatron (orange solid line) are given in the left panel of Fig. 11.4. The differential flux

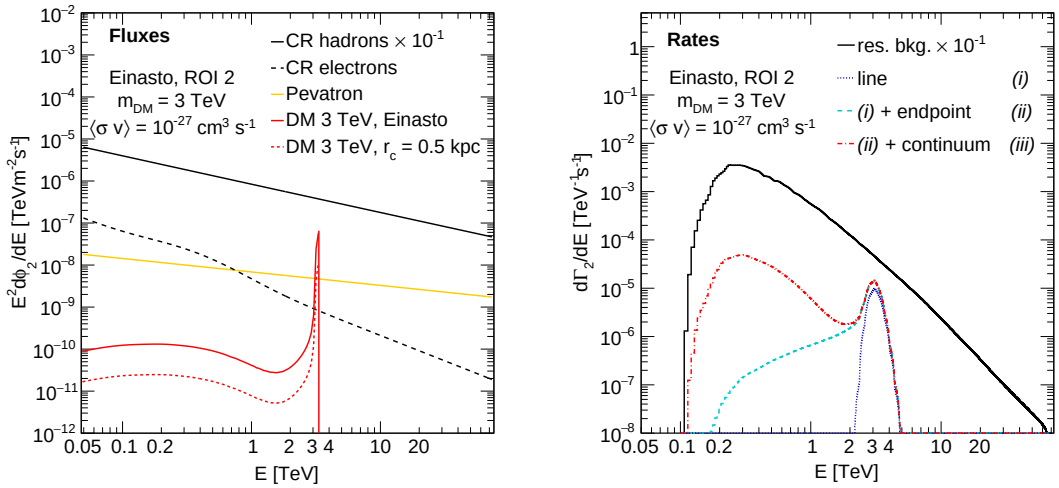

Figure 11.4: Differential flux and rate of the expected Wino signal and modeled H.E.S.S.-I-like residual background. *Left panel:* The differential fluxes of CR hadrons (black solid line) and electrons (black dashed line), Pevatron (orange solid line) and Wino signal for $m_{\rm DM} = 3$ TeV and $\langle\sigma v\rangle = 10^{-27}$ cm^3 s^{-1}, assuming Einasto (red solid line) and 500-pc-size cored (red dashed line) DM density profile, respectively, are shown. *Right panel:* Energy differential rates of residual background (black solid line) and Wino *line only* (blue dotted line), *line + endpoint* (cyan dashed line) and *line + endpoint + continuum* (red solid line) signal for $m_{\rm DM} = 3$ TeV and $\langle\sigma v\rangle = 10^{-27}$ cm^3 s^{-1}, assuming an Einasto profile, are shown.

a 3 TeV Wino for an Einasto (red solid line) and a 500-pc-size cored profile (red dashed line) are also plotted, assuming $\langle\sigma v\rangle = 10^{-27}$ cm^3 s^{-1} and the full spectrum.

11.3.2 Expected residual background rate in the regions of interest

From the spectra $\mathrm{d}\phi_{\rm CR}/\mathrm{d}E$ the differential gamma-ray rate $\mathrm{d}\Gamma_{\rm CR}/\mathrm{d}E$ is computed convolving for the effective area and energy resolution of H.E.S.S. I:

$$\frac{\mathrm{d}\Gamma_{\rm CR}}{\mathrm{d}E}(E,\Delta\Omega) = \int_{-\infty}^{\infty} \mathrm{d}E' \frac{\mathrm{d}\phi_{\rm CR}}{\mathrm{d}E'}(E') A_{\rm eff}^{\rm CR}(E') \mathcal{G}(E,E')\Delta\Omega. \tag{11.2}$$

The CR acceptance $A_{\rm eff}^{\rm CR}$ for electrons is equal to the gamma-ray acceptance $A_{\rm eff}^{\gamma}$[3], while in case of protons and helium it is $A_{\rm eff}^{\rm CR} = \eta_{\rm had} A_{\rm eff}^{\gamma}$. The term $\eta_{\rm had} = 0.1$ is the hadron efficiency. The number of expected counts in an ROI is given by the integral of the gamma-ray rate over the energy bin, the observation time and the ROI size $\Delta\Omega$.
The procedure is repeated for each bin (i, j) according to the data analysis in Chap. 8. The

[3]Both CR electrons and gamma rays induce electromagnetic showers in the atmosphere. They can be distinguished by the depth of the first interaction. The procedure is not trivial, a limited discrimination is yet obtained. It is not part of the standard H.E.S.S. event selection and including the electrons in the residual background is a conservative approach.

2D-likelihood function in Eq. (7.8) and the LLRTS are used to derive the expected sensitivity as 95% upper limits on $\langle\sigma v\rangle$ as function of $m_{\rm DM}$. The right panel of Fig. 11.4 shows the counts rate in ROI 2 for the modeled CR residual background (black solid line) and the expected Wino signal for $m_{\rm DM} = 3$ TeV, Einasto cuspy profile and $\langle\sigma v\rangle = 10^{-27}$ cm^3 s^{-1}. The three contributions to the Wino spectrum, *line only* (blue dotted line), *line + endpoint* (cyan dashed line) and *line + endpoint + continuum* (red dotted dashed line), are highlighted. The most prominent signal feature is the *line + endpoint* bump of the spectrum, that is expected to dominate the sensitivity.

11.4 Forecast limits on Wino annihilation in H.E.S.S.-I-like observations

11.4.1 Limits on the annihilation cross section

Mean expected limits and containment bands are computed for the Wino full spectrum through Poisson realizations. In Fig. 11.5 this sensitivity (red solid line) is compared to the theoretical NLL annihilation cross section (gray solid line). The resonances in the

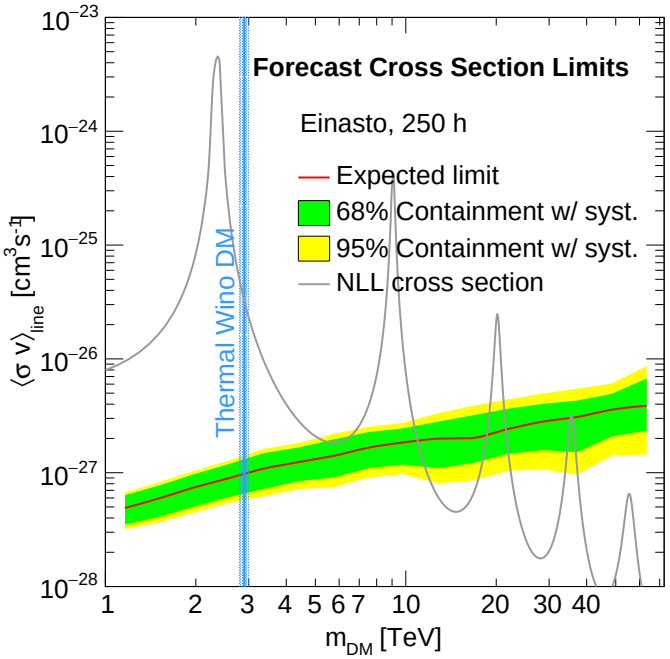

Figure 11.5: H.E.S.S.-I sensitivity to Wino DM for Einasto profile. Mean expected limits (red solid line) on $\langle\sigma v\rangle$ vs $m_{\rm DM}$ are given together with the 1σ (green area) and 2σ (yellow area) containment bands. The systematic uncertainties determined for H.E.S.S.-I *gamma line* searches towards the GC (see Chap. 8) are included in the bands. The theoretical cross section (gray solid line) and the thermal Wino DM mass (azure solid line) are shown.

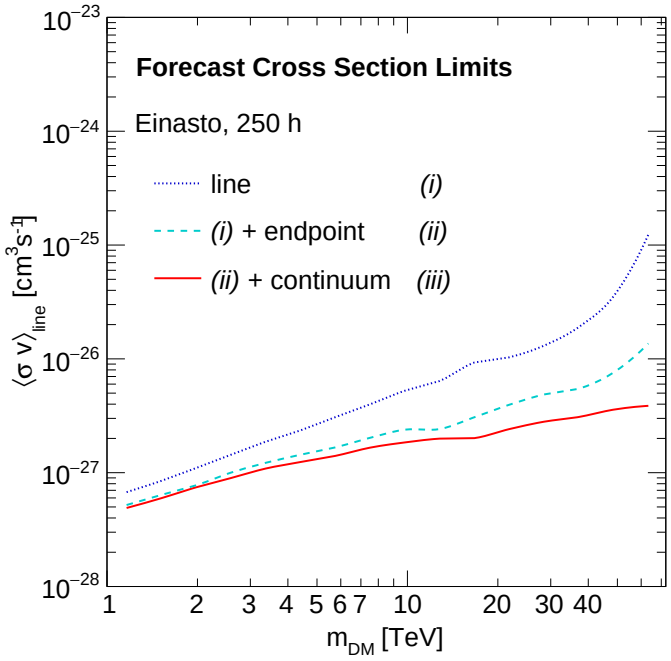

Figure 11.6: Impact of the spectral contributions to the Wino *gamma line*. The mean expected limits for *line only* (blue dotted line), *line + endpoint* (cyan dashed line) and *line + endpoint + continuum* (red solid line) signal are compared.

theoretical cross section are due to the Sommerfeld enhancement. All the DM mass values for which the theoretical cross section is larger than the limits obtained in this work are rejected. This puts strong constraints on the Wino. Note that the expected m_{DM} for Wino particles thermally produced in the early Universe (azure solid line) [266] is excluded. Only very massive Wino survives the limits on $\langle \sigma v \rangle$ obtained under the assumption of an Einasto cuspy profile. Masses above about 10 TeV are allowed outside resonances.

The systematic uncertainties obtained in the H.E.S.S.-I analysis towards the GC in Sec. 8.6 are included in the containment bands, as well as the theoretical uncertainty of 5%. The latter affects the limits at the order of percent, *i.e.* negligible, in most of the mass range and increases up to 10% in the last bins.

The impact of the different spectral components is studied in Fig. 11.6, where the limits for *line only* (blue dotted line), *line + endpoint* (cyan dashed line) and the full spectrum (red solid line) are compared. Both the impact of the *endpoint* and the *continuum* contributions increase with m_{DM}. The *endpoint* contribution provides an improvement of 1.4 at 2.3 TeV, 1.5 at 2.9 TeV and 2.1 at 9 TeV, respectively. The continuum has a smaller effect, of 8% at 2.3 TeV, 12% at 2.9 TeV and 27% at 9 TeV.

11.4.2 DM distribution at the Galactic Center for pure Wino DM

Constraints on the J-factor

Since the expected signal scales with $\langle\sigma v\rangle \times J$ the limits on the annihilation cross section for a fixed J can be reinterpreted as constraints on the J-factor for a fixed $\langle\sigma v\rangle$. Fig. 11.7 shows 95% C.L. upper limits on the J-factor assuming $\langle\sigma v\rangle$ equal to the predicted thermal cross section. Very strong constraints on J are found for $m_{\rm DM} = 2.3$ TeV or 9 TeV, at the position of the most prominent resonances. For example, at 2.3 TeV J-factors larger than 10^{18} GeV^2 cm^{-5}[4] are excluded.

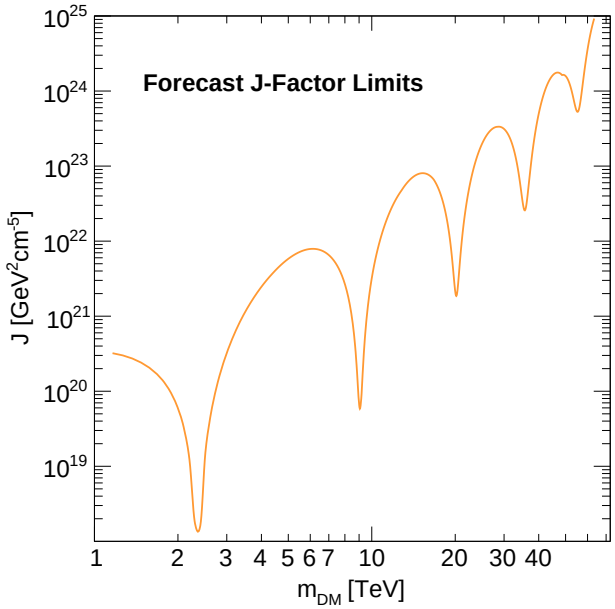

Figure 11.7: 95% C.L. upper limits on the J-factor as function of the Wino DM mass.

Constraints on DM profile core sizes

The previous results show that Wino DM can be rejected in a very significant mass range. If we want to keep the Wino model alive, since the spatial distribution of DM at the GC is subject to uncertainty, the DM density profile can be loosen. Indeed, for large cores the limits on the DM annihilation cross section become less stringent. In Fig. 11.8 the constraints on $\langle\sigma v\rangle$ as function of $m_{\rm DM}$ are given for the Einasto profile (orange solid line) and cores of size 150 pc (orange dotted line), 300 pc (orange dashed line), 500 pc (green solid line), 1 kpc (green dotted line), 1.5 kpc (green dashed line), 2 kpc (blue solid line), 3 kpc (blue dotted line) and 5 kpc (blue dashed line). Comparing to the theoretical annihilation

[4]This is a J-factor value typical of classical dSph, while it is a small J-factor for the GC region.

cross section (gray solid line), a less wide $m_{\rm DM}$ range is reject for increasing-size cored profiles. The constraints degrade up to a factor about 200 when assuming a 5-kpc-size cored profile at the GC with respect to Einasto profile.

The impact of the size of the core on the limits is underlined in the right panel of Fig. 11.8. The lower limits on the core size that allow the Wino to survive H.E.S.S.-I observations is given as function of its mass. Cores of several kpc are excluded for the thermal Wino DM mass. Smaller cores are rejected at the position of the other resonances. Indeed, cores above 5 kpc are rejected for $m_{\rm DM} = 2.3$ TeV, while cores up to 3 kpc are excluded for the thermal Wino mass and for $m_{\rm DM} = 9$ TeV. Smaller cores up to about 300 pc are excluded for the resonance at 20 TeV. Most of the masses above 10 TeV cannot be excluded yet.

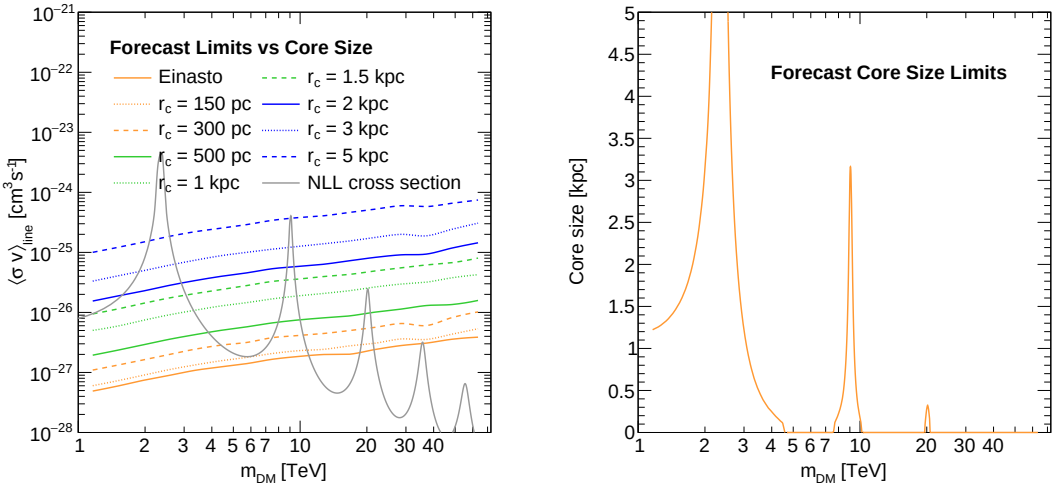

Figure 11.8: Upper limits on Wino DM annihilation cross section for a selection cored DM density profiles and lower limits on the size of the DM core. *Left panel:* The 95% C.L. upper limits on $\langle\sigma v\rangle$ vs $m_{\rm DM}$ are give for Einasto profile (orange solid line) and cored profiles with $r_{\rm c}$ of 150 pc (orange dotted line), 300 pc (orange dashed line), 500 pc (green solid line), 1 kpc (green dotted line), 1.5 kpc (green dashed line), 2 kpc (blue solid line), 3 kpc (blue dotted line) and 5 kpc (blue dashed line). The NLL theoretical cross section is overlaid (gray solid line). *Right panel:* 95% C.L. lower limits on the core radius size of cored DM profiles excluded by a H.E.S.S.-I-like search for Wino DM signals. Cores of several kpc are rejected for DM mass about 2 TeV.

11.5 Prospects for dark matter search with IGS-like observation strategy

11.5.1 IGS-like region of interest

The IGS pointing strategy described in Sec. 5.1, based on pointings at large Galactic latitudes, allows us to extend the signal region for DM search. The same idea can be applied to the mock analysis developed in this chapter. The H.E.S.S.-I IRFs are used here, but a H.E.S.S.-II-like approach is used in view of the IGS exposure maps (see Chap. 5). The *ON region* is then extended from 1° to 4°, *i.e.* from 7 to 37 annular ROIs. The 250-hours time exposure is considered flat over the 4°-*ON region*[5].

11.5.2 Expected limits for different cored DM profiles

The 95% C. L. upper limits are computed for the *line + endpoint + continuum* Wino signal using the usual LLRTS. The same DM density profiles described previously are tested for the new analysis set up. Fig. 11.9 shows the limits in the extended ROI for Einasto profile and cored profiles of size 150 pc, 300 pc, 500 pc, 1 kpc, 1.5 kpc, 2 kpc, 3 kpc and 5 kpc, respectively. The degradation for a 5 kpc core with respect to Einasto profile is now reduced to about 70. This is expected because with a more extended region of interest a more important fraction of the DM content is included in the signal region also for large cores and contributes to the expected signal. However, cores of dimension 1 kpc or more are still larger than the dimension of the ROI.

Two different approaches are compared in Fig. 11.9: doubling the statistics in the 1° region (black empty dots) or extending the ROI up to 4° (green empty squares). 95% C. L. upper limits on the annihilation cross section are shown as function of the dimension of the DM density profile for a Wino of mass $m_{\rm DM} = 2.9$ TeV. The first approach improves the H.E.S.S.-I-like limits (red filled dots) linearly for each DM profile approximately as $\sqrt{T_{obs}}$, *e.g.* a factor ~ 1.4 for doubled statistics. The second approach benefits not only from the increased statistics, but from the additional spatial information. The improvement with respect to 250-hours H.E.S.S.-I-like analysis is about a factor 2 for Einasto and small cores, but it increases up to about a factor 5 for 5 kpc cores. This makes the constraints obtained with the IGS-like approach for $r_{\rm c} = 5$ kpc 3.6 times stronger than those obtained doubling the exposure with an H.E.S.S.-I-like strategy. The extended-ROI approach is particularly powerful for an analysis with modeled background and increases significantly the sensitivity for large DM cores.

[5] In the H.E.S.S.-II analysis the IGS observations are focused on the Northern part of the Galactic plane. The real exposure is $50 - 70\%$ of what assumed here.

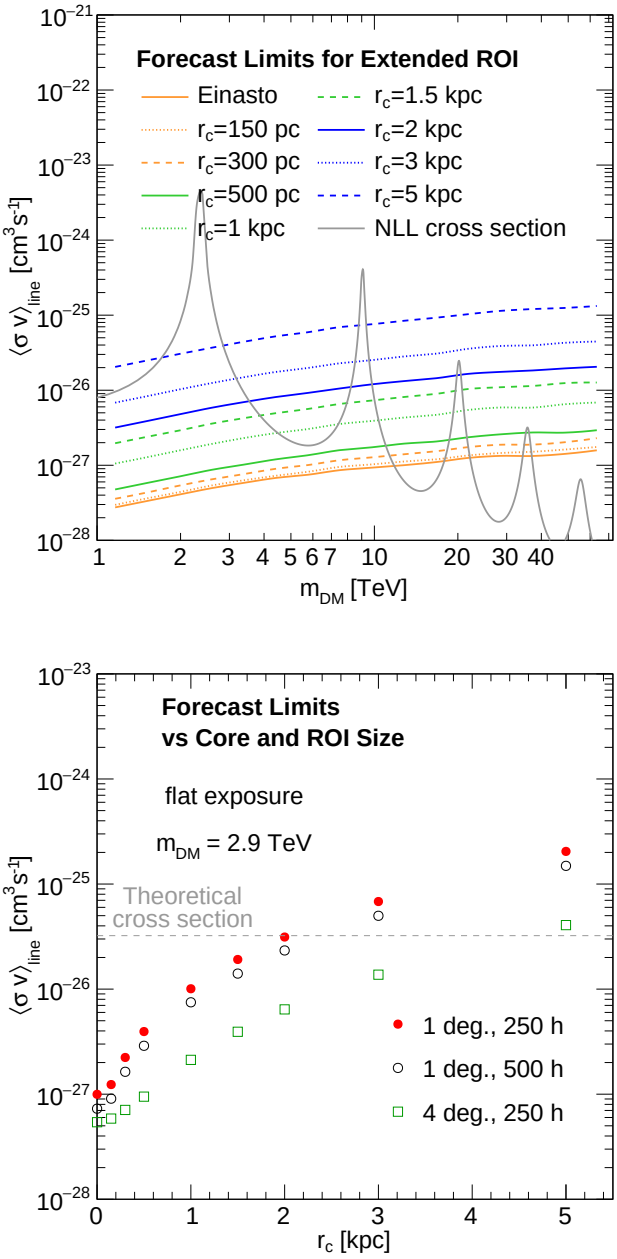

Figure 11.9: Forecast 95% C. L. limits on the Wino annihilation cross section for IGS-like observation strategy. *Top panel:* The H.E.S.S. sensitivity for DM search in a 4° region around the GC for 250 hours is shown together with the theoretical NLL cross section (gray line). Several DM density profiles are tested: Einasto cuspy profile (orange solid line) and cores of size 150 pc (orange dotted line), 300 pc (orange dashed line), 500 pc (green solid line), 1 kpc (green dotted line), 1.5 kpc (green dashed line), 2 kpc (blue solid line), 3 kpc (blue dotted line) and 5 kpc (blue dashed line). *Bottom panel:* Comparison of the H.E.S.S.-I-like and IGS-like observation approaches. 95% C. L. upper limits on $\langle \sigma v \rangle$ as function of the core radius r_c for $m_{\rm DM}$ are shown for 250-hours flat exposition in 1° (red filled dots, H.E.S.S.-I-like observations), 500 hours flat in 1° (H.E.S.S.-I-like observations with doubled statistics) and 250 hours flat in 4° (IGS-like observation strategy).

11.6 Discussion and perspectives

This study shows that H.E.S.S. observations of GC are very powerful to probe the Wino dark matter region. H.E.S.S. I is able to exclude the Wino in a wide range of masses assuming a cuspy DM profile at the GC. Limits are less stringent for large cored dark matter profiles. The latest calculations of the Wino spectrum including non-tree-level contributions in the *endpoint* region improve significantly the H.E.S.S. sensitivity. The theoretical uncertainty is found to be negligible with respect to the systematic uncertainties in the *gamma line* searches in the GC region.

An approach that allows us to extend our region of interest for dark matter search, like the one that is being applied with H.E.S.S. II during the Inner Galaxy Survey (see Chap. 5), is more performing than just increasing the photon statistics in a limited region around the Galactic Center. Prospects for search for dark matter with CTA in a several-degree-sized region around the Galactic Center are discussed in the next chapter.

Chapter 12

Prospects for the study of specific dark matter models with CTA towards the Galactic Center

Contents

12.1 The Cherenkov Telescope Array 218
12.1.1 A two-site observatory 218
12.1.2 Instrument response functions and flux sensitivity 220
12.2 CTA sensitivity to continuum and line dark matter signals 221
12.2.1 Definition of the region of interest and the expected signal and background 221
12.2.2 Forecast limits on dark matter properties with CTA towards the Galactic Center 222
12.3 Scanning the pMSSM parameter space 223
12.4 CTA sensitivity to heavy weakly-interacting DM 227
12.4.1 Sensitivity to Wino dark matter 227
12.4.2 Higgsino dark matter model 229
12.4.3 Constraints on Higgsino dark matter 230
12.5 Astrophysical backgrounds for CTA 232
12.5.1 Galactic Diffuse Emission 232
12.5.2 Low-latitude Fermi Bubbles templates 235
12.5.3 Point-like Fermi-LAT sources in the field of view 235
12.5.4 Effect of these components on the limits 237
12.6 Discussion and perspectives 238

The next-generation Imaging Atmospheric Cherenkov Telescope array, CTA, is expected to provide decisive input to the indirect dark matter search, thanks to its improved sensitivity with respect to current instruments. Forecast limits on dark matter annihilation cross section are computed in this chapter. The sensitivity achieved with CTA can be confronted to pMSSM predictions. In addition the sensitivity to some specific pure heavy dark matter models is derived.
In Sec. 12.1 the CTA observatory is briefly introduced together with its designed instrument response functions and flux sensitivity. Constraints on dark matter annihilation in *continuum* and *gamma lines* towards the Galactic Center are computed in Sec. 12.2 and used to constraint the pMSSM parameter space in Sec. 12.3 focusing on TeV dark matter models. This study is being published as Ref. [267]. The constraints for the specific Wino and Higgsino candidates are computed in Sec. 12.4 and the effect on the limits of several background components in the Galactic Center region is studied in Sec. 12.5. This work is being published as Ref. [268].

12.1 The Cherenkov Telescope Array

12.1.1 A two-site observatory

The Cherenkov Telescope Array (CTA) will be the next-generation IACTs array. It will consist of more than 100 telescopes in total of different sizes: small size telescopes (SSTs) of diameter $\sim$ 4 m, medium size telescopes (MSTs) of diameter $\sim$ 11 m and large size telescopes (LSTs) of diameter $\sim$ 23 m. The design of the telescopes of the three kinds is shown in Fig. 12.1. The final design for the SSTs and MSTs is still under discussion. The SSTs are expected to be sensitive in an energy range from 1 TeV up to 300 TeV, the MSTs from 150 GeV up to 50 TeV and the LSTs from 20 GeV up to 3 TeV [269].

The observatory will be split in two sites, one in each hemisphere, in order to cover almost the full sky. The Northern site will be located on the MAGIC site on the Canary island of La Palma on the existing site of the Instituto de Astrofisica de Canarias' (IAC's) Observatorio del Roque de los Muchachos in Villa de Garafia. It will host 4 LSTs and 15 MSTs and include the 2 MAGIC telescopes. No SST will be set in the Northern site. The Southern site will be located in the Atacama Desert in Chile near the existing European Southern Observatory's (ESO's) Paranal Observatory. It will host 4 LSTs, 25 MSTs and 70 SSTs. This is the ideal site of interest for a survey of the Galactic Center region. In what follows in this chapter the performances derived from Monte Carlo simulations for the Southern observatory are assumed. A schematic of the telescope array for the two sites is shown in Fig. 12.2.

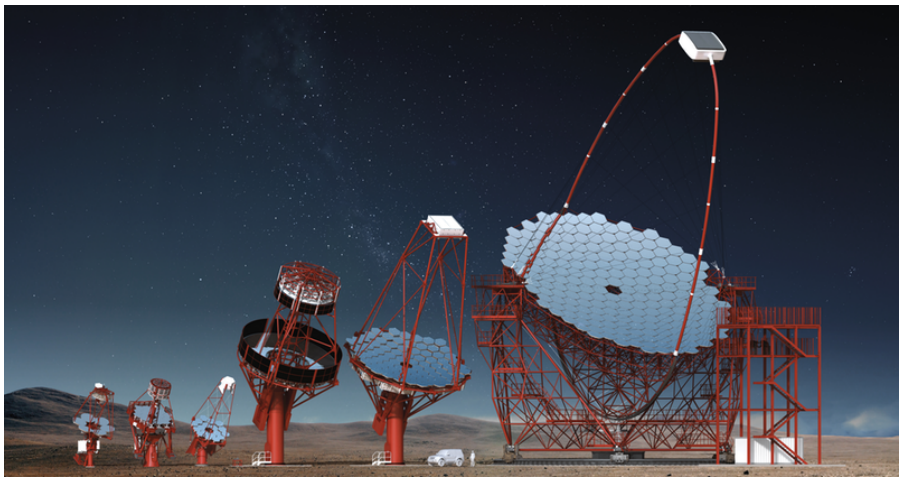

Figure 12.1: Artist view of CTA telescopes [269]. Three designs of the small size telescopes (SST) are shown on the left, two designs of medium size telescopes (MST) are in the middle and a design of the large size telescopes (LST) is given on the right.

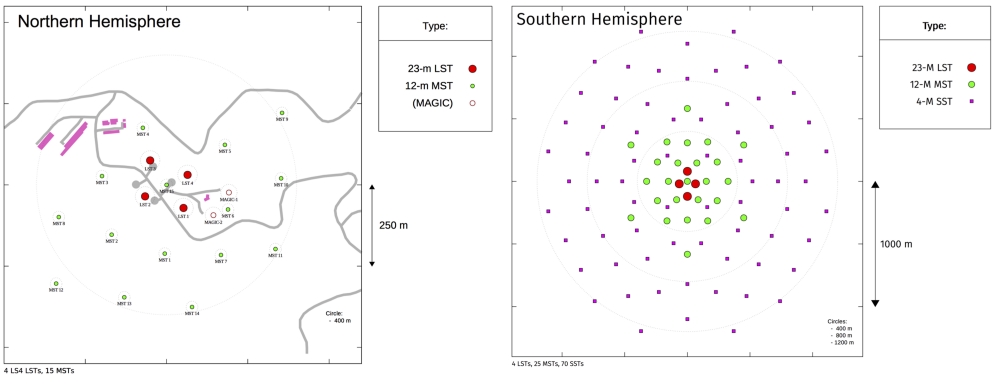

Figure 12.2: Schematic of the two CTA sites [269]. *Left panel:* the Northern site is expected to count 4 LSTs and 15 MSTs. The 2 MAGIC telescopes will be also added in the array. No SST is foreseen in the Northern site. *Right panel:* the Southern site is expected to host 4 LSTs, 25 MSTs and 70 SSTs.

12.1.2 Instrument response functions and flux sensitivity

The IRFs for the two CTA sites are made publicly available by the CTA Collaboration [269]. They are produced [265] through Monte Carlo simulations of the gamma-ray and CR-induced atmospheric showers with CORSIKA [270] and of the detector with the package sim_telarray [40] developed for HEGRA. The IRFs for the Southern site for an average observation zenith angle of 20° and 50 h observations are used in this chapter.

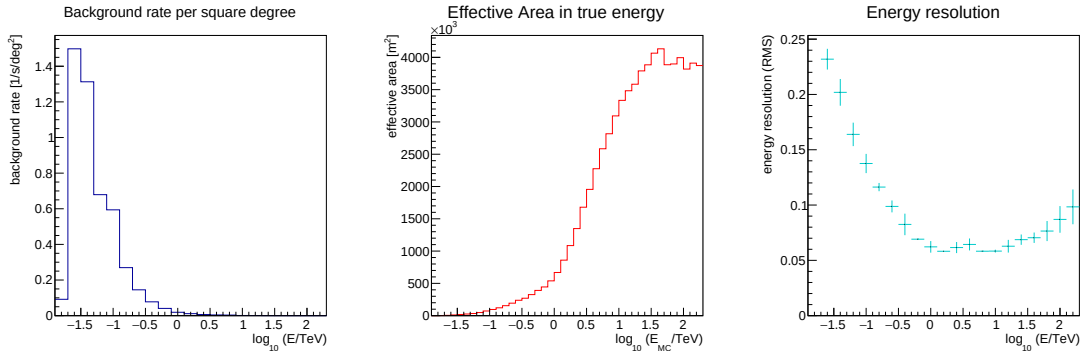

Figure 12.3: CTA instrument response functions for the Southern site [269]. *Left panel:* background rate per degree square as function of the energy $\log_{10}(E/1\,\mathrm{TeV})$. The background rate is obtained from simulations of the incoming CR flux and the detector responses. *Central panel:* effective area as function of the true energy $\log_{10}(E_{\mathrm{MC}}/1\,\mathrm{TeV})$. The effective area is given in m^2. *Right panel:* bin-by-bin energy resolution as function of the energy $\log_{10}(E/1\,\mathrm{TeV})$. The best resolution in the TeV energy range reaches 5%.

The residual background rate due to misidentified CRs is provided in terms of counts per second and per degree square. It is shown in the left panel of Fig. 12.3. The effective area as function of the true energy is given in the central panel of Fig. 12.3 and it assumes the presence of all the telescopes in the array pointing to the same direction. It reaches a maximum of $\sim 4 \times 10^6$ m^2 at $E \simeq 10$ TeV. The energy resolution as function of the energy is shown in the right panel of Fig. 12.3. It reaches 5% in the TeV energy range, while it degrades in the low-energy regime down to $\sim 20\%$.

CTA differential flux sensitivity is computed for both the arrays [269] for 50 h of observations. It is defined as the flux needed to obtain a 5σ detection of a point-like source. It is computed for five energy bins per decade. The sensitivity curves are shown in Fig. 12.4 and compared to the performances of the existing gamma-ray telescopes H.E.S.S. [271], MAGIC [272], VERITAS [273], HAWC [274] and Fermi-LAT [275].

The above IRFs and sensitivity are provided for sources that are observed near ($\sim 0.5°$) the center of the camera. As it was the case for H.E.S.S., the acceptance degrades radially from the center. The CTA strategy for the survey of the GC region foresees a grid of pointing positions, such that there will be overlapping between the FoV of one pointing position and the nearby one. In this way the pointing strategy will compensate for the acceptance

degradation and the overall observations are expected to be homogeneous in 5°, assuming that the proper amount of observations to successfully perform such a survey is granted.

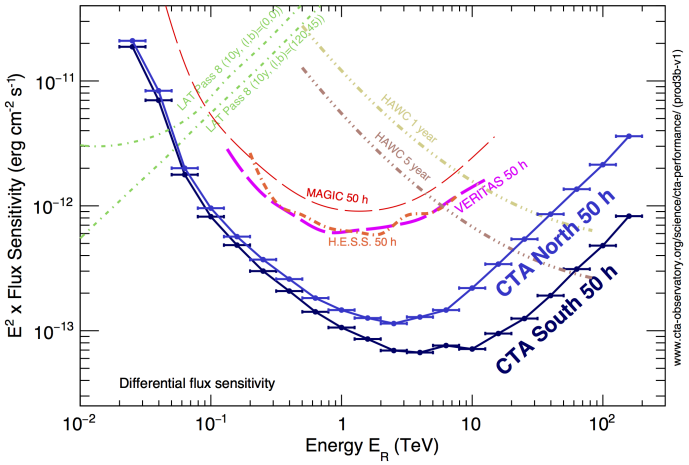

Figure 12.4: CTA expected flux sensitivity at 5σ for 50 hours of observations with the Northern (blue solid line) and the Southern (black solid line) arrays [276]. The sensitivity of the current gamma-ray telescopes H.E.S.S. [271], MAGIC [272], VERITAS [273], HAWC [274] and Fermi-LAT [275] are also plotted.

12.2 CTA sensitivity to continuum and line dark matter signals

12.2.1 Definition of the region of interest and the expected signal and background

For the computation of the sensitivity of CTA to DM in the GC region we follow the CTA Collaboration strategy [276, 277]. We assume 500 h of homogeneous observations of the inner part of the Galactic halo, as foreseen for the future CTA Southern array. The *ON region* for DM search is then defined as a square of dimension ±5° in Galactic longitude and latitude respectively, centered at the GC. It is then split into 400 squared sub-regions of interest (ROIs) of size $0.5° \times 0.5°$ each. This choice is made in order to be able to exploit the spatial features of the DM profile, that would otherwise get lost in a large integration region up to 5°. The ROIs act as spatial bins for the likelihood approach that is applied for the DM search and their dimension is a compromise to optimize the signal-to-noise ratio. The same exclusion regions as in H.E.S.S. analysis are applied: band of ±0.3° around the Galactic plane and disk of radius 0.4° at the position of HESS J1745-303. The residual background per ROI is estimated from the background rate provided by the CTA Consortium, rescaling for the proper live time and ROI size of this analysis. The expected signal is computed

from Eq. (6.13) by convolving for CTA energy resolution and effective area. Several DM annihilation channels are used in the sensitivity computation.

12.2.2 Forecast limits on dark matter properties with CTA towards the Galactic Center

The sensitivity of CTA is computed for an Einasto DM profile and both the *continuum* and the monoenergetic *gamma line* annihilation channels, assuming only residual background. In order to derive the constraints a 3D-likelihood approach is applied. Eq. (7.8) is extended to a 3D function with binning in energy i, Galactic longitude j and Galactic latitude k. The total likelihood is the product over the three indexes. The spatial bins coincide with the ROIs. The spectral binning is based on the energy bins of the IRFs (five logarithmically-spaced bins per decade, 0.2 dex). A hard threshold is set at 30 GeV to avoid the energies corresponding to very small effective area where systematics could arise. The LLRTS is computed, following H.E.S.S. studies, to derived the 95% C.L. expected upper limits on $\langle\sigma v\rangle$ as function of the DM mass. In the left panel of Fig. 12.5 the constrains on the W^+W^-, ZZ, ZH, hh (pink solid line), $c\bar{c}$, $b\bar{b}$, $t\bar{t}$, e^+e^-, $\mu^+\mu^-$ and $\tau^+\tau^-$ annihilation channels, respectively, are shown. In the right panel of Fig. 12.5 the constraints on $\langle\sigma v\rangle$ in the $\gamma\gamma$ channel are shown together with the limits obtained by H.E.S.S. I with 10 years of observations of the GC region [228] for a total of about 250 live hours (see Chap. 8), those obtained by 6 years of Fermi-LAT [256] towards the Inner Galactic halo and 160 h of observations of Segue 1 by MAGIC [232]. CTA is $5-20$ times more sensitive than H.E.S.S., that currently sets the most stringent constraints on $\langle\sigma v\rangle$ in the TeV energy range.

In the left panel of Fig. 12.6 the CTA sensitivity in the W^+W^- channel is compared to observed constraints on the annihilation cross section derived by the existing gamma-ray telescopes. Limits obtained by H.E.S.S. with 250 h of observations of the GC [236] and Fermi-LAT with 6 years observations on 15 dSph [256] are shown. CTA is significantly more sensitive than existing experiments. It will be able to probe the thermal relic cross section in several annihilation channels for cuspy profiles at the GC.
Since the DM profile at the GC is not well constrained the limits obtained for the W^+W^-, $b\bar{b}$, $t\bar{t}$ and $\tau^+\tau^-$ channels assuming an Einasto profile are compared to those derived for a NFW profile and a 3-kpc-size cored profile. They are shown in the right panel of Fig. 12.6. The limits degrade of about a factor two for the NFW and 17 for the cored profile, respectively, with respect to the Einasto profile. The degradation for a large DM core is smaller than in H.E.S.S. prospects thanks to the exposure up to 5° in radius, corresponding to about 750 pc. The thermal relic cross section is still at reach when assuming a NFW profile, while only the sensitivity in the $\tau^+\tau^-$ channel is close to the natural scale in case of a 3 kpc cored DM profile.

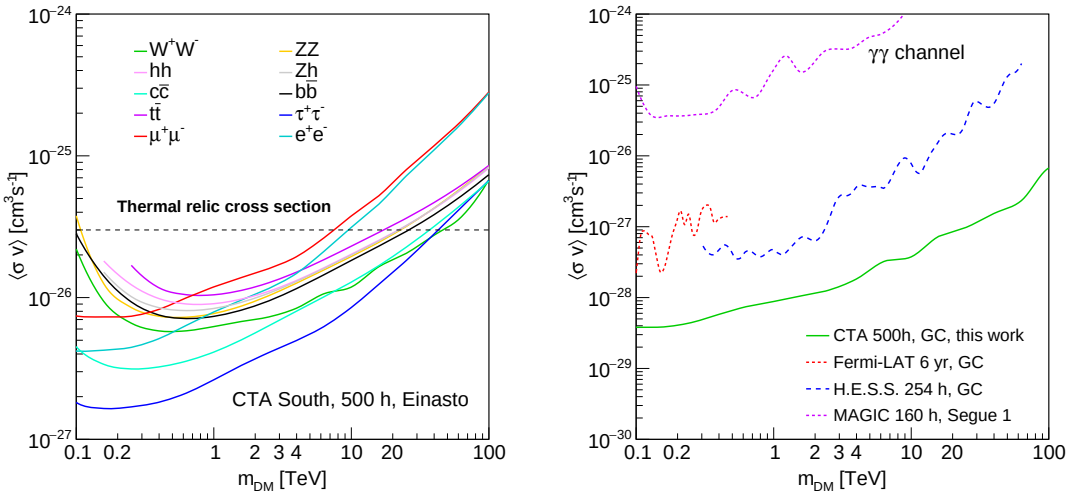

Figure 12.5: 95% C.L. forecast upper limits for CTA on $\langle\sigma v\rangle$ as function of $m_{\rm DM}$ for 500 h of observations of the inner 5° of the Galactic halo, assuming an Einasto profile. *Left panel:* The W^+W^- (green solid line), ZZ (orange solid line), Zh (gray solid line), hh (pink solid line), $c\bar{c}$ (teal solid line), $b\bar{b}$ (black solid line), $t\bar{t}$ (violet solid line), e^+e^- (cyan solid line), $\mu^+\mu^-$ (red solidl line) and $\tau^+\tau^-$ (blue solid line) annihilation channels are tested. The thermal relic cross section is marked as a black dashed line. *Right panel:* CTA constraints on *gamma lines* (green solid line), compared to those from H.E.S.S. [228] observations towards the GC (254 h, blue dashed line), Fermi-LAT [95] data in the GC region (6 years, red dotted line) and MAGIC observations of Segue 1 [232] (160 h, violet dotted line).

12.3 Scanning the pMSSM parameter space

The pMSSM is the phenomenological Minimal Supersymmetric Standard Model [278]. It is developed in the context of SUSY [279] and reduces the global supersymmetric parameter space including 105 free parameters in addition to the 19 parameters of the SM [280]. The main assumptions to build the pMSSM are CP conservation, minimal flavor violation at the electroweak scale, degenerate first two generations of sfermion soft-mass parameters and negligible Yukawa couplings and trilinear couplings for the first two generations [281]. A review of the pMSSM can be found in Ref [282]. In this work we use a pMSSM reduced to 9 free parameters[1] (p9MSSM) applying additional constraints: the gluino mass, the third-generation down-type right soft squark mass, and the first two generations of soft slepton masses are set.

The main experimental constraints to the p9MSSM parameter space come from:

- **Measurement of the CDM relic abundance**. The relic abundance derived by Planck is used [143]. The Sommerfeld effect is included in the treatment of the freeze-

[1]Using additional parameters does not affect significantly the results of the scan for the purpose of DM search only.

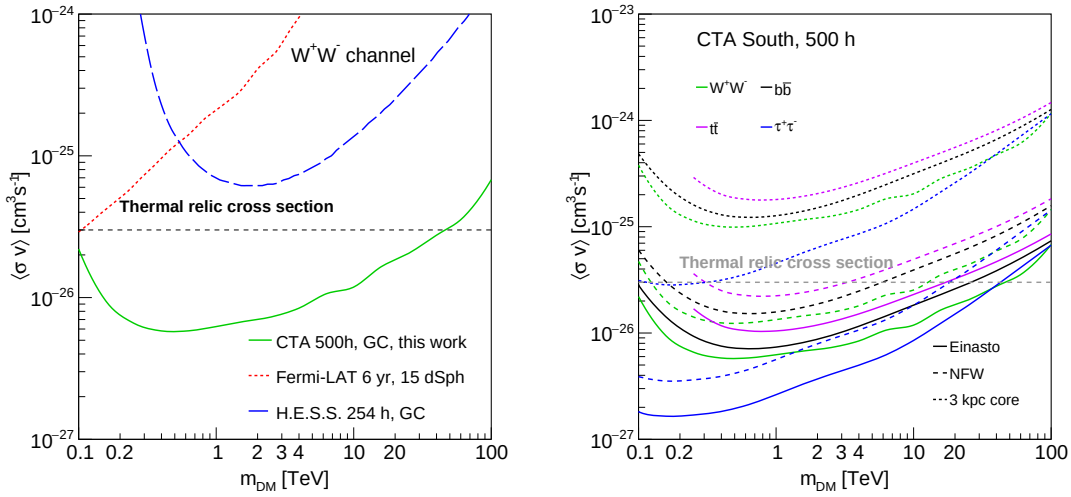

Figure 12.6: *Left panel:* CTA constraints on $\langle\sigma v\rangle$ (green solid line) in the inner 5° of the GC for the W^+W^- channel, compared to those by H.E.S.S. [236] (blue dashed line) and Fermi-LAT [256] (red dotted line) in the GC region. *Right panel:* CTA constraints on $\langle\sigma v\rangle$ derived assuming an Einasto profile (solid lines) for the Galactic Center halo, compared to those obtained for a NFW profile (dashed lines) or a cored profile of size 3 kpc (dotted lines). The W^+W^- (green lines), $b\bar{b}$ (black lines), $t\bar{t}$ (violet lines) and $\tau^+\tau^-$ (blue lines) channels are tested. The thermal relic cross section (gray dashed line) is shown.

out since it affects the estimate of the present-day thermal neutralino annihilation cross section and the neutralino relic density [283]. This measurement gives the strongest constraints on the pMSSM.

- **Direct DM search**. Stringent constraints are set on the spin-independent cross section of neutralino scattering off nucleons of the target material. Limits by PandaX-2 [284], PICO-60 [285] and Xenon1T [286] are used. Constraints on the spin-dependent cross section of the neutralino off the proton or neutron have been set by IceCube [287] through measurements of neutrino from the Milky Way, the Sun and Earth. These constraints are significantly less stringent than those obtained in direct search.

- **Indirect DM search with gamma-ray and CR telescopes**. Constraints on DM annihilation into gamma-rays set by Fermi-LAT are not included in the likelihood function used for the initial scan, but they are included in the reprocessing of the results of this initial scan. Fermi-LAT limits obtained through observation of dSphs during 6 years of data taking are used [237]. Constraints on DM annihilation are set by AMS [288] by measuring the flux of antiprotons, compared to the number of protons, but are not included because they are less stringent and are subject to large uncertainty for the CR diffusion and propagation in the ISM.

- The DM self-annihilation cross section can be constrained as well by requiring that the CMB power spectrum is not significantly affected too much by the pre- and post-recombination energy injection from DM [289]. This constraint has a minor impact on the pMSSM with respect to the previous set of constraints.

- **Dark matter search at colliders**. Constraints on Susy particles obtained by LHC [290], LEP and Tevatron are used, even if they poorly constrain the TeV mass range. In addition, the pMSSM is constrained as well by LHC measurements in the Higgs sector, *e.g.* the mass and couplings of heavy Higgs boson.

- **Flavor constraints** [291]. Limits set on the measurement of the coupling of the rare B mesons decay into a couple of muons or a strange particle and a photon, $B_S^0 \to \mu^+\mu^-$ and $B \to X_S\gamma$, significantly affect the pMSSM. These bounds are imposed *a posteriori*.

The H.E.S.S. and CTA *continuum* and *gamma line* DM searches give additional constraints on the p9MSSM, and are the most relevant for TeV DM. A scan of the parameter space of the pMSSM is performed by means of a likelihood profiling over the 9 parameters [292]. The points that belong to the 95% C.L. region of the global profile-likelihood $-2\ln(\mathcal{L}/\mathcal{L}_{\max})$ are selected ($\Delta\chi^2 \leq 5.99$). Fig. 12.7 shows the p9MSSM points in the DM mass versus DM annihilation cross section space (m_χ, σv_0) (top panel) and in the DM annihilation cross section vs spin-independent DM-proton scattering cross section space ($\sigma_p^{\rm SI}$, σv_0) (bottom panel). The points corresponding to the pure ($\geq 90\%$ of the pure eigenstate) Wino (blue open dots), Bino (green open dots) and Higgsino (red open dots) and mixed Wino-Bino (cyan open dots) and Bino-Higgsino (orange open dots) parameter spaces are shown, respectively, together with the points at reach for CTA (black open triangles). The 95% C.L. upper limits on DM annihilation cross section obtained by Fermi-LAT (black dashed line), H.E.S.S. (black solid line) and CTA (black dash-dotted line) are shown in the top panel. Fermi-LAT limits are computed on the $b\bar{b}$ annihilation channel through observations of dSphs [237]. H.E.S.S. limits are the combination of the constraints on different channels from Ref. [236] weighted for the branching ration of each channel depending on the specific model. A test has been made to confirm that the simplified approach of re-weighting the constraints obtained in a given channel is a good approximation of a full re-computation of the 95% C.L. expected upper limits where the spectra themselves are weighted for the correct branching ratio when estimating the expected signal that enters in the LLRTS analysis methodology. Current H.E.S.S. observations allow us to probe the Wino region, but not the Higgsino one. The CTA sensitivity is a combination obtained with the same procedure applied to the constraints computed in Sec. 12.2. All the Wino parameter space and part of the Higgsino one are at reach for CTA. Points with bino-dominated neutralinos with annihilation cross section close to the thermal cross section could also be probed by CTA. The region of the pure-Bino with annihilation cross section smaller than the natural scale are out of reach for CTA.

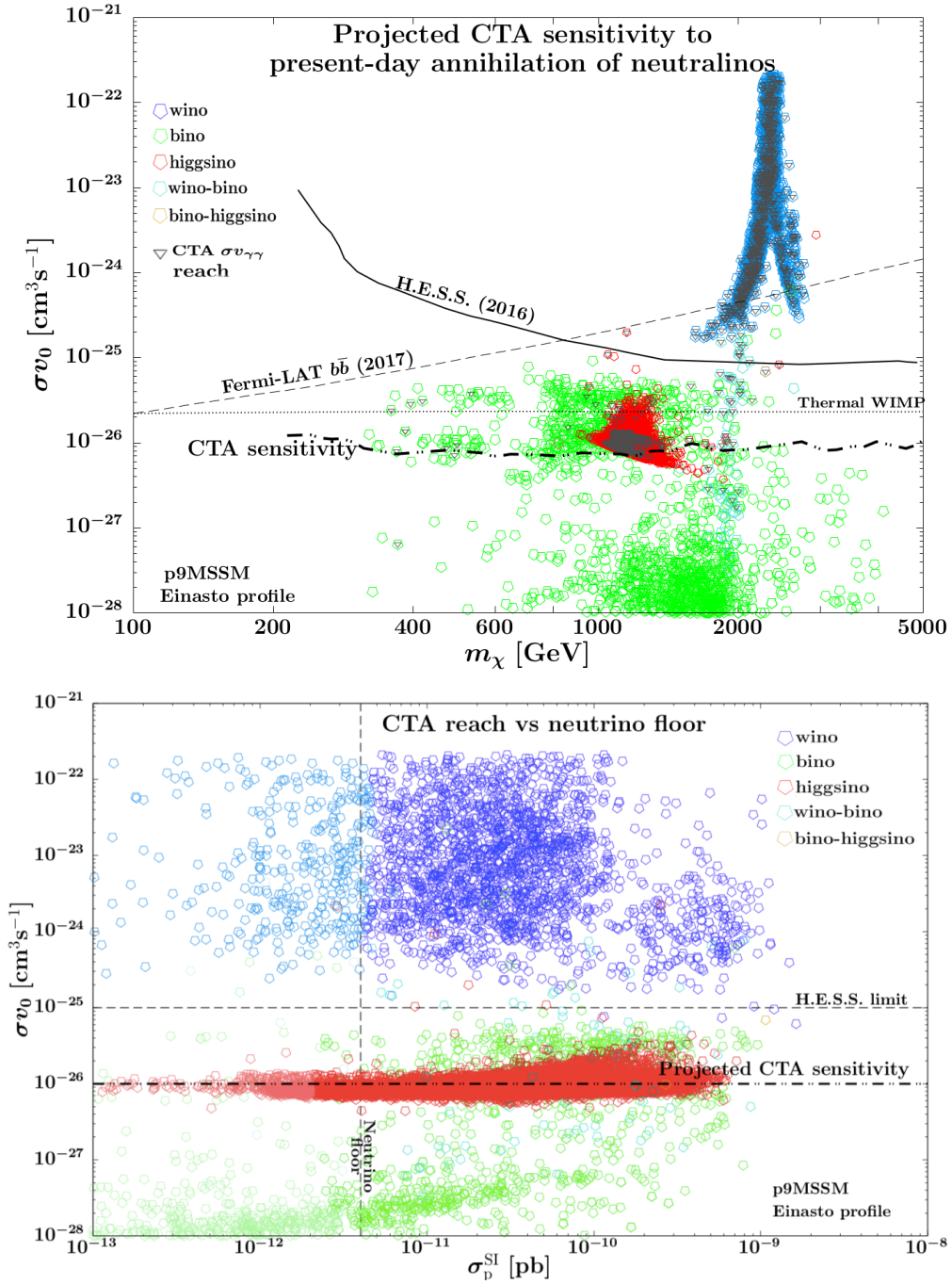

Figure 12.7: Distribution of p9MSSM points with $\Delta\chi^2 \leq 5.99$ for Wino (blue open dots), Bino (green open dots) and Higgsino (red open dots) and mixed Wino-Bino (cyan open dots) and Bino-Higgsino (orange open dots) models. *Top panel:* Distribution of p9MSSM points in the (m_χ, σv_0) space. Constraints set by Fermi-LAT [237] in the $b\bar{b}$ annihilation channel (black dashed line) and by the measured H.E.S.S. constraints [236] (black solid line) and forecast CTA constraints on several *continuum* annihilation channels (black dash-dotted line) are shown. The thermal relic cross section (black dotted line) is marked on the plot. *Bottom panel:* Distribution of p9MSSM points in the (σ_p^{SI}, σv_0). The observed H.E.S.S. limits for $m_\chi = 2.5$ TeV and CTA projected sensitivity for $m_\chi = 1$ TeV are shown.

The bottom panel of Fig. 12.7 shows the complementarity of the indirect DM searches with VHE gamma rays that constrain σ_{v_0} and direct DM searches that constrain σ_p^{SI}. H.E.S.S. limits for $m_\chi = 2.5$ TeV and CTA projections for $m_\chi = 1$ TeV are shown, as well as the spin-independent cross section corresponding to the neutrino floor (see Sec. 6.4). This plot shows the complementarity of direct and indirect DM searches. Spin-independent annihilation cross section constraints will face the neutrino floor which is the most challenging background for direct detection. With CTA we can probe DM models that lie well beyond the neutrino floor and are therefore very challenging to be accessible via direct detection.

12.4 CTA sensitivity to heavy weakly-interacting DM

12.4.1 Sensitivity to Wino dark matter

Some specific DM candidates are also tested with CTA. A first test is made on the Wino, using the latest NLL spectrum computation in Sec. 11.1. The three cases *line-only*, *line + endpoint* and *line + endpoint + continuum* (*full spectrum*) are considered, referring to Eq. (11.1). The 95% C.L. upper limits on $\langle\sigma v\rangle_{\mathrm{line}}$ as function of the Wino mass are computed

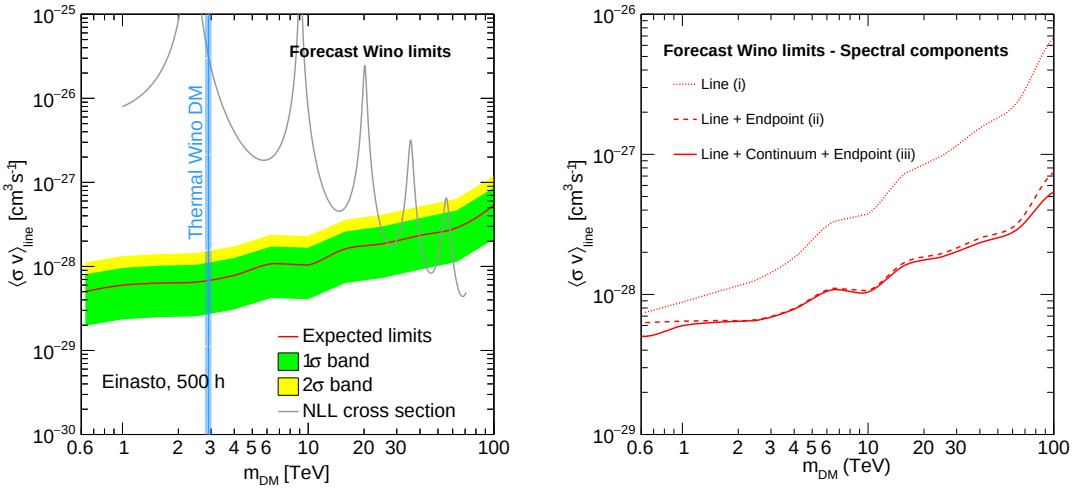

Figure 12.8: CTA forecast upper limits on Wino annihilation cross section as function of its mass, computed at a 95% C.L. for 500 h of observations towards the GC. The predicted NLL thermal cross section is shown (gray solid line). The resonances are due to Sommerfeld enhancement are shown. *Left panel:* The expected limits (red solid line) computed assuming an Einasto profile, are shown together with the 1σ (green band) and 2σ (yellow band) bands. The theoretical mass for Wino DM thermally produced in the early Universe is marked (cyan solid line). *Right panel:* the expected limits are shown for *line-only* (red dotted line), *line + endpoint* (red dashed line) and *full spectrum* (red solid line).

through the LLRTS, using a 3D-LLRTS approach. They assume an Einasto profile and

residual background only. For the *full spectrum* the constraints reach $\sim 6 \times 10^{-29}$ cm^3 s^{-1}. They are shown (red solid line) in the left panel of Fig. 12.8, together with the 1σ (green band) and 1σ (yellow band) containment bands. The containment bands are obtained from the Asimov dataset procedure, described in Sec. 7.2.4. The NLL predicted thermal cross section (gray solid line) and the expected thermal Wino mass (cyan solid line) are also shown. All the mass values $m_{\rm DM}$ up to 40 TeV are excluded as well as the masses corresponding to the Sommerfeld resonance peaking at about 60 TeV. The thermally produced Wino with $m_{\rm DM} = 2.9$ TeV is ruled out, as well as most of the reasonable mass range for this candidate.

The impact of the *endpoint* and *continuum* contributions to the full spectrum on the annihilation cross section constraints is also studied. The right panel of Fig. 12.8 shows the constraints for the *line-only* (red dotted line), the *line + endpoint* (red dashed line) and the *line + endpoint + continuum* (red solid line) cases. The major improvements come from

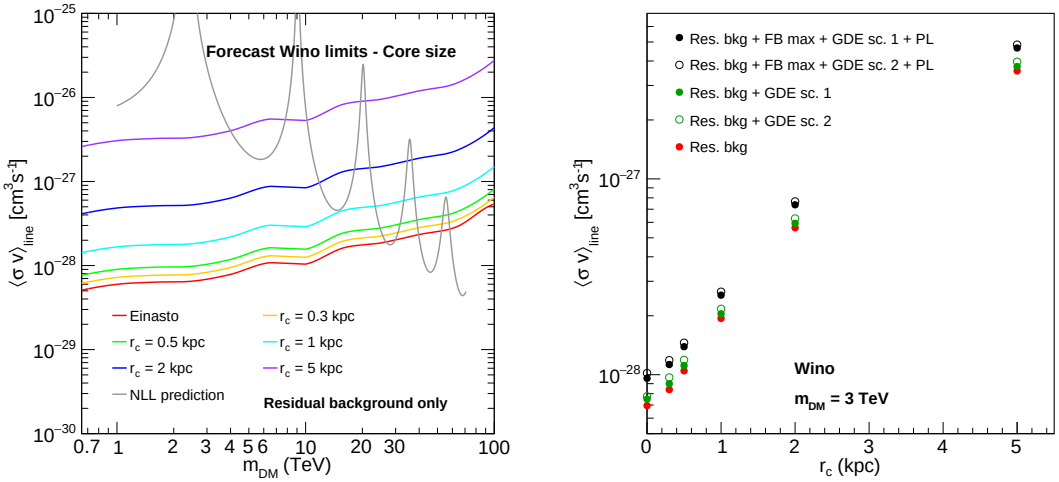

Figure 12.9: 95% C.L. CTA forecast limits on Wino annihilation cross section assuming different DM profiles. *Left panel:* CTA forecast upper limits on Wino annihilation cross section as function of its mass, computed at a 95% C.L. for 400 h of observations towards the GC. The predicted NLL thermal cross section is shown (gray solid line). The resonances are due to Sommerfeld enhancement. The limits are shown for the Einasto profile (red solid line) and cored profiles with core of size 300 pc (orange solid line), 500 pc (green solid line), 1 kpc (cyan solid line), 2 kpc (blue solid line) and 5 kpc (violet solid line), respectively. *Right panel:* Study of the interplay between the astrophysical background modeling and the dimension of the cored DM profiles. 95% C.L. upper limits on the line annihilation cross section of a 3 TeV Wino are computed for various $r_{\rm c}$ values and in presence of different backgrounds. The case of residual background only (red dots) is compared to those that include only the GDE (green dots) or also the Fermi Bubbles and the point-like sources (black dots). Both the GDE *scenario 1* (filled dots) and *scenario 2* (open dots) are considered.

the *endpoint* contribution in the regime $E_\gamma \approx m_{\rm DM}$. The factor of improvement is 1.5 at 1 TeV, 3 at 10 TeV and 7 at 50 TeV. An additional small improvement comes from the

continuum component, at the level of $1-5\%$ in the whole mass range. In Sec. 11.2 a larger effect of the continuum on the Wino limits had been observed for H.E.S.S.. This can be explained by the better energy resolution of CTA, down to 5% in the TeV range. In fact the sharp part at the end of the spectrum (including the *endpoint*) becomes stronger and the continuum more and more sub-dominant, which explains its small effect on the results for the *full spectrum*.

Another test is performed in order to evaluate the impact of the assumed DM density profile at the GC. The limits computed for an Einasto profile are compared in the left panel of Fig. 12.9 to those that assume a core of size r_c, built in such a way that the Einasto profile is recovered for $r_c \to 0$. Cores of size 300 pc, 500 pc, 1 kpc, 2 kpc and 5 kpc are tested. The degradation of the limits goes from about 20% for hundred-pc-sized cores to a factor about 50 for several-kpc-sized cores. The NLL predicted cross section is plotted in the same figure. Wino DM masses up to 4 TeV and at the position of the resonances at about 9 TeV and 20 TeV are excluded also for large cores of 5 kpc. CTA can probe the Wino DM candidate up to very large masses and very large cores.

12.4.2 Higgsino dark matter model

Besides the Wino triplet, another promising DM candidate that naturally comes out in SUSY is the Higgsino, a fermion doublet superpartner of the Higgs boson. Constraints from direct DM detection proved that the Higgsino cannot be a pure doublet [293], but it must mix with another state. Thus, in the Higgsino model, besides the mass, also the mass splittings between its neutral states δm_N and between the neutral and charged fermions δm_+ need to be set. These mass differences are more model-dependent than for the Wino, for which the splitting between the charged and neutral components measures 164.4 MeV [294]. For the Higgsino, to avoid scanning the wide range of allowed mass splittings we consider two relevant cases [295]. First, we consider a *splitting 1* scenario with $\delta m_N = 200$ keV and $\delta m_+ = 350$ MeV, where the δm_N value is the lowest allowed by the stringent constraints due to direct DM detection. Then, we consider a *splitting 2* scenario with $\delta m_N \gg \delta m_+$, where $\delta m_N = 2$ GeV and $\delta m_+ = 480$ MeV.
A partial computation of the Higgsino annihilation spectrum into gamma rays at tree level (leading order, LO) from Ref. [296] is used in this work. It includes the Sommerfeld effect and the *continuum* contribution from decay of W and Z, but not the NLO *endpoint* contribution. However, it is proven [295] that the resummed *endpoint* contribution is large for the Higgsino and it may be crucial for experiments like CTA that are expected to be sensitive to cross sections close to the one predicted for the Higgsino. Fig. 12.10 shows the Higgsino spectra used in this work for various mass values, including the *gamma line* (dashed lines) and the *continuum* (solid lines) components. Both the *splitting 1* (left panel) and *splitting 2* (right panel) scenarios are shown.

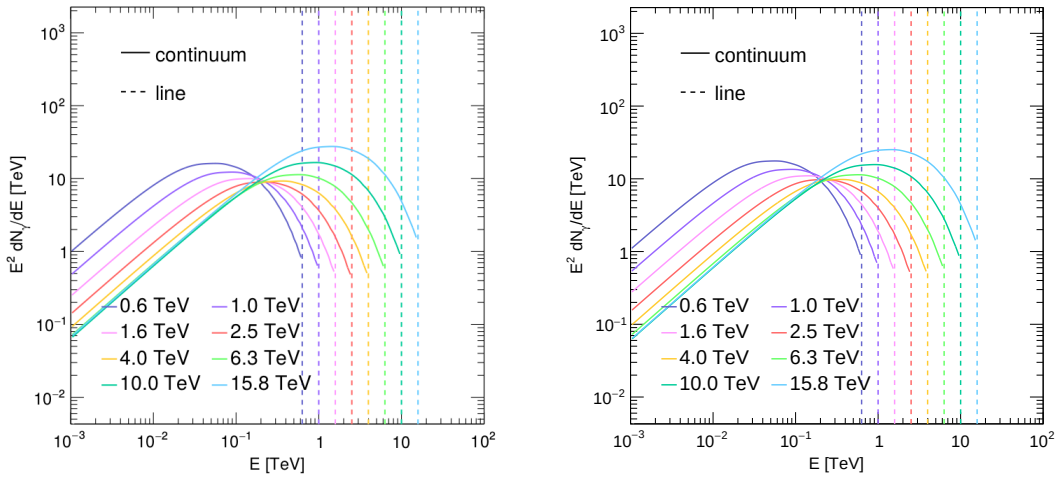

Figure 12.10: Higgsino annihilation spectrum for several masses between 600 GeV and 16 TeV. The line (dashed lines) and continuum (solid lines) contributions to the full spectrum are shown. *Left panel:* spectra obtained assuming splittings $\delta m_{\rm N} = 200$ keV and $\delta m_{+} = 350$ MeV. *Right panel:* spectra obtained assuming splittings $\delta m_{\rm N} = 2$ GeV and $\delta_{+} = 480$ MeV.

12.4.3 Constraints on Higgsino dark matter

The 95% C.L. expected upper limits for CTA on the Higgsino annihilation cross section as function of its mass for an Einasto profile and residual background only are computed as well with the 3D-likelihood approach and a LLRTS. They are computed for both splitting hypotheses and they are shown (red solid line) in the top panels of Fig. 12.11, with the 1σ (green band) and 2σ (yellow band) containment bands obtained from the Asimov dataset. The LO predicted cross section (gray solid line) and the thermal Higgsino DM mass at 1.0 ± 0.1 TeV [297] are shown. The *line-only* constraints are also shown for comparison. The *continuum* contribution to the Higgsino spectrum produces more stringent limits in the low mass range. This component improves the limits at 600 GeV of a factor 3.5 for the *splitting 1* hypothesis and 4 for the *splitting 2* hypothesis. For the *splitting 1* hypothesis, the thermally produced Higgsino is at reach for CTA, as well as Higgsino DM with mass below 10 TeV and near the resonance at about 25 TeV. For the *splitting 2* hypothesis, the thermally produced Higgsino is at reach for CTA, as well as Higgsino DM with mass below 2 TeV, in the range 6-15 TeV where there is a Sommerfeld resonance, and near another resonance at about 40 TeV.

Constraints are computed also assuming cored DM profiles. In the bottom panels of Fig. 12.11, for the two splitting hypothesis, the 95% C.l. limits on $\langle \sigma v \rangle_{\rm line}$ are compared for the Einasto profile and cores of size 300 pc, 500 pc, 1 kpc , 2 kpc and 5 kpc, respectively. The LO thermal cross section (gray solid line) is also shown. The Higgsino thermally

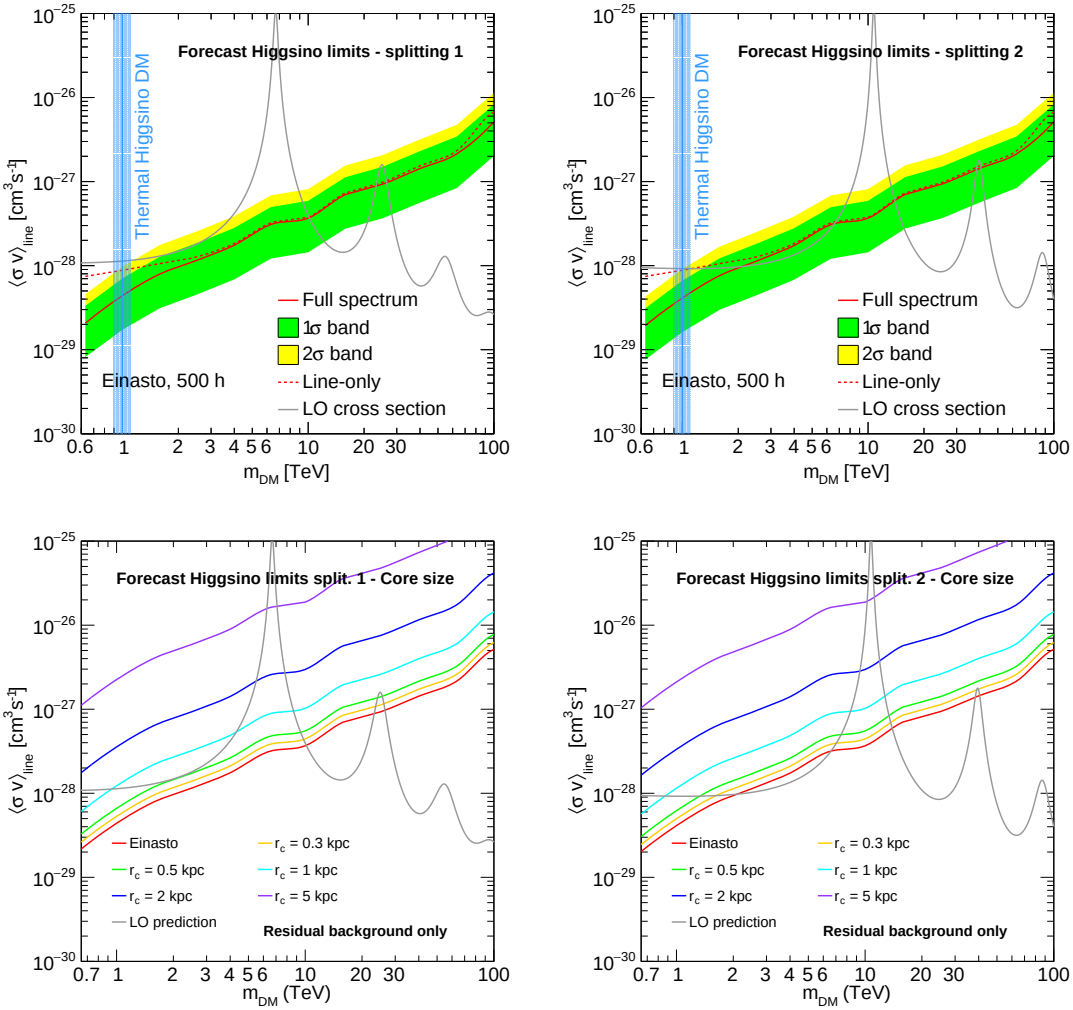

Figure 12.11: CTA forecast upper limits on Higgsino annihilation cross section as function of its mass, computed at a 95% C.L. for 400 h of observations towards the GC and residual background only. The predicted LO thermal cross section is shown (gray solid line). The resonances are due to Sommerfeld enhancement. *Top panels:* The expected limits (red solid line) computed assuming an Einasto profile are shown together with the 1σ (green band) and 2σ (yellow band) bands. The theoretical mass for Higgsino DM thermally produced in the early Universe is marked (cyan solid line). The *line-only* constraints are shown for comparison (red dashed line). *Bottom panels:* The limits for the Einasto profile (red solid line) are compared to those obtained with cored profiles with core of size 300 pc (orange solid line), 500 pc (green solid line), 1 kpc (cyan solid line), 2 kpc (blue solid line) and 5 kpc (violet solid line). *Left panels:* limits obtained assuming splittings $\delta m_{\rm N} = 200$ keV and $\delta m_{+} = 350$ MeV. *Right panels:* limits obtained assuming splittings $\delta m_{\rm N} = 2$ GeV and $\delta_{+} = 480$ MeV.

produced in the early Universe with a mass of 1 TeV is not at reach for CTA assuming kpc-sized cores. The degradation of the limits for large cores has the same behavior as in the case of the Wino DM candidate. The Higgsino is probed independently on the assumed DM core at the position of the resonance at about 7 TeV for the *splitting 1* hypothesis and 9 TeV for the *splitting 2* hypothesis.

12.5 Astrophysical backgrounds for CTA

12.5.1 Galactic Diffuse Emission

Scenario 1

Some extended standard astrophysical emissions are observed in the GC region (see Sec. 3.3 and Sec. 3.4) that could degrade the sensitivity to DM signals. For the first model of Galactic Diffuse Emission (*GDE scenario 1* or "This work") the spectra extrapolated in the TeV energy range and maps provided by a recomputation of the results from Ref. [298] in a region of $\pm 15°$ around the GC are used. These reference used a new release of GALPROP v56 that includes more realistic 3D models for the interstellar radiation field and interstellar gas distributions [299][2]. The maps are provided for each energy bin used in the CTA analysis in order to have a proper source-dependent modeling at different energies. The maps per pixel of size $0.5° \times 0.5°$ have been normalized to the flux provided in an squared integration region of $15° \times 15°$ centered at the GC with overall size 0.07 sr. Two GDE components are treated separately, then summed: the gas-correlated component which include emissions from pion decay and bremsstrahlung, and the ICS component that is more sensitive to the sources distribution.

Scenario 1			
Component	ϕ_0 [TeV^{-1}cm^{-2}s^{-1}sr^{-1}]	Γ	$E_{\rm cut}$ [TeV]
gas-correlated	7×10^{-10}	2.48	-
ICS	3×10^{-10}	2.46	70
Scenario 2			
Component	ϕ_0 [TeV^{-1}cm^{-2}s^{-1}sr^{-1}]	Γ	$E_{\rm cut}$ [TeV]
gas-correlated	8×10^{-10}	2.48	-
ICS	5×10^{-10}	2.40	100

Table 12.1: Parameters of the spectral model of the two GDE scenarii. The gas correlated component is modeled as a power-law and the ICS component as a power-law with exponential cut-off.

[2]It does not assume anymore the 2D Galactocentric cylindrical symmetry in the propagation of CRs which has a non-negligible impact for analyses of the GC region.

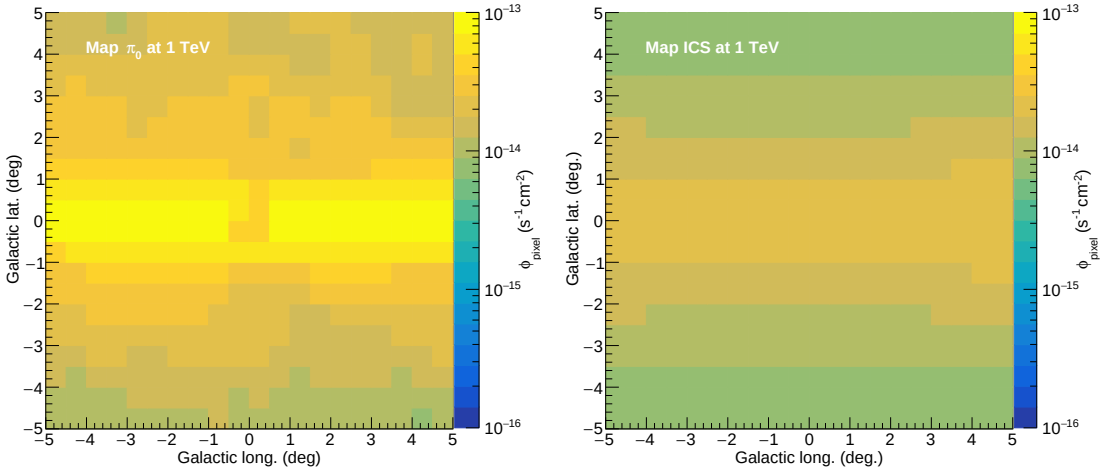

Figure 12.12: Spatial map of the *scenario 1* in Galactic coordinates, given in terms of the flux integrated in a spatial bin of size $0.5° \times 0.5°$ and a spectral bin centered at 1 TeV with width $\Delta \log_{10}(E/1\,\text{TeV}) = 0.2$. *Left panel:* map of the gas-correlated (bremsstrahlung and pion decay) component. *Right panel:* map of the ICS component.

The differential flux is modeled as a power-law (see Eq. (5.1)) for the gas-correlated component and as a power-law with exponential cut-off (see Eq. (5.2)) for the ICS component. The parameters are given in Tab. 12.1. The spatial maps are shown in Fig. 12.12. They are given in terms of integrated flux in a $0.5° \times 0.5°$ spatial bin and in a spectral bin centered at 1 TeV with width $\Delta \log_{10}(E/1\text{ TeV}) = 0.2$. Fig. 12.13 shows in the left panel the differential energy flux of each background component and the Wino and Higgsino spectra. In the right panel the expected count rate in a central ROI obtained after convolution with CTA IRFs. The Wino and Higgsino expected signals are also shown.

Scenario 2

For the second model of GDE (*GDE scenario 2* or "Fwrmi '17") the spectra are obtained from Fermi-LAT analysis in Ref. [89]. The spatial maps for the gas-correlated component are modeled from the measured distribution of interstellar dust throughout the Milky Way [300]. In fact π_0 are produced in the interaction of the accelerated protons with the interstellar medium and molecular clouds. The spatial behavior of the ICS component is extrapolated as in Ref. [99], using the analytic shape $ICS(b,\ell) \approx \exp\left[-\frac{\ell^2}{2(30°)^2}\right](\csc[\max(2°,|b|)] - 1)$ where csc is the cosecant function. It is constrained for latitudes $< 0°$ to avoid a singularity along the Galactic plane. The maps per pixel of size $0.5° \times 0.5°$ have been normalized to the flux provided in an circular integration region of radius 10° around the GC ($\Delta\Omega \simeq 0.1$ sr). The gas-correlated differential flux is modeled as a power-law and the ICS one as a power-law with exponential cut-off. The parameters are given in Tab. 12.1. The spatial maps are

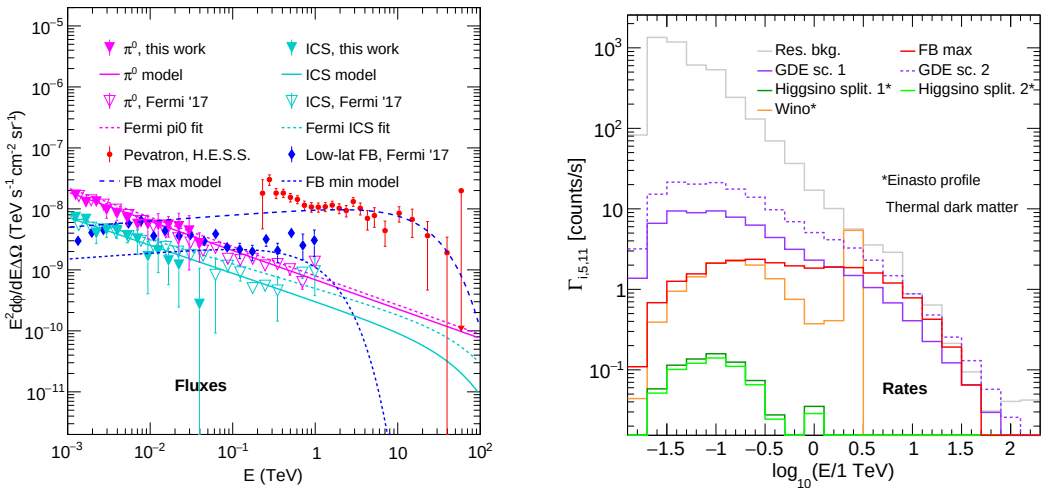

Figure 12.13: Background and DM differential flux and count rate with CTA. *Left panel:* Background differential energy fluxes are shown for *GDE scenario 1* (magenta and cyan filled triangles), *GDE scenario 2* from Fermi-LAT (magenta and cyan empty triangles) together with their models (solid and dashed lines respectively), Pevatron from H.E.S.S. (red dots) and low-latitude Fermi Bubbles (blue diamonds) together with the corresponding models. *Right panel:* Expected count rate in the ROI with indexes $(\mathrm{j}, \mathrm{k}) = (11, 5)$ for the residual background (gray line), the two GDE models (violet lines), the Fermi Bubble optimistic model (red line) and the thermally produced Wino (orange line) and Higgsino (green lines).

shown in Fig. 12.14. They are given in terms of integrated flux in a $0.5° \times 0.5°$ spatial bin and in a spectral bin centered at 1 TeV with width $\Delta \log_{10}(E/1\ \text{TeV}) = 0.2$. The same spatial template is used in each energy bin.

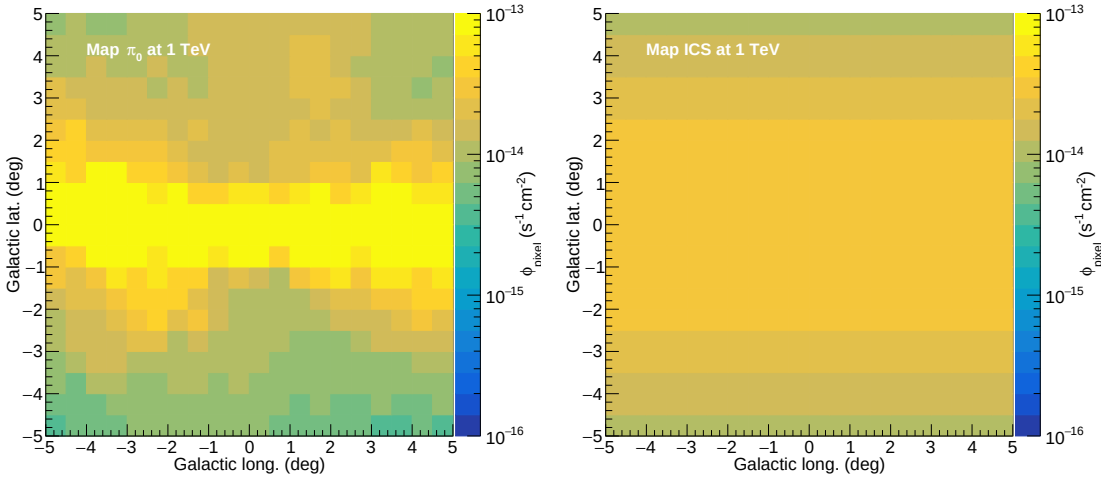

Figure 12.14: Spatial map of the *GDE scenario 2* in Galactic coordinates, given in terms of the flux integrated in a spatial bin of size $0.5° \times 0.5°$ and a spectral bin centered at 1 TeV with width $\Delta \log_{10}(E/1\,\text{TeV}) = 0.2$. *Left panel:* map of the gas-correlated (bremsstrahlung and pion decay) component. *Right panel:* map of the ICS component.

12.5.2 Low-latitude Fermi Bubbles templates

The law-latitude Fermi Bubbles (see Sec. 3.4) are extracted from Ref. [89]. They are also similarly reproduced by Ref. [298] from which the *GDE scenario 2* is modeled. The spatial maps for Fermi Bubbles are interpolated in the exclusion region of Fermi-LAT near the Galactic plane. The Fermi Bubbles spatial flux templates are shown in Fig. 12.15. They are normalized in order to reproduce the spectrum integrated in the region for latitudes $< 10°$ used in the Fermi-LAT analysis. The spectrum of the Fermi Bubbles is modeled as a power-law with exponential cut-off. Two empirical modelings are extrapolated at high energies: an optimistic model *FB max* that goes through the largest spectral points of the measured spectrum and a pessimistic model *FB min* that pass through the lowest points of the measured spectrum. The parameters of the spectral model are given in Tab. 12.2

12.5.3 Point-like Fermi-LAT sources in the field of view

Numerous point-like (PL) sources shine in gamma-rays in the GC region, above the GDE. High-energy PL Fermi-LAT sources that could be detected by CTA have been extracted from the third Fermi-LAT high-energy source list, known as 3FHL catalog [301]. Sources

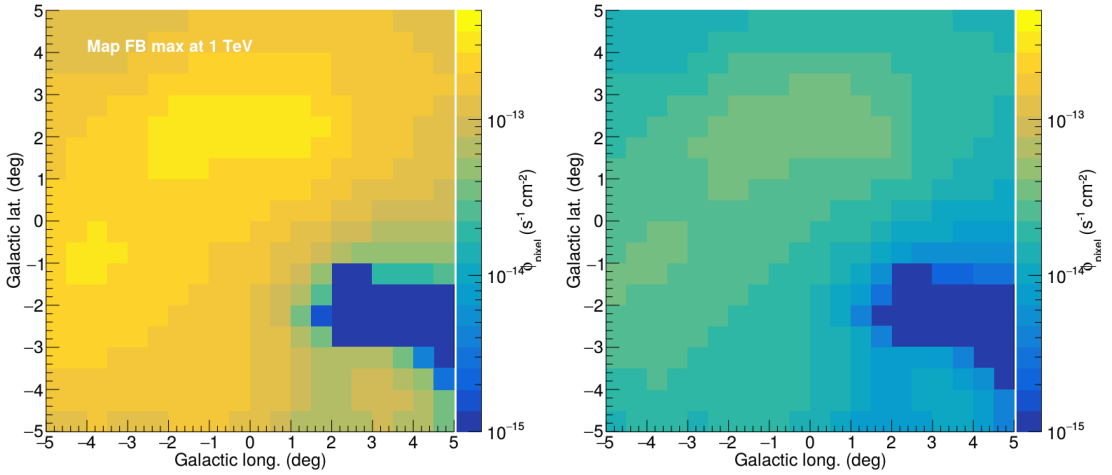

Figure 12.15: Spatial map of the low-latitude Fermi Bubbles in Galactic coordinates, given in terms of the flux integrated in a spatial bin of size $0.5° \times 0.5°$ and a spectral bin centered at 1 TeV with width $\Delta \log_{10}(E/1\,\mathrm{TeV}) = 0.2$. *Left panel:* for the *FB max* model. *Right panel:* for the *FB min* model.

Model	ϕ_0 **cm^{-2} s^{-1} sr^{-1}**	Γ	**E$_{\mathrm{cut}}$ TeV**
FB max	$1. \times 10^{-8}$	1.9	20
FB min	5×3^{-9}	1.9	1

Table 12.2: Parameters of the exponential cutoff power-law spectrum of the Fermi Bubbles. An optimistic *FB max* and a conservative *FB min* models are produced. They are modeled as a power-laws with exponential cut-off.

with a power-law spectrum that expends up to VHE energy and position withing $\pm 5^\circ$ in Galactic longitude and latitude have been selected. In order to avoid modeling all these sources, a mask of radius 0.25° is put on each of them to reject them from the ROIs. These masks reduce the size of the overall region of interest of less than 1%. The choice of the dimension of the mask is made in order to avoid significant leakages from the sources, knowing that Fermi-LAT PSF is about 0.1° in the GeV energy range at 68% containment radius.

12.5.4 Effect of these components on the limits

The presence of several background components affect the sensitivity to a weak DM signal. The constraints on $\langle \sigma v \rangle$ are recomputed adding to the residual background some or all the astrophysical backgrounds mentioned above. Four cases are tested and the 95% C.L. upper limits on the cross section for the Wino (left panel) and the Higgsino (right panel, under *splittings 1* hypothesis) are shown in Fig. 12.16: residual background only ("Res. bkg.", red solid line), Res. bkg + FB max (blue solid line), Res. bkg + FB max + *GDE scenario 1* (cyan solid line), Res. bkg + FB max + *GDE scenario 1* + point-like (PL) Fermi sources (black solid line), Res. bkg + FB max + *GDE scenario 2* + PL Fermi sources (black dashed line). The Fermi Bubbles under the model *FB max* degrade the limits by about 30%, while the *FB min* model is negligible. The GDE has an additional impact of between 5% and 20% for *scenario 1* and up to 25% for *scenario 2*. Masking the PL Fermi sources has a negligible effect since the size of the masks is less than 1% of the total *ON region*.

A further study shows the interplay between the background components and the size of the DM profile. The goal was to test if some spatial features could affect the CTA sensitivity to DM in a different way depending on the DM profile. For example, a concentration of standard gamma-rays at 4° from the GC would have a larger impact on the limits obtained for a 1 kpc sized core than on a 300-kpc cored profile that degrades quickly beyond 2° distances. Thus, constraints on the line cross section are computed for the different core sizes in the case where only the GDE is present above the residual background and the case where all the above mentioned astrophysical backgrounds are detected. The case with GDE-only background is treated in this case because it increases the sensitivity to the different GDE spatial distributions of the two scenarii. Otherwise, the behavior of the constraints is dominated by the stronger emission from the Fermi Bubbles. The right panel of Fig. 12.8 shows the limits on $\langle \sigma v \rangle_{\rm line}$ for a Wino particle with mass 3 TeV as function of the dimension of the DM density profile. The constraints obtained in case of residual background only (red dots) are compared to those that include the GDE emission (green dots) and those that consider all the additional astrophysical backgrounds due to the Fermi Bubbles and the point-like sources (black dots). Both the *GDE scenario 1* (filled dots) and the *GDE scenario 2* (open dots) are shown. None of the GDE background scenarii have

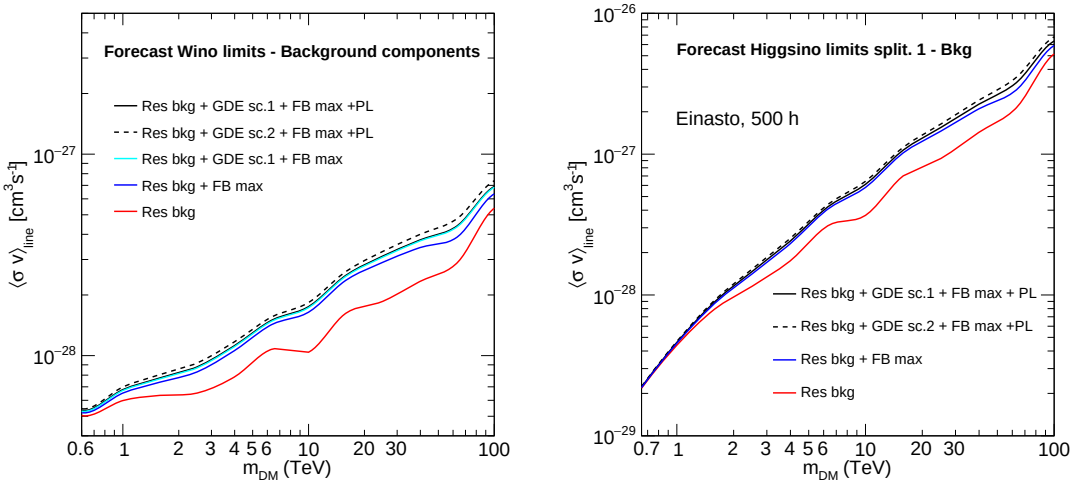

Figure 12.16: CTA forecast limits on heavy DM annihilation cross section assuming different background contributions. The 95% upper limits obtained considering only the residual background (red solid line) are compared to those that include also the Fermi Bubbles for the *FB max* model (blue solid line), the GDE for *scenario 1* (cyan solid line) and *scenario 2* (black dashed line) and the point-like (PL) high-energy Fermi-LAT sources (black solid line). *Left panel:* limits for Wino DM. *Right panel:* limits for Higgsino DM. For both candidates the background the major impact on the DM constraints comes from the Fermi Bubbles, for the *FB max* model. The limits obtained with a *FB min* Fermi Bubbles modeling are not shown because the effect of the bubbles on the constraints is negligible.

a spatial behavior that makes one of the computed $\langle\sigma v\rangle_{\rm line}$ deviate significantly from the others in correspondence a specific $r_{\rm c}$ value.

12.6 Discussion and perspectives

The CTA observations are very promising for dark matter detection with a dedicated survey of the Galactic Center region. CTA has the sensitivity to reach the thermal relic cross section in several annihilation channels. From scanning of the pMSSM it is observed that the Wino candidate is mostly probed and the Higgsino is also at reach. They can be probed in regions of the parameter space that can be reached only by CTA. Specific searches for pure Wino and pure Higgsino annihilation show the significant sensitivity of CTA to TeV dark matter. The Wino could be indeed completely ruled out by CTA. In addition, the Higgsino at its thermal mass is barely at reach (with small margin). The computation of the expected non-negligible *endpoint* contribution (included in the Wino spectrum) would improve significantly the CTA sensitivity.

The strategy for DM search with CTA will be to model as much as possible the astrophysical backgrounds that are detected in the GC region above the residual background.

This approach could improve the sensitivity up to about 50%. In fact, the Galactic Diffuse Emission can degrade the sensitivity up to a factor 20% and the low-latitude Fermi Bubbles up to an additional 30%. The difference between the GDE models extrapolated under different assumptions affects the limits only at the few percent level. The limits are found to be not very sensitive to the different spatial behaviors of the different background templates.

CTA is expected to have the sensitivity to probe the thermal relic cross section in many annihilation channels for cuspy DM density profiles and it may also be able to probe the Higgsino at its thermal mass and rule out the Wino in all the reasonable mass range. So CTA may be able to provide a crucial input to find an answer to the question about DM nature in the most natural heavy dark matter models.

If dark matter particles are not WIMPs CTA can also provide crucial input for dark matter in the form of axion-like particles (ALPs, see Sec. 6.2). These particles can couple to photons in galactic/intergalactic magnetic fields and modify the measured spectrum of extragalactic sources, like blazars, due to photon-ALP conversion during the propagation. The spectral signature would be *wiggles* in the energy spectrum due to ALP-photon oscillations, in addition to the attenuation from the interaction of the VHE gamma rays with the Extragalactic Background Light. The probability of conversion depends on the structure and intensity of the magnetic field along the line of sight of the blazar and also on the coupling between photons and ALPs. The previous studies with gamma-ray telescopes set constraints on the parameter space of ALP-photon coupling $g_{a\gamma}$ versus ALP mass m_a [302, 303]. CTA will be sensitive to axion-like particles in the range of $g_{a\gamma} \gtrsim 2 \times 10^{-11}$ GeV^{-1} and m_a between 10^{-10} and 10^{-7} eV [304].

Conclusions

In this work studies of the Galactic Center region in very-high-energy gamma rays and dark matter indirect searches in the GeV-TeV mass range have been presented.

The Galactic Center region is a rich environment to study VHE gamma-ray astrophysics. Besides point-like and extended sources, a TeV diffuse emission has been detected in the inner 50 pc around the Galactic Center. While the most plausible interpretation is based on a single source that accelerates protons up to PeV energies, *a Pevatron*, for which Sagittarius A* is the most likely counterpart, an alternative scenario has been discussed. While yet unresolved, a population of millisecond pulsars in the Galactic bulge recently argued in light of the detection of a Galactic Center excess by Fermi-LAT, could produce such a diffuse TeV emission. A model of the acceleration and propagation of protons in the interstellar medium sets constraint the hypothetical bulge population to $N_{\rm b}(L_{\rm CR}(t_{\rm sd}) > 10^{33}\,{\rm erg\,s^{-1}}) \sim 7 \times 10^4$ millisecond pulsars, in order to match H.E.S.S. diffuse spectrum and gamma-ray luminosity. Recently the Inner Galaxy Survey (IGS) performed with H.E.S.S. II in the several inner degrees of the Galactic Center showed that the diffuse emission in this region is becoming more spatially extended with the new observation strategy. Dedicated analyses in H.E.S.S. are ongoing in order to study if the origin could be related to the previously detected Pevatron, the radio Lobe outflows or the low-latitude Fermi Bubbles. New IGS observations could also help discriminating between the *Pevatron* and millisecond pulsar population scenarii at the Galactic Center.

Given its proximity, the Galactic Center region which is expected to host a large amount of dark matter is the most promising target for indirect dark matter searches with VHE gamma rays. Ten years of observations of the Galactic Center region with H.E.S.S. I were analyzed to set the most constraining limits so far on dark matter annihilation cross section in the channel $\chi\chi \to \gamma\gamma$. At 1 TeV they reached 4×10^{-28} cm^3 s^{-1}, improving the previous results of a factor about six.
Five years of H.E.S.S. II data taken during the Inner Galaxy Survey have been also analyzed for indirect dark matter search. The expected sensitivity lies below the thermal relic cross section in the $\chi\chi \to W^+W^-$ channel, the natural scale for dark matter annihilation is however probed only in the $\chi\chi \to \tau^+\tau^-$ channel due to a slight excess in the signal region. The high sensitivity of CT5 in the hundred GeV energy range improved the previous H.E.S.S.

limits at 300 GeV of a factor $5-7$, depending on the annihilation channel. The ongoing *Combined* analysis that exploits the stereoscopy and the hybrid array is expected to further improve the constraints in the TeV mass range.

Alternative targets for dark matter search are considered since the Galactic Center region harbors a challenging standard astrophysical background and its central dark matter density profile is pretty uncertain. A cleaner environment is offered by dwarf galaxies where no standard GeV-TeV emission is detected. For nearby dwarf galaxies, and particularly true for the ultra-faint dwarf galaxies, a large dark matter signal is expected. A selection of satellites of the Milky Way with large dark matter content discovered by DES has been observed by H.E.S.S. to search for dark matter both in the *gamma-line* and *continuum* channels. In absence of significant signal, the first constraints from IACTs on these targets have been derived on the dark matter annihilation cross section, the most constraining one for DM masses above 10 TeV. In order to exploit the complementarity among the current gamma-ray instruments and their datasets a project is ongoing in order to make a combined search with Fermi-LAT, HAWC, H.E.S.S., MAGIC and VERITAS towards dwarf galaxies.

Beyond the above-mentioned model-independent dark matter searches, specific dark matter models can be tested with H.E.S.S. Forecast limits on the annihilation cross section for Wino dark matter mass have been derived from mock H.E.S.S.-I-like observations of the Galactic Center region. This study showed that H.E.S.S. can exclude Wino dark matter up to a mass of 10 TeV for cuspy DM profiles at the Galactic Centre. A Wino dark matter candidate of mass 2.9 TeV as expected from thermal production in the early Universe can be excluded for cored dark matter density profiles with core radii up to 5 kpc.
The search for dark matter in the inner Galactic halo is a key-science topic also for the upcoming CTA. Mock observations of the Galactic Center region with the CTA-South observatory following the planned observation strategy by the CTA Collaboration, have been used to compute the sensitivity to dark matter annihilating into *gamma lines* and *continuum* channels. CTA will have the sensitivity to probe the thermal relic cross section in most of the *continuum* annihilation channels for cuspy DM profiles. It will probe a significant region of the pMSSM model, including regions which are very challenging or even out of reach for direct detection, *i.e.* below the neutrino floor, and collider searches for WIMP above 1 TeV. Two specific heavy dark matter candidates, the Wino and the Higgsino, respectively, have been considered. CTA will be able to probe the Wino model up to 40 TeV and the Higgsino up to several TeV, depending on the assumptions on the annihilation spectrum, including at the thermal Higgsino mass of 1 TeV. The impact of standard astrophysical background such as the Galactic Diffuse Emission and possibly the low-latitude Fermi Bubbles emission, on the expected CTA sensitivity have been derived and showed a degradation of the limits up to a 50%. Provided that the astrophysical background can be carefully modeled and the systematics uncertainties controlled to a level significantly below of that of current IACTs,

CTA observation of the Galactic Center region will provide a crucial input to TeV WIMP dark matter.

Bibliography

[1] M.S. Longair. *High Energy Astrophysics: Volume 2, Stars, the Galaxy and the Interstellar Medium*. High Energy Astrophysics. ISBN 9780521435840.

[2] D. Pacini. La radiazione penetrante alla superficie ed in seno alle acque. *Il Nuovo Cimento*, 3:93–100, December 1912. doi: 10.1007/BF02957440. ArXiv 1002.1810.

[3] Victor F. Hess. Über Beobachtungen der durchdringenden Strahlung bei sieben Freiballonfahrten. *Phys. Z.*, 13:1084–1091, 1912.

[4] R. A. Millikan and G. H. Cameron. The Origin of the Cosmic Rays. *Physical Review*, 32:533–557, October 1928. doi: 10.1103/PhysRev.32.533.

[5] R. Blandford et al. Cosmic Ray Origins: An Introduction. *Nucl. Phys. Proc. Suppl.*, 256-257:9–22, 2014. doi: 10.1016/j.nuclphysbps.2014.10.002. ArXiv 1409.2589.

[6] A. V. Olinto. Ultrahigh-energy cosmic rays: The Theoretical challenge. *Phys. Rept.*, 333:329–348, 2000. doi: 10.1016/S0370-1573(00)00028-4.

[7] E. Fermi. On the origin of the cosmic radiation. *Phys. Rev.*, 75:1169–1174, Apr 1949. doi: 10.1103/PhysRev.75.1169.

[8] W. I. Axford and others. The acceleration of cosmic rays by shock waves. *International Cosmic Ray Conference*, 11:132–137, 1977.

[9] A. R. Bell. The acceleration of cosmic rays in shock fronts. I. *Mon. Not. Roy. Astron. Soc.*, 182:147–156, January 1978. doi: 10.1093/mnras/182.2.147.

[10] G. B. Rybicki. *Radiative Processes in Astrophysics*. Wiley-VCH, 2004.

[11] G. R. Blumenthal and R. J. Gould. Bremsstrahlung, synchrotron radiation, and compton scattering of high-energy electrons traversing dilute gases. *Rev. Mod. Phys.*, 42:237–270, 1970. doi: 10.1103/RevModPhys.42.237.

[12] K. R. Lang. NASA's Cosmos - The Material Between the Stars. https://ase.tufts.edu/cosmos/view_images.asp?id=50, 2010.

[13] S. Jeff. The Bremsstrahlung, Synchrotron and Compton effects as emission processes in Astrophysics. http://www.jeffstanger.net/Astronomy/emissionprocesses.html, 2005.

[14] F. W. Stecker. Neutral-pion decay gamma-rays from the galaxy and the interstellar gas content. *Astrophys. J.*, 185:499–504, 1973. doi: 10.1086/152435.

[15] M. Kachelriess. Lecture notes on high energy cosmic rays. 2008. ArXiv 0801.4376.

[16] S. Gabici. Gamma-Ray Emission from Supernova Remnants and Surrounding Molecular Clouds. *AIP Conf. Proc.*, 1792(1):020002, 2017. doi: 10.1063/1.4968887. ArXiv 1610.06234.

[17] F. Aharonian. Primary particle acceleration above 100 TeV in the shell-type Supernova Remnant RX J1713.7-3946 with deep H.E.S.S. observations. *Astron. Astrophys.*, 464: 235–243, 2007. doi: 10.1051/0004-6361:20066381.

[18] P. N. Bhat et al. The Third Fermi gbm Gamma-ray Burst Catalog: the First six Years. *Astrophys. J. Suppl.*, 223(2):28, 2016. doi: 10.3847/0067-0049/223/2/28. ArXiv 1603.07612.

[19] First time detection of a GRB at sub-TeV energies; MAGIC detects the GRB 190114C. http://www.astronomerstelegram.org/?read=12390&fbclid=IwAR1cp8oc04mXVsf7P3HLpJU7KsrREiwtH2NfI-4VzUQLtW1TZ3vNPuf3MPU.

[20] E. L. Ruiz-Velasco and the H.E.S.S. Collaboration. Discovery of Late-Time VHE Emission from a Gamma-ray Burst Afterglow by H.E.S.S. CTA Science Symposium, 2019.

[21] R. Blandford et al. Relativistic Jets in Active Galactic Nuclei. 2018. ArXiv 1812.06025.

[22] L. Maraschi and others. On the broad band energy distribution of blazars. In T. Courvoisier and A. Blecha, editors, *Multi-Wavelength Continuum Emission of AGN*, volume 159 of *IAU Symposium*, pages 221–232, 1994.

[23] F. Aharonian et al. An Exceptional Very High Energy Gamma-Ray Flare of PKS 2155-304. *Astrophys. J.*, 664:L71–L78, 2007. doi: 10.1086/520635. ArXiv 0706.0797.

[24] H. Abdalla et al. First Ground-based Measurement of Sub-20 GeV to 100 GeV γ-rays from the Vela Pulsar with H.E.S.S. II. *Astron. Astrophys.*, 620:A66, 2018. doi: 10.1051/0004-6361/201732153. ArXiv 1807.01302.

[25] A. Djannati-Ataï, others, and H.E.S.S. Collaboration. Probing Vela pulsar down to 20 GeV with H.E.S.S. II observations. In *6th International Symposium on High Energy Gamma-Ray Astronomy*, volume 1792 of *American Institute of Physics Conference Series*, page 040028, January 2017. doi: 10.1063/1.4968932.

[26] W. Bednarek and M. Bartosik. Gamma-rays from the pulsar wind nebulae. *Astron. Astrophys.*, 405:689, 2003. doi: 10.1051/0004-6361:20030593.

[27] F. Aharonian et al. Observations of the Crab Nebula with H.E.S.S. *Astron. Astrophys.*, 457:899–915, 2006. doi: 10.1051/0004-6361:20065351.

[28] AGILE - Astro-rivelatore Gamma a Immagini Leggero. http://agile.rm.iasf.cnr.it/, .

[29] Fermi Gamma-Ray Space Telescope. https://fgst.slac.stanford.edu/WhatIsLAT.asp.

[30] HAWC - The High-Altitude Water Cherenkov Gamma-Ray Observatory. https://www.hawc-observatory.org/.

[31] H.E.S.S. - High Energy Spectroscopic System. https://www.mpi-hd.mpg.de/hfm/HESS/, .

[32] MAGIC - Major Atmospheric Gamma-ray Imaging Cherenkov Telescope. http://www.magic.iac.es/, .

[33] VERITAS - Very Energetic Radiation Imaging Telescope Array System. https://veritas.sao.arizona.edu/, .

[34] HFACT - The First G-APD Cherenkov Telescope. https://www.isdc.unige.ch/fact/, .

[35] A. Franceschini and G. Rodighiero. The extragalactic background light revisited and the cosmic photon-photon opacity. *Astron. Astrophys.*, 603:A34, 2017. doi: 10.1051/0004-6361/201629684. ArXiv 1705.10256.

[36] J. Bolmont et al. Search for Lorentz Invariance Violation effects with PKS 2155-304 flaring period in 2006 by H.E.S.S. In *Proceedings on 44th Rencontres de Moriond on Very High Energy Phenomena in the Universe: La Thuile, Italy, February 1-8, 2009*, pages 133–136, 2009. ArXiv 0904.3184.

[37] M. Lorentz and P. Brun. Limits on Lorentz invariance violation at the Planck energy scale from H.E.S.S. spectral analysis of the blazar Mrk 501. *EPJ Web Conf.*, 136: 03018, 2017. doi: 10.1051/epjconf/201713603018. ArXiv 1606.08600.

[38] J-F. Glicenstein et al. Limits on Primordial Black Hole evaporation with the H.E.S.S. array of Cherenkov telescopes. In *Proceedings, 33rd International Cosmic Ray Conference (ICRC2013): Rio de Janeiro, Brazil, July 2-9, 2013*.

[39] A. Abramowski et al. Acceleration of petaelectronvolt protons in the Galactic Centre. *Nature*, 531:476, 2016. doi: 10.1038/nature17147. ArXiv 1603.07730.

[40] K. Bernlohr. Simulation of Imaging Atmospheric Cherenkov Telescopes with CORSIKA and sim-telarray. *Astropart. Phys.*, 30:149–158, 2008. doi: 10.1016/j.astropartphys.2008.07.009. ArXiv 0808.2253.

[41] H. J. Völk and K. Bernlöhr. Imaging Very High Energy Gamma-Ray Telescopes. *Exper. Astron.*, 25:173–191, 2009. doi: 10.1007/s10686-009-9151-z. ArXiv 0812.4198.

[42] W. Hofmann. Status of the High Energy Stereoscopic System (H.E.S.S.) project. In *27th International Cosmic Ray Conference (ICRC 2001) Hamburg, Germany, August 7-15, 2001*.

[43] K Bernlöhr et al. The optical system of the HESS imaging atmospheric Cherenkov telescopes, Part 1: Layout and components of the system. *Astropart. Phys.*, 20: 111–128, 2003. doi: 10.1016/S0927-6505(03)00171-3.

[44] R. Cornils et al. The optical system of the HESS imaging atmospheric Cherenkov telescopes, Part 2: Mirror alignment and point spread function. *Astropart. Phys.*, 20: 129–143, 2003. doi: 10.1016/S0927-6505(03)00172-5.

[45] O. Le Blanc et al. Final characterisation and design of the Gamma-ray Cherenkov Telescope (GCT) for the Cherenkov telescope array. *Proc. SPIE Int. Soc. Opt. Eng.*, 10700:1070010, 2018. doi: 10.1117/12.2313158.

[46] F. Krayzel et al. Improved sensitivity of H.E.S.S.-II through the fifth telescope focus system. In *Proceedings, 33rd International Cosmic Ray Conference (ICRC2013): Rio de Janeiro, Brazil, July 2-9, 2013*.

[47] G. Giavitto et al. A major electronics upgrade for the H.E.S.S. Cherenkov telescopes 1-4. *PoS*, ICRC2015:996, 2016. doi: 10.22323/1.236.0996. [34,996(2015)].

[48] S. Vorobiov and others. NECTAr: New electronics for the Cherenkov Telescope Array. *Nuclear Instruments and Methods in Physics Research A*, 639:62–64, May 2011. doi: 10.1016/j.nima.2010.08.112.

[49] G. Vacanti et al. Muon ring images with an atmospheric Cherenkov telescope. *Astropart. Phys.*, 2:1–11, 1994. doi: 10.1016/0927-6505(94)90012-4.

[50] J. Devin et al. Impact of h.e.s.s. lidar profiles on crab nebula data. *EPJ Web of Conferences*, 197:01001, 01 2019. doi: 10.1051/epjconf/201919701001.

[51] V. Lefranc. *Search for dark matter, Galactic Center observation with H.E.S.S. and upgrade of the H.E.S.S. I camera*. Theses, Université Paris-Saclay, June 2016. URL https://tel.archives-ouvertes.fr/tel-01374541.

[52] R. Chalmé-Calvet. *Calibration of the fifth telescope of the H.E.S.S. experiment and observation of the Galactic Centre above 30 GeV*. Theses, Université Pierre et Marie Curie - Paris VI, November 2015. URL https://tel.archives-ouvertes.fr/tel-01307151.

[53] M. de Naurois and L. Rolland. A high performance likelihood reconstruction of gamma-rays for Imaging Atmospheric Cherenkov Telescopes. *Astropart. Phys.*, 32: 231, 2009. doi: 10.1016/j.astropartphys.2009.09.001. ArXiv 0907.2610.

[54] A. M. Hillas. Differences between gamma-ray and hadronic showers. *Space Sci. Rev.*, 75:17–30, 1996. doi: 10.1007/BF00195021.

[55] A. M. Hillas. Cerenkov light images of EAS produced by primary gamma. *International Cosmic Ray Conference*, 3, August 1985.

[56] M. P. Kertzman and G. H. Sembroski. Computer simulation methods for investigating the detection characteristics of TeV air Cherenkov telescopes. *Nuclear Instruments and Methods in Physics Research A*, 343:629–643, April 1994. doi: 10.1016/0168-9002(94)90247-X.

[57] J. Guy. Thèse de doctorat - Premiers résultats de l'expérience HESS et étude dupotentiel de détection de matière noire supersymétrique. Master's thesis, Université Pierre et Marie Currie„ Paris IV, 2003. URL https://tel.archives-ouvertes.fr/file/index/docid/45622/filename/tel-00003488.pdf.

[58] M. Seglar-Arroyo and F. Schüssler. Gravitational wave alert follow-up strategy in the H.E.S.S. multi-messenger framework. In *Proceedings, 52nd Rencontres de Moriond on Very High Energy Phenomena in the Universe: La Thuile, Italy, March 18-25, 2017*, pages 175–182, 2017. ArXiv 1705.10138.

[59] R. Chalme-Calvet et al. Muon efficiency of the H.E.S.S. telescope. In *International Workshop on Atmospheric Monitoring for High-Energy Astroparticle Detectors (AtmoHEAD 2013) Gif-sur-Yvette, France, June 10-12, 2013*, 2014. ArXiv 1403.4550.

[60] W. Benbow. The Status and Performance of H.E.S.S. In F. A. Aharonian, H. J. Völk, and D. Horns, editors, *High Energy Gamma-Ray Astronomy*, volume 745 of *American Institute of Physics Conference Series*, pages 611–616, February 2005. doi: 10.1063/1.1878471.

[61] D. Berge et al. Background Modelling in Very-High-Energy gamma-ray Astronomy. *Astron. Astrophys.*, 466:1219–1229, 2007. doi: 10.1051/0004-6361:20066674.

[62] S. Christian and the H.E.S.S. collaboration.

[63] M. Holler et al. Photon Reconstruction for H.E.S.S. Using a Semi-Analytical Model. *PoS*, ICRC2015:980, 2016. doi: 10.22323/1.236.0980. ArXiv 1509.02896.

[64] MeerKAT radio telescope inaugurated in South Africa – reveals clearest view yet of centre of the Milky Way. http://www.ska.ac.za/media-releases/meerkat-radio-telescope-inaugurated-in-south-africa-reveals-clearest-view-yet-of-center-of-the-milky-

[65] Spitzer View of the Center of the Milky Way. http://www.spitzer.caltech.edu/images/1541-ssc2006-02a1-Spitzer-View-of-the-Center-of-the-Milky-Way.

[66] Chandra X-ray Observatory - Galactic Center: New Vista of Milky Way Center Unveiled. http://chandra.harvard.edu/photo/2009/gcenter/.

[67] F. K. Baganoff et al. Chandra X-Ray Spectroscopic Imaging of Sagittarius A* and the Central Parsec of the Galaxy. *Astrophys. J.*, 591:891–915, July 2003. doi: 10.1086/375145.

[68] F. Aharonian et al. Discovery of very-high-energy gamma-rays from the galactic centre ridge. *Nature*, 439:695–698, 2006. doi: 10.1038/nature04467.

[69] H. Boyce et al. Simultaneous X-ray and Infrared Observations of Sagittarius A*'s Variability. *Astrophys. J.*, 871(2):161, 2019. doi: 10.3847/1538-4357/aaf71f. ArXiv 1812.05764.

[70] F. Aharonian. Spectrum and variability of the Galactic Center VHE gamma-ray source HESS J1745-290. *Astron. Astrophys.*, 503:817, 2009. doi: 10.1051/0004-6361/200811569. ArXiv 0906.1247.

[71] S.-M. Liu et al. Stochastic acceleration in the galactic center hess source. *Astrophys. J.*, 647:1099–1105, 2006. doi: 10.1086/505171.

[72] H. Abdalla et al. Characterising the VHE diffuse emission in the central 200 parsecs of our Galaxy with H.E.S.S. *Astron. Astrophys.*, 612:A9, 2018. doi: 10.1051/0004-6361/201730824. ArXiv 1706.04535.

[73] Q. D. Wang et al. X-ray thread G0.13-0.11: a Pulsar wind nebula? *Astrophys. J.*, 581:1148–1153, 2002. doi: 10.1086/344401.

[74] F. Aharonian et al. Very high energy gamma rays from the composite SNR G0.9+0.1. *Astron. Astrophys.*, 432:L25–L29, 2005. doi: 10.1051/0004-6361:200500022.

[75] D. J. Helfand and R. H. Becker. G0.9 + 0.1 and the emerging class of composite supernova remnants. *Astrophys. J.*, 314:203–214, March 1987. doi: 10.1086/165050.

[76] S. Mereghetti et al. Discovery of X-rays from the composite supernova remnant G0.9+0.1 with the BeppoSAX satellite. *Astron. Astrophys.*, 331:L77, 1998.

[77] F. Aharonian. Exploring a SNR/Molecular Cloud Association Within HESS J1745-303. *Astron. Astrophys.*, 483:509–517, 2008. doi: 10.1051/0004-6361:20079230. ArXiv 0803.2844.

[78] T. Ohnishi et al. X-Ray Spectrum of a Peculiar Supernova Remnant G359.1-0.5. *Publ. Astron. Soc. Jap.*, 63:527, 2011. doi: 10.1093/pasj/63.3.527. ArXiv 1103.0348.

[79] M. Bitran and others. A large scale CO survey of the Galactic center region. *Astron. Astrophys. Suppl. Ser.*, 125:99–138, October 1997. doi: 10.1051/aas:1997214.

[80] S. Funk et al. The GeV-TeV Connection in Galactic gamma-ray Sources. *Astrophys. J.*, 679:1299–1314, 2008. doi: 10.1086/587129. ArXiv 0710.1584.

[81] H. Abdalla et al. The H.E.S.S. Galactic plane survey. *Astron. Astrophys.*, 612:A1, 2018. doi: 10.1051/0004-6361/201732098. ArXiv 1804.02432.

[82] M. Morris and E. Serabyn. The Galactic Center Environment. *Annual Review of Astronomy and Astrophysics*, 34:645–702, 1996. doi: 10.1146/annurev.astro.34.1.645.

[83] A. W. Strong et al. Cosmic-ray propagation and interactions in the Galaxy. *Ann. Rev. Nucl. Part. Sci.*, 57:285–327, 2007. doi: 10.1146/annurev.nucl.57.090506.123011.

[84] M. Ackermann et al. Fermi-LAT Observations of the Diffuse Gamma-Ray Emission: Implications for Cosmic Rays and the Interstellar Medium. *Astrophys. J.*, 750:3, 2012. doi: 10.1088/0004-637X/750/1/3. ArXiv 1202.4039.

[85] doi: 10.1086/589615.

[86] A. E. Vladimirov and others. GALPROP WebRun: An internet-based service for calculating galactic cosmic ray propagation and associated photon emissions. *Computer Physics Communications*, 182:1156–1161, May 2011. doi: 10.1016/j.cpc.2011.01.017. ArXiv 1008.3642.

[87] I. V. Moskalenko and A. W. Strong. Production and propagation of cosmic ray positrons and electrons. *Astrophys. J.*, 493:694–707, 1998. doi: 10.1086/305152.

[88] doi: 10.1086/306470.

[89] M. Ackermann et al. The Fermi Galactic Center GeV Excess and Implications for Dark Matter. *Astrophys. J.*, 840(1):43, 2017. doi: 10.3847/1538-4357/aa6cab. ArXiv 1704.03910.

[90] M. Ackermann et al. The Spectrum and Morphology of the *Fermi* Bubbles. *Astrophys. J.*, 793(1):64, 2014. doi: 10.1088/0004-637X/793/1/64. ArXiv 1407.7905.

[91] J. F. Navarro and others. A Universal Density Profile from Hierarchical Clustering. *The Astrophysical Journal*, 490:493–508, December 1997. doi: 10.1086/304888.

[92] L. Goodenough and D. Hooper. Possible Evidence For Dark Matter Annihilation In The Inner Milky Way From The Fermi Gamma Ray Space Telescope. 2009. ArXiv 0910.2998.

[93] doi: 10.1088/1742-6596/718/4/042010.

[94] T. Daylan et al. The characterization of the gamma-ray signal from the central Milky Way: A case for annihilating dark matter. *Phys. Dark Univ.*, 12:1–23, 2016. doi: 10.1016/j.dark.2015.12.005. ArXiv 1402.6703.

[95] M. Ackermann et al. Updated search for spectral lines from Galactic dark matter interactions with pass 8 data from the Fermi Large Area Telescope. *Phys. Rev.*, D91 (12):122002, 2015. doi: 10.1103/PhysRevD.91.122002. ArXiv 1506.00013.

[96] M. Ajello et al. Fermi-LAT Observations of High-Energy γ-Ray Emission Toward the Galactic Center. *Astrophys. J.*, 819(1):44, 2016. doi: 10.3847/0004-637X/819/1/44. ArXiv 1511.02938.

[97] M. Ajello et al. Characterizing the population of pulsars in the inner Galaxy with the Fermi Large Area Telescope. *Submitted to: Astrophys. J.*, 2017. ArXiv 1705.00009.

[98] A. R. Bell et al. Cosmic ray acceleration and escape from supernova remnants. *Mon. Not. Roy. Astron. Soc.*, 431:415, 2013. doi: 10.1093/mnras/stt179. ArXiv 1301.7264.

[99] M. Su et al. Giant Gamma-ray Bubbles from Fermi-LAT: AGN Activity or Bipolar Galactic Wind? *Astrophys. J.*, 724:1044–1082, 2010. doi: 10.1088/0004-637X/724/2/1044. ArXiv 1005.5480.

[100] Y. Sofue and T. Handa. A radio lobe over the galactic centre. *Nature*, 310:568, August 1984. doi: 10.1038/310568a0.

[101] C. J. Law et al. GBT Multiwavelength Survey of the Galactic Center Region. *Astrophys. J. Suppl.*, 177:255, 2008. doi: 10.1086/533587. ArXiv 0801.4294.

[102] F. K. Baganoff et al. Chandra x-ray spectroscopic imaging of Sgr A* and the central parsec of the Galaxy. *Astrophys. J.*, 591:891–915, 2003. doi: 10.1086/375145.

[103] G. Ponti et al. The Galactic Centre Chimney. 2019. doi: 10.1038/s41586-019-1009-6. [Nature567,347(2019)].

[104] C. Guépin et al. Pevatron at the Galactic Center: Multi-Wavelength Signatures from Millisecond Pulsars. *JCAP*, 1807(07):042, 2018. doi: 10.1088/1475-7516/2018/07/042. ArXiv 1806.03307.

[105] F. Acero et al. Development of the Model of Galactic Interstellar Emission for Standard Point-Source Analysis of Fermi Large Area Telescope Data. *Astrophys. J. Suppl.*, 223 (2):26, 2016. doi: 10.3847/0067-0049/223/2/26. ArXiv 1602.07246.

[106] O. K. Thielheim. Pulsars as Cosmic Ray Accelerators -The Modified Acceleration Boundary. *International Cosmic Ray Conference*, 4:23, 1990.

[107] D. R. Lorimer. The Galactic Millisecond Pulsar Population. *IAU Symp.*, 291:237–242, 2013. doi: 10.1017/S1743921312023769. ArXiv 1210.2746.

[108] F. Calore et al. Radio detection prospects for a bulge population of millisecond pulsars as suggested by Fermi LAT observations of the inner Galaxy. *Astrophys. J.*, 827(2): 143, 2016. doi: 10.3847/0004-637X/827/2/143. ArXiv 1512.06825.

[109] D. Hooper et al. TeV Gamma Rays From Galactic Center Pulsars. *Phys. Dark Univ.*, 21:40–46, 2018. doi: 10.1016/j.dark.2018.05.004. ArXiv 1705.09293.

[110] P. Blasi and E. Amato. Diffusive propagation of cosmic rays from supernova remnants in the Galaxy. I: spectrum and chemical composition. *JCAP*, 1201:010, 2012. doi: 10.1088/1475-7516/2012/01/010. ArXiv 1105.4521.

[111] D. R. Lorimer et al. The Parkes multibeam pulsar survey – VII. Timing of four millisecond pulsars and the underlying spin-period distribution of the Galactic millisecond pulsar population. *Mon. Not. Roy. Astron. Soc.*, 450(2):2185–2194, 2015. doi: 10.1093/mnras/stv804. ArXiv 1501.05516.

[112] S. A. Story et al. Population synthesis of radio and gamma-ray millisecond pulsars from the Galactic disk. *Astrophys. J.*, 671:713–726, 2007. doi: 10.1086/521016. ArXiv 0706.3041.

[113] D. R. Lorimer. Binary and Millisecond Pulsars. *Living Rev. Rel.*, 11:8, 2008. doi: 10.12942/lrr-2008-8. ArXiv 0811.0762.

[114] A. Kolmogorov. The Local Structure of Turbulence in Incompressible Viscous Fluid for Very Large Reynolds' Numbers. *Akademiia Nauk SSSR Doklady*, 30:301–305, 1941.

[115] D. R. Lorimer. The galactic population and birth rate of radio pulsars. 2003. [IAU Symp.218,105(2004)].

[116] F. Calore et al. Diffuse gamma-ray emission from galactic pulsars. *Astrophys. J.*, 796: 1, 2014. doi: 10.1088/0004-637X/796/1/14. ArXiv 1406.2706.

[117] H. Ploeg et al. Consistency Between the Luminosity Function of Resolved Millisecond Pulsars and the Galactic Center Excess. *JCAP*, 1708(08):015, 2017. doi: 10.1088/1475-7516/2017/08/015. ArXiv 1705.00806.

[118] D. Hooper and T. Linden. Millisecond Pulsars, TeV Halos, and Implications For The Galactic Center Gamma-Ray Excess. *Phys. Rev.*, D98(4):043005, 2018. doi: 10.1103/PhysRevD.98.043005. ArXiv 1803.08046.

[119] Q. Yuan and K. Ioka. Testing the millisecond pulsar scenario of the Galactic center gamma-ray excess with very high energy gamma-rays. *Astrophys. J.*, 802(2):124, 2015. doi: 10.1088/0004-637X/802/2/124. ArXiv 1411.4363.

[120] M. Dainotti et al. GRB 060218 and GRBs associated with Supernovae Ib/c. *Astron. Astrophys.*, 471:L29–L32, 2007. doi: 10.1051/0004-6361:20078068. ArXiv 0706.3209.

[121] A. U. Abeysekara et al. Extended gamma-ray sources around pulsars constrain the origin of the positron flux at Earth. *Science*, 358(6365):911–914, 2017. doi: 10.1126/science.aan4880. ArXiv 1711.06223.

[122] E. Carlson et al. Cosmic-Ray Injection from Star-Forming Regions. *Phys. Rev. Lett.*, 117(11):111101, 2016. doi: 10.1103/PhysRevLett.117.111101. ArXiv 1510.04698.

[123] R. Braun et al. Advancing Astrophysics with the Square Kilometre Array. *PoS*, AASKA14:174, 2015. doi: 10.22323/1.215.0174.

[124] H. Abdalla et al. H.E.S.S. Limits on Linelike Dark Matter Signatures in the 100 GeV to 2 TeV Energy Range Close to the Galactic Center. *Phys. Rev. Lett.*, 117(15): 151302, 2016. doi: 10.1103/PhysRevLett.117.151302. ArXiv 1609.08091.

[125] M. Su and D. P. Finkbeiner. Strong Evidence for Gamma-ray Line Emission from the Inner Galaxy. 2012. ArXiv 1206.1616.

[126] M. Tsuboi and others. Dense Molecular Clouds in the Galactic Center Region. I. Observations and Data. *Astrophys. J.*, 120:1–39, January 1999. doi: 10.1086/313165.

[127] R. Parsons et al. Sgr A* Observations with H.E.S.S. II. *PoS*, ICRC2015:830, 2016. doi: 10.22323/1.236.0830. [34,830(2015)].

[128] F. Zwicky. On the Masses of Nebulae and of Clusters of Nebulae. *Astrophysical Journal*, 86:217, October 1937. doi: 10.1086/143864.

[129] V. C. Rubin and W. K. Ford, Jr. Rotation of the Andromeda Nebula from a Spectroscopic Survey of Emission Regions. *Astrophysical Journal*, 159:379, February 1970. doi: 10.1086/150317.

[130] T. S. van Albada and others. Distribution of dark matter in the spiral galaxy NGC 3198. *Astrophys. J.*, 295:305–313, August 1985. doi: 10.1086/163375.

[131] R. Massey et al. The dark matter of gravitational lensing. *Rept. Prog. Phys.*, 73: 086901, 2010. doi: 10.1088/0034-4885/73/8/086901. ArXiv 1001.1739.

[132] New Hubble image of galaxy cluster Abell 1689. https://www.spacetelescope.org/news/heic1317/.

[133] M. Markevitch. Chandra observation of the most interesting cluster in the universe. 2005. [ESA Spec. Publ.604,723(2006)].

[134] D. Clowe et al. A direct empirical proof of the existence of dark matter. *Astrophys. J.*, 648:L109–L113, 2006. doi: 10.1086/508162.

[135] M. Markevitch et al. Direct constraints on the dark matter self-interaction cross-section from the merging galaxy cluster 1E0657-56. *Astrophys. J.*, 606:819–824, 2004. doi: 10.1086/383178.

[136] A. Friedman. Über die krümmung des raumes. *Zeitschrift für Physik*, 10(1):377–386, Dec 1922. ISSN 0044-3328. doi: 10.1007/BF01332580.

[137] G. Lemaître. Un Univers homogène de masse constante et de rayon croissant rendant compte de la vitesse radiale des nébuleuses extra-galactiques. *Annales de la Société Scientifique de Bruxelles*, 47:49–59, 1927.

[138] H. P. Robertson. Kinematics and World-Structure III. *Astrophysical Journal*, 83:257, May 1936. doi: 10.1086/143726.

[139] W. O. Kermack and W. H. McCrea. On Milne's theory of world structure. *MNRAS*, 93:519–529, May 1933. doi: 10.1093/mnras/93.7.519.

[140] P. J. E. Peebles. *The large-scale structure of the universe*. 1980.

[141] G. Bertone et al. Particle dark matter: Evidence, candidates and constraints. *Phys. Rept.*, 405:279–390, 2005. doi: 10.1016/j.physrep.2004.08.031.

[142] A. Einstein. The Foundation of the General Theory of Relativity. *Annalen Phys.*, 49 (7):769–822, 1916. doi: 10.1002/andp.200590044,10.1002/andp.19163540702. [Annalen Phys.354,no.7,769(1916)].

[143] N. Aghanim et al. Planck 2018 results. VI. Cosmological parameters. 2018. ArXiv 1807.06209.

[144] A. A. Penzias and R. W. Wilson. A Measurement of Excess Antenna Temperature at 4080 Mc/s. *Astrophysical Journal*, 142:419–421, July 1965. doi: 10.1086/148307.

[145] P. J. E. Peebles. Penzias and Wilson's Discovery of the Cosmic Microwave Background. *Astrophysical Journal*, 525:1067, November 1999.

[146] G. F. Smoot and others. Structure in the COBE differential microwave radiometer first-year maps. *Astrophysical Journal*, 396:L1–L5, September 1992. doi: 10.1086/186504.

[147] B. A. Bassett and R. Hlozek. Baryon Acoustic Oscillations. 2009. ArXiv 0910.5224.

[148] Alexei A. Starobinsky. A New Type of Isotropic Cosmological Models Without Singularity. *Phys. Lett.*, B91:99–102, 1980. doi: 10.1016/0370-2693(80)90670-X. [,771(1980)].

[149] A. Coc and E. Vangioni. Primordial nucleosynthesis. *Int. J. Mod. Phys.*, E26(08): 1741002, 2017. doi: 10.1142/S0218301317410026. ArXiv 1707.01004.

[150] J. R. Primack. Dark matter and structure formation. In *Midrasha Mathematicae in Jerusalem: Winter School in Dynamical Systems Jerusalem, Israel, January 12-17, 1997*, 1997.

[151] M. Colless et al. The 2dF Galaxy Redshift Survey: Spectra and redshifts. *Mon. Not. Roy. Astron. Soc.*, 328:1039, 2001. doi: 10.1046/j.1365-8711.2001.04902.x.

[152] D. G. York et al. The Sloan Digital Sky Survey: Technical Summary. *Astron. J.*, 120: 1579–1587, 2000. doi: 10.1086/301513.

[153] V. Springel et al. The large-scale structure of the Universe. *Nature*, 440:1137, 2006. doi: 10.1038/nature04805.

[154] Formation of the large-scale structure in the Universe: filaments. http://cosmicweb.uchicago.edu/filaments.html.

[155] V. Springel and others. Simulations of the formation, evolution and clustering of galaxies and quasars. *Nature*, 435:629–636, June 2005. doi: 10.1038/nature03597.

[156] L. Bergstrom. Nonbaryonic dark matter: Observational evidence and detection methods. *Rept. Prog. Phys.*, 63:793, 2000. doi: 10.1088/0034-4885/63/5/2r3.

[157] G. Jungman et al. Supersymmetric dark matter. *Phys. Rept.*, 267:195–373, 1996. doi: 10.1016/0370-1573(95)00058-5.

[158] D. P. Bennett et al. The MACHO project dark matter search. *ASP Conf. Ser.*, 88:95, 1996.

[159] Y. B. Zel'dovich and I. D. Novikov. The Hypothesis of Cores Retarded during Expansion and the Hot Cosmological Model. *Soviet Astronomy*, 10:602, February 1967.

[160] P. Tisserand et al. Limits on the Macho Content of the Galactic Halo from the EROS-2 Survey of the Magellanic Clouds. *Astron. Astrophys.*, 469:387–404, 2007. doi: 10.1051/0004-6361:20066017.

[161] B. Carr. Primordial black holes as dark matter and generators of cosmic structure. In *Symposium on Illuminating Dark Matter Kruen, Germany, May 13-19, 2018*, 2019. ArXiv 1901.07803.

[162] S. Bird et al. Did LIGO detect dark matter? *Phys. Rev. Lett.*, 116(20):201301, 2016. doi: 10.1103/PhysRevLett.116.201301. ArXiv 1603.00464.

[163] J. R. Primack and M. A. K. Gross. Hot dark matter in cosmology. pages 287–308, 2000.

[164] R. N. Mohapatra et al. Theory of neutrinos: A White paper. *Rept. Prog. Phys.*, 70: 1757–1867, 2007. doi: 10.1088/0034-4885/70/11/R02.

[165] M. Gell-Mann et al. Complex Spinors and Unified Theories. *Conf. Proc.*, C790927: 315–321, 1979. ArXiv 1306.4669.

[166] A. Merle. keV Neutrino Model Building. *Int. J. Mod. Phys.*, D22:1330020, 2013. doi: 10.1142/S0218271813300206. ArXiv 1302.2625.

[167] A. D. Dolgov and S. H. Hansen. Massive sterile neutrinos as warm dark matter. *Astropart. Phys.*, 16:339–344, 2002. doi: 10.1016/S0927-6505(01)00115-3.

[168] S. Dodelson and L. M. Widrow. Sterile-neutrinos as dark matter. *Phys. Rev. Lett.*, 72:17–20, 1994. doi: 10.1103/PhysRevLett.72.17.

[169] R. D. Peccei and H. R. Quinn. CP Conservation in the Presence of Instantons. *Phys. Rev. Lett.*, 38:1440–1443, 1977. doi: 10.1103/PhysRevLett.38.1440. [,328(1977)].

[170] L. D. Duffy and K. van Bibber. Axions as Dark Matter Particles. *New J. Phys.*, 11: 105008, 2009. doi: 10.1088/1367-2630/11/10/105008. ArXiv 0904.3346.

[171] R. Essig et al. Working Group Report: New Light Weakly Coupled Particles. In *Proceedings, 2013 Community Summer Study on the Future of U.S. Particle Physics: Snowmass on the Mississippi (CSS2013): Minneapolis, MN, USA, July 29-August 6, 2013*.

[172] H. P. Nilles. Supersymmetry, Supergravity and Particle Physics. *Phys. Rept.*, 110: 1–162, 1984. doi: 10.1016/0370-1573(84)90008-5.

[173] J. Fan and M. Reece. In Wino Veritas? Indirect Searches Shed Light on Neutralino Dark Matter. *JHEP*, 10:124, 2013. doi: 10.1007/JHEP10(2013)124. ArXiv 1307.4400.

[174] J. Hisano et al. Non-perturbative effect on thermal relic abundance of dark matter. *Phys. Lett.*, B646:34–38, 2007. doi: 10.1016/j.physletb.2007.01.012.

[175] Th. Kaluza. Zum Unitätsproblem der Physik. *Sitzungsber. Preuss. Akad. Wiss. Berlin (Math. Phys.)*, 1921:966–972, 1921. doi: 10.1142/S0218271818700017. [Int. J. Mod. Phys.D27,no.14,1870001(2018)].

[176] E. W. Kolb and R. Slansky. Dimensional Reduction in the Early Universe: Where Have the Massive Particles Gone? *Phys. Lett.*, 135B:378, 1984. doi: 10.1016/0370-2693(84)90298-3.

[177] P. Salucci. The mass distribution in spiral galaxies. *IAU Symp.*, 244:53–62, 2008. doi: 10.1017/S174392130701383X. ArXiv 0707.4370.

[178] J. S. Bullock. Notes on the Missing Satellites Problem. 2010. ArXiv 1009.4505.

[179] M. Milgrom. A Modification of the Newtonian dynamics as a possible alternative to the hidden mass hypothesis. *Astrophys. J.*, 270:365–370, 1983. doi: 10.1086/161130.

[180] S. Boran et al. GW170817 Falsifies Dark Matter Emulators. *Phys. Rev.*, D97(4): 041501, 2018. doi: 10.1103/PhysRevD.97.041501. ArXiv 1710.06168.

[181] J. D. Lewin and P. F. Smith. Review of mathematics, numerical factors, and corrections for dark matter experiments based on elastic nuclear recoil. *Astropart. Phys.*, 6:87–112, 1996. doi: 10.1016/S0927-6505(96)00047-3.

[182] M. Tanabashi et al. Review of Particle Physics. *Phys. Rev.*, D98(3):030001, 2018. doi: 10.1103/PhysRevD.98.030001.

[183] R. Bernabei et al. First Model Independent Results from DAMA/LIBRA–Phase2. *Universe*, 4(11):116, 2018. doi: 10.3390/universe4110116,10.15407/jnpae2018.04.307. [Nucl. Phys. Atom. Energy19,no.4,307(2018)].

[184] C. Bœhm et al. How high is the neutrino floor? *JCAP*, 1901:043, 2019. doi: 10.1088/1475-7516/2019/01/043. ArXiv 1809.06385.

[185] P. Fox et al. Missing Energy Signatures of Dark Matter at the LHC. *Phys. Rev.*, D85: 056011, 2012. doi: 10.1103/PhysRevD.85.056011. ArXiv 1109.4398.

[186] S. Liem et al. Effective field theory of dark matter: a global analysis. *JHEP*, 09:077, 2016. doi: 10.1007/JHEP09(2016)077. ArXiv 1603.05994.

[187] J. Abdallah et al. Simplified Models for Dark Matter Searches at the LHC. *Phys. Dark Univ.*, 9-10:8–23, 2015. doi: 10.1016/j.dark.2015.08.001. ArXiv 1506.03116.

[188] A. Boveia and C. Doglioni. Dark Matter Searches at Colliders. *Ann. Rev. Nucl. Part. Sci.*, 68:429–459, 2018. doi: 10.1146/annurev-nucl-101917-021008. ArXiv 1810.12238.

[189] M. G. Aartsen et al. Search for annihilating dark matter in the Sun with 3 years of IceCube data. *Eur. Phys. J.*, C77(3):146, 2017. doi: 10.1140/epjc/s10052-019-6702-y, 10.1140/epjc/s10052-017-4689-9. [Erratum: Eur. Phys. J.C79,no.3,214(2019)].

[190] S. Adrian-Martinez et al. Limits on Dark Matter Annihilation in the Sun using the ANTARES Neutrino Telescope. *Phys. Lett.*, B759:69–74, 2016. doi: 10.1016/j.physletb.2016.05.019. ArXiv 1603.02228.

[191] J. Conrad and O. Reimer. Indirect dark matter searches in gamma and cosmic rays. *Nature Phys.*, 13(3):224–231, 2017. doi: 10.1038/nphys4049. ArXiv 1705.11165.

[192] O. Adriani et al. An anomalous positron abundance in cosmic rays with energies 1.5-100 GeV. *Nature*, 458:607–609, 2009. doi: 10.1038/nature07942. ArXiv 0810.4995.

[193] M. Aguilar et al. First Result from the Alpha Magnetic Spectrometer on the International Space Station: Precision Measurement of the Positron Fraction in Primary Cosmic Rays of 0.5–350 GeV. *Phys. Rev. Lett.*, 110:141102, 2013. doi: 10.1103/PhysRevLett.110.141102.

[194] S. Profumo and T. E. Jeltema. Extragalactic Inverse Compton Light from Dark Matter Annihilation and the Pamela Positron Excess. *JCAP*, 0907:020, 2009. doi: 10.1088/1475-7516/2009/07/020. ArXiv 0906.0001.

[195] P. D. Serpico. Astrophysical models for the origin of the positron 'excess'. *Astropart. Phys.*, 39-40:2–11, 2012. doi: 10.1016/j.astropartphys.2011.08.007. ArXiv 1108.4827.

[196] A. Cuoco et al. Novel Dark Matter Constraints from Antiprotons in Light of AMS-02. *Phys. Rev. Lett.*, 118(19):191102, 2017. doi: 10.1103/PhysRevLett.118.191102. ArXiv 1610.03071.

[197] M. et al. Meyer. Future constraints of dark matter effective field theories and simplified models with the Cherenkov Telescope Array. https://indico.cern.ch/event/623880/contributions/2523949/attachments/1438677/2213569/mmeyer_cta_eft.pdf.

[198] CMS Collaboration. Search for dark matter in final states with an energetic jet, or a hadronically decaying W or Z boson using 12.9 fb^{-1} of data at $\sqrt{s} = 13$ TeV. 2016.

[199] D. S. Akerib et al. Results from a search for dark matter in the complete LUX exposure. *Phys. Rev. Lett.*, 118(2):021303, 2017. doi: 10.1103/PhysRevLett.118.021303. ArXiv 1608.07648.

[200] E. Aprile et al. XENON100 Dark Matter Results from a Combination of 477 Live Days. *Phys. Rev.*, D94(12):122001, 2016. doi: 10.1103/PhysRevD.94.122001. ArXiv 1609.06154.

[201] Georges Aad et al. Search for new phenomena in final states with an energetic jet and large missing transverse momentum in pp collisions at $\sqrt{s}$ =8 TeV with the ATLAS detector. *Eur. Phys. J.*, C75(7):299, 2015. doi: 10.1140/epjc/s10052-015-3517-3,10.1140/epjc/s10052-015-3639-7. [Erratum: Eur. Phys. J.C75,no.9,408(2015)].

[202] J. Einasto. On the Construction of a Composite Model for the Galaxy and on the Determination of the System of Galactic Parameters. *Trudy Astrofizicheskogo Instituta Alma-Ata*, 5:87–100, 1965.

[203] A. Burkert. The Structure of dark matter halos in dwarf galaxies. *IAU Symp.*, 171: 175, 1996. doi: 10.1086/309560. [Astrophys. J.447,L25(1995)].

[204] J. Binney and S. Tremaine. *Galactic Dynamics: Second Edition*. Princeton University Press, 2008.

[205] A. R. Duffy et al. Impact of baryon physics on dark matter structures: a detailed simulation study of halo density profiles. *Mon. Not. Roy. Astron. Soc.*, 405:2161, 2010. doi: 10.1111/j.1365-2966.2010.16613.x. ArXiv 1001.3447.

[206] J. Penarrubia et al. The Tidal Evolution of Local Group Dwarf Spheroidals. *Astrophys. J.*, 673:226, 2008. doi: 10.1086/523686. ArXiv 0708.3087.

[207] L. Pieri et al. Implications of High-Resolution Simulations on Indirect Dark Matter Searches. *Phys. Rev.*, D83:023518, 2011. doi: 10.1103/PhysRevD.83.023518. ArXiv 0908.0195.

[208] M. Cirelli et al. PPPC 4 DM ID: A Poor Particle Physicist Cookbook for Dark Matter Indirect Detection. *JCAP*, 1103:051, 2011. doi: 10.1088/1475-7516/2012/10/E01,10.1088/1475-7516/2011/03/051. [Erratum: JCAP1210,E01(2012)].

[209] F. Nesti and P. Salucci. The Dark Matter halo of the Milky Way, AD 2013. *JCAP*, 1307:016, 2013. doi: 10.1088/1475-7516/2013/07/016. ArXiv 1304.5127.

[210] T. Lacroix et al. Connecting the new H.E.S.S. diffuse emission at the Galactic Center with the Fermi GeV excess: A combination of millisecond pulsars and heavy dark matter? *Phys. Rev.*, D94(12):123008, 2016. doi: 10.1103/PhysRevD.94.123008. ArXiv 1603.05977.

[211] J. A. R. Cembranos et al. Spectral Study of the HESS J1745-290 Gamma-Ray Source as Dark Matter Signal. *JCAP*, 1304:051, 2013. doi: 10.1088/1475-7516/2013/04/051. ArXiv 1302.6871.

[212] O. Newton et al. The total satellite population of the Milky Way. *Mon. Not. Roy. Astron. Soc.*, 479(3):2853–2870, 2018. doi: 10.1093/mnras/sty1085. ArXiv 1708.04247.

[213] doi: 10.1088/2041-8205/795/1/l13.

[214] T. E. Jeltema et al. Gamma Rays from Clusters and Groups of Galaxies: Cosmic Rays versus Dark Matter. *Phys. Rev.*, D80:023005, 2009. doi: 10.1103/PhysRevD.80.023005. ArXiv 0812.0597.

[215] V. A. Acciari et al. Constraining Dark Matter lifetime with a deep gamma-ray survey of the Perseus Galaxy Cluster with MAGIC. *Phys. Dark Univ.*, 22:38–47, 2018. doi: 10.1016/j.dark.2018.08.002. ArXiv 1806.11063.

[216] doi: 10.1088/1475-7516/2012/11/050.

[217] S. Profumo. Hunting the lightest lightest neutralinos. *Phys. Rev.*, D78:023507, 2008. doi: 10.1103/PhysRevD.78.023507. ArXiv 0806.2150.

[218] L. Bergstrom and P. Ullio. Full one loop calculation of neutralino annihilation into two photons. *Nucl. Phys.*, B504:27–44, 1997. doi: 10.1016/S0550-3213(97)00530-0.

[219] M. Cirelli and P. Panci. Inverse Compton constraints on the Dark Matter e+e- excesses. *Nucl. Phys.*, B821:399–416, 2009. doi: 10.1016/j.nuclphysb.2009.06.034. ArXiv 0904.3830.

[220] Á. Moliné et al. Characterization of subhalo structural properties and implications for dark matter annihilation signals. *Mon. Not. Roy. Astron. Soc.*, 466(4):4974–4990, 2017. doi: 10.1093/mnras/stx026. ArXiv 1603.04057.

[221] A. Charbonnier et al. Dark matter profiles and annihilation in dwarf spheroidal galaxies: prospectives for present and future gamma-ray observatories - I. The classical dSphs. *Mon. Not. Roy. Astron. Soc.*, 418:1526–1556, 2011. doi: 10.1111/j.1365-2966.2011.19387.x. ArXiv 1104.0412.

[222] P. Ciafaloni et al. On the Importance of Electroweak Corrections for Majorana Dark Matter Indirect Detection. *JCAP*, 1106:018, 2011. doi: 10.1088/1475-7516/2011/06/018. ArXiv 1104.2996.

[223] A. Sommerfeld. Über die Beugung und Bremsung der Elektronen. *Annalen der Physik*, 403:257–330, 1931. doi: 10.1002/andp.19314030302.

[224] M. Lattanzi and J. I. Silk. Can the WIMP annihilation boost factor be boosted by the Sommerfeld enhancement? *Phys. Rev.*, D79:083523, 2009. doi: 10.1103/PhysRevD.79.083523. ArXiv 0812.0360.

[225] G. Cowan et al. Asymptotic formulae for likelihood-based tests of new physics. *Eur. Phys. J.*, C71:1554, 2011. doi: 10.1140/epjc/s10052-011-1554-0,10.1140/epjc/s10052-013-2501-z. [Erratum: Eur. Phys. J.C73,2501(2013)].

[226] T. P. Li and Y. Q. Ma. Analysis methods for results in gamma-ray astronomy. *Astrophys. J.*, 272:317–324, 1983. doi: 10.1086/161295.

[227] H. Silverwood et al. A realistic assessment of the CTA sensitivity to dark matter annihilation. *JCAP*, 1503(03):055, 2015. doi: 10.1088/1475-7516/2015/03/055. ArXiv 1408.4131.

[228] H. Abdallah et al. Search for γ-Ray Line Signals from Dark Matter Annihilations in the Inner Galactic Halo from 10 Years of Observations with H.E.S.S. *Phys. Rev. Lett.*, 120(20):201101, 2018. doi: 10.1103/PhysRevLett.120.201101. ArXiv 1805.05741.

[229] M. Holler et al. Run-Wise Simulations for Imaging Atmospheric Cherenkov Telescope Arrays. *PoS*, ICRC2017:755, 2018. doi: 10.22323/1.301.0755. ArXiv 1711.01118.

[230] L. Bergstrom et al. Observability of gamma-rays from dark matter neutralino annihilations in the Milky Way halo. *Astropart. Phys.*, 9:137–162, 1998. doi: 10.1016/S0927-6505(98)00015-2.

[231] A. Abramowski et al. Search for Photon-Linelike Signatures from Dark Matter Annihilations with H.E.S.S. *Phys. Rev. Lett.*, 110:041301, 2013. doi: 10.1103/PhysRevLett.110.041301. ArXiv 1301.1173.

[232] J. Aleksić et al. Optimized dark matter searches in deep observations of Segue 1 with MAGIC. *JCAP*, 1402:008, 2014. doi: 10.1088/1475-7516/2014/02/008. ArXiv 1312.1535.

[233] V. Bonnivard et al. Dark matter annihilation and decay in dwarf spheroidal galaxies: The classical and ultrafaint dSphs. *Mon. Not. Roy. Astron. Soc.*, 453(1):849–867, 2015. doi: 10.1093/mnras/stv1601. ArXiv 1504.02048.

[234] S. Archambault et al. Dark Matter Constraints from a Joint Analysis of Dwarf Spheroidal Galaxy Observations with VERITAS. *Phys. Rev.*, D95(8):082001, 2017. doi: 10.1103/PhysRevD.95.082001. ArXiv 1703.04937.

[235] R. Catena and P. Ullio. A novel determination of the local dark matter density. *JCAP*, 1008:004, 2010. doi: 10.1088/1475-7516/2010/08/004. ArXiv 0907.0018.

[236] H. Abdallah et al. Search for dark matter annihilations towards the inner Galactic halo from 10 years of observations with H.E.S.S. *Phys. Rev. Lett.*, 117(11):111301, 2016. doi: 10.1103/PhysRevLett.117.111301. ArXiv 1607.08142.

[237] A. Albert et al. Searching for Dark Matter Annihilation in Recently Discovered Milky Way Satellites with Fermi-LAT. *Astrophys. J.*, 834(2):110, 2017. doi: 10.3847/1538-4357/834/2/110. ArXiv 1611.03184.

[238] A. U. Abeysekara et al. A Search for Dark Matter in the Galactic Halo with HAWC. *JCAP*, 1802(02):049, 2018. doi: 10.1088/1475-7516/2018/02/049. ArXiv 1710.10288.

[239] H. Abdallah et al. Search for dark matter signals towards the recently-detected des dwarf galaxy satellites of the milky way with h.e.s.s.. *Currently under collaboration review*, 2019. Paper draft available on request.

[240] K. Bechtol et al. Eight New Milky Way Companions Discovered in First-Year Dark Energy Survey Data. *Astrophys. J.*, 807(1):50, 2015. doi: 10.1088/0004-637X/807/1/50.

[241] D. Kim and H. Jerjen. Horologium II: a Second Ultra-faint Milky Way Satellite in the Horologium Constellation. *Astrophys. J.*, 808:L39, 2015. doi: 10.1088/2041-8205/808/2/L39. ArXiv 1505.04948.

[242] A. Drlica-Wagner et al. Eight Ultra-faint Galaxy Candidates Discovered in Year Two of the Dark Energy Survey. *Astrophys. J.*, 813(2):109, 2015. doi: 10.1088/0004-637X/813/2/109. ArXiv 1508.03622.

[243] W. E. Harris. A Catalog of Parameters for Globular Clusters in the Milky Way. *Astron. J.*, 112:1487, 1996. doi: 10.1086/118116.

[244] V. Bonnivard et al. Spherical Jeans analysis for dark matter indirect detection in dwarf spheroidal galaxies - Impact of physical parameters and triaxiality. *Mon. Not. Roy. Astron. Soc.*, 446:3002–3021, 2015. doi: 10.1093/mnras/stu2296. ArXiv 1407.7822.

[245] L. E. Strigari. Dark matter in dwarf spheroidal galaxies and indirect detection: a review. *Rept. Prog. Phys.*, 81(5):056901, 2018. doi: 10.1088/1361-6633/aaae16. ArXiv 1805.05883.

[246] V. Lefranc et al. Prospects for annihilating Dark Matter towards Milky Way's dwarf galaxies by the Cherenkov Telescope Array. *JCAP*, 1609(09):021, 2016. doi: 10.1088/1475-7516/2016/09/021. ArXiv 1605.02793.

[247] V. Bonnivard et al. Dark matter annihilation and decay profiles for the Reticulum II dwarf spheroidal galaxy. *Astrophys. J.*, 808(2):L36, 2015. doi: 10.1088/2041-8205/808/2/L36. ArXiv 1504.03309.

[248] Matthew G. Walker et al. Magellan/M2FS spectroscopy of Tucana 2 and Grus 1. *Astrophys. J.*, 819(1):53, 2016. doi: 10.3847/0004-637X/819/1/53. ArXiv 1511.06296.

[249] J. D. Simon et al. Nearest Neighbor: The Low-Mass Milky Way Satellite Tucana III. *Astrophys. J.*, 838(1):11, 2017. doi: 10.3847/1538-4357/aa5be7. ArXiv 1610.05301.

[250] K. Hayashi et al. Dark matter annihilation and decay from non-spherical dark halos in galactic dwarf satellites. *Mon. Not. Roy. Astron. Soc.*, 461(3):2914–2928, 2016. doi: 10.1093/mnras/stw1457. ArXiv 1603.08046.

[251] N. Bernal et al. Systematic uncertainties from halo asphericity in dark matter searches. *JCAP*, 1409:004, 2014. doi: 10.1088/1475-7516/2014/09/004. ArXiv 1405.6240.

[252] V. Bonnivard et al. Contamination of stellar-kinematic samples and uncertainty about dark matter annihilation profiles in ultrafaint dwarf galaxies: the example of Segue I. *Mon. Not. Roy. Astron. Soc.*, 462(1):223–234, 2016. doi: 10.1093/mnras/stw1691. ArXiv 1506.08209.

[253] J. Klimentowski et al. The orientation and kinematics of inner tidal tails around dwarf galaxies orbiting the Milky Way. *Mon. Not. Roy. Astron. Soc.*, 400:2162, 2009. doi: 10.1111/j.1365-2966.2009.15626.x. ArXiv 0908.4022.

[254] N. W. Evans et al. Simple J-Factors and D-Factors for Indirect Dark Matter Detection. *Phys. Rev.*, D93(10):103512, 2016. doi: 10.1103/PhysRevD.93.103512. ArXiv 1604.05599.

[255] A. Abramowski et al. Search for dark matter annihilation signatures in H.E.S.S. observations of Dwarf Spheroidal Galaxies. *Phys. Rev.*, D90:112012, 2014. doi: 10.1103/PhysRevD.90.112012. ArXiv 1410.2589.

[256] M. L. Ahnen et al. Limits to Dark Matter Annihilation Cross-Section from a Combined Analysis of MAGIC and Fermi-LAT Observations of Dwarf Satellite Galaxies. *JCAP*, 1602(02):039, 2016. doi: 10.1088/1475-7516/2016/02/039. ArXiv 1601.06590.

[257] A. Albert et al. Dark Matter Limits From Dwarf Spheroidal Galaxies with The HAWC Gamma-Ray Observatory. *Astrophys. J.*, 853(2):154, 2018. doi: 10.3847/1538-4357/aaa6d8. ArXiv 1706.01277.

[258] L. Rinchiuso et al. Hunting for Heavy Winos in the Galactic Center. *Phys. Rev.*, D98 (12):123014, 2018. doi: 10.1103/PhysRevD.98.123014. ArXiv 1808.04388.

[259] G. F. Giudice et al. Gaugino mass without singlets. *JHEP*, 12:027, 1998. doi: 10.1088/1126-6708/1998/12/027.

[260] L. J. Hall et al. Spread Supersymmetry with Wino LSP: Gluino and Dark Matter Signals. *JHEP*, 01:036, 2013. doi: 10.1007/JHEP01(2013)036. ArXiv 1210.2395.

[261] M. Baumgart et al. Precision Photon Spectra for Wino Annihilation. *JHEP*, 01:036, 2019. doi: 10.1007/JHEP01(2019)036. ArXiv 1808.08956.

[262] M. Baumgart et al. Resummed Photon Spectra for WIMP Annihilation. *JHEP*, 03: 117, 2018. doi: 10.1007/JHEP03(2018)117. ArXiv 1712.07656.

[263] P. Mollitor et al. Baryonic and dark matter distribution in cosmological simulations of spiral galaxies. *Mon. Not. Roy. Astron. Soc.*, 447(2):1353–1369, 2015. doi: 10.1093/mnras/stu2466. ArXiv 1405.4318.

[264] D. Hooper. The Density of Dark Matter in the Galactic Bulge and Implications for Indirect Detection. *Phys. Dark Univ.*, 15:53–56, 2017. doi: 10.1016/j.dark.2016.11.005. ArXiv 1608.00003.

[265] K. Bernlöhr et al. Monte Carlo design studies for the Cherenkov Telescope Array. *Astropart. Phys.*, 43:171–188, 2013. doi: 10.1016/j.astropartphys.2012.10.002. ArXiv 1210.3503.

[266] M. Beneke et al. Relic density of wino-like dark matter in the MSSM. *JHEP*, 03:119, 2016. doi: 10.1007/JHEP03(2016)119. ArXiv 1601.04718.

[267] A. Hryczuk et al. Testing dark matter with Cherenkov light - prospects of H.E.S.S. and CTA for exploring minimal supersymmetry. 2019. Paper draft available on request.

[268] L. Rinchiuso et al. Prospects for heavy wimp dark matter with cta: the wino and higgsino cases. *In preparation for Phys. Rev. D*, 2019. Paper draft available on request.

[269] CTA Performance. https://www.cta-observatory.org/science/cta-performance/.

[270] D. Heck and others. *CORSIKA: a Monte Carlo code to simulate extensive air showers.* February 1998.

[271] M. Holler et al. Observations of the Crab Nebula with H.E.S.S. Phase II. *PoS*, ICRC2015:847, 2016. doi: 10.22323/1.236.0847. ArXiv 1509.02902.

[272] J. Aleksić et al. The major upgrade of the MAGIC telescopes, Part II: A performance study using observations of the Crab Nebula. *Astropart. Phys.*, 72:76–94, 2016. doi: 10.1016/j.astropartphys.2015.02.005. ArXiv 1409.5594.

[273] VERITAS Specifications. https://veritas.sao.arizona.edu/about-veritas-mainmenu-81/veritas-specifications-mainmenu-111.

[274] A. U. Abeysekara et al. Observation of the Crab Nebula with the HAWC Gamma-Ray Observatory. *Astrophys. J.*, 843(1):39, 2017. doi: 10.3847/1538-4357/aa7555. ArXiv 1701.01778.

[275] Fermi-LAT Performance. http://www.slac.stanford.edu/exp/glast/groups/canda/lat_Performance.htm.

[276] B. S. Acharya et al. *Science with the Cherenkov Telescope Array.* WSP, 2018. ISBN 9789813270084. doi: 10.1142/10986. ArXiv 1709.07997.

[277] E. Moulin et al. Dark Matter Programme. In *Science with the Cherenkov Telescope Array*, pages 45–81. 2019. doi: 10.1142/9789813270091_0004.

[278] A. Djouadi et al. The Minimal supersymmetric standard model: Group summary report. In *GDR (Groupement De Recherche) - Supersymetrie Montpellier, France, April 15-17, 1998*, 1998.

[279] J. Wess and J. Bagger. *Supersymmetry and supergravity.* Princeton University Press, Princeton, NJ, USA, 1992. ISBN 9780691025308.

[280] S. Dimopoulos and D. W. Sutter. The Supersymmetric flavor problem. *Nucl. Phys.*, B452:496–512, 1995. doi: 10.1016/0550-3213(95)00421-N.

[281] V. Khachatryan et al. Phenomenological MSSM interpretation of CMS searches in pp collisions at sqrt(s) = 7 and 8 TeV. *JHEP*, 10:129, 2016. doi: 10.1007/JHEP10(2016)129. ArXiv 1606.03577.

[282] I. J. R. Aitchison. Supersymmetry and the MSSM: An Elementary introduction. 2005.

[283] A. Hryczuk et al. Relic densities including Sommerfeld enhancements in the MSSM. *JHEP*, 03:069, 2011. doi: 10.1007/JHEP03(2011)069. ArXiv 1010.2172.

[284] X. Cui et al. Dark Matter Results From 54-Ton-Day Exposure of PandaX-II Experiment. *Phys. Rev. Lett.*, 119(18):181302, 2017. doi: 10.1103/PhysRevLett.119.181302. ArXiv 1708.06917.

[285] C. Amole et al. Dark Matter Search Results from the PICO-60 C_3F_8 Bubble Chamber. *Phys. Rev. Lett.*, 118(25):251301, 2017. doi: 10.1103/PhysRevLett.118.251301. ArXiv 1702.07666.

[286] E. Aprile et al. Dark Matter Search Results from a One Ton-Year Exposure of XENON1T. *Phys. Rev. Lett.*, 121(11):111302, 2018. doi: 10.1103/PhysRevLett.121.111302. ArXiv 1805.12562.

[287] M. G. Aartsen et al. Search for Neutrinos from Dark Matter Self-Annihilations in the center of the Milky Way with 3 years of IceCube/DeepCore. *Eur. Phys. J.*, C77(9):627, 2017. doi: 10.1140/epjc/s10052-017-5213-y. ArXiv 1705.08103.

[288] A. Cuoco et al. Constraining heavy dark matter with cosmic-ray antiprotons. *JCAP*, 1804(04):004, 2018. doi: 10.1088/1475-7516/2018/04/004. ArXiv 1711.05274.

[289] N. Padmanabhan and D. P. Finkbeiner. Detecting dark matter annihilation with CMB polarization: Signatures and experimental prospects. *Phys. Rev.*, D72:023508, 2005. doi: 10.1103/PhysRevD.72.023508.

[290] K. Kowalska. Phenomenological MSSM in light of new 13 TeV LHC data. *Eur. Phys. J.*, C76(12):684, 2016. doi: 10.1140/epjc/s10052-016-4536-4. ArXiv 1608.02489.

[291] F. U. Bernlochner et al. FlavBit: A GAMBIT module for computing flavour observables and likelihoods. *Eur. Phys. J.*, C77(11):786, 2017. doi: 10.1140/epjc/s10052-017-5157-2. ArXiv 1705.07933.

[292] R. Trotta et al. The Impact of priors and observables on parameter inferences in the Constrained MSSM. *JHEP*, 12:024, 2008. doi: 10.1088/1126-6708/2008/12/024. ArXiv 0809.3792.

[293] N. Nagata and S. Shirai. Higgsino Dark Matter in High-Scale Supersymmetry. *JHEP*, 01:029, 2015. doi: 10.1007/JHEP01(2015)029. ArXiv 1410.4549.

[294] M. Ibe et al. Mass Splitting between Charged and Neutral Winos at Two-Loop Level. *Phys. Lett.*, B721:252–260, 2013. doi: 10.1016/j.physletb.2013.03.015. ArXiv 1212.5989.

[295] M. Baumgart and V. Vaidya. Semi-inclusive wino and higgsino annihilation to LL. *JHEP*, 03:213, 2016. doi: 10.1007/JHEP03(2016)213. ArXiv 1510.02470.

[296] J. Hisano et al. Non-perturbative effect on dark matter annihilation and gamma ray signature from galactic center. *Phys. Rev.*, D71:063528, 2005. doi: 10.1103/PhysRevD.71.063528.

[297] M. Cirelli et al. Cosmology and Astrophysics of Minimal Dark Matter. *Nucl. Phys.*, B787:152–175, 2007. doi: 10.1016/j.nuclphysb.2007.07.023. ArXiv 0706.4071.

[298] O. Macias et al. Strong Evidence that the Galactic Bulge is Shining in Gamma Rays. 2019. ArXiv 1901.03822.

[299] T. A. Porter et al. High-Energy Gamma Rays from the Milky Way: Three-Dimensional Spatial Models for the Cosmic-Ray and Radiation Field Densities in the Interstellar Medium. *Astrophys. J.*, 846(1):67, 2017. doi: 10.3847/1538-4357/aa844d. ArXiv 1708.00816.

[300] D. Schlegel et al. Maps of dust IR emission for use in estimation of reddening and CMBR foregrounds. *Astrophys. J.*, 500:525, 1998. doi: 10.1086/305772.

[301] M. Ajello et al. 3FHL: The Third Catalog of Hard Fermi-LAT Sources. *Astrophys. J. Suppl.*, 232(2):18, 2017. doi: 10.3847/1538-4365/aa8221. ArXiv 1702.00664.

[302] A. Abramowski et al. Constraints on axionlike particles with H.E.S.S. from the irregularity of the PKS 2155-304 energy spectrum. *Phys. Rev.*, D88(10):102003, 2013. doi: 10.1103/PhysRevD.88.102003. ArXiv 1311.3148.

[303] D. Malyshev, A. Neronov, D. Semikoz, A. Santangelo, and J. Jochum. Improved limit on axion-like particles from γ-ray data on Perseus cluster. 2018. ArXiv 1805.04388.

[304] Manuel Meyer and J. Conrad. Sensitivity of the Cherenkov Telescope Array to the detection of axion-like particles at high gamma-ray opacities. *JCAP*, 1412(12):016, 2014. doi: 10.1088/1475-7516/2014/12/016. ArXiv 1410.1556.

université PARIS-SACLAY | ÉCOLE DOCTORALE PHENIICS

Titre : Étude du Centre Galactique et recherche de matière noire avec H.E.S.S.

Mots clés : Astronomie gamma, Télescopes Tcherenkov, Matière noire, Centre Galactique, Galaxies naines

Résumé : L'expérience H.E.S.S. (High Energy Spectroscopic System) composée de cinq télescopes Tcherenkov observe le ciel en rayons gamma au-delà d'une centaine de GeV jusqu'à plusieurs dizaines de TeV. Les rayons gamma sont produits par des phénomènes non-thermiques parmi les plus violents dans l'univers au voisinage d'objets astrophysiques comme les pulsars, supernovae ou trous noirs, mais pourraient être également produits par l'annihilation de particules de matière noire. De nombreuses sondes cosmologiques et astrophysiques suggèrent que 85% de la matière dans l'Univers est d'origine inconnue. Cette matière appelée matiére noire, de nature non baryonique, serait constituée de particules non encore découvertes dont les candidats privilégiés seraient des particules massives interagissant faiblement (WIMPs) avec la matière ordinaire, particules prédites au-delà du Modèle Standard de la physique des particules. Des particules de matière noire peuvent s'annihiler en particules du Modèle Standard dans les régions denses de l'Univers. Parmi les produits d'annihilations se trouvent les photons dont la détection à hautes énergies par des télescopes au sol à effet Tcherenkov pourrait apporter des informations uniques sur la nature de de la matière noire. H.E.S.S. observe des régions du ciel dense en matière noire comme le Centre Galactique et des galaxies naines satellites de la Voie Lactée. Une interprétation d'un excès de rayons gamma détectée au Centre Galactique par H.E.S.S. en termes d'accélération de protons par une population de pulsars millisecondes est présenté. 10 ans d'observations du Centre Galactique avec le réseau H.E.S.S. I de quatre télescopes, cinq ans de prise de données vers la région du Centre Galactique avec le réseau complet H.E.S.S. II, et un jeu de deux ans de données vers des galaxies naines découvertes récemment sont analysés. Les recherches de signaux d'annihilation de matière noire vers ces cibles ont produit les limites plus fortes à présent sur la section efficace d'annihilation de matière noire dans la plage en masse du TeV. Le potentiel de détection de matière noire avec le futur réseau de télescopes CTA (Cherenkov Telescope Array) vers la région central du halo Galactique est étudiés.

Title : Galactic Center study and dark matter searches with H.E.S.S.

Keywords : Gamma-ray astronomy, Cherenkov telescopes, Dark matter, Galactic Center, Dwarf galaxies

Abstract : The H.E.S.S. (High Energy Spectroscopic System) experiment is an array of five Cherenkov telescopes that observe the sky in gamma rays from about 100 GeV up to several ten TeV. Gamma rays are produced in violent non-thermal phenomena in the Universe in the neighborhood of pulsars, supernovae, black holes, ..., and could also be produced by the annihilation of dark matter particles. Numerous cosmological and astrophysical probes suggest that 85% of the total matter budget in the Universe is of unknown origin. This component of matter known as dark matter is non baryonic and could consist of yet undiscovered particles which privileged candidates are arguably massive particles with electroweak couplings with ordinary matter (WIMPs). Dark matter particles may annihilate into Standard Model particles in dense regions of the Universe. Among the annihilation products are photons whose detection at high energy with ground-based Cherenkov telescopes could bring unique information on the nature of the dark matter. H.E.S.S. observes dark-matter-dense regions of the sky such as the Galactic Center and dwarf galaxy satellites of the Milky Way. A study on the interpretation of an excess of gamma rays detected by H.E.S.S. at the Galactic Center in terms of acceleration of protons by a population of unresolved millisecond pulsars is performed. 10 years of observations of the Galactic Center with the four-telescope H.E.S.S.-I array, five years of data taking towards the Galactic Center region with the full H.E.S.S.-II array and a two-years dataset towards newly discovered dwarf spheroidal galaxies are analyzed. The search for dark matter annihilation signals towards these targets provided the strongest limits so far on dark matter annihilation cross section in gamma rays of TeV energies. The potential of dark matter detection with the upcoming Cherenkov Telescope Array (CTA) towards the inner Galactic halo are studied.

Université Paris-Saclay
Espace Technologique / Immeuble Discovery
Route de l'Orme aux Merisiers RD 128 / 91190 Saint-Aubin, France